

Air Force Institute of Technology

AFIT Scholar

Theses and Dissertations

Student Graduate Works

6-18-2015

Creep of Sylramic-iBN Fiber Tows at Elevated Temperature in Air and in Silicic Acid-Saturated Steam

Kevin B. Sprinkle

Follow this and additional works at: <https://scholar.afit.edu/etd>



Part of the [Structures and Materials Commons](#)

Recommended Citation

Sprinkle, Kevin B., "Creep of Sylramic-iBN Fiber Tows at Elevated Temperature in Air and in Silicic Acid-Saturated Steam" (2015). *Theses and Dissertations*. 206.

<https://scholar.afit.edu/etd/206>

This Thesis is brought to you for free and open access by the Student Graduate Works at AFIT Scholar. It has been accepted for inclusion in Theses and Dissertations by an authorized administrator of AFIT Scholar. For more information, please contact richard.mansfield@afit.edu.



**CREEP OF SYLRAMIC-IBN FIBER TOWS AT ELEVATED TEMPERATURE
IN AIR AND IN SILICIC ACID-SATURATED STEAM**

THESIS
JUNE 2015

Kevin B. Sprinkle, Captain, USAF

AFIT-ENY-15-J-46

**DEPARTMENT OF THE AIR FORCE
AIR UNIVERSITY**

AIR FORCE INSTITUTE OF TECHNOLOGY

Wright-Patterson Air Force Base, Ohio

**DISTRIBUTION STATEMENT A:
APPROVED FOR PUBLIC RELEASE; DISTRIBUTION UNLIMITED.**

The views expressed in this thesis are those of the author and do not reflect the official policy or position of the United States Air Force, Department of Defense, or the United States Government. This material is declared a work of the U.S. Government and is not subject to copyright protection in the United States.

AFIT-ENY-15-J-46

**CREEP OF SYLRAMIC-FIBER TOWS AT ELEVATED TEMPERATURE
IN AIR AND IN SILICIC ACID-SATURATED STEAM**

THESIS

Presented to the Faculty

Department of Aeronautical and Astronautical Engineering

Graduate School of Engineering and Management

Air Force Institute of Technology

Air University

Air Education and Training Command

In Partial Fulfillment of the Requirements for the

Degree of Master of Science in Material Science

Kevin B. Sprinkle, B.S.

Captain, USAF

June 2015

DISTRIBUTION STATEMENT A:
APPROVED FOR PUBLIC RELEASE; DISTRIBUTION UNLIMITED.

AFIT-ENY-15-J-46

**CREEP OF SYLRAMIC-IBN FIBER TOWS AT ELEVATED TEMPERATURE
IN AIR AND IN SILICIC ACID-SATURATED STEAM**

Kevin B. Sprinkle, B.S.
Captain, USAF

Committee Membership:

Dr. Marina B. Ruggles-Wrenn
Chair

Dr. Randall S. Hay
Member

Dr. Thomas G. Eason III
Member

Abstract

Oxidation of SiC to SiO₂ is a critical concern for structural ceramics in aerospace applications, such as thermal protection systems (TPS). Passive oxidation of SiC is in most cases controlled by interstitial diffusion of O₂ molecules through the amorphous silica (SiO₂) scale. Advanced load-bearing TPS concepts imply that the SiO₂ scale will be under externally applied stress. Externally applied tensile stress increases oxidation rates of silicon, and recently the same has been demonstrated for SiC fibers. Unlike silicon, when SiC oxidizes carbon is incorporated in the oxide scale. Network carbon in SiO₂ stiffens the structure, making it less permeable to O₂. The slower oxidation rates of SiC compared to those of silicon are attributed to carbon in the oxide scale. Oxidation of SiC-SiC ceramic matrix composites (CMCs) has been thoroughly studied, but there are still aspects that are poorly understood, and a comprehensive modeling framework for sustainment and design is lacking.

Stressed oxidation experiments on Sylramic-iBN fiber tows were performed to evaluate the novel fiber's mechanical performance, creep behavior, and creep mechanisms. This research effort investigated creep response of Sylramic-iBN fiber tows at elevated temperatures in both air and in silicic acid-saturated steam environments. Creep experiments were conducted at creep stresses ranging from 127 to 762 MPa at 400°C and 500°C in order to examine the mechanical behavior of the Sylramic-iBN fiber tows at temperatures below and above the melting point of boria (450°C). Sylramic-iBN fibers are known to have excellent creep resistance, better than most other non-oxide

fibers and significantly better than oxide fibers. These fibers have a near-stoichiometric SiC composition, so they are a strong candidate for use in advanced aerospace CMCs.

This research effort is a pilot program on the study of the effects of steam on Sylramic-iBN fibers. Previous attempts to study creep of SiC fiber tows in steam at elevated temperatures at the Air Force Institute of Technology's (AFIT) Mechanics of Advanced Aerospace Materials Research Laboratory have yielded inconclusive results. Prior work at AFIT showed that the steam extracted silicon from the fiber tow and became saturated with silicic acid ($\text{Si}[\text{OH}]_4$). As the steam traveled along the SiC fiber, it also chemically altered the fiber surface producing inconsistent chemical compositions along the length of the fiber tow specimen. Along the fiber portion exposed to the unsaturated steam, the fiber experienced a chemical change leading to material loss, while the fiber portion exposed to the saturated steam experienced a silica scale growth along the fiber surface. A new test facility had to be designed to accurately evaluate the effects of steam on SiC fibers. The facility design incorporated an apparatus for saturating steam with silicic acid prior to entering the test chamber. The facility was validated by performing creep tests of SiC fiber tows in saturated steam at elevated temperature.

Acknowledgements

This thesis could not have been written without the guidance of Dr. Marina Ruggles-Wrenn. She always made me feel like a priority in her schedule, even on the most hectic days. She always encouraged me, especially when facing the most challenging of times in my Master's degree. Most importantly, she helped refine my skills as a researcher and taught me the valuable lesson to know when "good" is "good enough" (otherwise achieving perfection may never produce results). I would like to thank Dr. R. H. and Dr. K. S. for their expertise on scanning electron microscopy imaging and the confirmation of my research method. I would like to thank J. H. and W. L. for their urgency and patience with obtaining laboratory equipment on short notices, and for their technical support. I would like to thank S. R. for his constant encouragement and assistance both in and outside of the laboratory. In all honesty, my research experience would not have been the same without him working alongside of me. I would like to thank my parents and T. A. for their daily words of encouragement and love. Finally, and most importantly, I would like to thank God for His grace, patience, and wisdom enabling me to complete this milestone in my life.

Kevin B. Sprinkle

Table of Contents

Abstract	iv
Acknowledgements	vi
Table of Figures	ix
Table of Tables	xix
I. Introduction.....	1
II. Background.....	8
2.1 Ceramic Matrix Composites	8
2.2 Creep in Ceramics.....	13
2.3 Silicon Carbide Fibers.....	16
2.4 Fiber Coatings.....	23
2.5 Previous Research Efforts.....	27
III. Material and Test Specimen.....	35
3.1 Material.....	35
3.2 Test Specimen.....	36
IV. Experimental Arrangements and Procedures.....	38
4.1 Experimental Facility.....	38
4.1.1 Temperature Profiles	43
4.1.2 Strain Measurement.....	45
4.2 Obtaining Steam.....	49
4.3 Improving the Experimental Facility	52
V. Monotonic Tension and Tensile Creep of Sylramic-iBN Fiber Tows	61
5.1 Monotonic Tension	61

5.2 Creep of Sylramic-iBN Fiber Tows at 400°C in Air and in Silicic Acid-Saturated Steam.....	64
5.3 Creep of Sylramic-iBN Fiber Tows at 500°C in Air and in Silicic Acid-Saturated Steam.....	68
5.4 Microstructure of Sylramic-iBN Fiber Tow	72
VI. Conclusions and Recommendations	100
6.1 Conclusions.....	100
6.2 Recommendations for Future Research	102
Appendix A: Stress-Weight Index Table.....	104
Appendix B: Specifications of Furnace and Steam Generator Settings	105
Appendix C: Supporting SEM Micrographs.....	106
Bibliography	153

Table of Figures

Figure 1: Superalloy turbine blade with cooling ports, reproduced from Shillig [9]	4
Figure 2: Service temperature limits of various classes of materials.....	5
Figure 3: The strength-weight ratios of select aerospace materials as a function of temperature. Note the significant improvement of CMCs over traditional materials at high temperatures.....	6
Figure 4: Service temperatures for various high-temperature aerospace materials	6
Figure 5: Typical stress-strain curves for monolithic ceramics and CMCs in tension	10
Figure 6: Crack propagation for weak fiber-matrix interface	10
Figure 7: Crack propagation as a function of fiber-matrix interface	11
Figure 8: Scanning Electron Microscopy (SEM) of extensive fiber pullout and matrix cracking of BN-coated Nextel 480 fibers (left), and uncoated Hi-Nicalon fibers (right)	12
Figure 9: Stages of a typical creep curve	14
Figure 10: Various steps involved in processing non-oxide fibers via polymer rout	16
Figure 11: Rupture strength behavior for various high-performance SiC fibers at 1400°C in air. Sylramic and Sylramic-iBN from COI Ceramics, Tyranno SA fiber from UBE Industries; Hi-Nicalon Type S fiber from Nippon, Carbon	23
Figure 12: Nicalon fiber with pyrocarbon coating.....	24
Figure 13: Crack deflection through the multi-layered BN coating deposited on SiC fiber tow.....	26
Figure 14: Different simple or engineered interphases used SiC-matrix composites: (a) single layer pyrocarbon or hexagonal BN interphases, (b) porous SiC single layer interphase, (c) multilayered (X-Y) _n interphase, with X=PyC or BN and Y=SiC (schematic), (d) crack deflection in a multilayered (PyC-SiC) ₁₀ interphase, according to Naslain (a-c) and Bertrand et al.	27
Figure 15: Typical creep-rupture curves for various near stoichiometric SiC fibers	30
Figure 16: Rupture strengths of SiC fibers at 1400 °C in air.....	30
Figure 17: Stress-Strain curves for different fiber-type melt-infiltrated composites.....	32

Figure 18: Tensile creep total strain (elastic plus time-dependent) curves at (a) 1200°C and (b) 1315°C for different SiC fiber-type melt-infiltrated composites.....	33
Figure 19: Fiber tow creep test specimen preparation process	37
Figure 20: Two-zone resistance-heated MTS 653.03A furnace with SiC heating elements, R type control thermocouples and a 90-mm (3.5-in.) hot zone	39
Figure 21: Alumina susceptor and feeding tube assembled in one half of the furnace, along with fiber tow specimen mounted and running through the alumina susceptor	40
Figure 22: Fiber tow specimen mounted in the dead weight creep testing facility	42
Figure 23 : Temperature profile obtained for Sylramic-iBN fiber tow specimen in steam at 400°C (a) and 500°C (b)	44
Figure 24: HGA-H (MHI) steam generator	49
Figure 25: Effect of stem impinging on fiber tows upon entry into the test chamber	50
Figure 26: SEM micrographs of the Hi-Nicalon™-S fiber tows subjected to creep at 800°C in steam. Variations along the length of the fiber tow are evident. (a) Fiber degradation due to active oxidation, typically found in bottom sections of the fiber tow. (b) SiO ₂ scale growth typically found in top sections of the fiber tow	52
Figure 27: Steam bleed-off system designed to achieve the desired steam temperature and flow rate in the test chamber	56
Figure 28: Layers of alumina block insulation and aluminosilicate blanket insulation assembled between CX1300 heating unit and test furnace.....	57
Figure 29: Silica wool placed inside the heating tube to achieve saturation of heated steam with silicic acid.....	58
Figure 30: The newly designed test facility permits testing of SiC fiber tows at elevated temperature in silicic acid-saturated steam	59
Figure 31: Batch to batch variation in Archimedes density for BN/SiC coated Sylramic fiber perform specimens	64
Figure 32: Batch to batch variation in open porosity for BN/SiC coated Sylramic fiber perform specimens	64
Figure 33: Creep strain vs. time curves for Sylramic-iBN fiber tows obtained at 400°C in compressed dry air	66
Figure 34: Creep strain vs. time curve obtained for Sylramic-iBN fiber tow at 400°C in silicic acid-saturated steam	67

Figure 35: Creep strain vs. time curves obtained for Sylramic-iBN fiber tows at 500°C in compressed dry air	69
Figure 36: Sylramic-iBN fiber tow specimen “Air 16” after 100 h at 500°C in air under applied load of 127 MPa.....	70
Figure 37: Creep strain vs. time curve obtained for Sylramic-iBN fiber tow at 500°C in silicic acid-saturated steam	71
Figure 38: Sylramic-iBN fiber tow specimen mounted on an aluminum SEM puck.....	72
Figure 39: SEM micrograph of an untested Sylramic-iBN fiber.....	74
Figure 40: SEM micrograph of the cross-section of an untested Sylramic-iBN fiber. It is possible that the BN fiber coating is shown as the significantly brighter layer around the fiber.	75
Figure 41: SEM micrographs (a) and (b) of the Sylramic-iBN specimen “Air 5” tested at 400°C in air showing the cross-section and BN coating of a fiber cut at mid-length ($\sigma_{cr} = 508$ MPa, $t_f = 0$ s)	77
Figure 42: SEM micrograph of the Sylramic-iBN specimen “Air 5” tested at 400°C in air showing the rough surface of a fiber at mid-fiber length ($\sigma_{cr} = 508$ MPa, $t_f = 0$ s)	78
Figure 43: SEM micrograph of the Sylramic-iBN specimen “Air 4” tested at 400°C in air showing the cross-section and BN coating of a fiber cut at mid-length ($\sigma_{cr} = 444$ MPa, $t_f > 100$ h)	79
Figure 44: SEM micrograph of the Sylramic-iBN specimen “Air 4” tested at 400°C in air showing the rough surface of a fiber at mid-fiber length ($\sigma_{cr} = 444$ MPa, $t_f > 100$ h).....	80
Figure 45: SEM micrograph of the Sylramic-iBN specimen “Air 11” tested at 500°C in air showing general surface characteristics of a fiber at mid-fiber length ($\sigma_{cr} = 508$ MPa, $t_f = 0$ s)	83
Figure 46: SEM micrograph of the Sylramic-iBN specimen “Air 11” tested at 500°C in air showing the rough surface of a fiber at mid-fiber length ($\sigma_{cr} = 508$ MPa, $t_f = 0$ s).....	84
Figure 47: SEM micrograph of the Sylramic-iBN specimen “Air 11” tested at 500°C in air showing a fiber in the vicinity of fracture ($\sigma_{cr} = 508$ MPa, $t_f = 0$ s).....	85
Figure 48: SEM micrograph of Sylramic-iBN specimen “Air 11” tested at 500°C in air showing the fracture surface. ($\sigma_{cr} = 508$ MPa, $t_f = 0$ s).....	86

Figure 49: SEM micrograph of the Sylramic-iBN specimen “Air 6” tested at 500°C in air showing the rough fiber surface at mid-fiber length ($\sigma_{cr} = 508$ MPa, $t_f \geq 25$ h)....	87
Figure 50: SEM micrograph of the Sylramic-iBN specimen “Air 16” tested at 500°C in air showing a fiber at mid-fiber length ($\sigma_{cr} = 127$ MPa, $t_f > 100$ h)	88
Figure 51: SEM micrograph of the Sylramic-iBN specimen “SS 20” tested at 400°C in steam showing the rough fiber surface at mid-fiber length ($\sigma_{cr} = 508$ MPa, $t_f = 0$ s)	91
Figure 52: SEM micrograph of the Sylramic-iBN specimen “SS 20” tested at 400°C in steam showing a fiber in the vicinity of fracture ($\sigma_{cr} = 508$ MPa, $t_f = 0$ s).....	92
Figure 53: SEM micrograph of the Sylramic-iBN specimen “SS 17” tested at 400°C in steam showing a fiber at mid-fiber length ($\sigma_{cr} = 444$ MPa, $t_f > 100$ h)	93
Figure 54: SEM micrograph of the Sylramic-iBN specimen “SS 17” tested at 400°C in steam showing cross section of the fiber cut at mid-fiber length ($\sigma_{cr} = 444$ MPa, $t_f > 100$ h).....	94
Figure 55: SEM micrograph of the Sylramic-iBN specimen “SS 23” tested at 500°C in steam showing rough fiber surface at mid-fiber length ($\sigma_{cr} = 381$ MPa, $t_f = 0$ s)....	95
Figure 56: SEM micrograph of the Sylramic-iBN specimen “SS 23” tested at 500°C in steam showing a fiber in the vicinity of fracture ($\sigma_{cr} = 381$ MPa, $t_f = 0$ s).....	96
Figure 57: SEM micrograph of the Sylramic-iBN specimen “SS 24” tested at 500°C in steam showing rough fiber surface at mid-fiber length ($\sigma_{cr} = 254$ MPa, $t_f > 100$ h)	97
Figure 58: SEM micrograph of the Sylramic-iBN fiber tow specimens: (a) untested specimen, (b) Air-4 specimen subjected to 100 h of creep at 400°C in air, (c) Air-6 specimen subjected to 100 h of creep at 500°C in air, (d) SS-17 specimen subjected to 100 h of creep at 400°C in steam, (e) SS-24 specimen subjected to 100 h of creep at 500°C in steam.	99
Figure 59: SEM micrograph of a virgin Sylramic-iBN fiber (1)	106
Figure 60: SEM micrograph of a virgin Sylramic-iBN fiber (2)	106
Figure 61: SEM micrograph of a virgin Sylramic-iBN fiber (3)	107
Figure 62: SEM micrograph of a virgin Sylramic-iBN fiber (4)	107
Figure 63: SEM micrograph of a virgin Sylramic-iBN fiber (5)	108

Figure 64: SEM micrograph of a virgin Sylramic-iBN fiber (6)	108
Figure 65: SEM micrograph of a virgin Sylramic-iBN fiber; note the uniformity amongst the fibers (1)	109
Figure 66: SEM micrograph of a virgin Sylramic-iBN fiber; note the uniformity amongst the fibers (2)	109
Figure 67: SEM micrograph of a virgin Sylramic-iBN fiber observed at a cut surface (1)	110
Figure 68: SEM micrograph of a virgin Sylramic-iBN fiber observed at a cut surface (2)	110
Figure 69: SEM micrograph of a virgin Sylramic-iBN fiber observed at a cut surface (3)	111
Figure 70: SEM micrograph of the cross section of a virgin Sylramic-iBN fiber	111
Figure 71: SEM micrograph of the Sylramic-iBN specimen “Air 4” examining general surface characteristics of fibers at mid-fiber length ($\sigma_{cr} = 444$ MPa, $t_f > 100$ h)..	112
Figure 72: SEM micrograph of the Sylramic-iBN specimen “Air 5” examining general surface characteristics of fibers at mid-fiber length ($\sigma_{cr} = 508$ MPa, $t_f = 0$ s)	112
Figure 73: SEM micrograph of the Sylramic-iBN specimen “Air 4” examining rough surface of a fiber at mid-fiber length ($\sigma_{cr} = 444$ MPa, $t_f > 100$ h)	113
Figure 74: SEM micrograph of the Sylramic-iBN specimen “Air 4” examining rough surface of a fiber at mid-fiber length ($\sigma_{cr} = 444$ MPa, $t_f > 100$ h)	113
Figure 75: SEM micrograph of the Sylramic-iBN specimen “Air 4” examining rough surface of a fiber at mid-fiber length ($\sigma_{cr} = 444$ MPa, $t_f > 100$ h)	114
Figure 76: SEM micrograph of the Sylramic-iBN specimen “Air 4” examining rough surface of a fiber at mid-fiber length ($\sigma_{cr} = 444$ MPa, $t_f > 100$ h)	114
Figure 77: SEM micrograph of the Sylramic-iBN specimen “Air 5” examining rough surface of a fiber at mid-fiber length ($\sigma_{cr} = 508$ MPa, $t_f = 0$ s)	115
Figure 78: SEM micrograph of the Sylramic-iBN specimen “Air 5” examining rough surface of a fiber at mid-fiber length ($\sigma_{cr} = 508$ MPa, $t_f = 0$ s)	115
Figure 79: SEM micrograph of the Sylramic-iBN specimen “Air 5” examining rough surface of a fiber at mid-fiber length ($\sigma_{cr} = 508$ MPa, $t_f = 0$ s)	116
Figure 80: SEM micrograph of the Sylramic-iBN specimen “Air 5” examining rough surface of a fiber at mid-fiber length ($\sigma_{cr} = 508$ MPa, $t_f = 0$ s)	116

Figure 81: SEM micrograph of the Sylramic-iBN specimen “Air 5” examining cross section of a fiber ($\sigma_{cr} = 508$ MPa, $t_f = 0$ s).....	117
Figure 82: SEM micrograph of the Sylramic-iBN specimen “Air 5” examining cross section of a fiber ($\sigma_{cr} = 508$ MPa, $t_f = 0$ s).....	117
Figure 83: SEM micrograph of the Sylramic-iBN specimen “Air 5” examining fracture surface of a fiber ($\sigma_{cr} = 508$ MPa, $t_f = 0$ s)	118
Figure 84: SEM micrograph of the Sylramic-iBN specimen “Air 11” examining rough surface of several fibers at mid-fiber length ($\sigma_{cr} = 508$ MPa, $t_f = 0$ s)	118
Figure 85: SEM micrograph of the Sylramic-iBN specimen “Air 11” examining rough surface of a fiber at mid-fiber length ($\sigma_{cr} = 508$ MPa, $t_f = 0$ s)	119
Figure 86: SEM micrograph of the Sylramic-iBN specimen “Air 11” examining rough surface of a fiber at mid-fiber length ($\sigma_{cr} = 508$ MPa, $t_f = 0$ s)	119
Figure 87: SEM micrograph of the Sylramic-iBN specimen “Air 11” examining rough surface of a fiber at mid-fiber length ($\sigma_{cr} = 508$ MPa, $t_f = 0$ s)	120
Figure 88: SEM micrograph of the Sylramic-iBN specimen “Air 11” examining rough surface of a fiber at mid-fiber length ($\sigma_{cr} = 508$ MPa, $t_f = 0$ s)	120
Figure 89: SEM micrograph of the Sylramic-iBN specimen “Air 11” examining fracture surface of a fiber ($\sigma_{cr} = 508$ MPa, $t_f = 0$ s)	121
Figure 90: SEM micrograph of the Sylramic-iBN specimen “Air 11” examining fracture surface of a fiber ($\sigma_{cr} = 508$ MPa, $t_f = 0$ s)	121
Figure 91: SEM micrograph of the Sylramic-iBN specimen “Air 11” examining fracture surface of a fiber ($\sigma_{cr} = 508$ MPa, $t_f = 0$ s)	122
Figure 92: SEM micrograph of the Sylramic-iBN specimen “Air 11” examining fracture surface of a fiber ($\sigma_{cr} = 508$ MPa, $t_f = 0$ s)	122
Figure 93: SEM micrograph of the Sylramic-iBN specimen “Air 11” examining fracture surface of a fiber ($\sigma_{cr} = 508$ MPa, $t_f = 0$ s)	123
Figure 94: SEM micrograph of the Sylramic-iBN specimen “Air 11” examining fracture surface of a fiber ($\sigma_{cr} = 508$ MPa, $t_f = 0$ s)	123
Figure 95: SEM micrograph of the Sylramic-iBN specimen “Air 11” examining a cut surface of a fiber at mid-fiber length ($\sigma_{cr} = 508$ MPa, $t_f = 0$ s)	124
Figure 96: SEM micrograph of the Sylramic-iBN specimen “Air 11” examining a cut surface of a fiber at mid-fiber length ($\sigma_{cr} = 508$ MPa, $t_f = 0$ s)	124

Figure 97: SEM micrograph of the Sylramic-iBN specimen “Air 16” examining general surface characteristics of a fiber ($\sigma_{cr} = 127$ MPa, $t_f \geq 100$ h)	125
Figure 98: SEM micrograph of the Sylramic-iBN specimen “Air 16” examining general surface characteristics of a fiber ($\sigma_{cr} = 127$ MPa, $t_f \geq 100$ h)	125
Figure 99: SEM micrograph of the Sylramic-iBN specimen “Air 16” examining general surface characteristics of a fiber ($\sigma_{cr} = 127$ MPa, $t_f \geq 100$ h)	126
Figure 100: SEM micrograph of the Sylramic-iBN specimen “Air 16” examining rough surface of a fiber ($\sigma_{cr} = 127$ MPa, $t_f \geq 100$ h)	126
Figure 101: SEM micrograph of the Sylramic-iBN specimen “Air 16” examining rough surface of a fiber ($\sigma_{cr} = 127$ MPa, $t_f \geq 100$ h)	127
Figure 102: SEM micrograph of the Sylramic-iBN specimen “Air 16” examining rough surface of a fiber ($\sigma_{cr} = 127$ MPa, $t_f \geq 100$ h)	127
Figure 103: SEM micrograph of the Sylramic-iBN specimen “Air 6” examining a cut surface of a fiber at mid-fiber length ($\sigma_{cr} = 508$ MPa, $t_f > 25$ h)	128
Figure 104: SEM micrograph of the Sylramic-iBN specimen “Air 6” examining rough surface of a fiber at mid-fiber length ($\sigma_{cr} = 508$ MPa, $t_f > 25$ h)	128
Figure 105: SEM micrograph of the Sylramic-iBN specimen “Air 6” examining a cut surface of a fiber at mid-fiber length ($\sigma_{cr} = 508$ MPa, $t_f > 25$ h)	129
Figure 106: SEM micrograph of the Sylramic-iBN specimen “Air 6” examining a cross section of a cut surface of a fiber ($\sigma_{cr} = 508$ MPa, $t_f > 25$ h)	129
Figure 107: SEM micrograph of the Sylramic-iBN specimen “Air 6” examining a cut surface of a fiber at mid-fiber length ($\sigma_{cr} = 508$ MPa, $t_f > 25$ h)	130
Figure 108: SEM micrograph of the Sylramic-iBN specimen “Air 6” examining a cut surface of a fiber at mid-fiber length ($\sigma_{cr} = 508$ MPa, $t_f > 25$ h)	130
Figure 109: SEM micrograph of the Sylramic-iBN specimen “Air 6” examining a cut surface of a fiber at mid-fiber length; notice the rough surface and BN coating ($\sigma_{cr} = 508$ MPa, $t_f > 25$ h).....	131
Figure 110: SEM micrograph of the Sylramic-iBN specimen “SS 17” examining rough surface of a fiber at mid-fiber length ($\sigma_{cr} = 444$ MPa, $t_f \geq 100$ h)	131
Figure 111: SEM micrograph of the Sylramic-iBN specimen “SS 17” examining rough surface of a fiber at mid-fiber length ($\sigma_{cr} = 444$ MPa, $t_f \geq 100$ h)	132
Figure 112: SEM micrograph of the Sylramic-iBN specimen “SS 17” examining rough surface of a fiber at mid-fiber length ($\sigma_{cr} = 444$ MPa, $t_f \geq 100$ h)	132

Figure 113: SEM micrograph of the Sylramic-iBN specimen “SS 17” examining rough surface of a fiber at mid-fiber length ($\sigma_{cr} = 444$ MPa, $t_f \geq 100$ h) 133

Figure 114: SEM micrograph of the Sylramic-iBN specimen “SS 17” examining rough surface of a fiber at mid-fiber length ($\sigma_{cr} = 444$ MPa, $t_f \geq 100$ h) 133

Figure 115: SEM micrograph of the Sylramic-iBN specimen “SS 17” examining general surface characteristics of a fiber at mid-fiber length ($\sigma_{cr} = 444$ MPa, $t_f \geq 100$ h) 134

Figure 116: SEM micrograph of the Sylramic-iBN specimen “SS 17” examining general surface characteristics of a fiber at mid-fiber length ($\sigma_{cr} = 444$ MPa, $t_f \geq 100$ h). 134

Figure 117: SEM micrograph of the Sylramic-iBN specimen “SS 17” examining a cut surface of a fiber at mid-fiber length ($\sigma_{cr} = 444$ MPa, $t_f \geq 100$ h) 135

Figure 118: SEM micrograph of the Sylramic-iBN specimen “SS 17” examining a cut surface of a fiber at mid-fiber length; notice the rough surface ($\sigma_{cr} = 444$ MPa, $t_f \geq 100$ h) 135

Figure 119: SEM micrograph of the Sylramic-iBN specimen “SS 20” examining rough surface of a fiber toward mid-fiber length ($\sigma_{cr} = 508$ MPa, $t_f = 0$ s) 136

Figure 120: SEM micrograph of the Sylramic-iBN specimen “SS 20” examining rough surface of a fiber toward mid-fiber length ($\sigma_{cr} = 508$ MPa, $t_f = 0$ s) 136

Figure 121: SEM micrograph of the Sylramic-iBN specimen “SS 20” examining rough surface of a fiber toward mid-fiber length ($\sigma_{cr} = 508$ MPa, $t_f = 0$ s) 137

Figure 122: SEM micrograph of the Sylramic-iBN specimen “SS 20” examining rough surface of a fiber toward mid-fiber length ($\sigma_{cr} = 508$ MPa, $t_f = 0$ s) 137

Figure 123: SEM micrograph of the Sylramic-iBN specimen “SS 20” examining rough surface of a fiber toward mid-fiber length ($\sigma_{cr} = 508$ MPa, $t_f = 0$ s) 138

Figure 124: SEM micrograph of the Sylramic-iBN specimen “SS 20” examining rough surface of a fiber at mid-fiber length; notice surface pieces have stripped off ($\sigma_{cr} = 508$ MPa, $t_f = 0$ s)..... 138

Figure 125: SEM micrograph of the Sylramic-iBN specimen “SS 20” examining rough surface of a fiber toward fracture end ($\sigma_{cr} = 508$ MPa, $t_f = 0$ s) 139

Figure 126: SEM micrograph of the Sylramic-iBN specimen “SS 20” examining rough surface of a fiber toward fracture end ($\sigma_{cr} = 508$ MPa, $t_f = 0$ s) 139

Figure 127: SEM micrograph of the Sylramic-iBN specimen “SS 20” examining rough surface of a fiber toward fracture end ($\sigma_{cr} = 508$ MPa, $t_f = 0$ s) 140

Figure 128: SEM micrograph of the Sylramic-iBN specimen “SS 20” examining rough surface of a fiber toward fracture end ($\sigma_{cr} = 508$ MPa, $t_f = 0$ s) 140

Figure 129: SEM micrograph of the Sylramic-iBN specimen “SS 17” examining fracture end of a fiber; notice the rough surface ($\sigma_{cr} = 444$ MPa, $t_f \geq 100$ h) 141

Figure 130: SEM micrograph of the Sylramic-iBN specimen “SS 17” examining fracture end of a fiber ($\sigma_{cr} = 444$ MPa, $t_f \geq 100$ h)..... 141

Figure 131: SEM micrograph of the Sylramic-iBN specimen “SS 17” examining fracture end of a fiber; notice the rough surface ($\sigma_{cr} = 444$ MPa, $t_f \geq 100$ h) 142

Figure 132: SEM micrograph of the Sylramic-iBN specimen “SS 23” examining rough surface of a fiber toward mid-fiber length ($\sigma_{cr} = 381$ MPa, $t_f = 0$ s) 142

Figure 133: SEM micrograph of the Sylramic-iBN specimen “SS 23” examining rough surface of a fiber toward mid-fiber length ($\sigma_{cr} = 381$ MPa, $t_f = 0$ s) 143

Figure 134: SEM micrograph of the Sylramic-iBN specimen “SS 23” examining rough surface of a fiber toward mid-fiber length ($\sigma_{cr} = 381$ MPa, $t_f = 0$ s) 143

Figure 135: SEM micrograph of the Sylramic-iBN specimen “SS 23” examining rough surface of a fiber toward mid-fiber length ($\sigma_{cr} = 381$ MPa, $t_f = 0$ s) 144

Figure 136: SEM micrograph of the Sylramic-iBN specimen “SS 23” examining rough surface of a fiber toward mid-fiber length ($\sigma_{cr} = 381$ MPa, $t_f = 0$ s) 144

Figure 137: SEM micrograph of the Sylramic-iBN specimen “SS 23” examining rough surface of a fiber toward mid-fiber length ($\sigma_{cr} = 381$ MPa, $t_f = 0$ s) 145

Figure 138: SEM micrograph of the Sylramic-iBN specimen “SS 23” examining cut surface of a fiber at mid-fiber length ($\sigma_{cr} = 381$ MPa, $t_f = 0$ s) 145

Figure 139: SEM micrograph of the Sylramic-iBN specimen “SS 23” examining fracture surface of a fiber ($\sigma_{cr} = 381$ MPa, $t_f = 0$ s) 146

Figure 140: SEM micrograph of the Sylramic-iBN specimen “SS 23” examining fracture surface of a fiber ($\sigma_{cr} = 381$ MPa, $t_f = 0$ s) 146

Figure 141: SEM micrograph of the Sylramic-iBN specimen “SS 23” examining fracture surface of a fiber ($\sigma_{cr} = 381$ MPa, $t_f = 0$ s) 147

Figure 142: SEM micrograph of the Sylramic-iBN specimen “SS 24” examining general surface characteristics of multiple fibers; notice the uniformity between the fibers ($\sigma_{cr} = 254$ MPa, $t_f > 100$ h) 147

Figure 143: SEM micrograph of the Sylramic-iBN specimen “SS 24” examining rough surface of a fiber toward mid-fiber length ($\sigma_{cr} = 254$ MPa, $t_f > 100$ h)..... 148

Figure 144: SEM micrograph of the Sylramic-iBN specimen “SS 24” examining rough surface of a fiber toward mid-fiber length ($\sigma_{cr} = 254$ MPa, $t_f > 100$ h)..... 148

Figure 145: SEM micrograph of the Sylramic-iBN specimen “SS 24” examining rough surface of a fiber toward mid-fiber length ($\sigma_{cr} = 254$ MPa, $t_f > 100$ h)..... 149

Figure 146: SEM micrograph of the Sylramic-iBN specimen “SS 24” examining rough surface of a fiber toward mid-fiber length ($\sigma_{cr} = 254$ MPa, $t_f > 100$ h)..... 149

Figure 147: SEM micrograph of the Sylramic-iBN specimen “SS 24” examining rough surface of a fiber toward mid-fiber length ($\sigma_{cr} = 254$ MPa, $t_f > 100$ h)..... 150

Figure 148: SEM micrograph of the Sylramic-iBN specimen “SS 24” examining rough surface of a fiber toward mid-fiber length ($\sigma_{cr} = 254$ MPa, $t_f > 100$ h)..... 150

Figure 149: SEM micrograph of the Sylramic-iBN specimen “SS 24” examining cut surface of a fiber at mid-fiber length; notice the BN coating ($\sigma_{cr} = 254$ MPa, $t_f > 100$ h)..... 151

Figure 150: SEM micrograph of the Sylramic-iBN specimen “SS 24” examining cut surface of a fiber at mid-fiber length; notice the BN coating ($\sigma_{cr} = 254$ MPa, $t_f > 100$ h)..... 151

Figure 151: SEM micrograph of the Sylramic-iBN specimen “SS 24” examining cut surface of a fiber at mid-fiber length; notice the BN coating ($\sigma_{cr} = 254$ MPa, $t_f > 100$ h)..... 152

Table of Tables

Table 1: Composition, Young's modulus and density of first generation Nippon Carbon SiC fibers	17
Table 2: Details of manufacturer, cross linking method, composition, and diameter of all three generations of fibers.....	21
Table 3: Specifications and Material Properties of various SiC Fiber Tows.....	22
Table 4: Nominal properties of near stoichiometric β SiC fibers	29
Table 5: Composite room temperature mechanical properties	32
Table 6: Sylramic-iBN fiber tow properties	36
Table 7 : Effective gage lengths of Sylramic-iBN fiber tows in air and in steam at test temperatures	49
Table 8: Ultimate Tensile Strength (UTS) of Sylramic-iBN fiber tows at various temperatures	61
Table 9 Relationship between microstructure, fiber roughness (denoted by R_q), and interfacial sliding stress of near-stoichiometric SiC fibers	63
Table 10: Summary of creep results for Sylramic-iBN SiC fiber tows obtained at 400°C in dry air and in silicic acid-saturated steam.....	65
Table 11: Summary of creep results for Sylramic-iBN SiC fiber tows obtained at 500°C in dry air and in silicic acid-saturated steam.....	68

CREEP OF SYLRAMIC-IBN FIBER TOWS AT ELEVATED TEMPERATURE IN AIR AND IN SILICIC ACID-SATURATED STEAM

I. Introduction

Technology advancements are limited by available natural and engineered materials, and thus drive research and development of improved material systems. In the aerospace industry, there has always been a constant drive toward higher performance in fuel efficiency, engine thrust, flight duration, and durable components. Advanced aerospace applications such as aircraft turbine engine components, hypersonic flight vehicles, and spacecraft reentry thermal protection systems require structural materials that have superior mechanical properties in extreme environments. These needs prompted research into lighter and more durable materials for high-temperature aerospace applications, such as engine turbine components. The class of materials which shows the greatest potential as a material solution is composites, specifically Ceramic Matrix Composites (CMCs).

The selection of ceramics over other classes of materials requires careful consideration. Ceramics generally have higher hardness, strength and elastic modulus than metals and polymers, along with lower density, thermal expansion coefficient and thermal conductivity [1]. These material characteristics, especially low density and thermal expansion coefficients, are of particular interest in the aerospace applications mentioned above. Ceramics can be categorized as conventional ceramics, such as tile and brick, and advanced or engineered ceramics, such as Silicate, Alumina, Cordierite, and Mullite. A conventional ceramic is typically a monolithic material with high strength,

stiffness, hardness, wear resistance, and low density. It is fairly chemically inert, but has little to no mobility of dislocations, resulting in no plastic deformation. Because plastic deformation is an energy-absorbing phenomenon, monolithic ceramics exhibit poor toughness in tensile and impact loads, leading to catastrophic failure under mechanical loading. This undesirable behavior can be treated by incorporating an energy dissipating mechanism into the ceramic, resulting in a damage-tolerant mechanical behavior. This was accomplished by developing a composite, a material that has a chemically and/or physically distinct phase, such as particles, chopped fibers, or continuous fibers distributed within a continuous phase or matrix [1].

The origin of composites has been dated back to the ancient Egyptians, where their renowned straw-reinforced clay-bricks trumped over the traditional clay brick. The straw acted as a reinforcement medium held within the clay matrix, creating a tougher material than the monolithic clay ceramic. Composites have become more widely researched and developed over time, especially during the 20th century. Glass-fiber reinforced polymers were developed. Continuous glass fibers were first produced commercially in 1939 [2]. Advanced fibers of boron and carbon were developed in the 1950's and 1960's [3]. In the 1960's, the United States Air Force began to invest in developing composite materials for aircraft electronic control surfaces. Once the US Air Force recognized the potential composites could have in the aerospace industry, they began to invest substantially in composite research and development. Since then, the US Air Force has lead research and development efforts in high performance fiber-reinforced composites for structural applications to improve aircraft performance [4, 5].

Composite materials have quickly become a primary choice in high performance aerospace materials. In the 1950's, the Boeing 707 consisted of only two percent (by weight) fiberglass composite. In the 1970's, the F-15 and F-16 fighter aircrafts incorporated about two percent (by weight) composites into the airframe. Today, the world's most advanced fighter aircrafts, the F-22A and the F-35 Joint Strike Fighter, are built with nearly 25% and 42% (by weight), respectfully, composite material components [6, 7]. The Boeing 787 Dreamliner, introduced in 2011, consists of over 50% composite materials [8]. The desirable high strength-to-weight ratio of composites has made them a part of aircraft designs aiming to decrease the overall weight of the aircraft, resulting in increased fuel efficiency.

Composites have not just become a solution to structural improvements, such as lighter and stronger aircraft skins, but have been developed to address the need for improved engine performance. Ceramic matrix composites exhibit superior mechanical behavior at higher operational temperatures. Hence CMCs are prime candidate materials for engine components such as turbine blades. The use of CMCs can reduce or even eliminate the need for cooling systems like those used in engines with conventional Nickel-based superalloy turbine blades, such as in **Figure 1** [1, 9]. **Figure 2** shows that the service temperature limits of ceramic class of materials are superior to those of metals and polymers. **Figure 3** illustrates how the strength to weight ratio of CMCs compares to that of other prior aerospace materials. Ceramic matrix composites have higher strength-to-weight ratios, lower thermal expansion coefficients, and lower thermal conductivities than conventional alloys; therefore, they increase the engine's thrust while reducing fuel consumption and emissions [10]. **Figure 4** shows comparison of service temperature

limits of conventional turbine blade superalloys (Thermal Barrier Coated superalloys) to that of CMCs. Composite materials are providing solutions to improve aircraft performance.

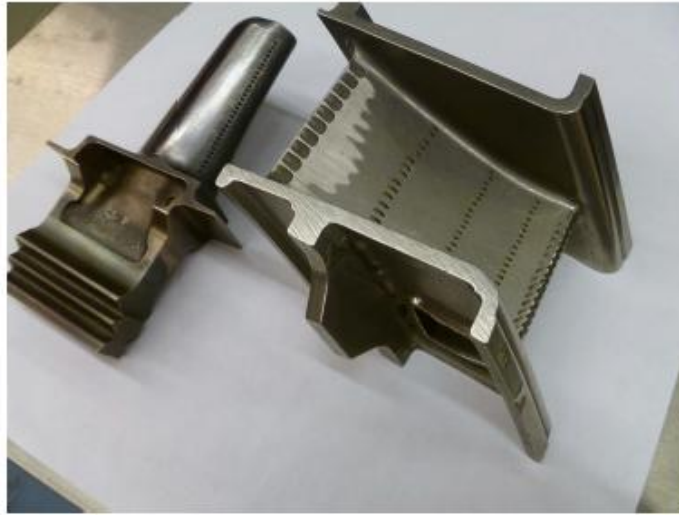


Figure 1: Superalloy turbine blade with cooling ports, reproduced from Shillig [9]

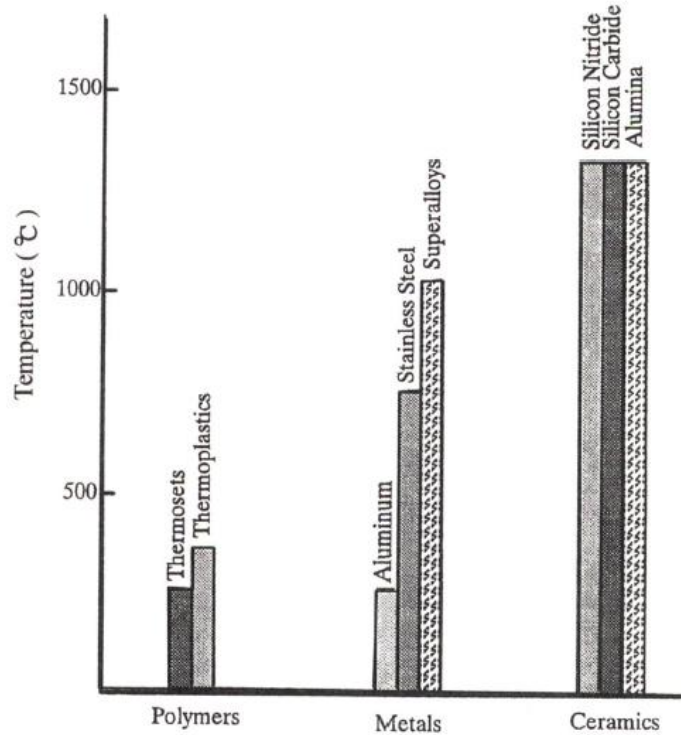


Figure 2: Service temperature limits of various classes of materials; Reproduced with kind permission from Springer Science & Business Media B.V. [1] pg. 5, Chapter 1: Introduction, Figure 1.3. Copyright c 2003 by Kluwer Academic Publishers. All rights reserved. No part of this work may be reproduced, stored in a retrieval system, or transmitted in any form or by any means, electronic, mechanical, photocopying, microfilming, recording or otherwise, without the written permission from the Publisher, with the exception of any material supplied specifically for the purpose of being entered and executed on a computer system, for exclusive use by the purchaser of the work.

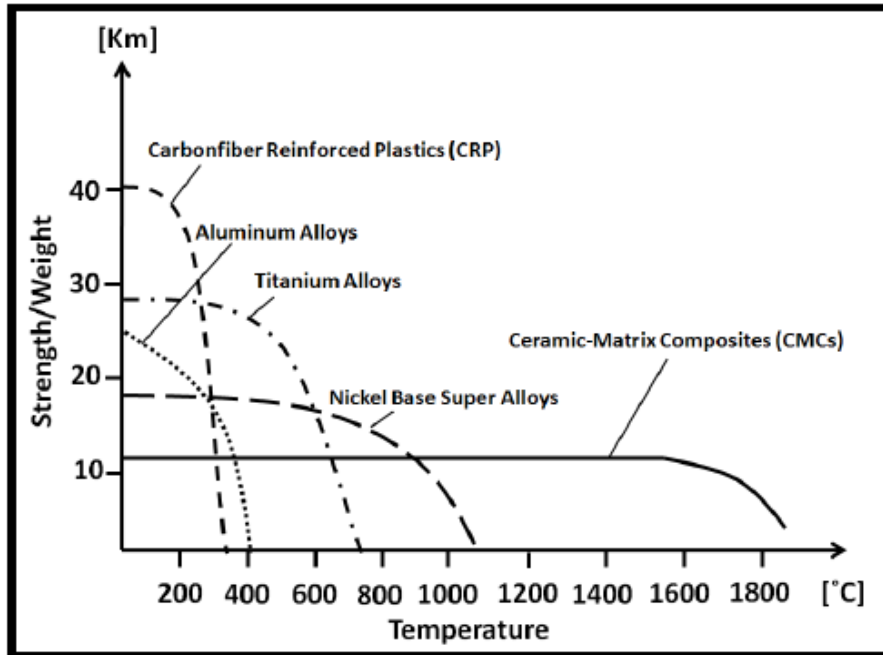


Figure 3: The strength-weight ratios of select aerospace materials as a function of temperature. Note the significant improvement of CMCs over traditional materials at high temperatures. Reproduced from [11], pg. 410, Copyright © 2004, with permission from Elsevier and from the original author.

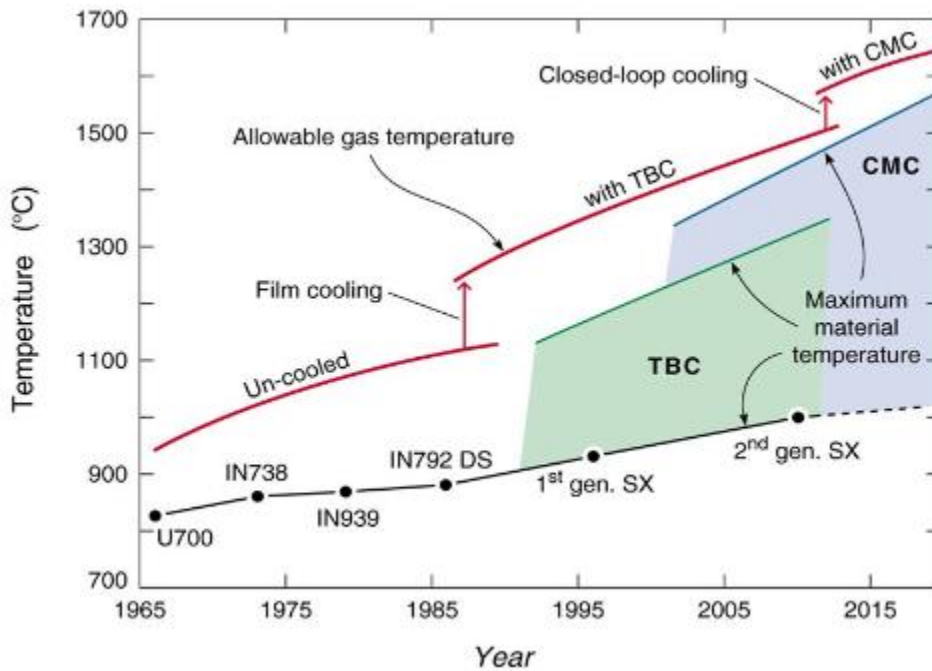


Figure 4: Service temperatures for various high-temperature aerospace materials; reproduced with permissions from Dr Wadley of University of Virginia [12]

The mechanical behavior of a composite depends on its constituents. The ceramic matrix serves as an energy dispersion medium, toughening the composite, while the reinforcement serves as the strength mechanism, contributing to the load bearing capacity of the composite. The analysis of the reinforcement, Sylramic-iBN ceramic fiber tows, will be the focus of this research effort.

II. Background

2.1 Ceramic Matrix Composites

The general purpose of a composite is to combine the desired properties of the matrix material and the strength of the fiber reinforcement. In the case of a continuous-fiber ceramic composite, the monolithic ceramic matrix is reinforced with continuous ceramic fibers. A monolithic ceramic is typically very strong but very brittle. These properties are attributed to the ionic and covalent bonding where there is an inherent resistance to dislocation motion in the lattice structure. In a crystalline ceramic, stress concentrations cannot be relieved by plastic deformation (except, to some degree, at high temperatures) and thus the ceramic fails catastrophically under tensile loading. This attribute of ceramics led to research into toughening mechanisms needed to engineer the ceramic into a practical structural material for high temperature applications [1].

The addition of high-strength reinforcement fibers to a low modulus ceramic matrix allows for a material that is tougher and stronger material than the two individual components [1]. Ceramic matrix composites exhibit superior toughness, tolerance to the presence of defects, and a more graceful failure compared to monolithic ceramics, as seen in **Figure 5**. This is achieved by controlling the interface between the fiber and matrix [13]. A weak fiber-matrix interface provides for crack deflection around the fibers, which in turn allows the CMC to avoid brittle failure for as long as the fibers are able to maintain load-bearing capability while the crack propagation activity continues throughout the matrix. An illustration of crack deflection due to a weak fiber-matrix interface can be seen in **Figure 6**. Conversely, if the fiber-matrix interface is strong, the matrix crack will not be deflected around the fiber, but will propagate through the fiber

resulting in fiber fracture. An illustration of crack propagation as a function of fiber-matrix interface can be seen in **Figure 7**. The CMC can be designed to exhibit non-brittle fracture behavior and improved damage tolerance by introducing a weak fiber-matrix interface, which serves to deflect matrix cracks and to allow subsequent fiber pull-out [1, 3, 8]. An example of fiber pullout can be seen in **Figure 8**.

Controlling the fiber-matrix interface is a delicate balance; if the fiber-matrix interface is too weak, then there will be inadequate load transfer from the matrix to the fibers. However, if the fiber-matrix interface is too strong, then the load transfer from the matrix to the fibers will cause any crack propagation in the matrix to continue through the fibers [1, 14]. Mechanical characteristics of the interface govern the performance of the composite [1]. Another important consideration is thermal stresses in CMCs due to mismatch between the thermal expansion coefficients of the matrix and fiber materials. If the thermal expansion coefficient of the matrix is higher than that of the fibers, during heating to high temperatures, the matrix will “clamp” the fibers and result in a strong fiber-matrix interface, thus causing the composite to become more brittle and less damage tolerant.

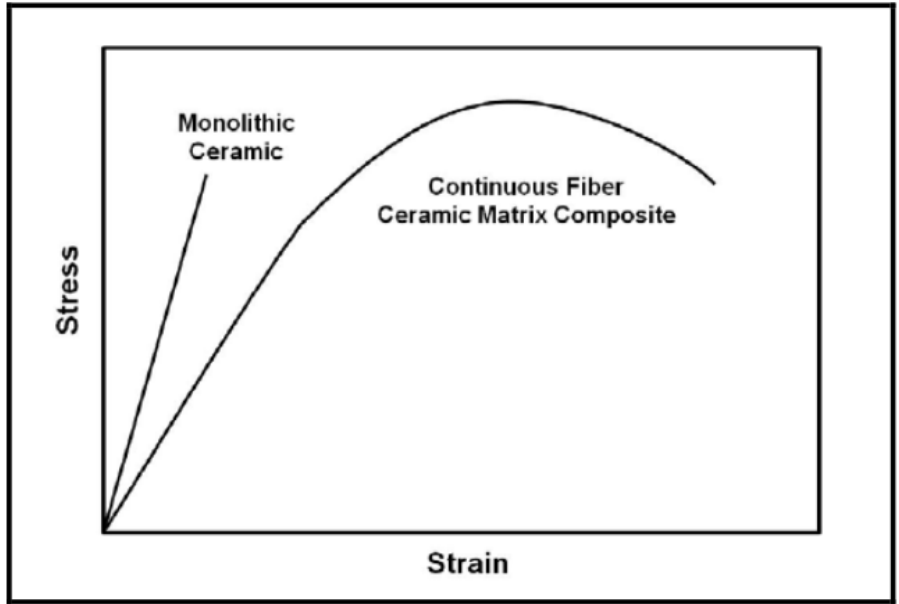


Figure 5: Typical stress-strain curves for monolithic ceramics and CMCs in tension; reproduced from Armani [15]

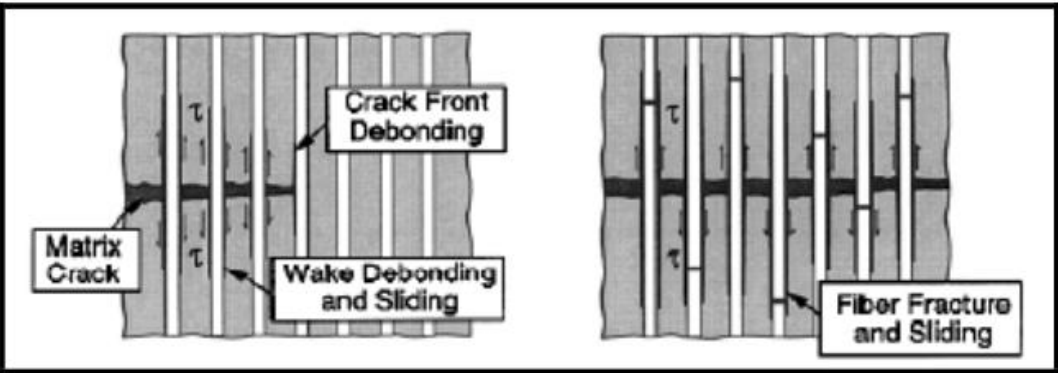


Figure 6: Crack propagation for weak fiber-matrix interface; reproduced from Zok [16], with kind permission from Wiley and Sons

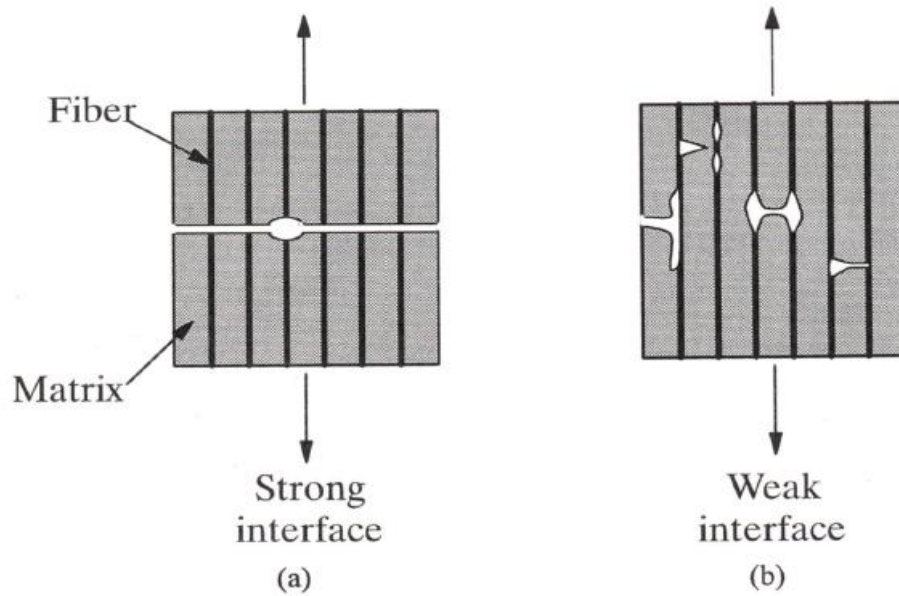


Figure 7: Crack propagation as a function of fiber-matrix interface; Reproduced with kind permission from Springer Science & Business Media B.V. [1] pg. 148, Chapter 5: Interface, Figure 15.6. Copyright © 2003 by Kluwer Academic Publishers. All rights reserved. No part of this work may be reproduced, stored in a retrieval system, or transmitted in any form or by any means, electronic, mechanical, photocopying, microfilming, recording or otherwise, without the written permission from the Publisher, with the exception of any material supplied specifically for the purpose of being entered and executed on a computer system, for exclusive use by the purchaser of the work.

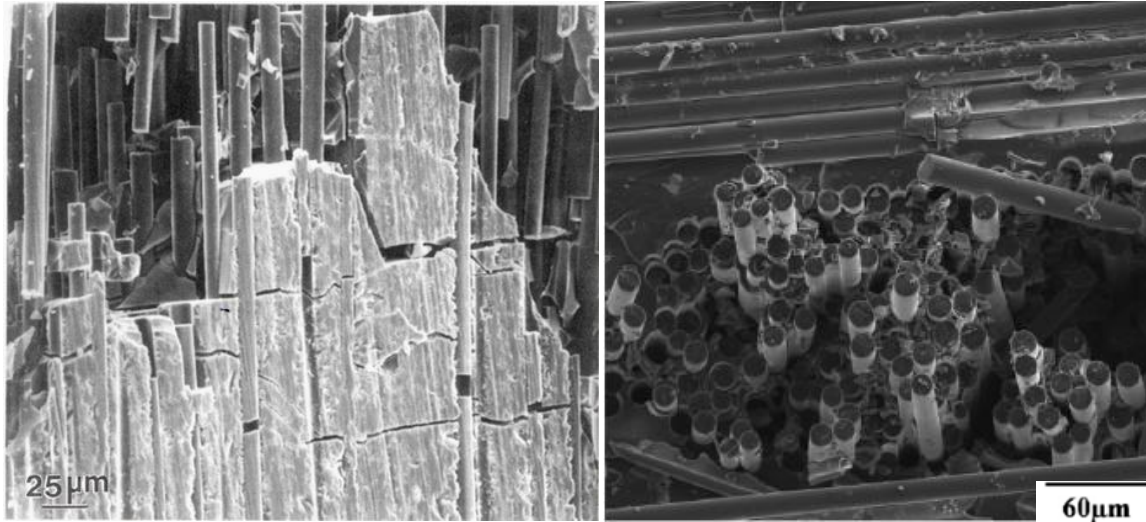


Figure 8: Scanning Electron Microscopy (SEM) of extensive fiber pullout and matrix cracking of BN-coated Nextel 480 fibers (left) [1], and uncoated Hi-Nicalon fibers (right) [17]; Reproduced with kind permission from Springer Science & Business Media B.V. [1] pg. 327, Chapter 9: Interface Mechanics and Toughness, Figure 9.16 (b). Copyright © 2003 by Kluwer Academic Publishers. All rights reserved. No part of this work may be reproduced, stored in a retrieval system, or transmitted in any form or by any means, electronic, mechanical, photocopying, microfilming, recording or otherwise, without the written permission from the Publisher, with the exception of any material supplied specifically for the purpose of being entered and executed on a computer system, for exclusive use by the purchaser of the work.

Another notable aspect of ceramic matrix composites is that they retain superior long-term mechanical properties under high temperatures. However, even though ceramics are relatively inert compared to other materials, they are not invulnerable to the harsh environments they are exposed to in aerospace applications, such as combustion environments. At high temperatures and levels of moisture, the CMCs are susceptible to oxidation. This corrosive environment degrades the mechanical properties of the CMC causing early failure due to embrittlement, and limits the life of aerospace components made from CMCs [18]. Oxidation embrittlement occurs when the fibers and fiber coatings react with the oxygen that diffuses through the matrix, causing the matrix and

fibers to form strong bonds and defeating the intended crack-deflecting properties of a weak fiber-matrix interface [18]. Thus, development of fibers with improved oxidation resistance is ongoing. Considerable interest has been placed on the Sylramic-iBN ceramic fibers (SiC fibers), due to their impressive oxidation and creep resistance, along with their near stoichiometric, oxygen-free composition [19, 20, 21]. These beneficial properties have made Sylramic-iBN fibers a strong candidate for CMC applications.

2.2 Creep in Ceramics

Creep can be defined as a continuing inelastic deformation (permanent strain) under constant stress [1, 22]. Creep is typically accelerated at high-stress and high-temperature. Because advanced aerospace CMC components are subjected to considerable stresses at high temperatures for long durations, creep resistance is desired in CMCs.

A typical schematic of a creep curve can be seen in **Figure 9**. The creep curve is divided into three regions: primary, secondary, and tertiary creep. Primary creep is characterized by a decreasing strain rate. General structure changes in the material during this creep stage may include changes in grain size and dislocation density. Secondary creep is characterized by a constant strain rate, hence this phase is also known as steady-state creep. This type of creep is due to the deformation of the microstructure. This is typically the longest creep phase. Tertiary creep is characterized by an increasing strain rate and is typically very short in duration. Tertiary creep results in the failure of the material via formation of voids or cracks [1, 15].

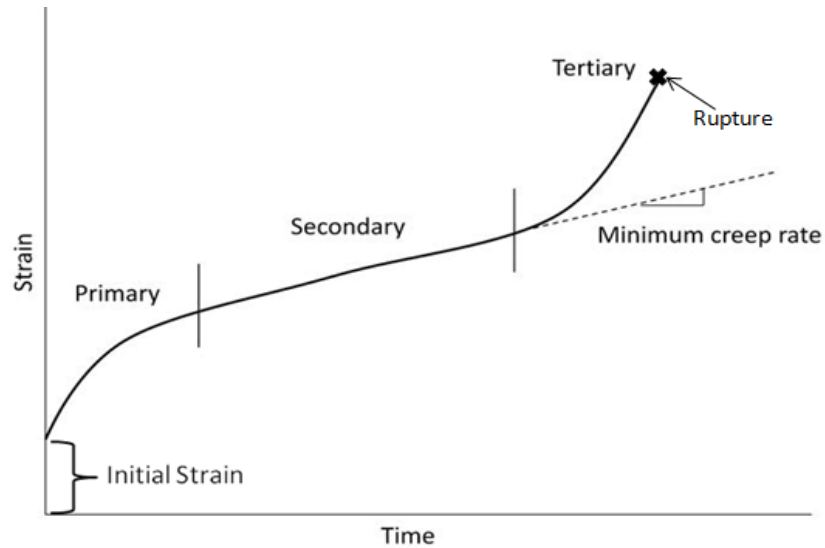


Figure 9: Stages of a typical creep curve; reproduced from Robertson [23]

In creep studies of ceramics, a focus is placed on the steady-state creep. Because most CMC constituents are polycrystalline, creep of CMCs at high temperatures proceeds predominately by diffusional creep or grain boundary sliding (GBS). Both mechanisms are always present and are coupled, but one or the other dominates. Diffusional creep occurs due to the transport of vacancies and matter through the grains (lattice diffusion, or Nabarro-Herring creep) or along the grain boundary (Coble creep). Diffusional creep results in grain elongation in the direction of the applied load. In the case of grain boundary sliding, however, entire grains move with respect to one another to relieve local stresses in the material. This grain movement causes elongation in the direction of the applied load. At elevated temperatures, this creep mechanism in CMCs is generally due to the softening of grain-boundary glassy phases [15].

It is widely accepted that the steady-state creep rate of materials can be modeled using the following form of the Arrhenius rate equation [24]:

$$\dot{\epsilon} = B \frac{D\mu b}{kT} \left(\frac{b}{d}\right)^p \left(\frac{\sigma}{\mu}\right)^n \quad (1)$$

where $\dot{\epsilon}$ is the strain rate, B is a constant, D is the diffusion coefficient, μ is the shear modulus, b is magnitude of the Burgers vector, k is the Boltzmann constant, T is the absolute temperature, d is the grain size diameter, σ is the applied tensile stress, p is the grain size power law exponent and n is the stress power law exponent [15, 24]. The diffusion coefficient D , is given by the expression:

$$D = D_o \exp\left(\frac{-Q}{RT}\right) \quad (2)$$

where D_o is a frequency factor [14], Q is the creep activation energy, and R is the universal gas constant.

Experimental creep data can be used to determine values of p and n in **Equation 1**. These two exponents correspond to different creep mechanisms. A detailed discussion and a summary of creep mechanisms in fine-grained polycrystalline ceramics and their corresponding power law creep exponents are given elsewhere [15].

Due to the relatively recent development of the third generation SiC fibers such as Sylramic-iBN their creep behavior has not been extensively examined. Only a limited number of studies have been devoted to creep of Sylramic-iBN reinforced CMCs. These are discussed in Section 2.5.

2.3 Silicon Carbide Fibers

The evolution of silicon carbide (SiC) fibers began in the mid 1960's, when SiC was deposited onto a tungsten or carbon core by chemical vapor deposition (CVD). The general steps involved in processing non-oxide fibers via polymer route can be seen in **Figure 10**. The first SiC fibers were large in diameter ($<100\mu\text{m}$), which limited the fibers' flexibility, making them unsuitable as a reinforcement in composite materials.

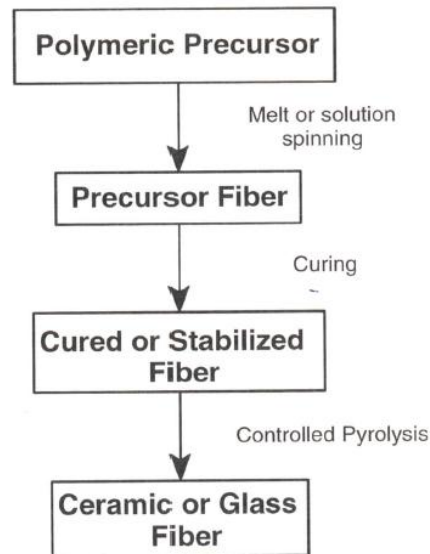


Figure 10: Various steps involved in processing non-oxide fibers via polymer route; Reproduced with kind permission from Springer Science & Business Media B.V. [1] pg. 81, Chapter 3: Ceramic Reinforcement, Figure 3.19. Copyright c 2003 by Kluwer Academic Publishers. All rights reserved. No part of this work may be reproduced, stored in a retrieval system, or transmitted in any form or by any means, electronic, mechanical, photocopying, microfilming, recording or otherwise, without the written permission from the Publisher, with the exception of any material supplied specifically for the purpose of being entered and executed on a computer system, for exclusive use by the purchaser of the work.

In the 1980's, the first generation of fine SiC fibers was pioneered in Japan by Nippon Carbon Co., who developed the Nicalon series, and by Ube Industries, who

manufactured the Tyranno series [25]. The Nicalon fibers became the standard for much of the CMC studies thereafter. These fibers had diameters of around 15 μm but were inconsistent along the fiber length due to processing difficulties. This issue led to discrepancies in published literature for these fibers. Another issue was related to the chemical composition of the fibers. Because SiC fibers are not made purely out of SiC, the composition is critical in the outcome of the fiber mechanical characteristics. The first generation Nicalon fibers contained free carbon embedded in an amorphous SiC_xO_y matrix. Due to the amorphous state of the matrix, the fiber stiffness was about 200 GPa, which is about half that of pure SiC. The fiber properties and composition can be seen in **Table 1**. At temperatures above 1200°C in air, free silicon oxidizes along the surface of these fibers, leading to severe strength degradation. Thus, the first generation fibers were limited to lower temperature applications [1, 25].

Table 1: Composition, Young’s modulus and density of first generation Nippon Carbon SiC fibers; reproduced from Bunsell and Piant [25], with kind permission from Springer Science and Business Media

Producer	Nippon Carbon
Fibre name	Nicalon 200
Precursor	PCS
Cured by	Oxidation
Si (wt%)	56.6
C (wt%)	31.7
O (wt%)	11.7
Ti (wt%)	0
C/Si	1.31
Young’s modulus (GPa)	200
Density (g/cm^3)	2.55

Multiple tests performed on the first generation SiC fibers demonstrated that the non-stoichiometric composition of these fibers limited their mechanical performance. Bunsell [25] performed tensile and creep tests of the Nicalon fibers, and after analyzing the fracture surfaces using transmission electron microscopy (TEM) and X-ray diffraction (XRD), concluded that the presence of the amorphous intergranular phase (Si-O-C) degraded the fiber's strength and creep performance. The first generation Nicalon fibers exhibited loss of strength and creep at temperatures around 1000-1100°C, while bulk SiC would be expected to resist creep at higher temperatures. These results indicated that the oxygen content had to be considerably reduced to improve the fiber's physical characteristics. Oxygen was embedded in the fibers due to the manufacturing process; thus, other means of cross-linking the polymer precursors had to be investigated to reduce the oxygen content in the fibers [25].

Many of the second generation small-diameter SiC fibers, such as Hi-Nicalon, are oxygen-free. This was achieved by curing via electron irradiation. The irradiation curing process interacts with the precursor polymers such that it produces free radicals by breaking chemical bonds in the chains: Si-CH₃, Si-H and C-H. This allowed Si-Si and Si-C bonds to be formed [25]. Following the irradiation curing (crosslinking), a heat treatment at 327°C is applied for a short time to eliminate the remaining free radicals. The reduction in the oxygen content in the second generation SiC fibers resulted in over 35% improvement in stiffness over that of the first generation fibers. The strength of the second generation fibers improved, maintaining a linear elastic response up to 1350°C (100°C improvement over the first generation fibers). Because the intergranular amorphous phase was not present in the second generation SiC fibers, they did not

degrade or creep below 1000°C, and began to exhibit secondary creep above 1200°C. At 1400°C, both generations of fibers were reported to exhibit nearly the same creep rates ($\sim 5 \times 10^{-7} \text{ s}^{-1}$) under an applied stress of 0.3 GPa. The primary creep mechanism was reported as grain boundary sliding, which can be enabled by layers of carbon between the grains. The ultimate failure in creep was concluded to be caused by surface defects, such as cavities or porous zones, which are typical sites for crack initiation [25]. The second generation of SiC fibers presented significant improvements over the first generation fibers. However, oxygen content and stoichiometric compositions were still a concern and had to be further addressed [25].

A third generation of small diameter SiC fibers was driven by the need for ceramic matrix composites that could perform at higher temperatures than nickel-based superalloys (max of 1150°C) for the gas turbine industry. It was during this era that COI Ceramics stepped in as a key manufacturer in this growing industry. Since the first two generations of fibers did not meet the required service temperatures, further development was needed. As a result the improved Hi-Nicalon-S fibers were developed by Nippon Carbon and the Sylramic and Sylramic-iBN fibers were developed by COI Ceramics. Nippon Carbon and COI Ceramics were able to produce Hi-Nicalon-S, Sylramic, and Sylramic-iBN fibers with near-stoichiometric composition [25].

The process for making the second generation fibers was modified to produce the third generation fibers: sintering aids were taken out of polycarbosilane (PCS) precursor, the fibers were cured by electron irradiation, then the fibers were heated to 1500°C in a hydrogen rich environment to reduce the excess carbon radicals [26]. Thus a process for making the third generation SiC fibers (Hi-Nicalon-S) was developed. The Hi-Nicalon-S

fibers have a carbon/silicon ratio of 1.05 (down from 1.39) and relatively large (20-200 nm) SiC grains, resulting in improved chemical resilience, and, thus improved oxidation resistance and thermal resistance [25, 26, 27]. The Hi-Nicalon-S fibers exhibit significant improvement in creep behavior compared to the prior two generations. At 1400°C, the Hi-Nicalon-S fibers were reported to exhibit creep rates of $\sim 10^{-8} \text{S}^{-1}$ [25, 28].

However, Dow Corning took a different route than Nippon Carbon in manufacturing their signature Sylramic and Sylramic-iBN SiC fibers. Dow Corning, a key manufacturer in the production of small diameter SiC fibers, investigated diffusing boron as a sintering aid into polytitanocarbosilane (PTC) produced SiC fibers. Dow Corning found that large grain growth and high density were achieved during a high temperature sintering phase (around 1400°C), where excess carbon and oxygen were removed from the precursor fiber. As a result a large grain, polycrystalline, oxygen-free, and nearly stoichiometric Sylramic fiber was produced. There are two versions of this fiber: Sylramic and Sylramic-iBN. The Sylramic-iBN fibers are developed with a treatment where the boron in the bulk of the precursor fiber diffuses to the surface. During this process, the boron reacts with nitrogen to form an in-situ boron nitride (BN) coating on the surface of the SiC fiber. The removal of the boron from the fiber bulk maintains a high tensile strength while improving the fiber's creep resistance along with increasing the fiber's oxidation resistance with the BN-rich surface. The Sylramic fibers undergo a heat treatment process which removes the BN coating from the surface of the SiC fiber [25].

The manufacturer, cross linking method, elemental composition, and average diameter of all three generations of fibers are summarized in **Table 2**. Specifications and

material properties of various SiC fiber tows are presented in **Table 3**. Fiber tows, as opposed to single continuous or chopped filaments, are used to improve the load capability in CMCs, since multifilament tows are more damage tolerant. Continuous fibers are desirable over chopped fibers or particles because they can be woven [1]. Fiber tow failure is more graceful than that of single filaments as the ultimate failure of fiber tows is preceded by failure of individual fibers.

Table 2: Details of manufacturer, cross linking method, composition, and diameter of all three generations of fibers; reproduced from Ishikawa [27], with kind permissions from Taylor & Francis

	Trade mark	Manufacturer	Cross linking method	Approximate maximum production temperature	Elemental composition (wt%)	Density (g/cm ³)	Average diameter (μm)	Cost (US \$/kg)
First Gen.	Nicalon 200	Nippon Carbon	Oxygen	1200°C	56Si + 32C + 12O	2.55	14	2000
	Tyranno LOX-M	Ube Ind.	Oxygen	1200°C	54Si + 32C + 12O + 2Ti	2.48	11	1250
Second Gen.	Hi-Nicalon	Nippon Carbon	Electron irradiation	1300°C	62.5Si + 37C + 0.5O	2.74	12	8000
	Tyranno LOX-E	Ube Ind.	Electron irradiation	1300°C	55Si + 37.5 + 5.5O + 2Ti	2.39	11	N/A
	Tyranno ZM	Ube Ind.	Oxygen	1300°C	57Si + 34.5C + 7.5O + 1Zr	2.48	11	1500
	Tyranno ZE	Ube Ind.	Electron irradiation	1300°C	58.5Si + 38.5C + 2O + 1Zr	2.55	11	N/A
	Tyranno SA 1	Ube Ind.	Oxygen	>1700°C	68Si + 32C + 0.6Al	3.02	11	N/A
Third Gen.	Tyranno SA 3	Ube Ind.	Oxygen	>1700°C	68Si + 32C + 0.6Al	3.1	7.5	5000
	Sylramic	COI ceramics	Oxygen	>1700°C	67Si + 29C + 0.8O + 2.3B + 0.4N + 2.1Ti	3.05	10	10000
	Sylramic iBN	COI Ceramics	Oxygen	>1700°C	N/A	3.05	10	>10000
	Hi-Nicalon Type-S	Nippon Carbon	Electron irradiation	>1500°C	69Si + 31C + 0.2O	3.05	12	13000

Table 3: Specifications and Material Properties of various SiC Fiber Tows; reproduced from Ishikawa [29], with kind permission from Springer Science and Business Media

□ : Nearly stoichiometric SiC fiber

	SiC Fibers							
	Nicalon			Tyranno				Sylramic
	NL-200	Hi-Nicalon	Hi-Nicalon-s	Lox M	ZMI	ZE	SA*	
Atomic Composition	SiC _{1.34} O _{0.36}	SiC _{1.39} O _{0.01}	SiC _{1.05}	SiTi _{0.02} C _{1.37} O _{0.32}	SiZr _{< 0.01} C _{1.44} O _{0.24}	SiZr _{< 0.01} C _{1.52} O _{0.05}	SiC O, Al < 0.008	SiCTi _{0.02} B _{0.09} O _{0.02}
Tensile Strength (GPa)	3.0	2.8	2.6	3.3	3.4	3.5	2.8	3.0
Tensile Modulus (GPa)	220	270	410	187	200	233	410	420
Elongation (%)	1.4	1.0	0.6	1.8	1.7	1.5	0.7	0.7
Density (g·cm ⁻³)	2.55	2.74	3.10	2.48	2.48	2.55	3.02	> 3.1
Diameter (μm)	14	14	12	8 & 11	8 & 11	11	8 & 10	10
Specific Resistivity (Ω·cm)	10 ^{3-10⁴}	1.4	0.1	30	2.0	0.3	—	—
Thermal Expansion coeff. (10 ⁻⁶ /K)	3.2 (25-500°C)	3.5 (25-500°C)	—	3.1	4.0	—	4.5 (20-1320°C)	—
Thermal Conductivity (W/mK)	2.97(25°C) 2.20(500°C)	7.77(25°C) 10.1(500°C)	18.4(25°C) 15.3(500°C)	—	2.52	—	64.6	40-45

Sylramic-iBN fibers retain their strength better than any available SiC fibers at elevated temperatures [20, 30, 31]. For CMC applications subjected to high-temperature and oxidizing environments, the in-situ BN surface coating on the Sylramic-iBN fibers appears to provide a more environmentally durable fiber. Investigation of creep behavior of Sylramic-iBN fiber tows is critical to characterizing novel CMCs reinforced with these fibers. Such investigation is the focus of this effort.

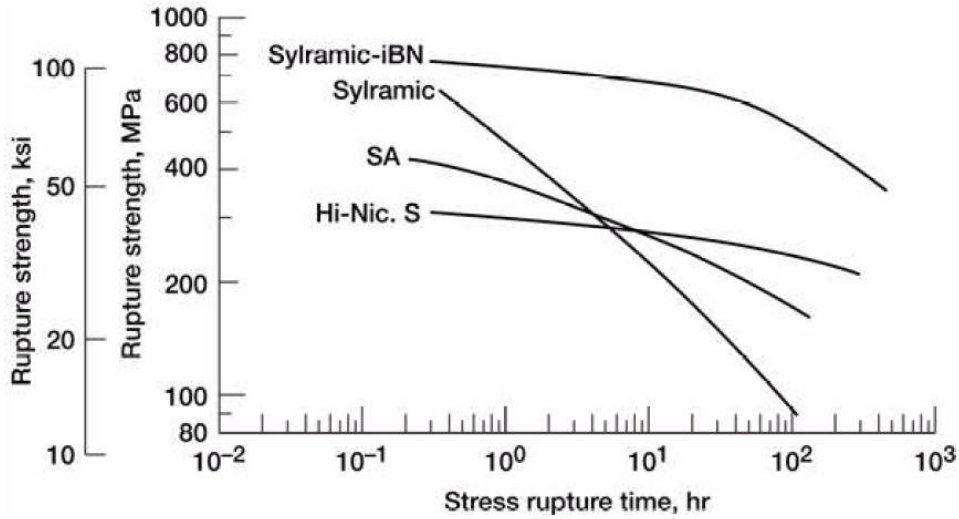


Figure 11: Rupture strength behavior for various high-performance SiC fibers at 1400°C in air. Sylramic and Sylramic-iBN from COI Ceramics, Tyranno SA fiber from UBE Industries; Hi-Nicalon Type S fiber from Nippon, Carbon; reproduced from Yun and DiCarlo [30]

2.4 Fiber Coatings

Proper control of the fiber-matrix interface in a ceramic matrix composite is critical to optimizing the mechanical properties, particularly toughness. The chemical interaction between the matrix and the fibers ultimately determines the ability of the fibers to debond at the interface and provide the toughening mechanism [1]. By incorporating fiber coatings, the strength of the fiber-matrix bond can be optimized. The choice of the coating is tailored to the fiber and matrix materials [1]. The interphase, or coating, has a “load transfer function where it aids in deflecting crack propagation between the matrix and the fiber” [26]. An example of a Nicalon fiber with a pyrocarbon interphase coating can be seen in **Figure 12**.

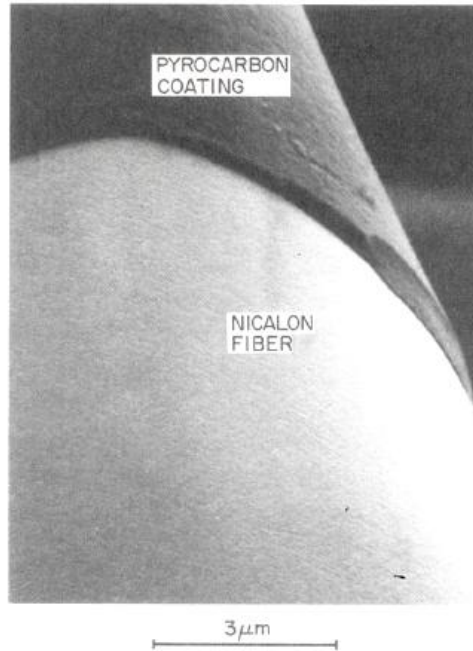


Figure 12: Nicalon fiber with pyrocarbon coating; Reproduced with kind permission from Springer Science & Business Media B.V. [1] pg. 325, Chapter 9: Interface Mechanics and Toughness, Figure 9.15 (a). Copyright © 2003 by Kluwer Academic Publishers. All rights reserved. No part of this work may be reproduced, stored in a retrieval system, or transmitted in any form or by any means, electronic, mechanical, photocopying, microfilming, recording or otherwise, without the written permission from the Publisher, with the exception of any material supplied specifically for the purpose of being entered and executed on a computer system, for exclusive use by the purchaser of the work.

Fiber coatings have a dual purpose. Not only do coatings ensure an optimally weak fiber-matrix interface, but they also protect the fibers from mechanical degradation due to environmental attack. Typical coatings have low shear strength, enabling graceful failure through the load transfer mechanism [26]. In harsh combustion environments, such as that experienced by jet turbine blades, where there is high partial pressures of water vapor, protective coatings will inevitably undergo oxidation. In these particular cases, the coating material is referred to as an environmental barrier coating (EBC) [26]. Environmental barrier coatings are usually applied in multiple layers around the fiber, where the outer layer acts as a sacrificial layer, which oxidizes and thus protects the

fibers from oxidizing. Without a protective layer, the SiC would react with oxygen to create a silica layer along the surface, which bonds the fibers to the matrix and to each other. Under this condition, once the matrix begins to crack, or when a weak fiber fails, the neighboring fibers fail because there is no load diffusion barrier present [19].

Armani [15], Steffens [32], and Shillig [9] have shown that degradation of fibers is generally accelerated in the presence of moisture. In a moisture rich environment, the water constituents react more readily with the SiC fiber where the oxygen displaces the carbon and then bonds with free silicon atoms. Because SiC/SiC composite constituents are intrinsically oxidation-prone, oxidation embrittlement is the most significant problem hindering them in harsh corrosive environments. **Figure 13** shows crack deflection through the multi-layered BN coating deposited on an SiC fiber tow, moving in a temperature gradient ($T_1 < T_2 < T_3$) [22]. Additionally, in steam environments, silicon is easily removed as it oxides to form silica, which leads to a non-uniform composition along the fiber length and weakens the fibers. Fiber coatings are used to protect the silicon carbide based fibers from exposure to the oxygen-rich environment.

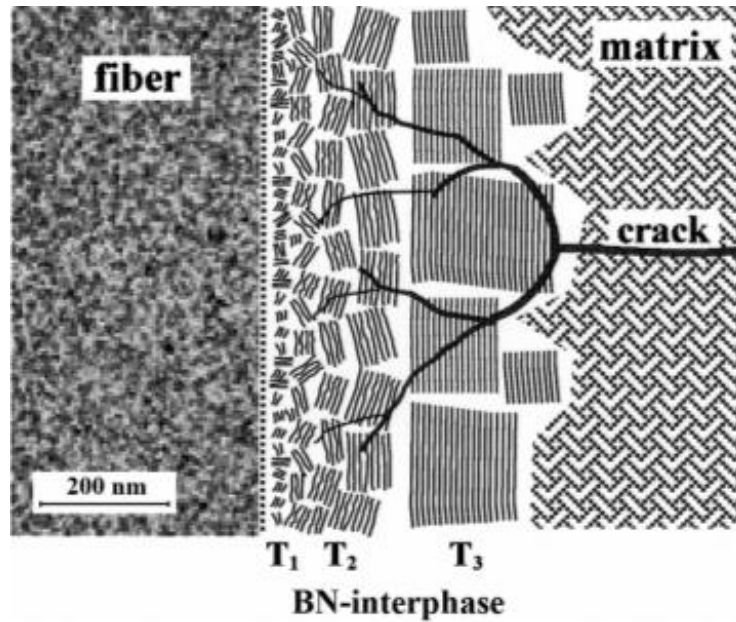


Figure 13: Crack deflection through the multi-layered BN coating deposited on SiC fiber tow; reproduced from Naslain [33], with kind permission from Wiley and Sons

To further address the complexities in the kinematics of crack propagation throughout a SiC fiber reinforced CMC, **Figure 14** illustrates crack propagation along a simple interphase, such as a single BN coating along a SiC fiber, a porous interphase, and a multilayered interphase. We can relate the data in **Figure 11** to the crack diffusion mechanisms illustrated in **Figure 14**. The in-situ BN coating of the Sylramic-iBN fibers produces a more environmentally durable fiber by creating a physical barrier between the fibers and the oxidizing environment. Furthermore, because the BN coating is less oxidation resistant than the bulk SiC fiber, it reacts with oxygen to form an oxide glass, which inhibits oxygen penetration [19].

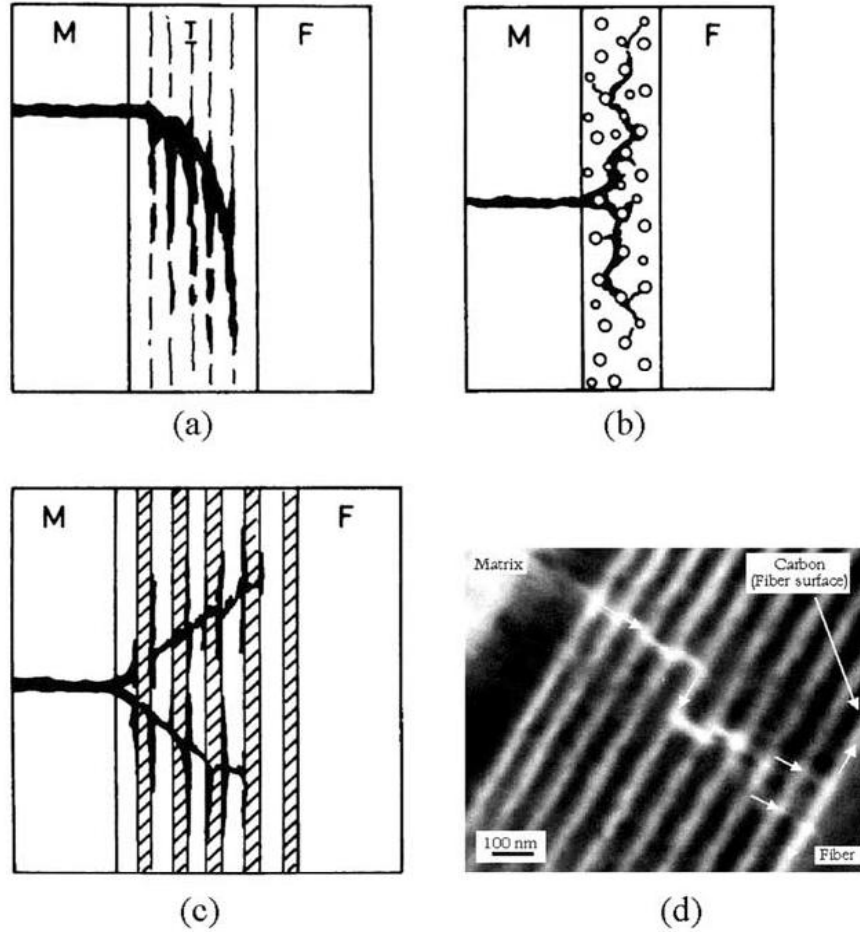


Figure 14: Different simple or engineered interphases used SiC-matrix composites: (a) single layer pyrocarbon or hexagonal BN interphases, (b) porous SiC single layer interphase, (c) multilayered $(X-Y)_n$ interphase, with $X=PyC$ or BN and $Y=SiC$ (schematic), (d) crack deflection in a multilayered $(PyC-SiC)_{10}$ interphase, according to Naslain (a-c) [34] and Bertrand et al. [35]; reproduced from Naslain [26], pg. 161, Copyright © 2004, with permission from Elsevier

2.5 Previous Research Efforts

The mechanical performance of SiC-based fibers at elevated temperature has been of particular interest in the past decade. Lamon and co-workers reported on delayed failure of SiC fiber tows at 600°C-800°C in air [36, 37, 38]. Forio et al studied static fatigue of Nicalon fiber tows at 600°C-800°C in air and concluded that fiber oxidation led to slow crack growth and delayed failure of the fiber tows [36]. Gauthier and Lamon

investigated static fatigue of Hi-Nicalon and Hi-Nicalon-S fiber tows and single filaments at 500°C-800°C in air, and constructed a model to predict delayed failure of fiber tows [37]. Gauthier et al investigated static fatigue of the three generations of the Nicalon fiber tows (Nicalon, Hi-Nicalon, and Hi-Nicalon-S) at 500°C-800°C [38]. It was found that the oxidation along the grain boundaries led to subcritical crack growth and to the delayed failure of the fiber tows [38]. The initial damage to the fibers occurs at the crack tip, where the fiber is exposed to the environmental species. This exposure causes the formation of a thin outer oxide layer on the surface of the fiber [1, 39]. If oxygen or moisture diffuses through the oxide layer, then the crack may continue to propagate further into the fiber [1, 39]. If this process persists, the crack will eventually progress through the fiber until the fiber fails. Ladeveze et al [39] introduced a modeling approach that to subcritical crack propagation in ceramics that accounts for the degradation of the material due to oxidation.

Although little has been published on the Sylramic family of fibers, these fibers have already shown great potential as an improved reinforcement in high-temperature structural CMCs. In 1999, Yun and DiCarlo [20, 31] documented some of the first studies on the Sylramic family of fibers. Their investigations laid the foundation for understanding key strength properties of a host of SiC fibers, including Sylramic and Sylramic-iBN. **Table 4** summarizes results obtained by Yun and DiCarlo in tensile test of the six near-stoichiometric SiC fibers along with nominal properties of the fibers. Yun and DiCarlo performed tensile tests to failure of single fibers at room temperature. The average room-temperature tow strength of the Sylramic-iBN fibers (noted as Syl. (1) and Syl. (2) in references [19, 20, 31]) was determined as 1270 MPa [20]. The creep-rupture

tests of single fibers were performed at 1400 °C in air (see **Figure 15**). Results showed that at 1400°C in air the Syramic-iBN fibers exhibited high rupture strength (see **Figure 16**).

Table 4: Nominal properties of near stoichiometric β SiC fibers; reproduced from Yun and DiCarlo [31], with kind permissions from Wiley & Sons

Trade name	Hi-Nicalon S	SA(1)	SA(2)	Syramic	Syl. (1) Devel.	Syl. (2) Devel.
Manufacturer	Nippon carbon	Ube Industries	Ube Industries	Dow Corning	Dow Corning	Dow Corning
Process. (Sintering T. >1600 C)	Polymer D./ Sintering	Polymer D./ Sintering	Polymer D./ Sintering	Polymer D./ Sintering	Polymer D./ Sintering	Polymer D./ Sintering
Average grain size. ^a nm	22(XRD)	~150	>~150	~100	~100	~100
Second phases or impurity conc. (wt.%)	O(0.2)	Al (<2), O(0.3).	Al (<2), O(0.3).	TiB ₂ , B	Reduced B, TiB ₂ , B-N	Reduced B, TiB ₂ , C
Density, g/cm ³	3.0	3.02	3.1	3.1	>3.1	>3.1
Average diameter, mm	13	10	10	10	10	10
Number of filaments	500	800	800	800	800	800
PVA sizing, wt.%	1.2	(~1.0) ^b	(~1.0) ^b	~0.2	-----	-----
Modulus at RT (GPa)	400-420	306	375	~400	>400	>400
Tensile strength, MPa	~2500	2700	2800	3200	~3200	~3200
Tensile elongation, percent	~0.6	~0.9	~0.7	~0.8	<~0.8	<~0.8
Thermal cond. ^c (W/m ² C)	18.4	-----	64.6	46.0	>46	>46

^aMeasured on TEM microstructures

^bPEO sizing.

^cAt room temperature.

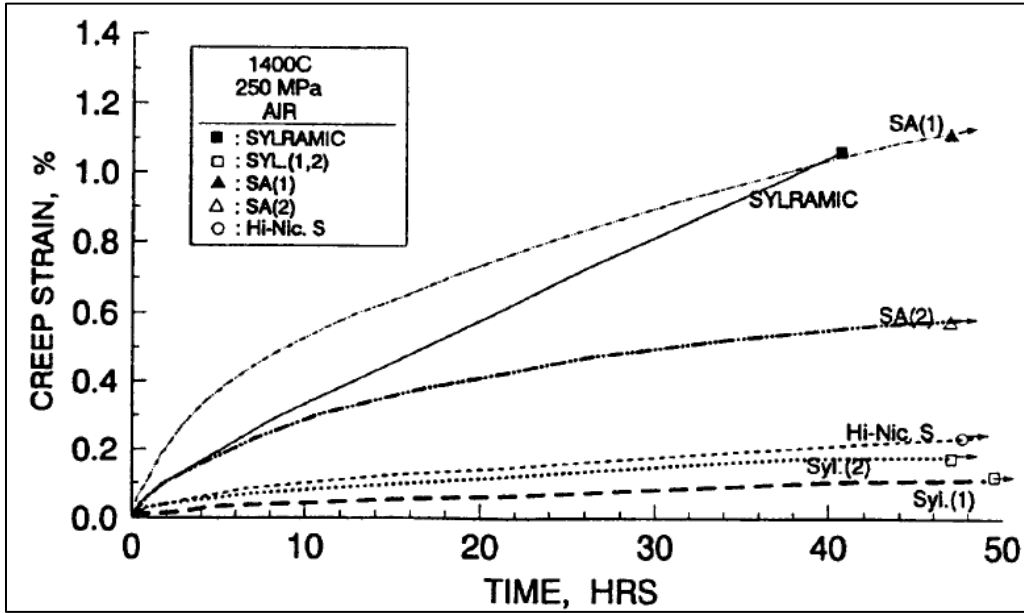


Figure 15: Typical creep-rupture curves for various near stoichiometric SiC fibers; reproduced from Yun and DiCarlo [31], with kind permission from Wiley & Sons

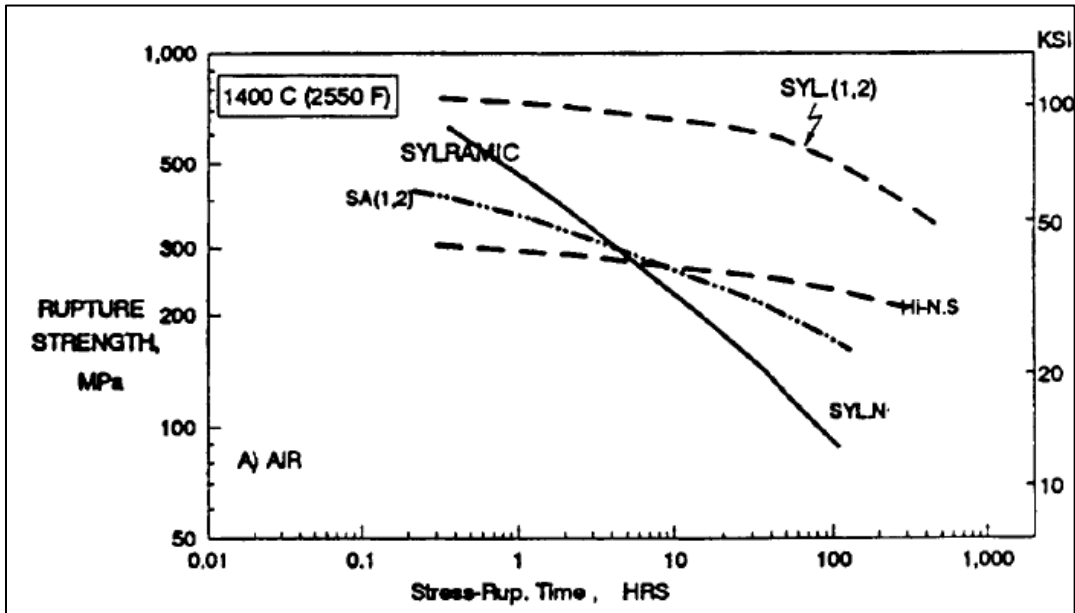


Figure 16: Rupture strengths of SiC fibers at 1400 °C in air; reproduced from Yun and DiCarlo [31], with kind permission from Wiley & Sons

Morscher and Pujar [21] examined mechanical performance of 0/90 woven SiC fiber-reinforced melt-infiltrated SiC/SiC CMCs. They evaluated and compared the performances of Tyranno ZMI and Sintered SiC (SA)-3 fibers, Hi-Nicalon fibers, and Sylramic-iBN fibers as CMC reinforcements. Composite room-temperature mechanical properties obtained by Morscher and Pujar are shown in **Table 5**. Stress-Strain curves obtained by Morscher and Pujar for different fiber-type melt-infiltrated composites are reproduced in **Figure 17**. It was found that Sylramic-iBN fiber-reinforced CMCs exhibited the highest average ultimate tensile strength (UTS), ranging from 361 to 444 MPa. Additionally, the Sylramic-iBN fiber-reinforced CMCs exhibited the highest modulus of elasticity (283 GPa) as seen in **Figure 17** [21]. Morscher and Pujar [21, 40] also investigated elevated temperature creep-rupture performance of the various SiC fiber-reinforced CMCs. Tensile creep-rupture studies were performed at both 1200°C and 1315°C in air. The strain vs. time curves are reproduced in **Figure 18**.

Table 5: Composite room temperature mechanical properties; reproduced from Morscher [21], with kind permission from Wiley & Sons

Panel	Average E (GPa) [#RT spec] (scatter)	Average UTS (MPa) [# specimens] (scatter)	Average ϵ (%) [# specimens] (scatter)	Average stress on fibers (GPa) [#RT spec] (scatter)	0.005% offset stress (MPa)	AE onset stress (MPa)	Residual stress (MPa)
SYLiBN-1	247 [3] (+0.007/-0.006)	361 [3] (+36/-32)	0.35 [3] (+0.04/-0.06)	1997 [2] (+79/-143)	194 [3] (+6/-9)	192 [2] ± 2	-60 [3] ± 7
SYLiBN-2	271 [2] (± 12)	465 [2] ± 37	0.47 [2] ± 0.03	2368 [2] ± 75	181 [2] ± 4	189 [2] ± 16	-60 [2] ± 10
SYLiBN-3	238 [1]	444 [1]	0.45 [1]	2210 [1]	176 [1]	155 [1]	-45 [1]
SA-1	254 [1]	358 [1]	0.33 [1]	2000 [1]	152 [1]	145 [1]	-20 [1]
SA-2	236 [1]	372 [1]	0.34 [1]	2047 [1]	178 [1]	138 [1]	-15 [1]
SA-3	230 [1]	334 [1]	0.30 [1]	1978 [1]	178 [1]	135 [1]	-30 [1]
HN	244 [7] (+43/-31)	311 [7] (+17/-10)	0.79 [7] (+0.12/-0.04)	2272 [7] (+208/-141)	126 [6] (+4/-5)	114 [6] (+12/-8)	-4 [6] (+7/-8)
Z-1	213 [4] (+5/-3)	279 [3] (+9/-6)	0.95 [3] (+0.04/-0.03)	1973 [4] (+66/-35)	111 [4] (+7/-6)	85 [4] (+10/-15)	+12 [4] (+5/-9)
Z-2	202 [4] (+5/-3)	261 [4] (+12/-6)	0.83 [4] (+0.02/-0.03)	1794 [4] (+49/-53)	107 [4] (+5/-4)	83 [4] (+11/-14)	+12 [4] (+8/-7)
HNS-1*	262 [1]	341 [1]	0.63 [1]	2278 [1]	154 [1]	150	-20
HNS-2*	232 [1]	412 [1]	0.60 [1]	2245 [1]	147 [1]	135	-20

*DiCarlo *et al.*⁶

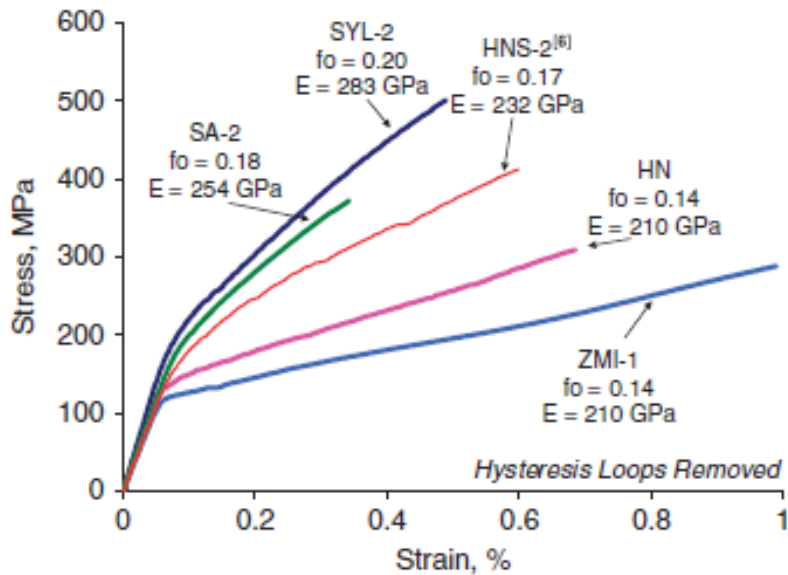


Figure 17: Stress-Strain curves for different fiber-type melt-infiltrated composites; reproduced from Morscher [21], with kind permission from Wiley & Sons

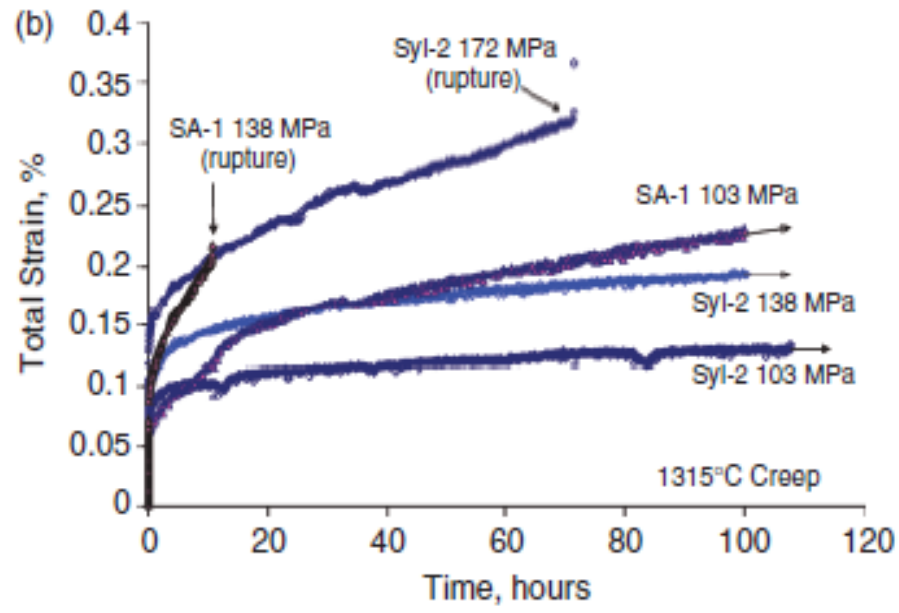
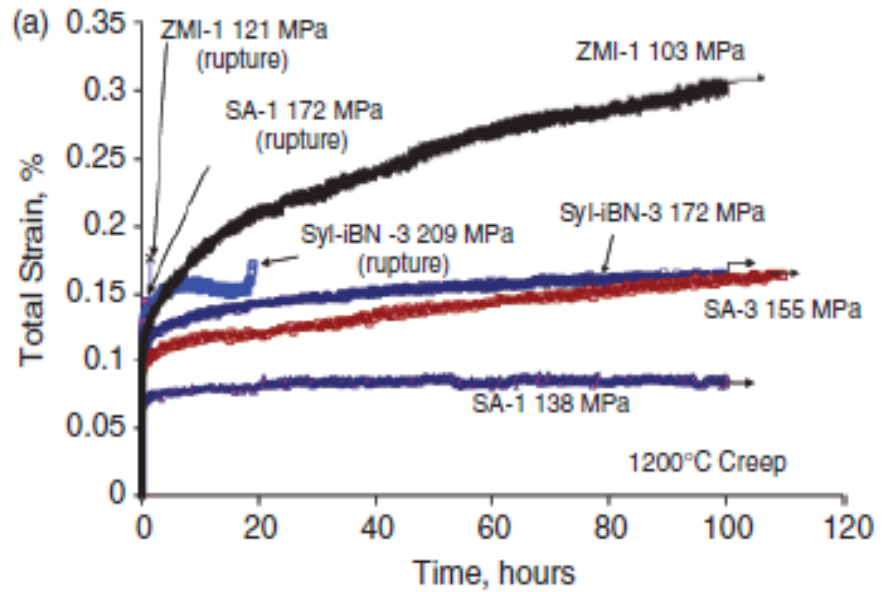


Figure 18: Tensile creep total strain (elastic plus time-dependent) curves at (a) 1200°C and (b) 1315°C for different SiC fiber-type melt-infiltrated composites; reproduced from Morscher [21, 40], with kind permission from Wiley & Sons

To date, there have not been any published studies on creep behavior of Sylramic-iBN fiber tows in the 400-500°C temperature range in air or in steam. This effort aims to investigate creep of Sylramic-iBN fiber tows at 400°C and 500°C in air and in steam. This study also aims to gain insight into what may happen to the in-situ BN coating at temperatures in the vicinity of the melting point of boria (450°C) and how that may affect the performance of the fiber.

III. Material and Test Specimen

3.1 Material

The material studied in this work was Sylramic-iBN fiber, developed at the NASA Glenn Research Center in conjunction with Dow Corning and currently manufactured by COI Ceramics. Sylramic-iBN is a near-stoichiometric SiC fiber that has an in-situ boron-nitride (BN) coating. The sintering process produces a very dense, strong and oxide-free fiber. However, there are no published studies on the exact Silicon to Carbon ratio in the bulk of the fiber. Sylramic-iBN fiber tows have a reported average grain size of approximately 100 nm, which is a significant contribution to the fiber tow's inherent creep resistance [31]. The tow consists of approximately 800 filaments with an average radius of 5 μ m [19, 20, 21]. Based on this data, a cross-sectional area of 6.28319 $\times 10^{-8}$ m² was used for all engineering stress calculations. Sylramic-iBN fiber tow properties are summarized in **Table 6**.

It is recognized that the tensile strength of ceramic fiber tows is generally less than the mean strength of fibers [19, 20, 31, 41, 36]. However, we propose that because composites utilize fiber tows, testing of fiber tows is more representative of the actual service conditions than testing of single filaments. Furthermore, Dassios et al. [42] and Calard et al. [41] also argue that experiments conducted on fiber tows are more representative of actual CMCs reinforced with the fiber tows rather than single filaments. These results and observations support the decision to test fiber tows rather than single filaments.

Table 6: Sylramic-iBN fiber tow properties; data reproduced from Yun, DiCarlo, and Morscher [19, 20, 21]

Property	Results	Units
Density	3.1	c/cm ³
Tensile strength*	1270	MPa
Tensile modulus	> 400	MPa
Number of filaments/tow	800	fibers
Average filament diameter	10	μm
Average grain size	100	nm
Max Process Temp	> 1700	°C

* UTS calculated from a 25-mm gage length tow at 23°C

3.2 Test Specimen

The fiber tow test specimens were prepared using the three-tab design and method developed by Steffens [32]. The process of fabricating a test specimen begins by preparing the three fiberglass tabs necessary to secure the fiber tows. Dimensions of the primary, secondary and tertiary tabs are 1.0 in. x 1.50 in., 1.00 in. x 1.00 in., 0.75 in. x 0.75 in., respectively. Then excess lengths (about 16 in) of tow are taken from the manufacturer’s spool. It is important to ensure that portions of the tow. Next the primary fiberglass tabs are positioned 7 in. apart on the grid-lined cutting board and secured to the board with tape. Each fiber tow section is placed on the cutting board with the tow ends centered on top of the tabs and utilizing grid lines for alignment. The fiber tow is then taped to the board. A two part epoxy (Hardman Double Bubble Epoxy, 04001) is applied to the tow section on top of the primary tab and to the secondary fiberglass tab. The secondary tab is placed on the primary tab such that the fiber tow and epoxy are sandwiched between the two tabs. After the adhesive is cured and hardened (approximately 5 minutes) the tape securing the fiber tow to the board is removed and the

excess tow protruding beyond the tabs is folded over the secondary tab toward the test section. The two part epoxy is then applied to the folded tow section on top of the secondary tab and to the tertiary tab. Finally a tertiary fiberglass tab is applied such that the fiber tow and epoxy are sandwiched between the secondary and tertiary fiberglass tabs. Once the epoxy adhesive is fully cured, any excess fiber tow protruding beyond the tertiary tab is cut with a razor blade. The final length of the fiber tow specimen measured between tabs was 7 in. For installation into the creep testing facility, a centerline hole was punched in the fiberglass tabs to permit hanging the fiber tow specimen on the hook fixtures. The same specimen design was used in all experiments. Test specimens in various stages of preparation are shown in **Figure 19**. The detailed description of the specimen preparation procedure is given by Steffens [32].

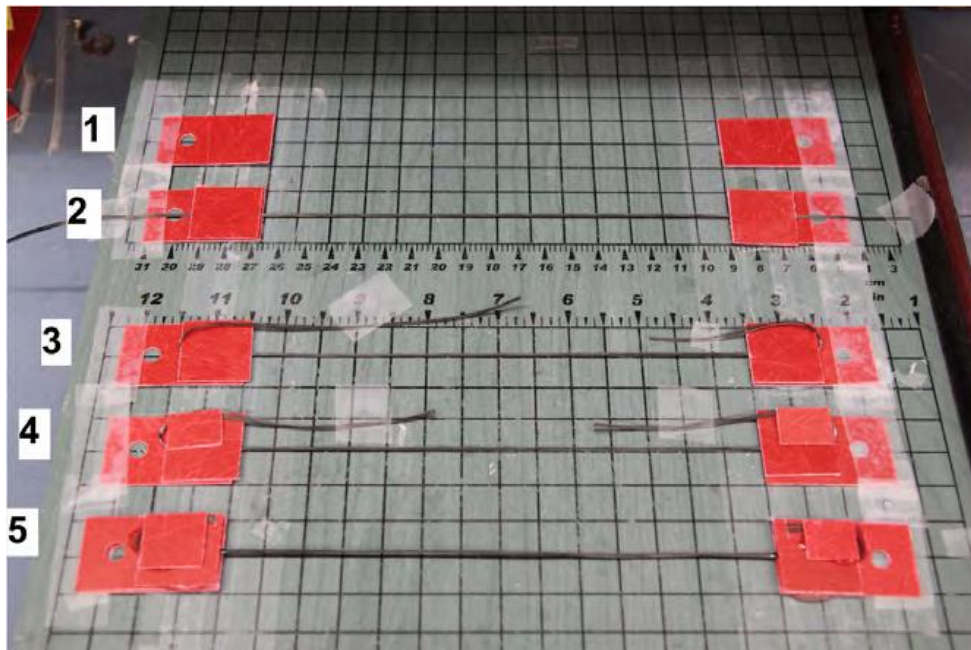


Figure 19: Fiber tow creep test specimen preparation process; reproduced from Shillig and Steffens [9, 32]

IV. Experimental Arrangements and Procedures

4.1 Experimental Facility

An experimental facility for testing SiC fiber tows at elevated temperatures in air and steam was designed and built by Armani [15] and modified by Steffens [32] and Shillig [9] in the Mechanics of Advanced Aerospace Materials Laboratory of the Department of Aeronautics and Astronautics at AFIT. Recent efforts [9, 32] demonstrated that mechanical testing of SiC fiber tows in steam at elevated temperatures is not a trivial matter. It was found that steam was chemically altered as it traveled along the SiC fiber tow specimen, extracting silicon from the fiber tow to become saturated with silicic acid ($\text{Si}[\text{OH}]_4$). As a result, scale thickness and composition varied along the length of the fiber tows indicating change in oxidation mechanisms. To combat these problems, a facility was designed in collaboration with Robertson [23] for creep testing of SiC fiber tows at elevated temperatures in air and in steam saturated with silicic acid.

An experimental facility for testing fiber tows at elevated temperature in air and in steam saturated with silicic acid was designed and configured at AFIT. An MTS FlexTest 40 digital controller was used for data acquisition. An MTS 653.03A two-zone resistance-heated furnace shown in **Figure 20** provides the high temperature test environment. The furnace is equipped with four silicon carbide heating elements and two R-type control thermocouples, which supply feedback to an MTS 409.83 temperature controller. The furnace has a 90-mm (3.5-in.) hot zone. A high resolution linear variable differential transformer (LVDT) was used to accurately measure the displacement of the specimen throughout the test. Temperature profiles were measured throughout the length of the furnace with a K-type thermocouple. Once the temperature profile is determined,

an effective gauge length of the fiber tow specimen can be calculated, which enabled the calculation of engineering strain from recorded displacement measurements. Technique for determining temperature profiles and methods for calculating strain from displacement measurements are discussed below.

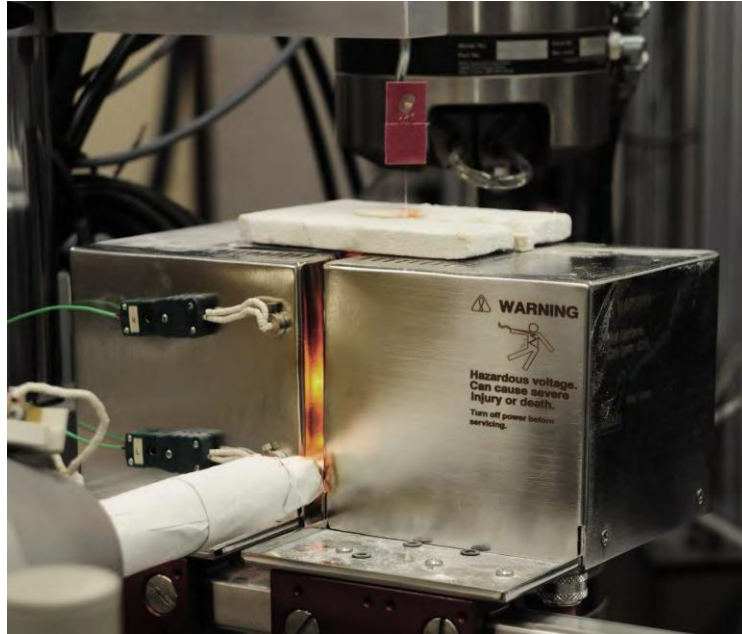


Figure 20: Two-zone resistance-heated MTS 653.03A furnace with SiC heating elements, R type control thermocouples and a 90-mm (3.5-in.) hot zone; reproduced from Armani [15]

All tests employed an alumina susceptor (ceramic tube with end caps) designed to fit inside the furnace chamber. The use of the susceptor has been shown to result in a more uniform and repeatable temperature distribution along the gauge section of the fiber tow specimen [9, 15]. The gauge section of the fiber tow specimen is located inside of the susceptor with the ends of the fiber tow specimen passing through slots in the susceptor

end caps. Dry air or silicic acid-saturated steam is supplied into the susceptor through an alumina feeding tube (see **Figure 21**).



Figure 21: Alumina susceptor and feeding tube assembled in one half of the furnace, along with fiber tow specimen mounted and running through the alumina susceptor; reproduced from Armani [15]

In this work tensile creep tests were performed using a dead-weight creep rig developed by Armani [15]. A fiber tow specimen is suspended from an extendable fixture. The elongation of the fiber tow specimen is measured with a Schaevitz M12-30 LVDT connected to the bottom tab of the fiber tow specimen. The rod extending from

the bottom of the LVDT core holds the dead weight. Slow application of the creep load is critical to preventing damage to the tow specimen during initial loading. Therefore a hand-driven screw elevator is used to apply the load to the fiber tow specimen. A detailed description of the specimens mounting procedure and of the creep test procedures is given elsewhere [15]. The creep load levels and the associated stackable weights are given in Appendix A. **Figure 22** shows a fiber tow specimen mounted in the dead weight creep testing facility.

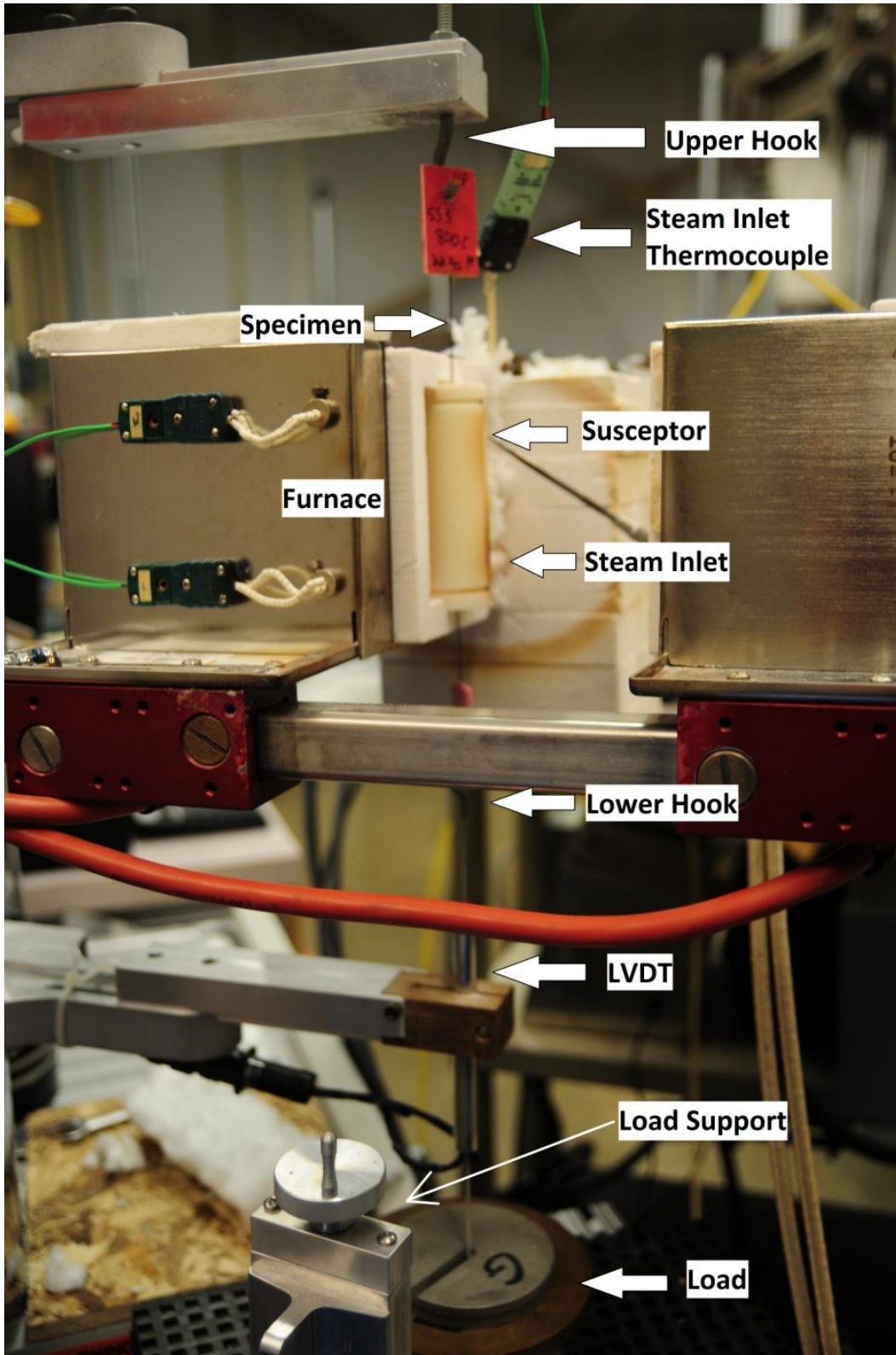
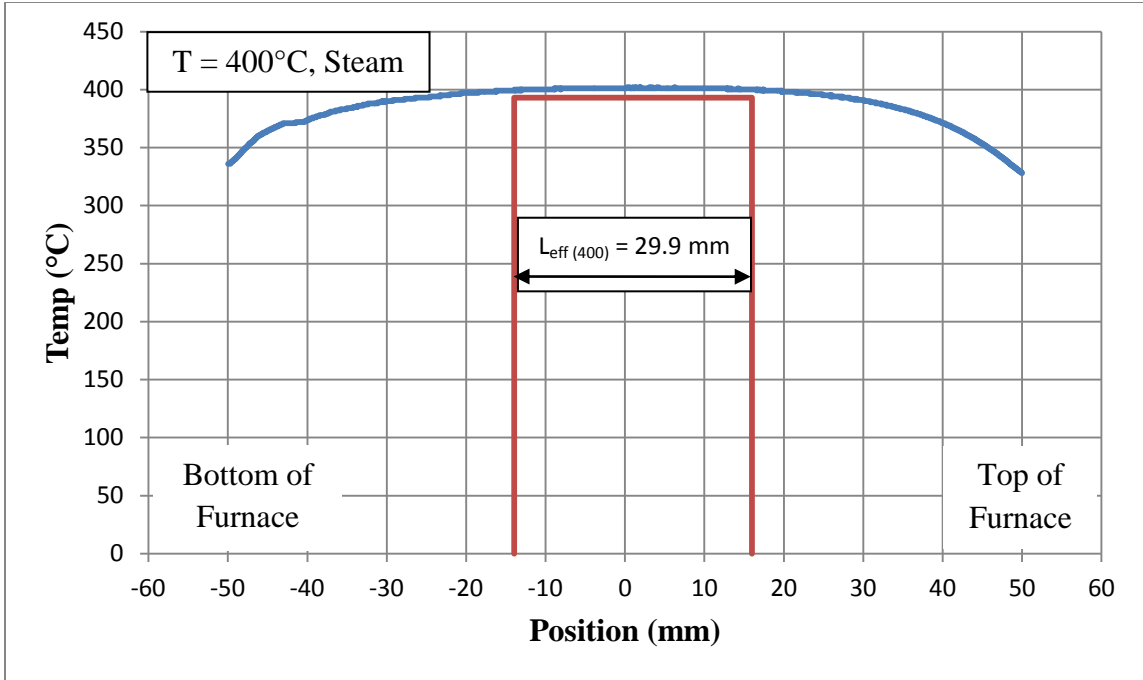


Figure 22: Fiber tow specimen mounted in the dead weight creep testing facility

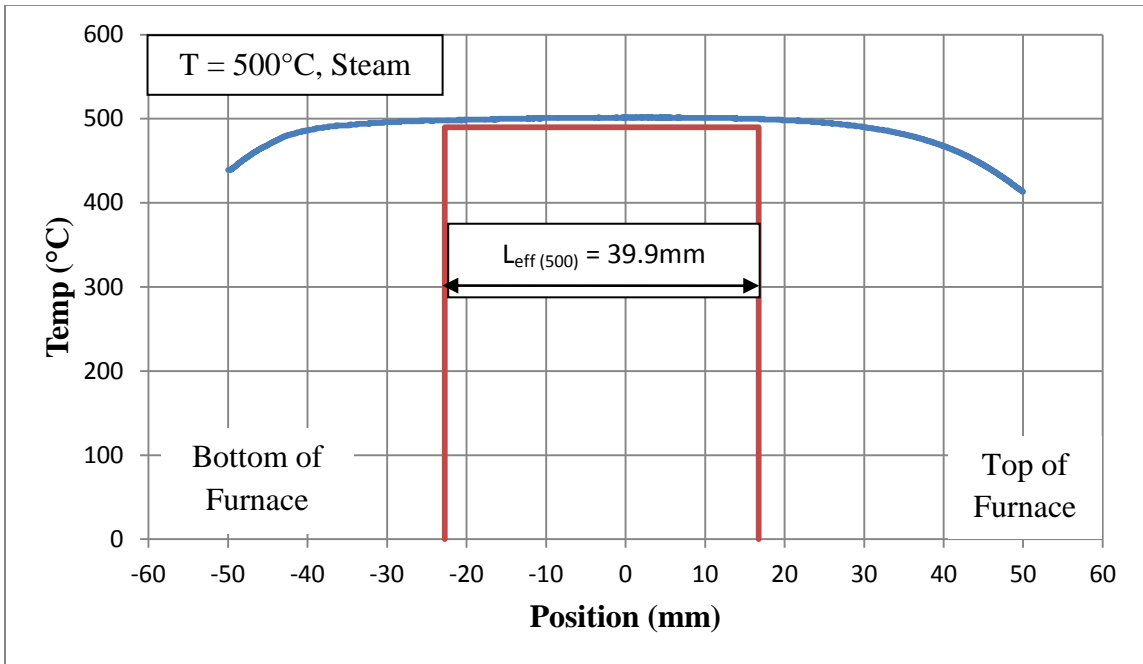
4.1.1 Temperature Profiles

Temperature profiles for fiber tow testing were determined using the same procedure as in Armani [15], Steffens [32], and Robertson [23]. Temperature profiles for fiber tow testing were determined by measuring the temperature along the centerline of the furnace with a K-type thermocouple with an accuracy of $\pm 3^{\circ}\text{C}$ up to 1200°C . The thermocouple was attached to the ram of the servo-hydraulic machine via a magnetic fixture, allowing for controlled probing throughout the height of the furnace. A CL3515R model thermometer with an accuracy of $\pm 1.5^{\circ}\text{C}$ was used for temperature readings.

In order to determine the furnace controller temperature setpoints, the thermocouple was positioned in the center of the furnace as the temperature was increased. To obtain the desired temperature setpoints of the upper and lower temperature controllers, an iterative process was performed by moving the thermocouple up and down from the center point of the furnace and adjusting the setpoints. Once the setpoints for the temperature controllers were determined, a detailed temperature profile was obtained by taking temperature measurements every 10 mm along the height of the furnace starting at the bottom inner surface and ending at the top inner surface of the susceptor. The temperature profiles obtained for 400°C and 500°C in steam are shown in **Figure 23**.



(a)



(b)

Figure 23 : Temperature profile obtained for Sylramic-iBN fiber tow specimen in steam at 400°C (a) and 500°C (b)

4.1.2 Strain Measurement

In this work tensile creep tests were performed using a dead-weight creep rig. The elongation of the fiber tow specimen was measured with a Schaevitz M12-30 LVDT connected to the bottom tab of the fiber tow specimen. The rod extending from the bottom of the LVDT core held the dead weight (see **Figure 22**).

A strain measurement device cannot be placed directly on a fiber tow specimen inside a furnace. Therefore, indirect methods detailed by Armani [15] were used to obtain strain measurements and to calculate strain and the strain rate of the specimen in the hot test section. These methods are briefly recapitulated here.

Extension of the fiber tow specimen is measured outside the furnace by linear variable displacement transducers (LVDT). This measurement incorporates the extensions produced over the entire specimen length throughout the temperature profile. In order to convert the LVDT measurement into a representative strain at the test temperature, the amount of displacement along the length of the test specimen subjected to the temperature profile must be determined. Note that the section of a fiber tow specimen subjected to a specific load at a higher temperature will produce larger displacement than another section of the same fiber tow specimen subjected to the same load at a lower temperature in the temperature profile. In order to convert the overall displacement of the fiber tow specimen to strain at the test temperature, the distribution of displacement along the temperature profile must be established. The method for calculating strain and strain rate from displacement measurements proposed by Armani [15] is similar to that of Morrell [43], Kandil and Dyson [44], and DiCarlo [45]].

This calculation of the effective gauge length takes into account the varying compliance along the fiber tow subjected to a temperature profile.

Consider a test specimen with a constant cross section and a length of $2L$. Defining the center of the specimen gauge section as zero, creep occurs over a total length $-L$ to L . Beyond these boundaries, creep is considered negligible [15, 23]. Thus, the total measured strain and total measured strain rate can be calculated as:

$$\varepsilon_m = \frac{\Delta l}{2L} = \int_0^t \dot{\varepsilon}_m dt \quad (3)$$

$$\dot{\varepsilon}_m = \frac{\text{measured extension rate}}{2L} = \frac{1}{2L} \int_{-L}^L \dot{\varepsilon} dl \quad (4)$$

Note that the total measured strain and strain rate calculated with **Equations 3 and 4** account for the variations in strain and strain rate along the length of the specimen subject to a temperature profile. At the hottest sections, the amount of strain or strain rate will be greater than at a lower temperature.

Denote the strain and strain rates at the desired maximum temperature at the center of the furnace by the subscript 0 . The strain at the center of the furnace is calculated as the time integral of the strain rate at the center of the furnace. It can also be described by the overall change in length of the specimen divided by a hypothetical length called the effective gauge length, $(2L)_{eff}$. The effective gauge length can also be described as the gauge length obtained under a hypothetical step-function temperature profile, in which all the strain is accumulated under the peak temperature and zero strain

is achieved under the lower temperature. The strain at the desired maximum temperature can be calculated as:

$$\varepsilon_o = \int_0^t \dot{\varepsilon}_o dt = \frac{\Delta l}{(2L)_{eff}} \quad (5)$$

Similarly, the strain rate at the desired maximum temperature, at the center of the furnace, can be expressed in terms of the effective gauge length as:

$$\dot{\varepsilon}_o = \frac{\text{measured extension rate}}{(2L)_{eff}} = \frac{1}{(2L)_{eff}} \int_{-L}^L \dot{\varepsilon} dl \quad (6)$$

The ratio of **Equations 4 and 6** yields the expression:

$$\frac{\dot{\varepsilon}_m}{\dot{\varepsilon}_o} = \frac{\Delta l}{(2L)_{eff}} \quad (7)$$

The general power-law creep equation (**Equation 2**) can now be applied considering that the stress is uniform and that the temperature is a function of location along the fiber tow specimen. The strain rate expression can now be expressed as:

$$\dot{\varepsilon} = A\sigma^n \exp\left(\frac{-Q}{RT(l)}\right) \quad (8)$$

Then, using **Equations 4, 7, and 8**, the ratio of the measured strain rate to the actual strain rate is expressed by a function of temperature only:

$$\frac{\dot{\epsilon}_m}{\dot{\epsilon}_o} = \frac{1}{2L} \int_{-L}^L \exp \left\{ \frac{-Q}{R} \left(\frac{1}{T(l)} - \frac{1}{T_o} \right) \right\} dl \quad (9)$$

Using a numerical summation of increments of length h such that $L = kh$, where k is an integer, the ratio of the measured strain rate to the actual strain rate now becomes:

$$\frac{\dot{\epsilon}_m}{\dot{\epsilon}_o} = \frac{1}{2k} \sum_{i=-k}^k \exp \left\{ \frac{-Q}{R} \left(\frac{1}{T(l)} - \frac{1}{T_o} \right) \right\} \quad (10)$$

As a result, an effective gauge length can now be calculated:

$$(2L)_{eff} = 2L \left(\frac{\dot{\epsilon}_m}{\dot{\epsilon}_o} \right) \quad (11)$$

The effective gauge length is then used to calculate strain as well as strain rate from displacement measurements taken outside the hot zone of the furnace.

Using the method described above, the temperature profiles reported in Section 4.1.1, and creep activation energy of 840 kJ/mol reported by DiCarlo [40], effective gauge lengths were calculated for Sylramic-iBN at each test temperature in air and in steam. The calculated values are listed in **Table 7**.

Table 7 : Effective gage lengths of Sylramic-iBN fiber tows in air and in steam at test temperatures

Temp (°C)	Effective Length (mm)	
	Air	Steam
400	29.6	29.9
500	43.2	39.5

4.2 Obtaining Steam

Previous studies at AFIT [15], [32], and [9] utilized a model HGA-H steam generator (MHI, Cincinnati OH) shown in **Figure 24**. Steam was produced using deionized water. Steam was supplied to the susceptor through a ceramic feeding tube (see **Figure 21**) in a continuous flow with a slightly positive pressure, expelling the dry air and creating a near 100% steam environment inside the susceptor.

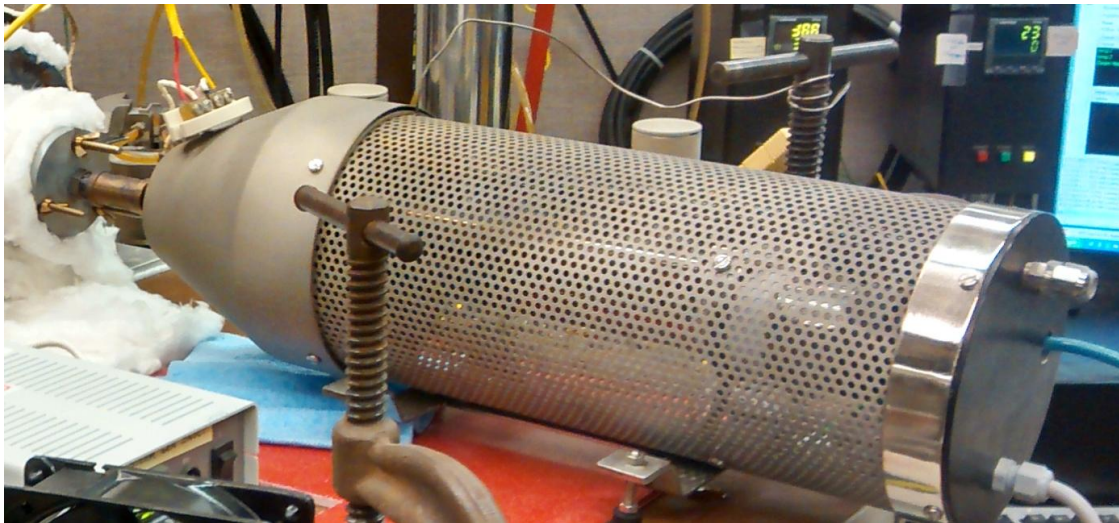


Figure 24: HGA-H (MHI) steam generator; reproduced from Robertson [23]

In the aforementioned previous studies, temperature of steam introduced into the susceptor ($\sim 100^{\circ}\text{C}$) was significantly below the temperature of the test specimen. Steffens [32] reported that all Hi-Nicalon-S fiber tow specimens tested at 800°C in steam failed at the same location along the fiber tow (see **Figure 25**). Moreover, all failures were localized at the point of steam entry into the susceptor (blue line in **Figure 25**). It was recognized that continuous stream of “cold” steam entering the “hot” test chamber caused a discontinuity in the temperature profile within the hot zone. Furthermore, the “cold” steam impinging on the fiber tow likely preferentially extracted silicon from the fibers at that location, weakening the fibers and causing failure.



Figure 25: Effect of steam impinging on fiber tows upon entry into the test chamber; reproduced from Steffens [32]

Shillig [9] developed and implemented a new design of the steam delivery system. Shillig replaced a simple open-ended alumina feeding tube used by Armani [15] and Steffens [32] with a capped alumina feeding tube with a circumferential slot cut halfway through. Shillig installed the feeding tube into the susceptor with the circumferential slot pointing downward, directing the flow of steam towards the bottom of the susceptor. Thus steam was diverted and no longer impinged directly on the fiber tow specimen.

While using the modified steam delivery system to study creep of Hi-NicalonTM-S SiC fiber tows at elevated temperature in steam, Shillig identified new challenges. Notably, exposure to steam at 800°C resulted in varying types and degrees of oxidation along the length of the fiber tow specimen. Apparently steam was chemically altered as it traveled upwards along the fiber tow, extracting silicon from the fiber tow to become saturated with silicic acid (Si[OH]₄) as it reached the top of the susceptor. The steam saturation process occurring inside the susceptor resulted in a gradual change in oxidation mechanism of the Hi-NicalonTM-S fiber tow. Bottom sections of the fiber tow exhibited degradation due to active oxidation (**Figure 26 a**). In contrast, the top sections of the fiber tow exhibited SiO₂ scale growth due to passive oxidation that occurs once the steam is saturated (**Figure 26 b**). These results led to the conclusion that steam must be saturated with silicic acid at test temperature prior to entering the susceptor to produce uniform oxidation along the length of the fiber tow specimen. In order to achieve this objective, two main challenges had to be overcome: (1) reaching desired steam temperatures and (2) saturating the steam with silicic acid.

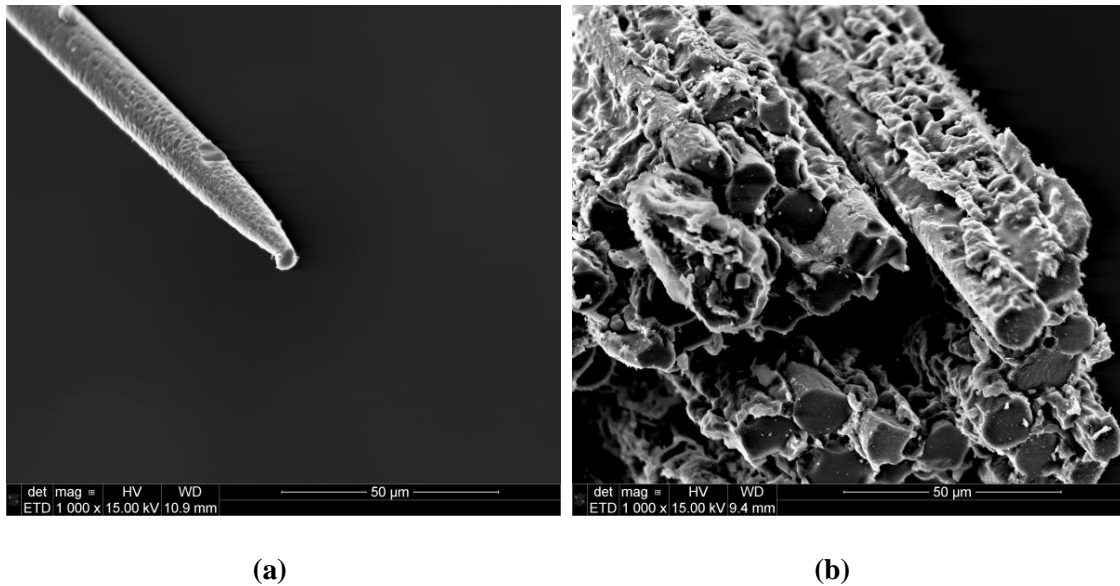


Figure 26: SEM micrographs of the Hi-Nicalon™-S fiber tows subjected to creep at 800°C in steam. Variations along the length of the fiber tow are evident. (a) Fiber degradation due to active oxidation, typically found in bottom sections of the fiber tow. (b) SiO₂ scale growth typically found in top sections of the fiber tow. Reproduced from Shillig [9]

4.3 Improving the Experimental Facility

4.3.1 Reaching Desired Steam Temperatures

The testing facility developed by Armani [15] and modified by Shillig [9] was redesigned to achieve the following objectives: (1) to preheat the steam to test temperature and (2) to saturate the steam with silicic acid before it enters the susceptor. These goals were attained in collaboration with Maj Scott Robertson.

As mentioned above, when “cold” steam enters the “hot” test chamber, the temperature profile within the hot zone is likely to be disrupted. Additionally, we recognize that steam is a temperature-dependent process. As the temperature increases so does the capacity of the steam to carry silicic acid. Hence it is critical that the saturated steam be at test temperature when it is injected into the susceptor. If steam temperature is

significantly below the test temperature, steam will be heated up inside the susceptor and its capacity to carry silicic acid will increase. As a result steam will extract silicon from the fiber tow in order to become saturated at test temperature. If steam temperature is significantly above the test temperature, the steam will cool down inside the susceptor resulting in precipitation of silica out of the saturated steam. The precipitated silica may be deposited on the fiber tow, interfering with the scale growth. Therefore, the temperature of the saturated steam must be carefully controlled [46].

The steam generator (Model HGA-S-01, MHI, Cincinnati, OH) used in this research is capable of delivering steam at temperatures up to approximately 500 °C. A companion heating unit (Model CX1300, MHI, Cincinnati, OH), capable of heating the steam up to 1300 °C, can be used to maintain and/or increase steam temperature. The heating unit is connected to the steam generator by a stainless steel transition apparatus. The CX1300 unit contains an alumina tube passing through a cylindrical insulated heating chamber with an electrically powered molybdenum disilicide resistance heating coil. The steam is heated as it passes through the CX1300 unit. The heated steam exiting the heating unit is funneled into an alumina tube of a smaller diameter, which is connected to the feeding tube delivering steam into the test chamber.

Not surprisingly steam temperature drops significantly as it moves through the tubing from the heating unit to the test chamber. In order to prevent the heat loss, aluminosilicate blanket insulation was wrapped around the tubing assembly connecting the heating unit to the test chamber. The use of insulation retarded the heat loss enough to achieve the 800°C steam temperature at maximum steam generator power settings. However, repeated removal and reapplication of the blanket insulation led to questionable

repeatability in the test procedure. Furthermore, a relatively high flow rate (12-16 ml/min) was needed to maintain the desired steam temperature (800-1200 °C) in the test chamber. However, steam entering the test chamber at such a high flow rate will aerodynamically damage the fiber tow specimen. The flow rate for fiber tow testing should be only high enough to induce a slight positive pressure, ensuring that the susceptor remains filled with heated steam throughout the test. Flow rates of only 0.8-2.0 ml/min were used in previous research [9, 15, 32]. Yet when low flow rate is used, the heated steam transitions from the heating unit to the test chamber slowly with the steam temperature dropping considerably.

In order to transition from a higher steam flow rate in the heating unit to a desired low flow rate in the test chamber, a method to bleed off steam was devised. A bleed-off system consisting of a bleed-off tube with two valves was introduced. Adjusting the two valves allowed for a more precise control of the flow rate. While this initial design of the bleed-off system was successful in controlling the flow rate, we could not maintain the desired steam temperature. Additionally, stainless steel components of the initial bleed-off system deteriorated rapidly. Metal debris was found contaminating the test specimen inside the test chamber. The overall steam delivery system had to be redesigned.

A new design of the steam delivery system was developed, which incorporated changes to the heating unit, insulation and the steam bleed-off system. The new design minimized the heat loss during transition from the heating unit and the test chamber as well as provided for precise control of the flow rates. The new steam delivery system was completed in several steps.

First, all metal tubing was replaced with alumina tubing. The 50-mm diameter alumina tube passing through the CX1300 heating unit, the center-hole stainless steel plate clamped to the alumina tube and the 6-mm diameter stainless steel tubing fitted to the plate were replaced by a single alumina tube that acts as a reducing nozzle. At one end the diameter of the replacement tube reduces sharply from 50-mm to 6-mm. The reduced end of this alumina tube was fitted onto a 75-mm long alumina transition tube, which in turn was fitted onto an alumina supply tube. The supply tube delivers steam to the test chamber. Notably, the finished distance between the transition tube and the furnace is less than 25 mm. An R-type thermocouple in alumina sheathing inserted through a tight-fit hole into the supply tube monitors the steam temperature just before it enters the test chamber.

Next, a new steam bleed-off system was designed and implemented, which permits transition from a higher steam flow rate in the heating unit to a desired low flow rate in the test chamber. The new bleed-off system employed ceramic tubing, but no metal parts. One end of an alumina bleed-off tube was cut at a 45° angle and inserted into a hole cut in the side of the transition tube. The outer diameter of the bleed-off tube was nearly the same as the inner diameter of the transition tube to insure a tight fit. The flow can now be regulated by simply rotating the bleed-off tube. Rotation of the bleed-off tube needed to achieve the desired steam temperature and flow rate in the test chamber are readily determined. **Figure 27** shows the steam bleed-off system.

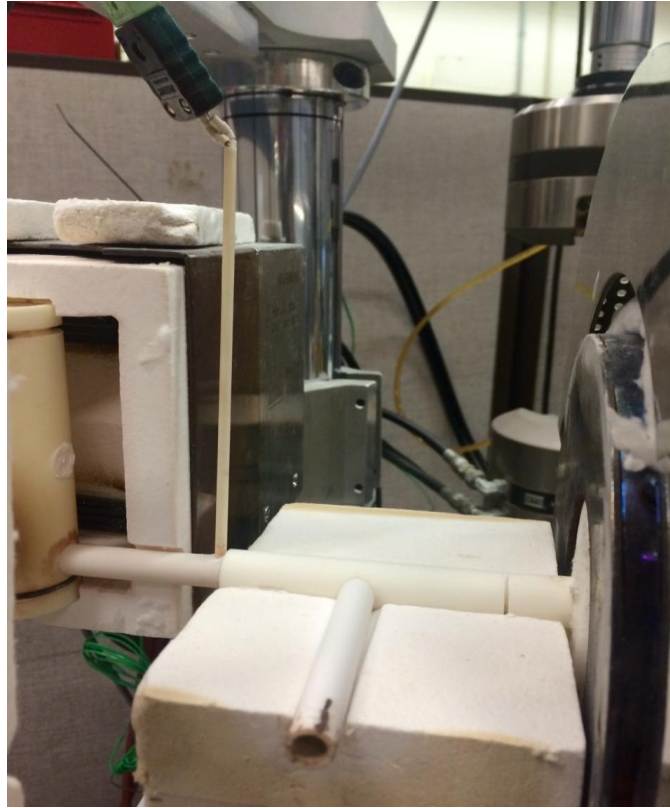


Figure 27: Steam bleed-off system designed to achieve the desired steam temperature and flow rate in the test chamber

The third development addressed the insulation. To ensure test-to-test repeatability, blanket insulation was replaced with solid block alumina insulation. Six 25-mm thick layers and two 12-mm thick layers of alumina block insulation (Rescor 902, Cotronics Corp., Brooklyn, NY) were machined and stacked to fit between the steam heating unit and the test furnace and around the transition and bleed-off tubes. Remaining gaps were filled with aluminosilicate blanket insulation. The insulation assembled between the heating unit and the test furnace is shown in **Figure 28**. Using stacked layers of solid block insulation allows for easy assembly and removal, as well as ensures repeatability.

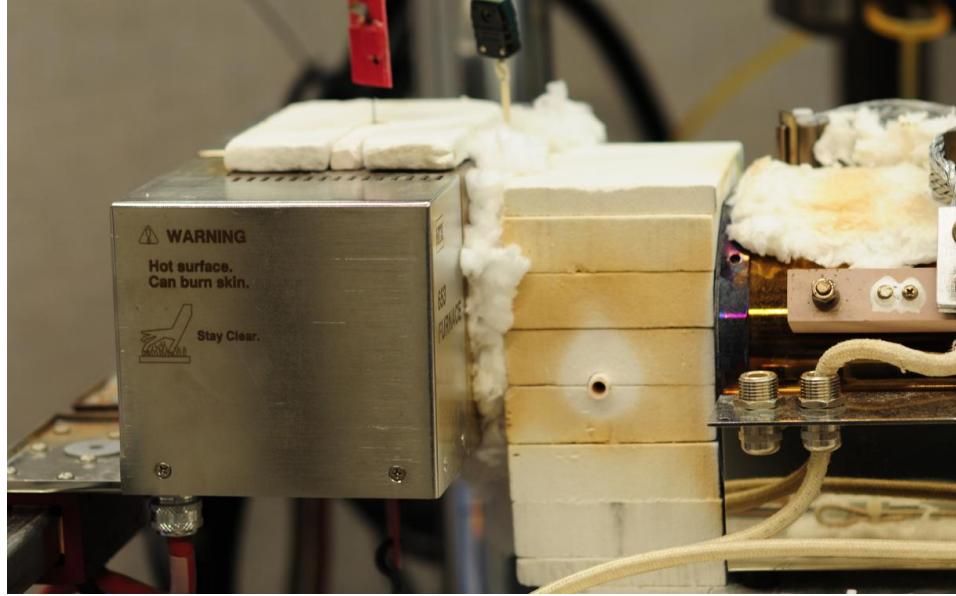


Figure 28: Layers of alumina block insulation and aluminosilicate blanket insulation assembled between CX1300 heating unit and test furnace.

The fourth development addressed the pre-heating of the steam to desired test temperatures. The new facility design employs two CX1300 heating units connected in series, rather than a single heating unit. By connecting two heating units in series we essentially double the length of the heating chamber and allow twice as much time for the steam to reach desired temperature. As a result we can consistently reach target steam temperatures at lower power settings. Note that the new design makes it possible to reach steam temperatures above 800°C.

Finally, the original CX1300 heating unit was redesigned to provide faster response to setting adjustments and to generate enough heat to produce steam temperatures above 1200°C. The original MoSi₂ resistance heating coil was replaced with a MoSi₂ coil of smaller thickness with an additional complete turn. The new heating coil was encased in insulation (KVS 174/400, RATH, Newark, DE) prior to insertion into the CX1300 shell. The re-designed facility employs two CX1300 heating units equipped with

modified coils. The new facility is capable of achieving target steam temperatures consistently in about 1/3 of the time required with the original facility.

4.3.2 Saturating the Steam with Silicic Acid

The results of prior research reviewed in Section 4.1.3 suggest that in order to study creep of SiC fiber tows at elevated temperature in steam, we must ensure that steam entering the test chamber is at test temperature and saturated with silicic acid. To accomplish steam saturation, silica wool (Hereaus Quartz, LLC USA, Austin, TX) was placed inside the large-diameter alumina tube (see **Figure 29**) that passes through the heating chambers of the two modified CX1300 heating units (see **Figure 30**). The high surface area of the fibrous silica wool allows for a faster reaction with the steam as it passes through, assuring steam saturation with silicic acid. Placing the silica wool inside the heating units assures that steam is at the target test temperature as it undergoes saturation. As a result, steam is saturated with silicic acid at test temperature prior to entering the test chamber.

Figure 30 shows the newly designed test facility.



Figure 29: Silica wool placed inside the heating tube to achieve saturation of heated steam with silicic acid

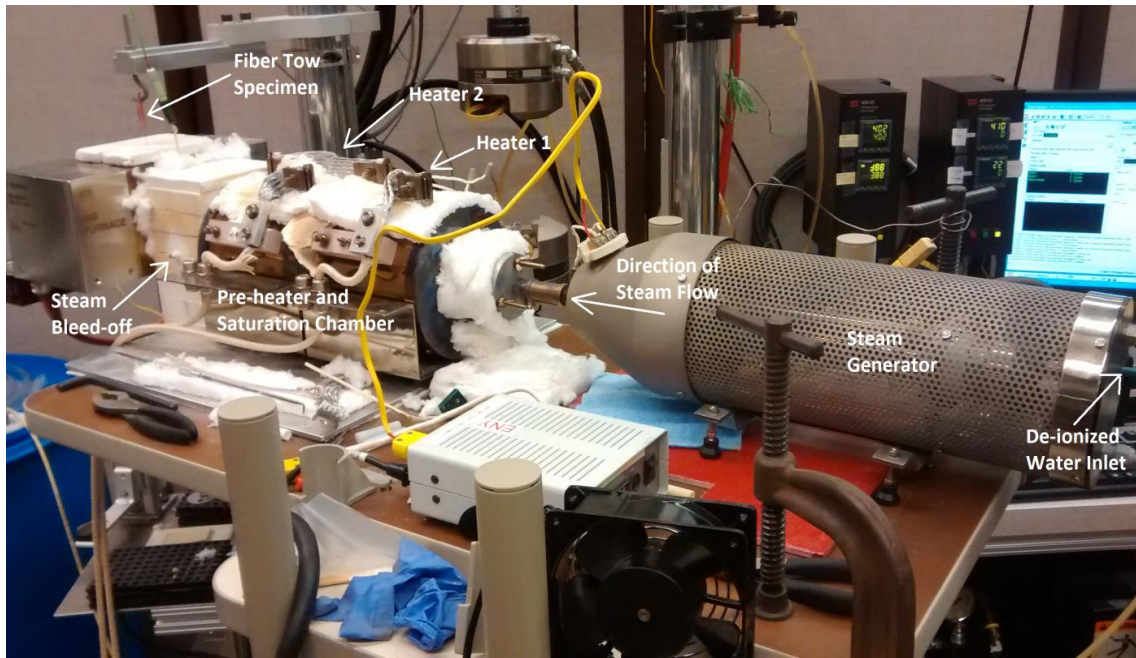


Figure 30: The newly designed test facility permits testing of SiC fiber tows at elevated temperature in silicic acid-saturated steam

4.3.1 Experimental Validation of the New Test Facility

The new test facility was validated by performing creep tests of Hi-NicalonTM S SiC fiber tow specimens at 800°C in silicic acid-saturated steam. The test specimens were fabricated from the spool of material used in previous studies [34, 9]. Creep tests were performed at 2.96 and 154 MPa. The test procedure was the same as that employed by Shillig [9] and Steffens [32] with the exception of using the silicic acid-saturated steam instead of the unsaturated steam. As expected, creep run-out of 100 h was achieved in both tests. Steady-state creep rates produced in both tests were negligible ($< 10^{-9} \text{ s}^{-1}$).

Robertson [23] analyzed the tested specimens using scanning electron microscopy (SEM) and energy dispersive spectroscopy (EDS). Robertson examined different sections of the fiber tow specimens within the gage section: near the center, approximately 25 mm below the center (near the bottom of the hot zone) and approximately 25 mm above the

center (near the top of the hot zone). Recall that fiber tow specimens tested by Steffens [32] and Shillig [9] showed significant change in chemical composition from the bottom to the top of the hot zone. Notably, fiber tow specimens tested by Robertson [23] in the newly re-designed test facility exhibited no significant chemical variation. Robertson reported that silica scale growth due to oxidation was minimal and relatively uniform along the length of the fiber tows. The new test facility successfully produced silicic acid-saturated steam at the target test temperature.

V. Monotonic Tension and Tensile Creep of Sylramic-iBN Fiber Tows

5.1 Monotonic Tension

Sylramic-iBN fiber tows were subjected to tension tests to failure at various temperatures in air. The objective was two-fold. First we aimed to evaluate the dependence of the UTS on temperature. Second, established UTS values would serve as a basis for selecting creep stress levels for tensile creep tests. The fiber tow specimens used in tension tests were fabricated as described in Section 3.2 above. An MTS Landmark™ 370 testing system with 1 Kip load capacity was used to apply load in tension tests. Tension tests were performed in load control. An MTS FlexTest 40 digital controller was for input signal generation as well as for data acquisition. A detailed description of the MTS Landmark™ 370 system and the controller tuning procedures is given by Armani [15].

Results of the tension tests performed at 23, 400 and 500°C are summarized in **Table 8**. The UTS results produced at all temperatures in this study are erratic. The degree of inconsistency and scatter is unacceptable.

Table 8: Ultimate Tensile Strength (UTS) of Sylramic-iBN fiber tows at various temperatures


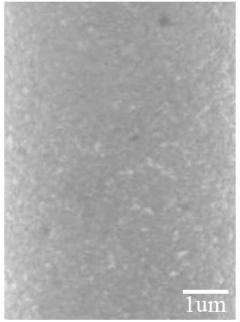
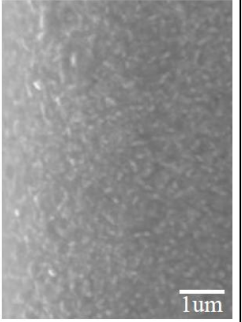
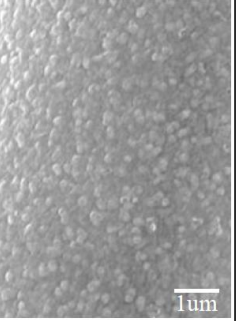
	UTS (MPa)					
21°C	873	*	692	394	301	378
400°C	*	68	201	268	312	293
500°C	293	-	-	-	-	-

* Inconclusive test

The inconsistent results of the tensile tests were initially perplexing. Nonetheless, we subsequently learned [47] that numerous researchers obtained similarly erratic results in tensile tests of Sylramic-iBN fiber tows. The inconsistencies in tensile properties were attributed to fiber processing.

It has been demonstrated that Sylramic-iBN fibers have a high surface roughness, and therefore require an interfacial coating in order to be effective in unidirectional loading applications [48]. Ozawa et al [48] compared the relationship between microstructure, fiber surface roughness, and the interfacial sliding stress for several near-stoichiometric SiC fibers, including Sylramic-iBN fibers (see **Table 9**). Ozawa et al reported Sylramic-iBN fibers to have an interfacial sliding stress (or frictional stress at the sliding surface) of 73 MPa, which is related to the high surface roughness of this fiber. If fibers in a bundle have high surface roughness, the load carried by a failing fiber will be transferred directly to the neighboring fibers rather than being more uniformly distributed across the entire bundle. As a result, the crack that propagated through the failed fiber continues to propagate through the neighboring fibers, causing cascading fiber failures followed by a pre-mature failure of the tow. It is possible that the Sylramic-iBN fiber tows used in this research lack consistent interfacial coating. Thus the high surface roughness resulted in failure at lower applied stresses than those reported by DiCarlo [30, 31].

Table 9: Relationship between microstructure, fiber roughness (denoted by R_q), and interfacial sliding stress of near-stoichiometric SiC fibers; reproduced from Ozawa [48], with kind permission from Wiley & Sons

Fiber	Hi-Nicalon Type-S	Tyranno-SA3	Exp-Sylramic	Exp-Sylramic-iBN
Surface Micro-structure				
R_q [nm]	•0.87, Hinoki (2001) •2.33, Sauder <i>et al.</i> (2010) •<10, Yun <i>et al.</i> (2001)	•1.71, Hinoki (2001) •8.04, Sauder <i>et al.</i> (2010)	•~10, Yun <i>et al.</i> (2001) •17.561, Brennan (2000)	•~27, Yun <i>et al.</i> (2001)
τ [MPa]	•8, This work •14.46, Sauder <i>et al.</i> (2008)	•15, This work •223, Sauder <i>et al.</i> (2008)	•16, This work	•73, This work
Interphase	•150 nm PyC	•150 nm PyC	•150 nm PyC	•n/a (Sylramic-iBN)

Bhatt et al [49] studied the microstructure and tensile properties of BN coated Hi-Nicalon and Sylramic SiC fiber performs of multiple batched fibers. The batch to batch variations in Archimedes density and porosity are shown in **Figures 31** and **32**, respectively. Bhatt et al reported roughly 20% variability in density and pore fraction amongst the batches, and roughly 10% variability amongst specimens tested within a single batch [49]. Dramatic variability in the UTS values obtained for Sylramic-iBN fiber tows in this research suggests that this batch of fiber may also exhibit significant variability in density and porosity. Further investigation of the fiber tow specimens used in this research is needed to reach a definitive conclusion regarding the porosity and density variability within this batch of fibers.

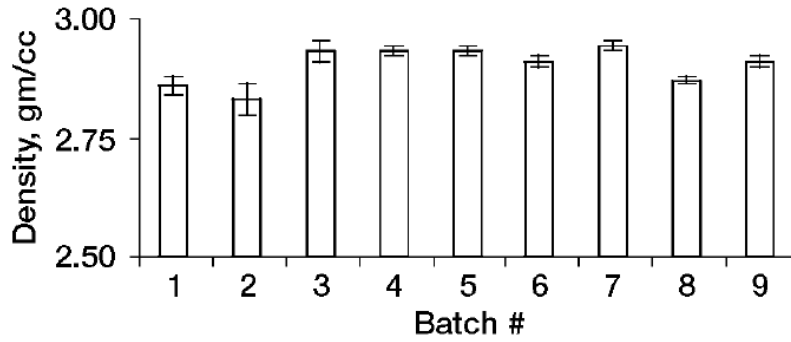


Figure 31: Batch to batch variation in Archimedes density for BN/SiC coated Sylramic fiber perform specimens; reproduced from Bhatt, et al [49], with kind permission from Springer Science and Business Media

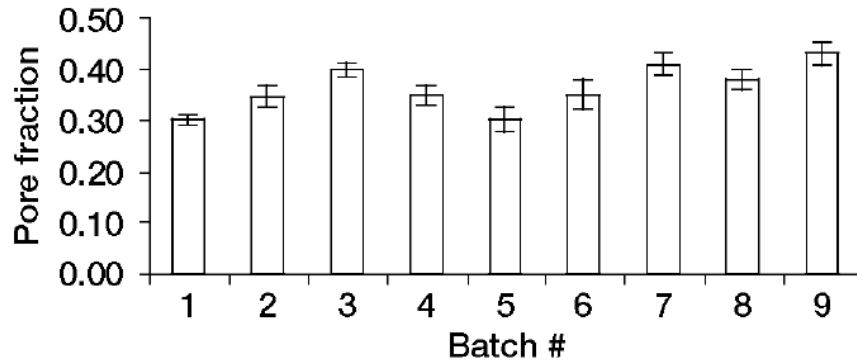


Figure 32: Batch to batch variation in open porosity for BN/SiC coated Sylramic fiber perform specimens; reproduced from Bhatt, et al [49], with kind permission from Springer Science and Business Media

5.2 Creep of Sylramic-iBN Fiber Tows at 400°C in Air and in Silicic Acid-Saturated Steam

Sylramic-iBN fiber tows were subjected to tensile creep at 400°C in compressed dry air and in silicic acid-saturated steam. The results of the creep-rupture tests are

summarized in **Table 10**. In this work creep run-out was defined at 100 hours at creep stress.

Table 10: Summary of creep results for Sylramic-iBN SiC fiber tows obtained at 400°C in dry air and in silicic acid-saturated steam

Specimen ID	Test Environment	Creep Stress (MPa)	Creep Lifetime (h)	Steady-State Creep Rate (s ⁻¹)	Creep Strain (%)
Air 1	Air	508	0†	-	-
Air 5	Air	508	0†	-	-
Air 4	Air	444	100‡	3.37 E -09	0.428
Air 3	Air	381	100‡	1.10 E -09	0.330
Air 2	Air	254	100‡	1.01 E -09	0.098
SS 20	Steam	762	0†	-	-
SS 19	Steam	572	0†	-	-
SS 18	Steam	508	0†	-	-
SS 17	Steam	444	100‡	4.32 E -09	0.419

† Broke upon loading

‡ Creep run-out defined as 100 h at creep stress. Failure did not occur when the test was terminated

The Sylramic-iBN fiber tows exhibit negligible creep at 400°C in air. Surprisingly, there is an abrupt transition from immediate failure to surviving 100 h of creep as the stress decreases from 508 to 444 MPa. Typically, progressively increasing creep lifetimes would be obtained as the creep stress decreases from the level that yields zero creep lifetime to the level that yields a 100-h lifetime. It is possible that such atypical behavior of the Sylramic-iBN fiber tows is caused by the variability of the fiber tow within the batch.

Creep curves obtained at 254, 381, and 444 MPa at 400°C in compressed dry air are shown in **Figure 33**. Note that all tests represented in **Figure 33** achieved a 100-h run-out. Primary and secondary creep regimes are observed in all tests. Tertiary creep was not noted in any of the tests. The transition from primary to secondary creep occurred early in the creep life. The steady-state creep rates produced in these tests were at or below $4.32 \times 10^{-9} \text{ s}^{-1}$. However, because it was expected that no measurable creep would be observed at such low temperatures, there exists a possibility that what was being recorded was due to progressive fiber failure of the fiber tow.

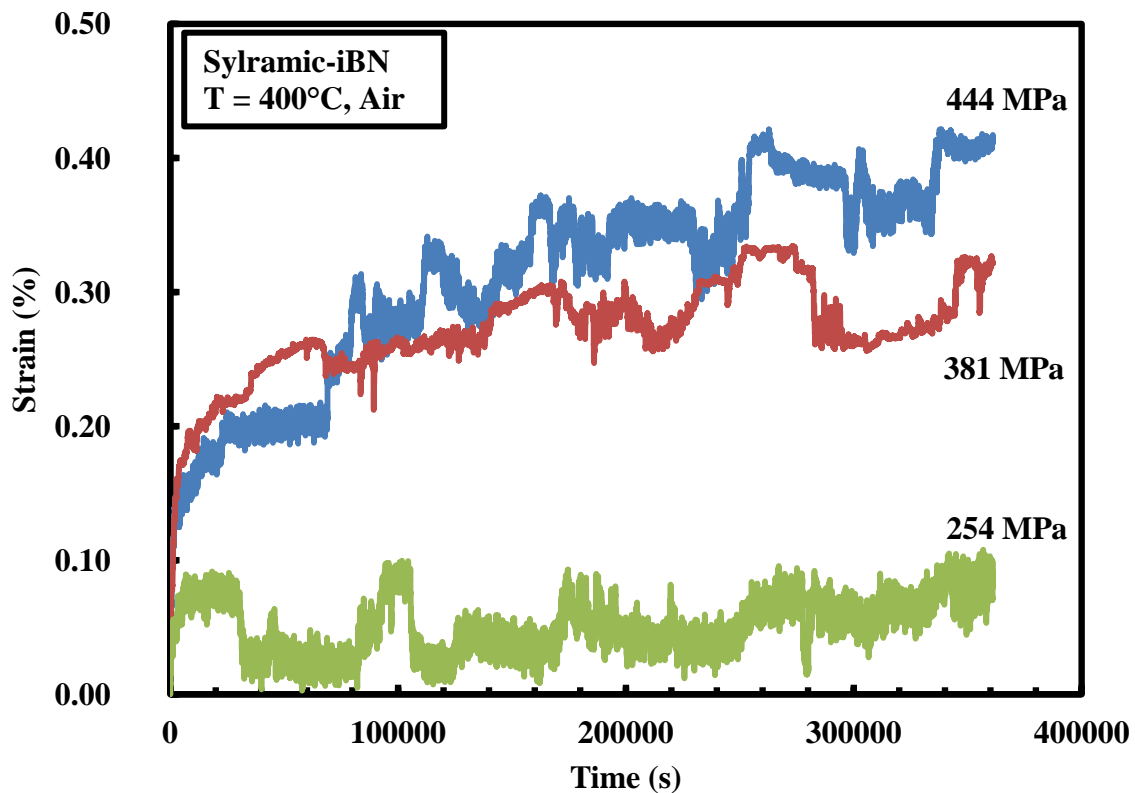


Figure 33: Creep strain vs. time curves for Sylramic-iBN fiber tows obtained at 400°C in compressed dry air

Results obtained at 400°C in silicic acid-saturated steam are very similar to those produced at 400°C in air. Sylramic-iBN fiber tows exhibit negligible creep at 400°C in steam. In steam there is also an abrupt transition from immediate failure to surviving 100 h of creep as the stress decreases from 508 to 444 MPa. Creep curve obtained at 400°C in silicic acid-saturated steam are shown in **Figure 34**. The specimen represented in **Figure 34** achieved a 100-h run-out. The creep curve exhibits primary and secondary creep regimes, but no tertiary creep. However, because it was expected that no measurable creep would be observed at such low temperatures, there exists a possibility that what was being recorded was due to progressive fiber failure of the fiber tow.

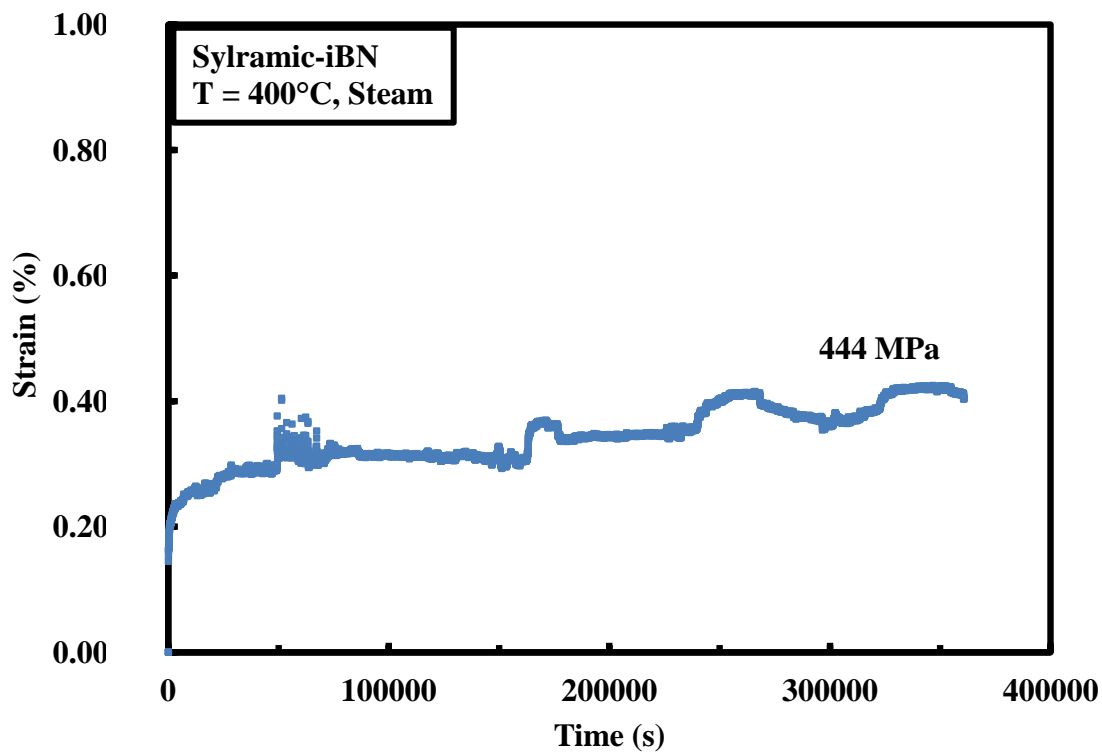


Figure 34: Creep strain vs. time curve obtained for Sylramic-iBN fiber tow at 400°C in silicic acid-saturated steam

5.3 Creep of Sylramic-iBN Fiber Tows at 500°C in Air and in Silicic Acid-Saturated Steam

Sylramic-iBN fiber tows were subjected to tensile creep at 500°C in compressed dry air and in silicic acid-saturated steam. The results of the creep-rupture tests are summarized in **Table 11**.

Table 11: Summary of creep results for Sylramic-iBN SiC fiber tows obtained at 500°C in dry air and in silicic acid-saturated steam

Specimen ID	Test Environment	Creep Stress (MPa)	Creep Lifetime (h)	Steady-State Creep Rate (s ⁻¹)	Creep Strain (%)
Air 7	Air	762	0†	-	-
Air 8	Air	635	0†	-	-
Air 9	Air	571	0†	-	-
Air 6	Air	508	25	7.59 E -08	0.374
Air 10	Air	508	0†	-	-
Air 11	Air	508	0†	-	-
Air 12	Air	444	0†	-	-
Air 13	Air	444	0†	-	-
Air 14	Air	381	0†	-	-
Air 15	Air	254	0†	-	-
Air 16	Air	127	100‡	3.44 E -10	0.272
SS 21	Steam	635	0†	-	-
SS 22	Steam	508	0†	-	-
SS 23	Steam	381	0†	-	-
SS 24	Steam	254	100‡	1.10 E -09	0.196

† Broke upon loading

‡ Creep run-out defined as 100 h at creep stress. Failure did not occur before test termination.

The Sylramic-iBN fiber tows exhibit negligible creep in 500°C in air. As at 400°C, there is an abrupt transition from immediate failure to surviving 100 h of creep as the stress decreases from 254 to 127 MPa. Surprisingly, one specimen tested at 508 MPa survived 25 h at creep stress. However, this result is anomalous and is likely due to the inconsistencies in the fibers.

Creep curves obtained at 127 and 508 MPa at 500°C in compressed dry air are shown in **Figure 35**. Primary and secondary creep regimes are observed in all tests. Tertiary creep was not noted in any of the tests. The transition from primary to secondary creep occurred early in the creep life. However, because it was expected that no measurable creep would be observed at such low temperatures, there exists a possibility that what was being recorded was due to progressive fiber failure of the fiber tow.

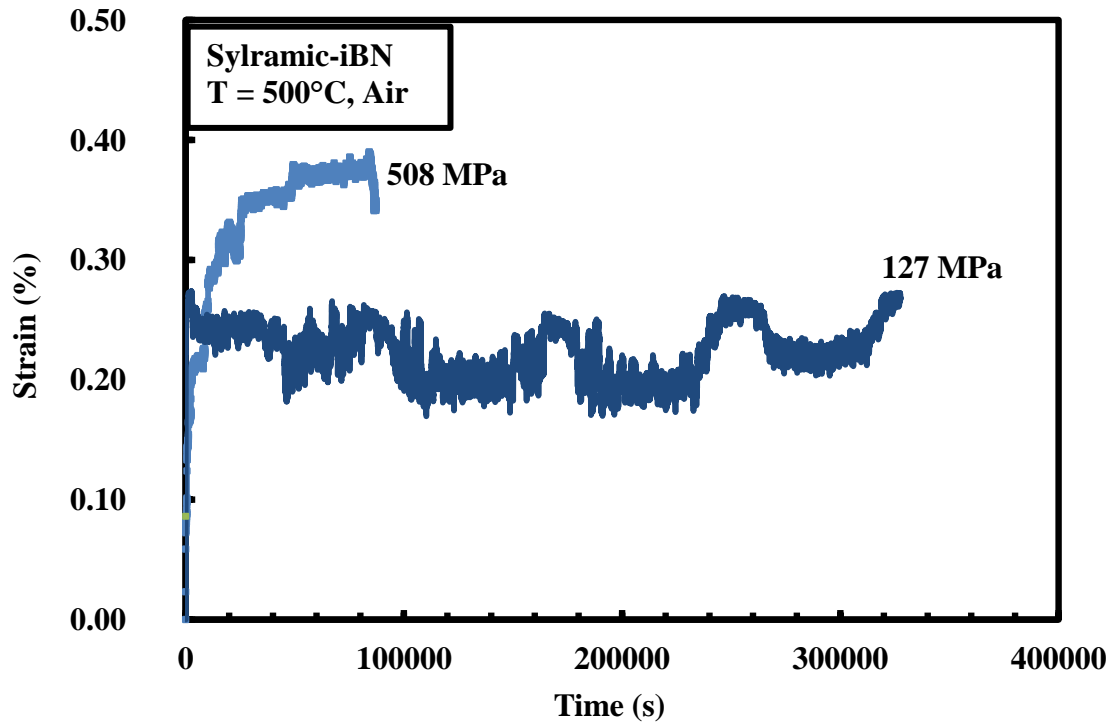


Figure 35: Creep strain vs. time curves obtained for Sylramic-iBN fiber tows at 500°C in compressed dry air

It was expected that at a temperature above the melting point of boria (450°C) a borosilicate glass layer would form on the surface of the fiber tows, creating a protective coating and thus increasing the creep resistance of the fibers. Yet, fibers in the Sylramic-iBN fiber tow specimen “Air 16” did not form a glassy borosilicate surface layer after 100 h at 500°C . A glassy layer is easily distinguished by optical observation of the fiber tow specimen. If a glassy layer is formed, the fibers would be held together rigidly and would have an evident glassy or shiny appearance. **Figure 36** shows the Sylramic-iBN fiber tow specimen “Air 16” after 100 h at 500°C . The specimen is purposefully placed in a manner that clearly shows that the fibers are not rigid, are not held together, and do not have a glassy appearance.

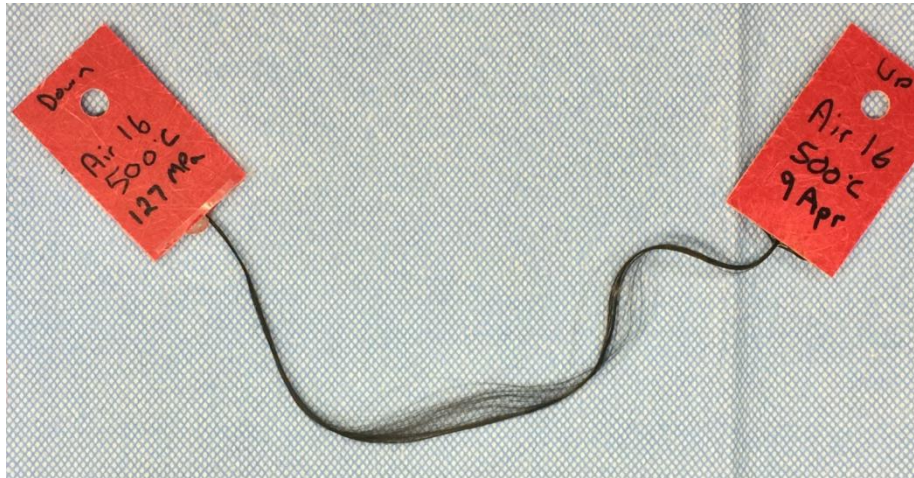


Figure 36: Sylramic-iBN fiber tow specimen “Air 16” after 100 h at 500°C in air under applied load of 127 MPa

As in air, the Sylramic-iBN fiber tows exhibit negligible creep at 500°C in steam. There is an abrupt transition from immediate failure to surviving 100 h of creep as the stress decreases from 381 to 254 MPa. It was expected that the fiber tow specimen may

more readily form a protective borosilicate glassy layer at 500°C in steam, but this did not occur. The fiber tows appear to exhibit greater creep resistance in steam than in air. While a 100-h run-out in air was achieved only at 127 MPa, creep run-out in steam was achieved at 254 MPa.

Creep curve obtained at 500°C in silicic acid-saturated steam are shown in **Figure 37**. Primary and secondary creep regimes are observed. Tertiary creep was not noted. The transition from primary to secondary creep occurred early in the creep life. The specimen represented in **Figure 37** achieved a 100-h run-out. However, because it was expected that no measurable creep would be observed at such low temperatures, there exists a possibility that what was being recorded was due to progressive fiber failure of the fiber tow.

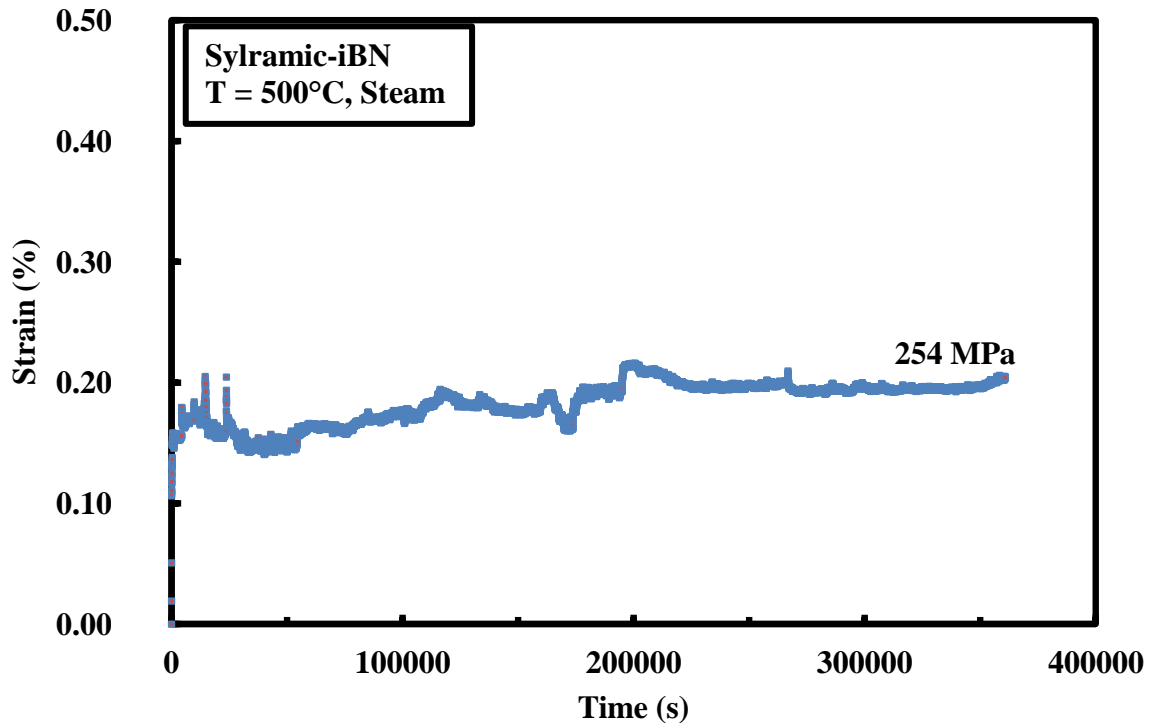


Figure 37: Creep strain vs. time curve obtained for Sylramic-iBN fiber tow at 500°C in silicic acid-saturated steam

5.4 Microstructure of Sylramic-iBN Fiber Tow

Microstructure of the tested Sylramic-iBN fiber tow specimens was analyzed using a scanning electron microscope (FEI Quanta 450). An untested Sylramic-iBN fiber tow was also examined under a scanning electron microscope (SEM) for comparison.

The fiber tows were mounted onto the 45° surface of an aluminum SEM specimen mounting puck. The fibers were carefully pressed to the surface of a two-sided adhesive carbon tape, which held the fiber tow on the aluminum puck. Once the fibers were in place, silver paint was used to firmly fix the fibers to the puck, and to provide sufficient electrical conductivity for imaging under SEM. The fibers were cut at the bottom of the 45° surface, releasing the fibers to be examined from the fiber tow specimen. A fiber tow specimen prepared for SEM analysis can be seen in **Figure 38**.

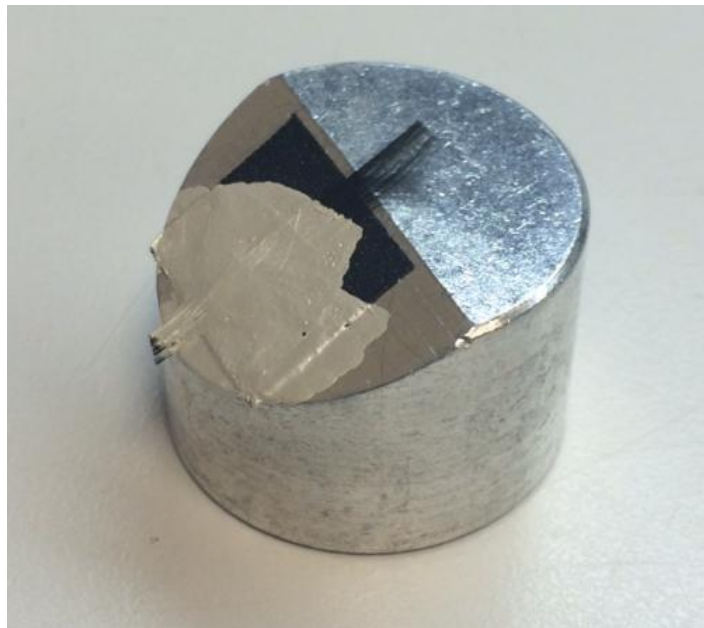


Figure 38: Sylramic-iBN fiber tow specimen mounted on an aluminum SEM puck

The fiber tow specimens failed in creep were prepared for SEM examination in two separate configurations in order: (1) to study the fracture surface of the fibers and (2) to evaluate the oxidation and chemical composition at the mid-point of the fiber tow. For the latter examination, the fiber tows were carefully placed on the 45° surface of the aluminum puck such that the mid-point segment was exposed above the 45° surface. If there were any long fibers protruding from the top of the aluminum puck, they were cut with a clean set of scissors to ensure no contamination. The fiber tow specimens that achieved creep run-out were cut mid length with a clean set of scissors and mounted on a puck in a similar fashion.

The SEM micrograph of the untested fiber tow is presented in **Figure 39** and **Figure 40**. It is noted that all fibers were uniform in size and texture. The fiber surface is rough as reported in literature [48]. There are differences in opinions between researchers on what the bright layer around the fiber is in **Figure 40**. While some believe it may be an artifact due to charging effects on the surface of the fiber, I assert that at this scale, it is possible that the layer may be the thin boron-nitride (BN) coating. However, further surface microstructure analysis must be performed for verification.

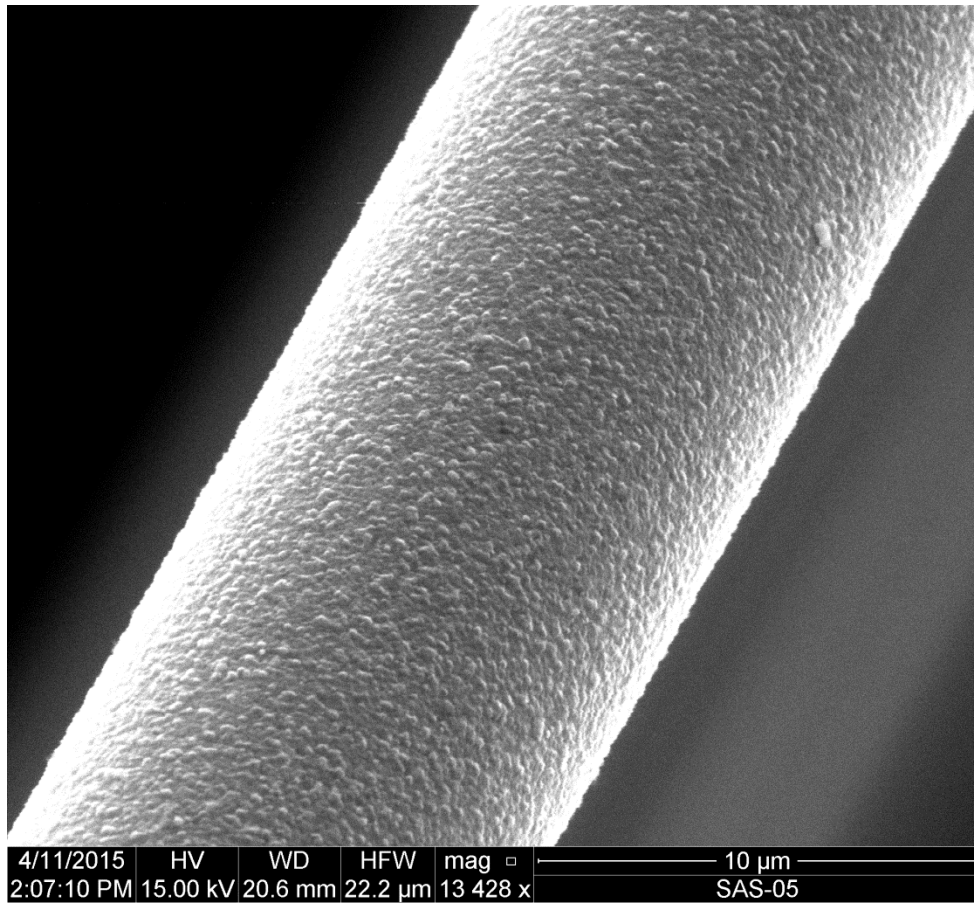


Figure 39: SEM micrograph of an untested Sylramic-iBN fiber

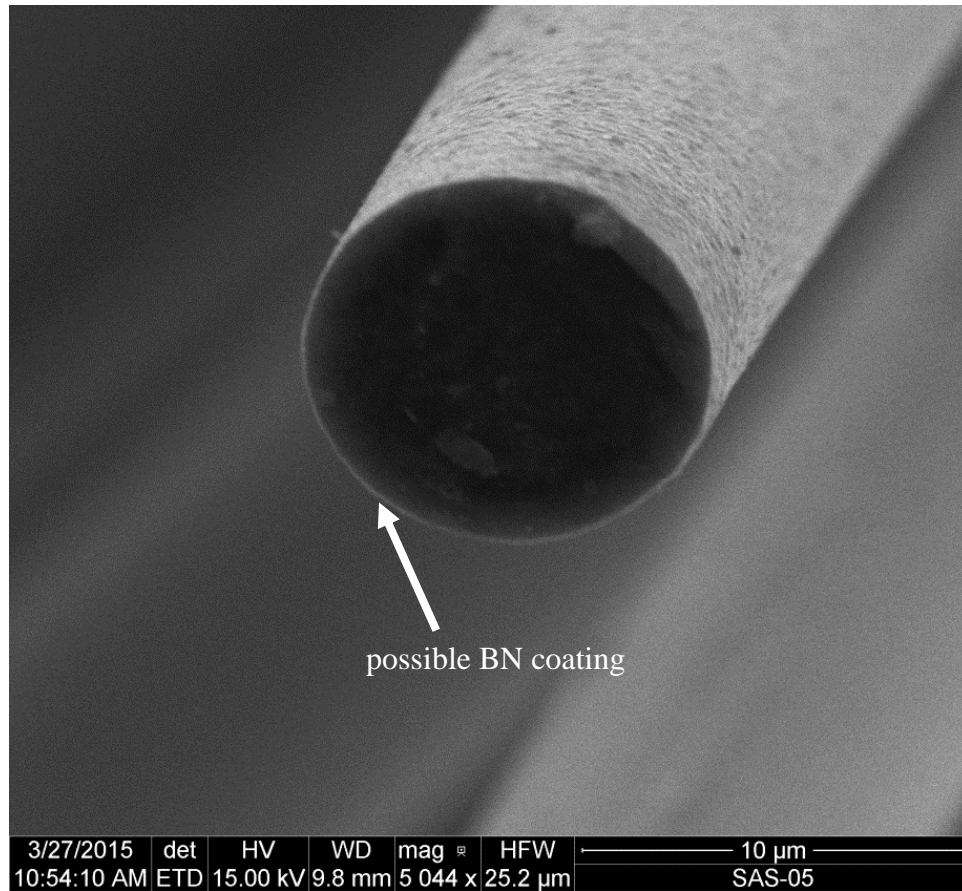
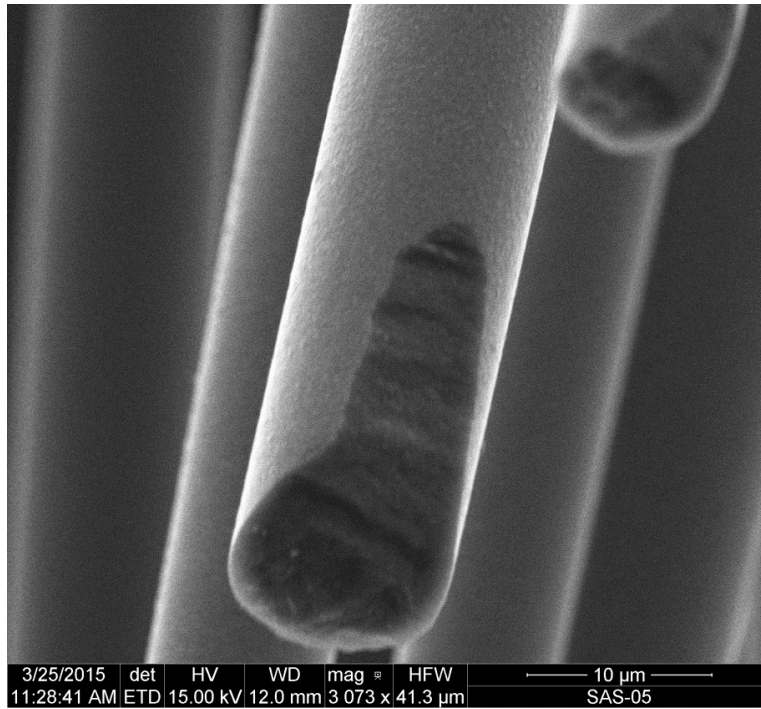


Figure 40: SEM micrograph of the cross-section of an untested Syramic-iBN fiber. It is possible that the BN fiber coating is shown as the significantly brighter layer around the fiber.

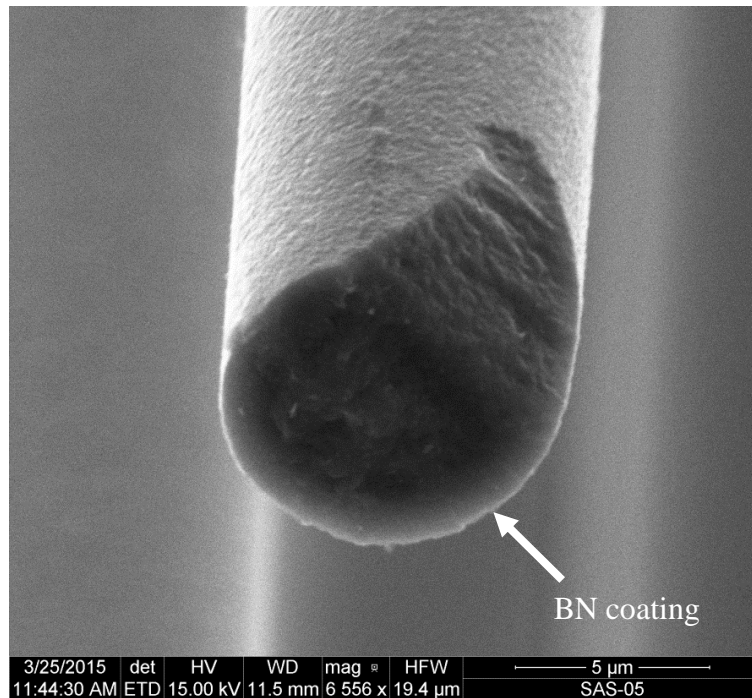
The SEM micrographs of the fibers subjected to creep in air at 400°C appear nearly identical to that of the untested fiber tow. This result was expected, as little to no oxidation was predicted to occur on the surface of the fibers at 400°C in a dry-air environment. Two different fiber tow specimens were examined to ensure an accurate report of the general characteristics: (1) a fiber tow specimen that failed and (2) a fiber tow specimen that achieved creep run-out.

Figure 41 shows an SEM micrograph of the Syramic-iBN fiber tow specimen “Air 5”, which failed upon loading. The micrograph in **Figure 41 (a)**, shows the fiber tow

examined at mid-length, captures the general surface characteristics of fiber tow. A closer look of that fiber fracture surface is shown in **Figure 41 (b)**. Again, a thin light grey circle around the dense, dark grey SiC core is seen. There are differences in opinions between researchers on what the bright layer around the fiber is. While some believe it may be an artifact due to charging effects on the surface of the fiber, I assert that at this scale, it is possible that the layer may be the thin boron-nitride (BN) coating. However, further surface microstructure analysis must be performed for verification. **Figure 42** shows the rough surface of the Sylramic-iBN fiber from specimen “Air 5”, which appears to be similar to the surface of the untested specimen. **Figure 43** and **44** shows an SEM micrograph of Sylramic-iBN specimen “Air 4”, which achieved creep run-out, examined at mid-specimen length. **Figure 43** shows a close examination of the fracture surface. **Figure 44** shows the rough surface of the Sylramic-iBN fiber from specimen “Air 4.” There appears to be little difference between the fiber tow specimen “Air 5” which failed upon loading and the fiber tow specimen “Air 4” which achieved creep run-out. The two specimens exposed in dry air at 400°C exhibit similar surface microstructure and roughness. Notably, all micrographs of the fiber tow specimens tested in air at 400°C appear to be nearly identical, suggesting that there was no measurable difference in their composition and that oxidation did not occur.



(a)



(b)

Figure 41: SEM micrographs (a) and (b) of the Sylramic-iBN specimen “Air 5” tested at 400°C in air showing the cross-section and BN coating of a fiber cut at mid-length ($\sigma_{cr} = 508$ MPa, $t_f = 0$ s)

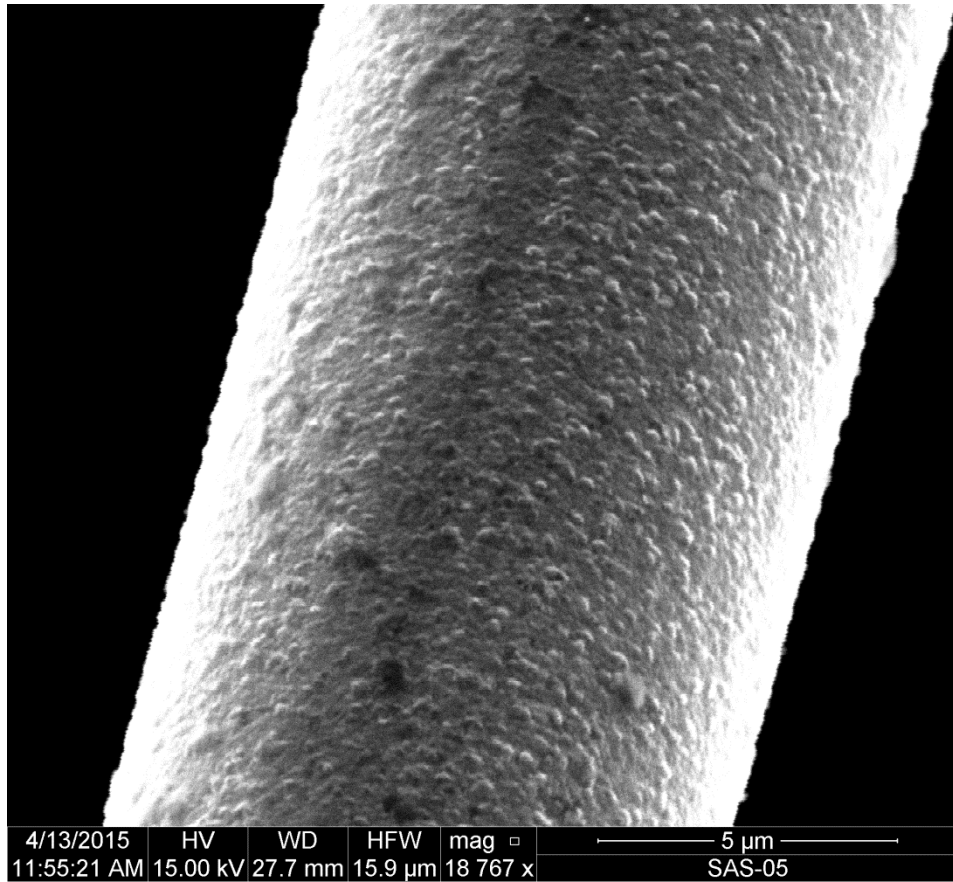


Figure 42: SEM micrograph of the Syramic-iBN specimen “Air 5” tested at 400°C in air showing the rough surface of a fiber at mid-fiber length ($\sigma_{cr} = 508$ MPa, $t_f = 0$ s)

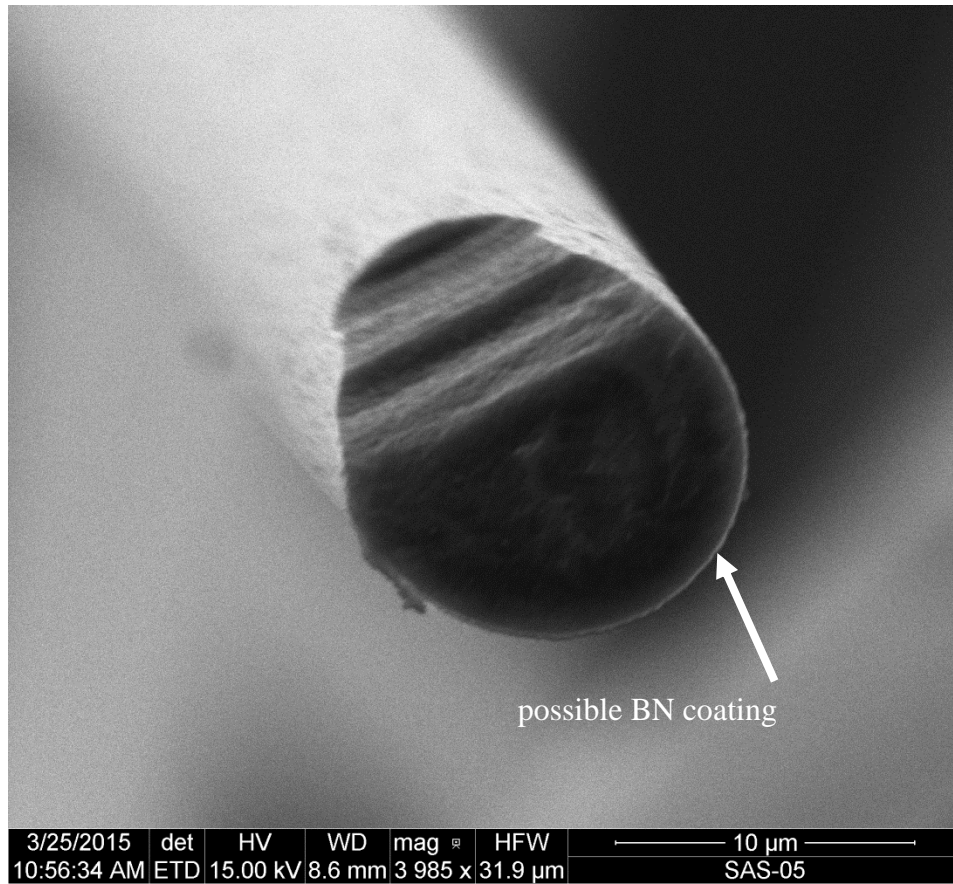


Figure 43: SEM micrograph of the Sylramic-iBN specimen “Air 4” tested at 400°C in air showing the cross-section and BN coating of a fiber cut at mid-length ($\sigma_{cr} = 444$ MPa, $t_f > 100$ h)

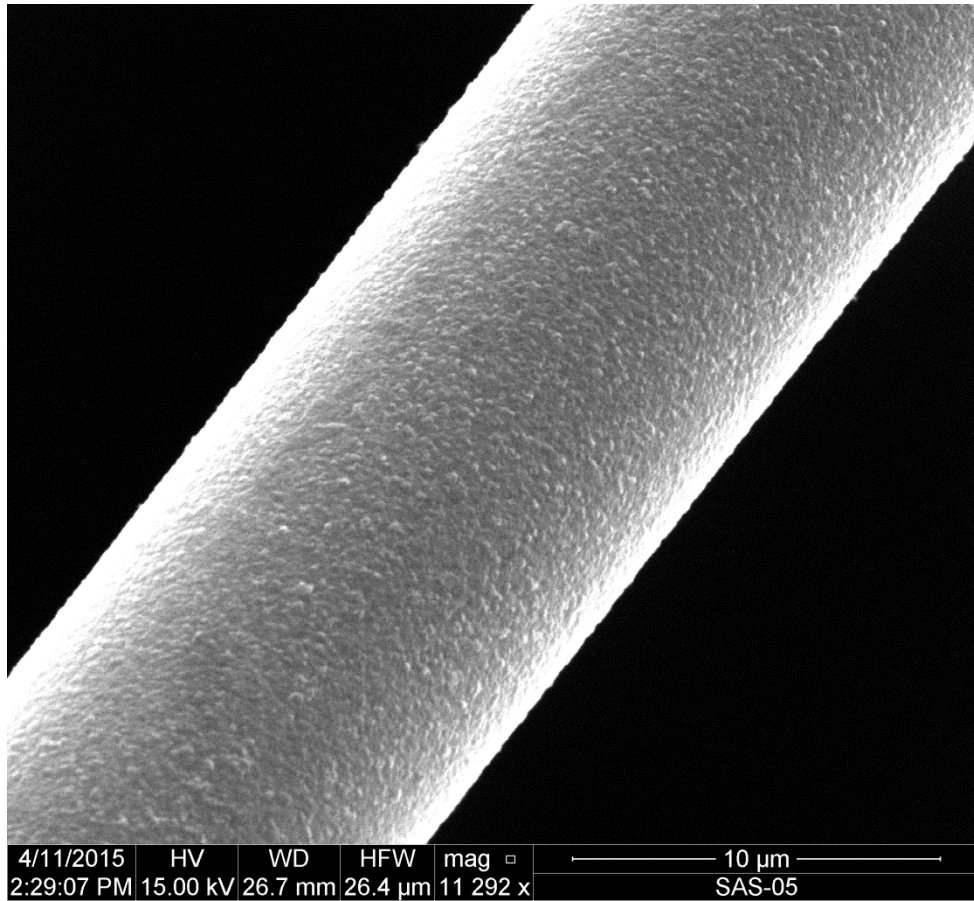


Figure 44: SEM micrograph of the Sylramic-iBN specimen “Air 4” tested at 400°C in air showing the rough surface of a fiber at mid-fiber length ($\sigma_{cr} = 444$ MPa, $t_f > 100$ h)

The micrographs of the fiber tows tested in air at 500°C appear to be nearly identical to those of the fiber tow specimens tested in air at 400°C. It was expected that at 500° C (temperature above the boron melting point of 450°C) a smooth and even layer of borosilicate glass would form on the surface of the fiber tows. However, the micrographs clearly show the same rough surface as that observed in the specimens tested at 400°C in air, which indicates that a borosilicate glassy layer was not formed. Three different specimens were examined to ensure an accurate report of the general characteristics: (1) a fiber tow specimen that failed upon loading, (2) a fiber tow specimen that was subjected to tensile creep for 25 h, and (3) a fiber tow specimen that achieved creep run-out.

Figure 45 shows an SEM micrograph of the Sylramic-iBN specimen “Air 11”, which failed upon loading, examined at mid-specimen length. The micrograph in **Figure 45** captures the general surface characteristics of fiber tow specimen. A closer inspection of the rough surface of specimen “Air 11” at mid-specimen length can be seen in **Figure 46**, which shows the rough surface of the fiber. A micrograph of specimen “Air 11” in **Figure 47** and **48** shows a fiber in the vicinity of fracture. Notably, the portion of the fiber in the vicinity of fracture (**Figures 47**) is similar in appearance to the portion of the fiber at mid specimen length in **Figure 49**. **Figure 48** shows an SEM micrograph of the Sylramic-iBN specimen “Air 11” examined at a fracture surface. Again, a thin light grey circle around the dense, dark grey SiC core is seen. There are differences in opinions between researchers on what the bright layer around the fiber is. While some believe it may be an artifact due to charging effects on the surface of the fiber, I assert that at this scale, it is possible that the layer may be the thin boron-nitride (BN) coating or silica scale growth. However, further surface microstructure analysis

must be performed for verification. A fragment of the surface layer stripped off from a neighboring fiber is seen adhering to the fiber shown in **Figure 47** and **48**.

Figure 49 shows an SEM micrograph of Sylramic-iBN specimen “Air 6” subjected to 25 h of creep at 508 MPa at 500°C in air, examined at mid-specimen length. The surface characteristics of the fibers from specimen “Air 6” are similar to those of the fibers from specimen “Air 11”, suggesting that 25-h exposure to 500°C in air under load did not cause physical changes on the fiber surface.

Figure 50 shows an SEM micrograph of Sylramic-iBN specimen “Air 16”, which achieved creep run-out at 127 MPa at 500°C in air, examined at mid-specimen length. Comparing the SEM micrograph of specimen “Air 16” (**Figure 50**) and that of specimen “Air 6” (**Figure 49**) we reach a conclusion that increasing exposure duration from 25 h to 100 h did not cause further oxidation or chemical change on the surface of the Sylramic-iBN fiber.

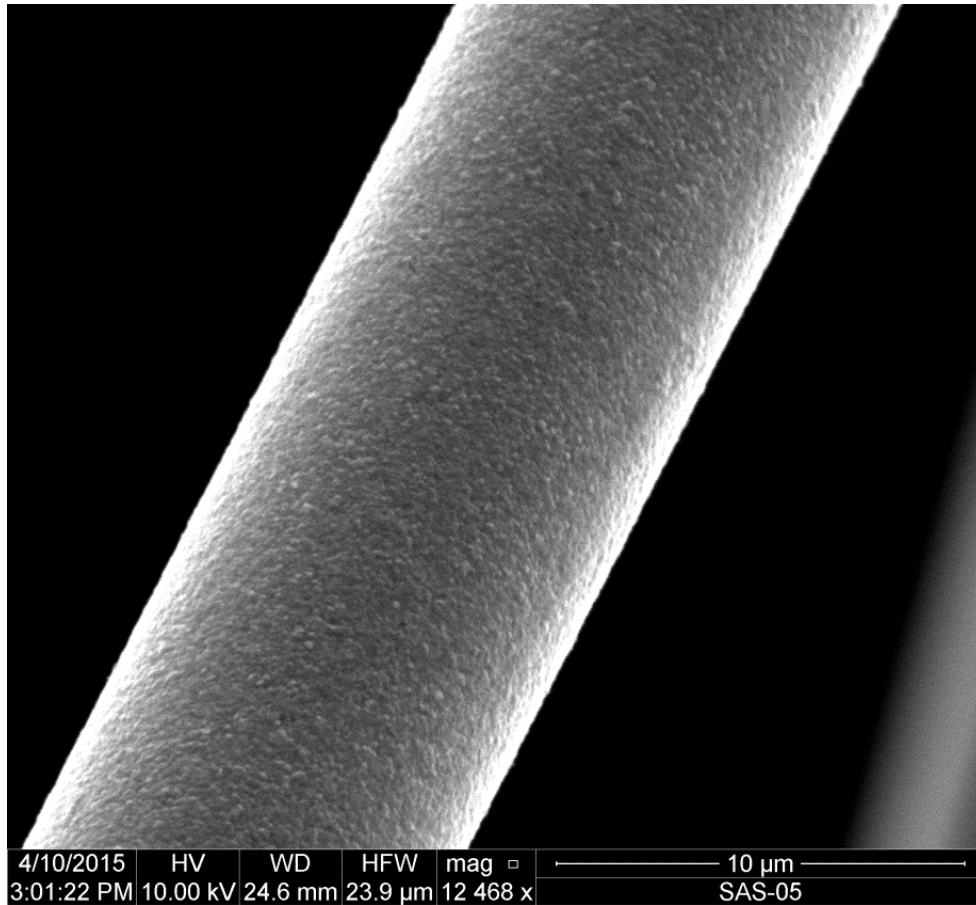


Figure 45: SEM micrograph of the Sylramic-iBN specimen “Air 11” tested at 500°C in air showing general surface characteristics of a fiber at mid-fiber length ($\sigma_{cr} = 508$ MPa, $t_f = 0$ s)

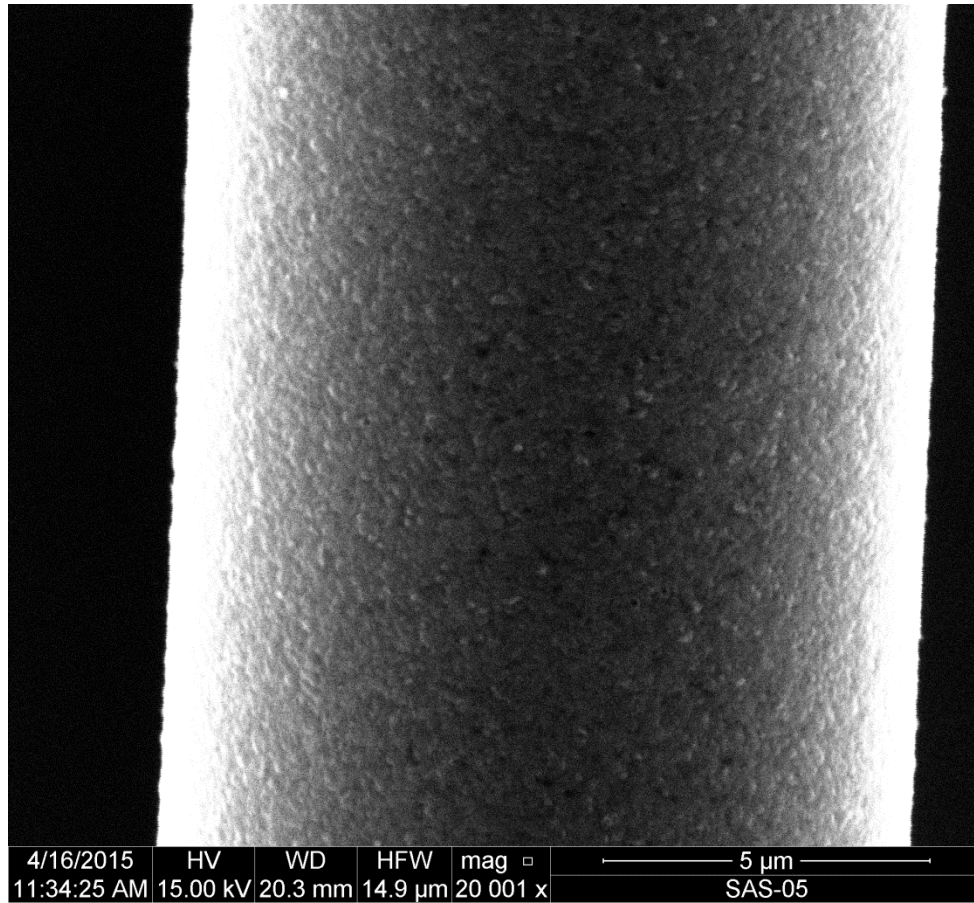


Figure 46: SEM micrograph of the Sylramic-iBN specimen “Air 11” tested at 500°C in air showing the rough surface of a fiber at mid-fiber length ($\sigma_{cr} = 508$ MPa, $t_f = 0$ s)

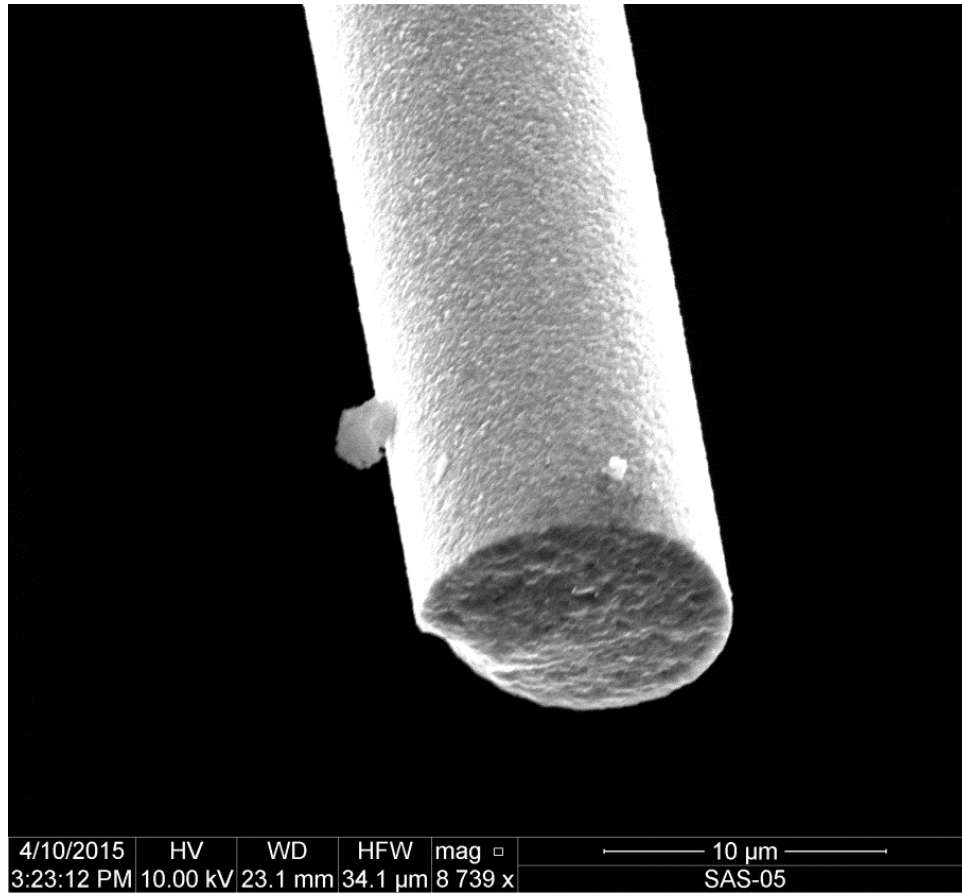


Figure 47: SEM micrograph of the Sylramic-iBN specimen “Air 11” tested at 500°C in air showing a fiber in the vicinity of fracture ($\sigma_{cr} = 508$ MPa, $t_f = 0$ s)

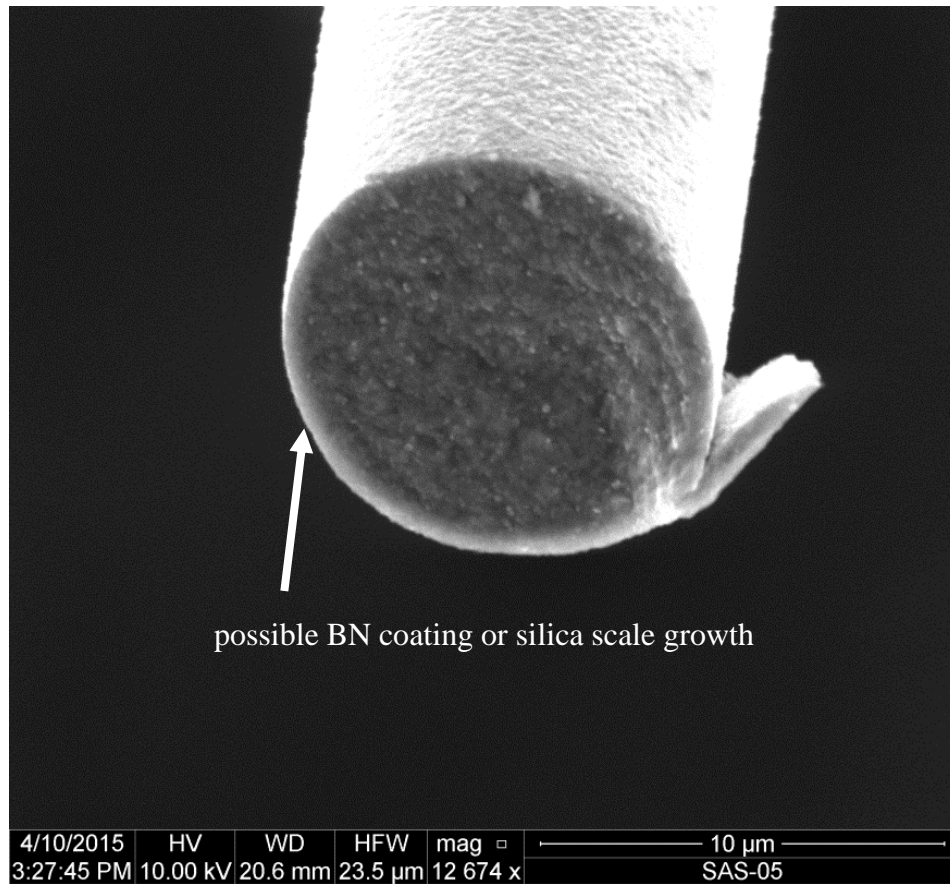


Figure 48: SEM micrograph of Sylramic-iBN specimen “Air 11” tested at 500°C in air showing the fracture surface. ($\sigma_{cr} = 508$ MPa, $t_f = 0$ s)

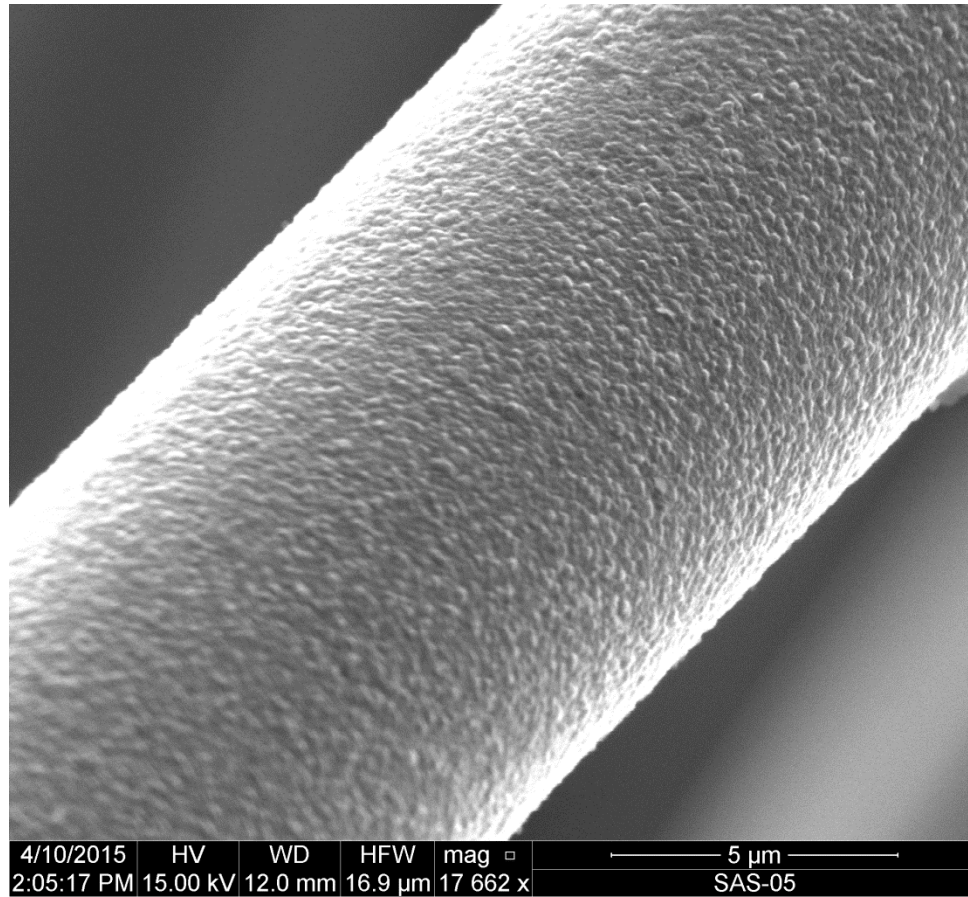


Figure 49: SEM micrograph of the Sylramic-iBN specimen “Air 6” tested at 500°C in air showing the rough fiber surface at mid-fiber length ($\sigma_{cr} = 508$ MPa, $t_f \geq 25$ h)

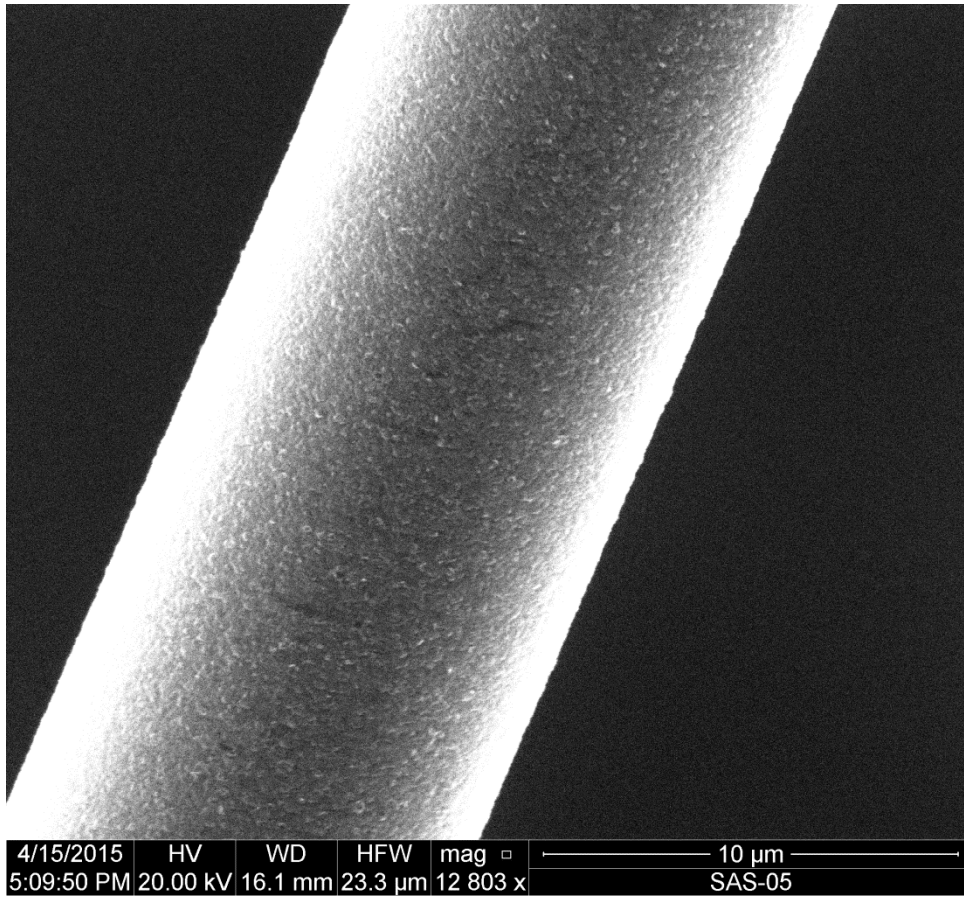


Figure 50: SEM micrograph of the Sylramic-iBN specimen “Air 16” tested at 500°C in air showing a fiber at mid-fiber length ($\sigma_{cr} = 127$ MPa, $t_f > 100$ h)

SEM micrographs of the fiber tow specimens tested at 400 and 500°C in steam saturated with silicic acid are presented in **Figures 51-57**. For each test environment two different specimens were examined to ensure an accurate report of the general characteristics: (1) a fiber tow specimen that failed upon loading and (2) a fiber tow specimen that achieved creep run-out. Surprisingly, the SEM micrographs in **Figures 51-57** do not reveal any significant effects of steam on fiber microstructure. The fibers tested in steam have surface characteristics and general appearance similar to those of the fibers tested in air as well as to those of the untested specimen.

Figure 51 shows an SEM micrograph of the Sylramic-iBN specimen “SS 20”, which failed upon loading at 400°C in steam, examined at mid-specimen length. The micrograph in **Figure 51** captures the general surface characteristics of fiber tow specimen. **Figure 52** shows an SEM micrograph of the Sylramic-iBN specimen “SS 20” examined at a fractured surface. Again, a thin light grey circle around the dense, dark grey SiC core is seen. There are differences in opinions between researchers on what the bright layer around the fiber is. While some believe it may be an artifact due to charging effects on the surface of the fiber, I assert that at this scale, it is possible that the layer may be the thin boron-nitride (BN) coating or silica scale growth. However, further surface microstructure analysis must be performed for verification. Note that the surface appears to be nearly unchanged by exposure at steam at 400°C. It appears that steam at 400°C does not chemically alter the BN coating.

An SEM micrograph in **Figure 53** shows the Sylramic-iBN fiber tow specimen “SS 17”, which has achieved 100-h creep run-out at 400°C in steam saturated with silicic acid. The rough fiber surface in **Figure 53** appears to be similar to the fiber surface of the

untested specimen, suggesting that the surface chemical composition was not significantly affected by exposure to steam at 400°C. **Figure 54** shows a cross section of a fiber from the fiber tow specimen “SS 17” cut at mid-length. Again, a thin light grey circle around the dense, dark grey SiC core is seen. There are differences in opinions between researchers on what the bright layer around the fiber is. While some believe it may be an artifact due to charging effects on the surface of the fiber, I assert that at this scale, it is possible that the layer may be the thin boron-nitride (BN) coating or silica scale growth. However, further surface microstructure analysis must be performed for verification.

Figures 55 and **56** show SEM micrographs of the Sylramic-iBN specimen “SS 23,” which failed upon loading at 500°C in steam. **Figure 55** shows the fiber surface, while **Figure 56** shows a fiber in the vicinity of fracture. Again, a thin light grey circle around the dense, dark grey SiC core is seen. There are differences in opinions between researchers on what the bright layer around the fiber is. While some believe it may be an artifact due to charging effects on the surface of the fiber, I assert that at this scale, it is possible that the layer may be the thin boron-nitride (BN) coating or silica scale growth. However, further surface microstructure analysis must be performed for verification. **Figure 57** shows an SEM micrograph of Sylramic-iBN specimen “SS 24”, which achieved run-out at 500°C in steam, examined at mid-specimen length. Micrographs in **Figures 55-57** do not show any significant differences between the fiber specimen “SS 23”, which failed upon loading and the fiber specimen “SS 24”, which achieved creep run-out. The two specimens tested at 500°C in steam exhibit similar surface microstructure and roughness. It is noteworthy that all micrographs of the fiber

two specimens tested in steam at 500°C appear to be nearly identical, suggesting that there was no measurable difference in their composition and that oxidation did not occur. However, further surface microstructure analysis must be made for verification.

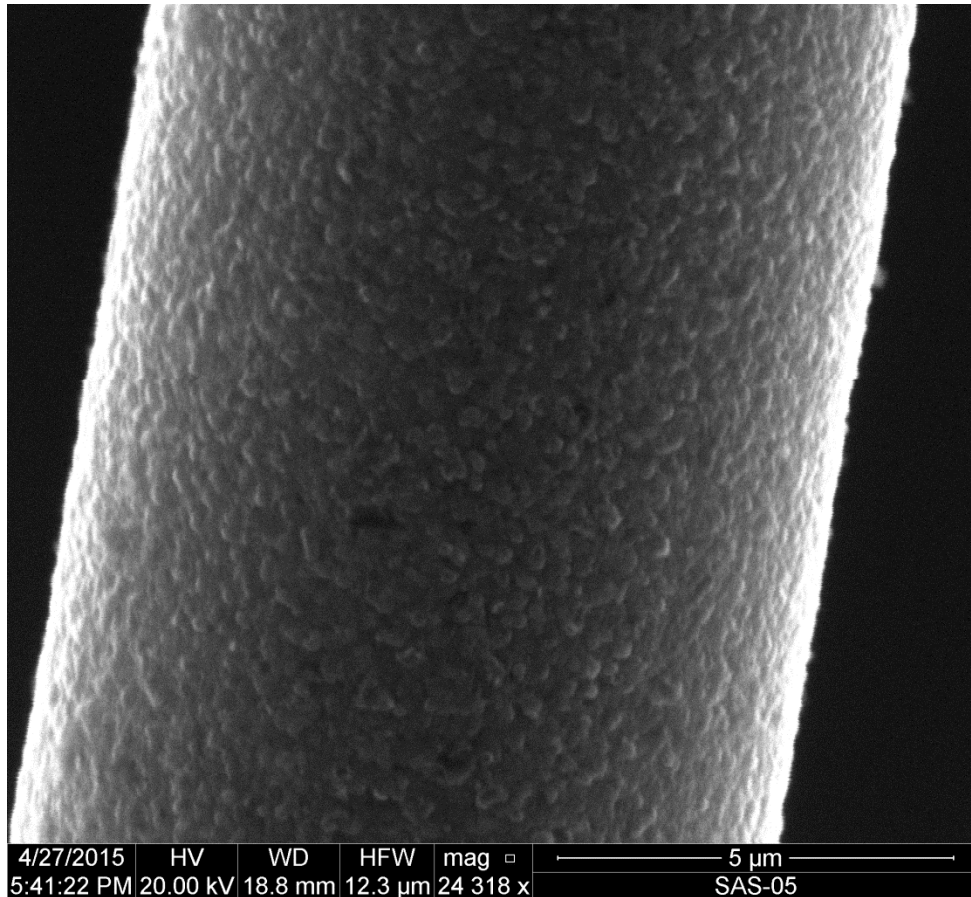


Figure 51: SEM micrograph of the Syramic-iBN specimen “SS 20” tested at 400°C in steam showing the rough fiber surface at mid-fiber length ($\sigma_{cr} = 508$ MPa, $t_f = 0$ s)

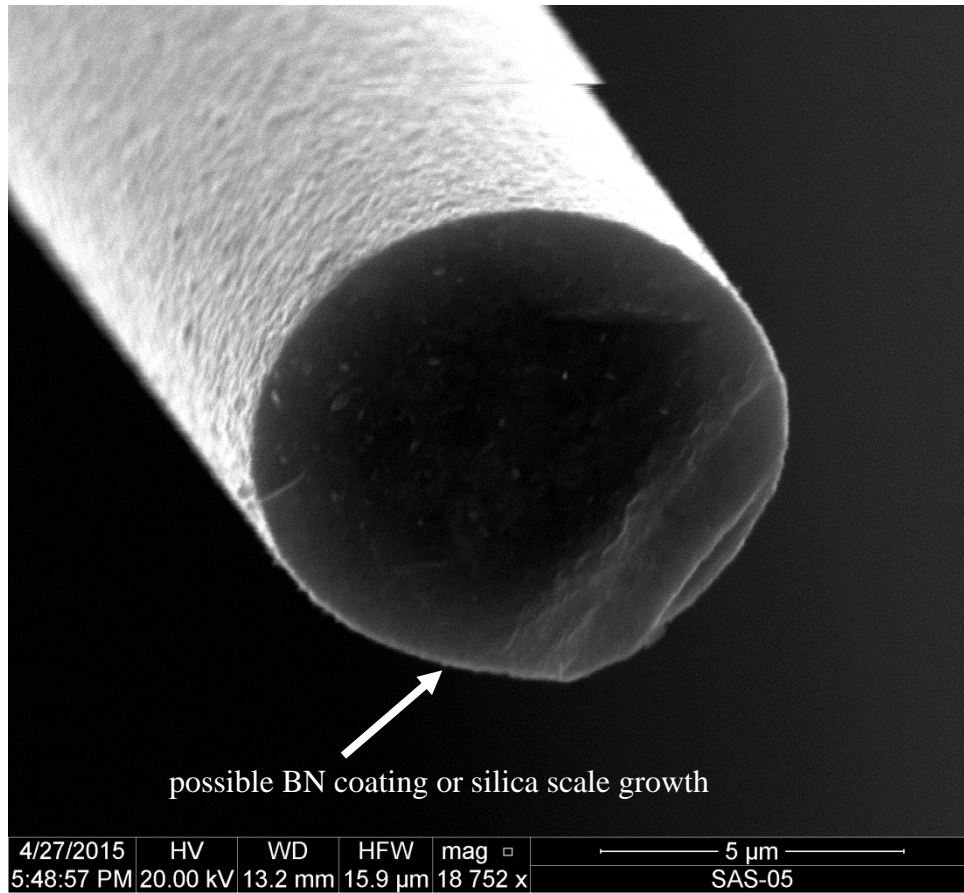


Figure 52: SEM micrograph of the Sylramic-iBN specimen “SS 20” tested at 400°C in steam showing a fiber in the vicinity of fracture ($\sigma_{cr} = 508$ MPa, $t_f = 0$ s)

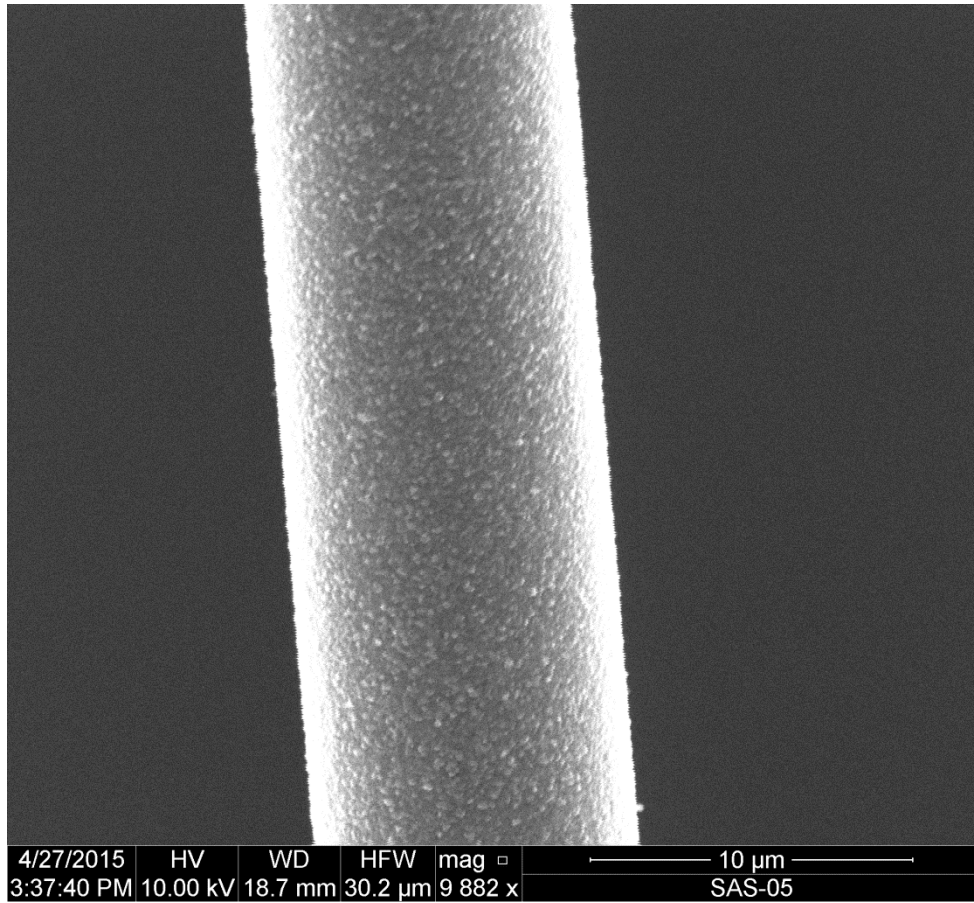


Figure 53: SEM micrograph of the Sylramic-iBN specimen “SS 17” tested at 400°C in steam showing a fiber at mid-fiber length ($\sigma_{cr} = 444$ MPa, $t_f > 100$ h)

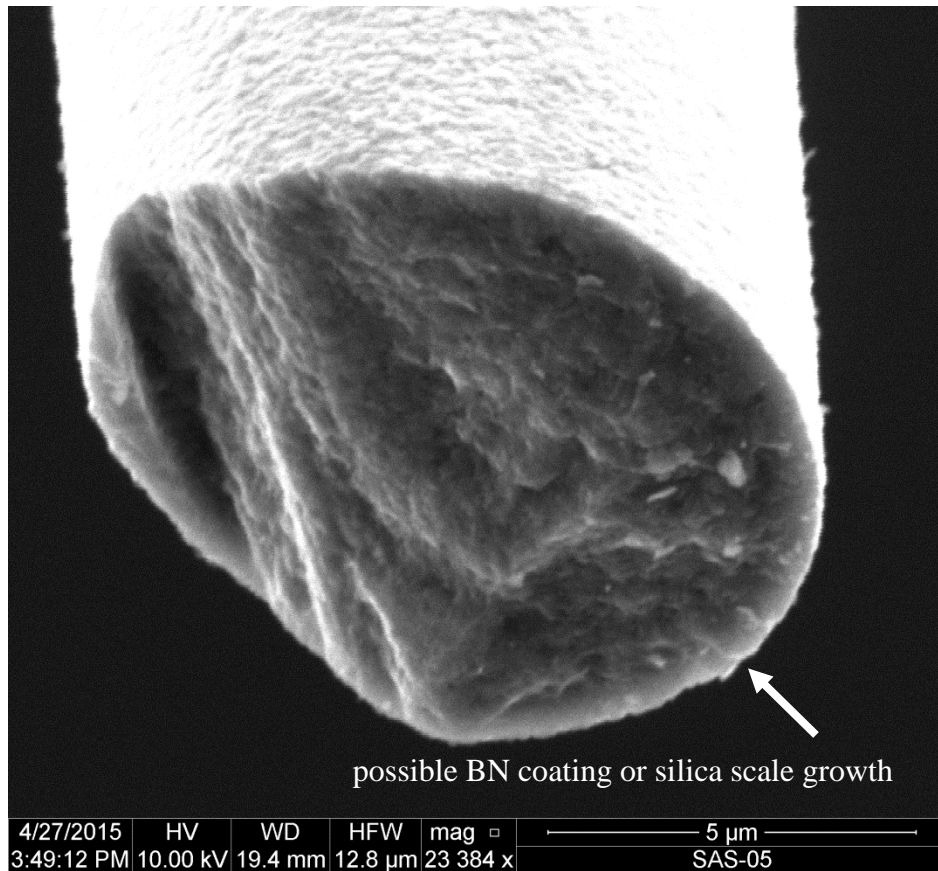


Figure 54: SEM micrograph of the Sylramic-iBN specimen “SS 17” tested at 400°C in steam showing cross section of the fiber cut at mid-fiber length ($\sigma_{cr} = 444$ MPa, $t_f > 100$ h)

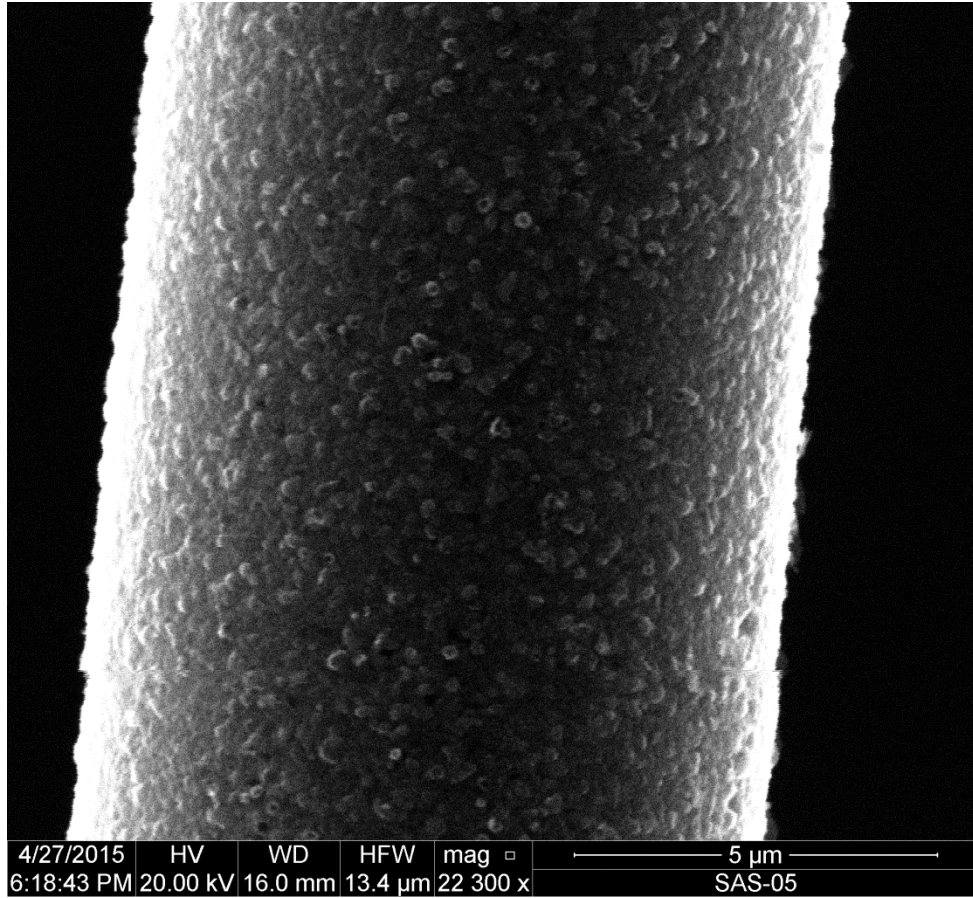


Figure 55: SEM micrograph of the Sylramic-iBN specimen “SS 23” tested at 500°C in steam showing rough fiber surface at mid-fiber length ($\sigma_{cr} = 381$ MPa, $t_f = 0$ s)

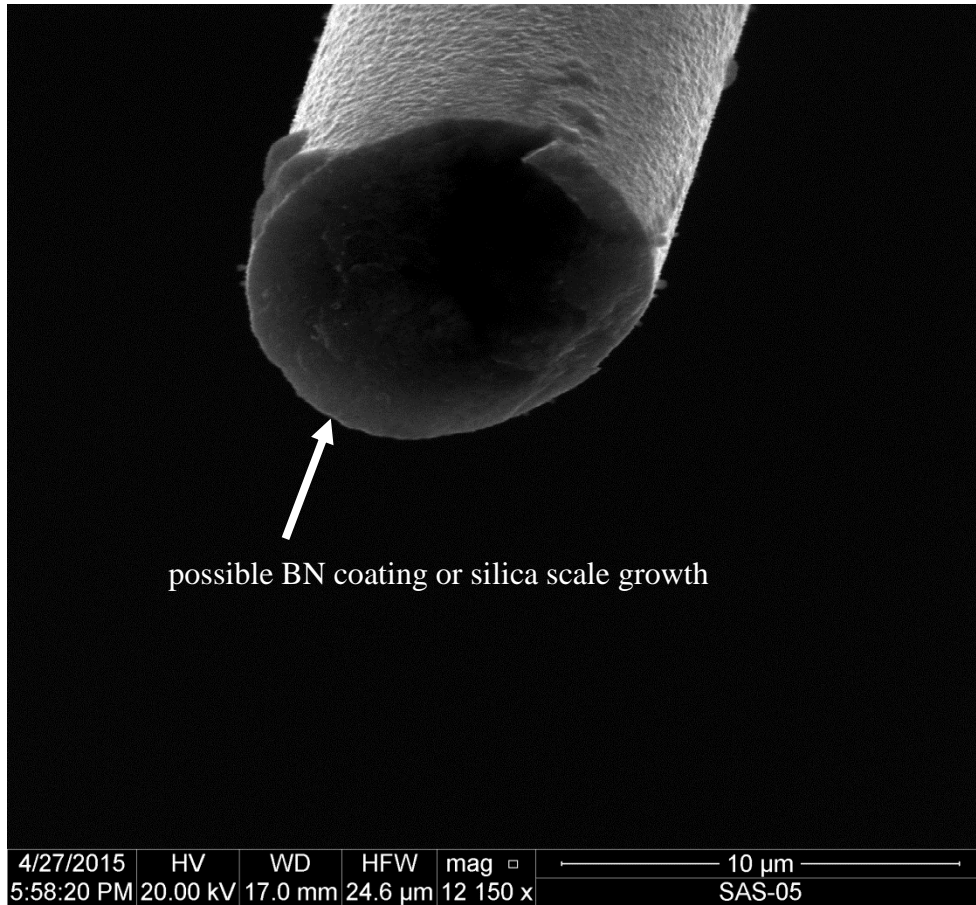


Figure 56: SEM micrograph of the Sylramic-iBN specimen “SS 23” tested at 500°C in steam showing a fiber in the vicinity of fracture ($\sigma_{cr} = 381$ MPa, $t_f = 0$ s)

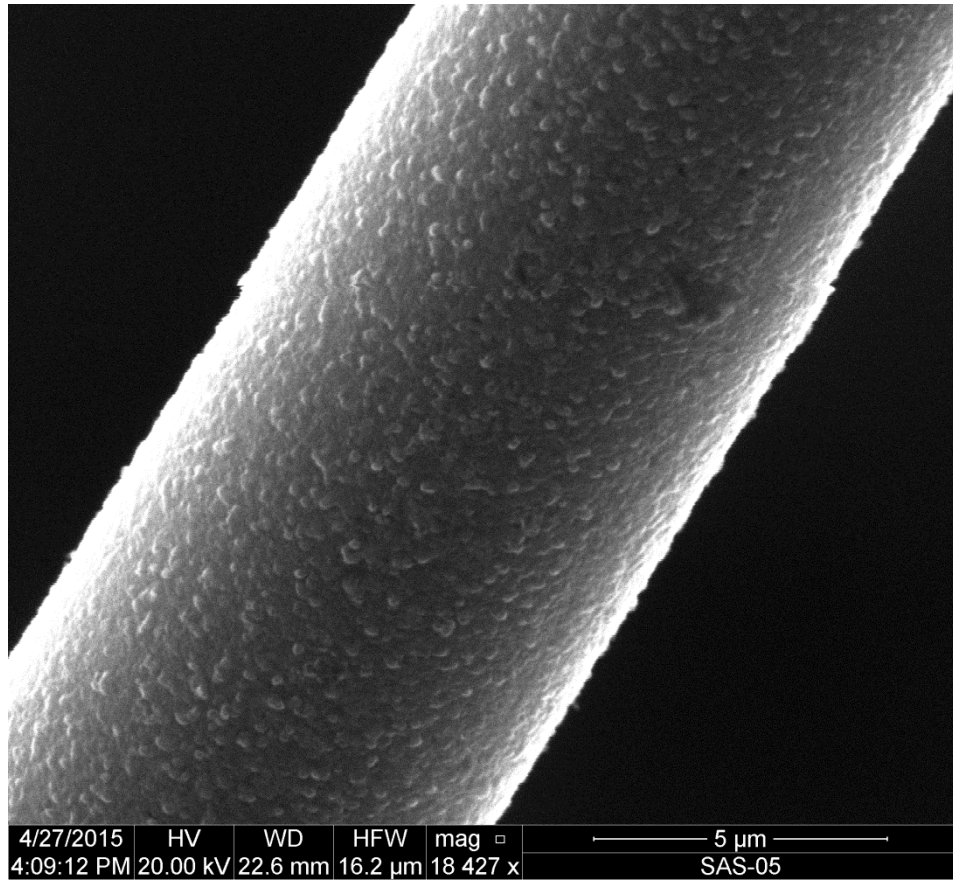


Figure 57: SEM micrograph of the Sylramic-iBN specimen “SS 24” tested at 500°C in steam showing rough fiber surface at mid-fiber length ($\sigma_{cr} = 254$ MPa, $t_f > 100$ h)

Figure 58 compares the general surface characteristics of the following Sylramic-iBN fiber tow specimens: (a) untested specimen, (b) Air-4 specimen subjected to 100 h of creep at 400°C in air, (c) Air-6 specimen subjected to 100 h of creep at 500°C in air, (d) SS-17 specimen subjected to 100 h of creep at 400°C in steam, and (e) SS-24 specimen subjected to 100 h of creep at 500°C in steam. It is noteworthy that all fiber surfaces in **Figure 58** appear to be nearly identical in roughness and general appearance. Based on the SEM examination, the surface microstructure of the Sylramic-iBN fibers is little affected by exposure to silicic acid-saturated steam or dry air at a given temperature. Moreover, exposure temperature also appears to have little influence on the surface microstructure of the Sylramic-iBN fibers. A borosilicate glassy layer was not formed in any of the tests performed in this study. A surface layer that we believe to be polycrystalline BN fiber coating or a thin silica scale remained unchanged by exposure under load to 400°C or 500°C in air or in steam.

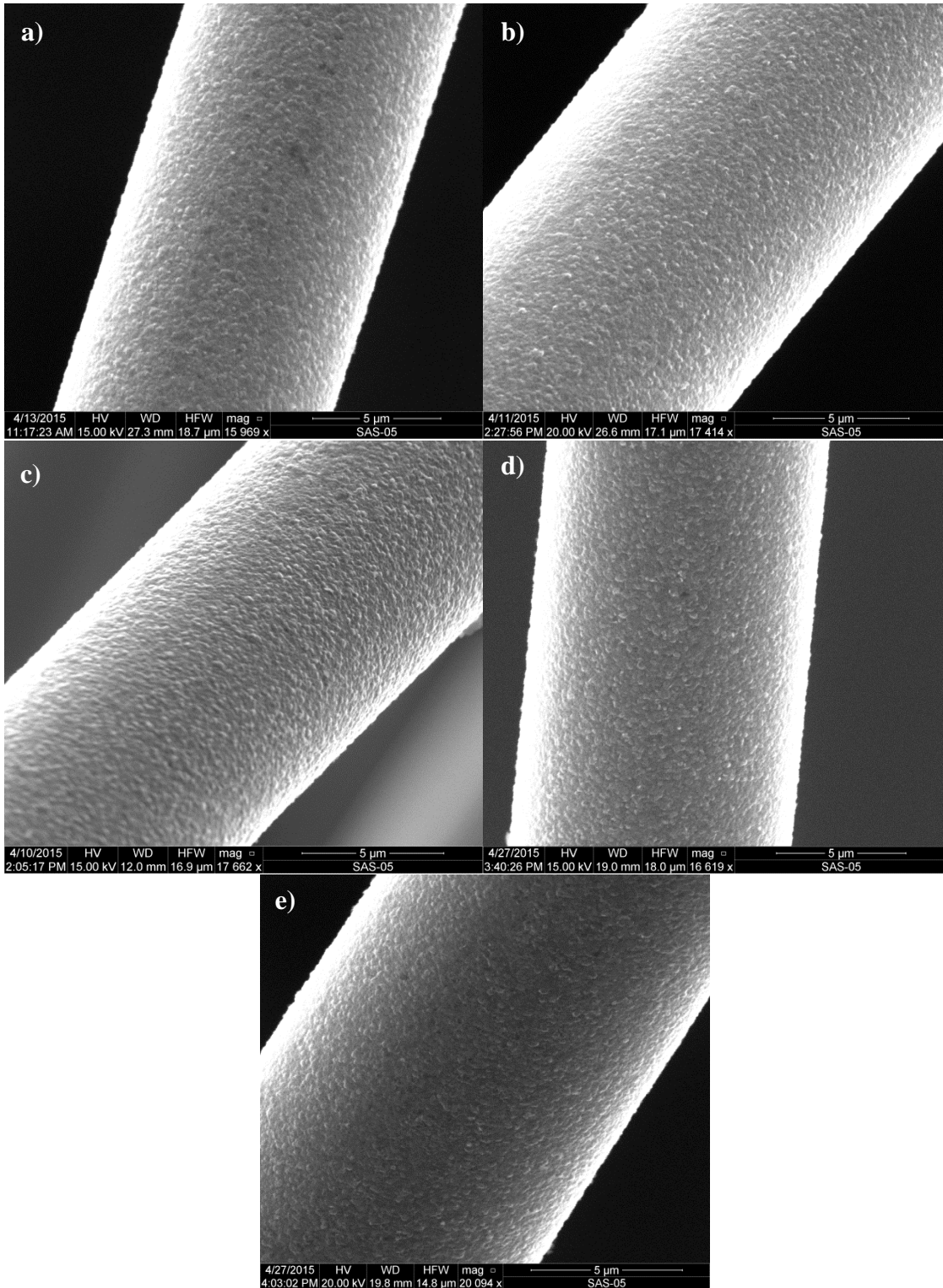


Figure 58: SEM micrograph of the Sylramic-iBN fiber tow specimens: (a) untested specimen, (b) Air-4 specimen subjected to 100 h of creep at 400°C in air, (c) Air-6 specimen subjected to 100 h of creep at 500°C in air, (d) SS-17 specimen subjected to 100 h of creep at 400°C in steam, (e) SS-24 specimen subjected to 100 h of creep at 500°C in steam.

VI. Conclusions and Recommendations

6.1 Conclusions

A facility for creep testing of SiC fiber tows at elevated temperature in air and in steam saturated with silicic acid was designed and constructed in collaboration with Robertson [46]. The newly developed test facility permits pre-heating of the steam up to 800°C as well as saturation of the steam with silicic acid before it enters the test chamber. The test facility was successfully validated by performing creep tests of Sylramic-iBN fiber tows at 400 and 500°C in dry air and in steam saturated with silicic acid. The fiber tow specimens tested in steam saturated with silicic acid exhibited consistent chemical composition along the length of the fiber tow.

Tensile tests to failure were also attempted in order to determine values of the ultimate tensile strength (UTS) for the Sylramic-iBN fiber tow at 23, 400 and 500°C. However, tensile tests did not produce meaningful results. Experimental values of UTS were erratic and inconsistent, ranging from 297 to 873 MPa at 23°C and from 68 to 1091 MPa at 400°C. A single specimen tested at 500°C produced the UTS of 293 MPa. Apparently other researchers obtained similarly erratic results when testing Sylramic-iBN fiber tows from the same production batch as the fiber tows used in this research [47, 49]. The erratic UTS results may be attributed to several causes: (1) possible lack of interfacial coating in the fiber tows tested in this work [48], (2) a known variability in density and porosity of the Sylramic-iBN fibers [49], and (3) damage to the fibers introduced during processing [47]. Further analysis of the microstructure of the fiber tows tested in this work may lend insight into correlations between the processing of the fiber tows and the mechanical behavior observed.

The Sylramic-iBN fiber tows exhibit negligible creep at 400 and 500°C in air or in silicic acid-saturated steam. At 400°C there is an abrupt transition from immediate failure to surviving 100 h of creep as the stress decreases from 508 to 444 MPa. At 500°C in air, there is an abrupt transition from failure upon loading to surviving 100 h of creep as the stress decreases from 254 to 127 MPa. Surprisingly, one specimen tested at 500°C in air survived 25 h at 508 MPa. This anomalous result is likely due to the inconsistencies in the fibers. At 500°C in steam, there is an abrupt transition from immediate failure to surviving 100 h of creep as the stress decreases from 381 to 254 MPa. Typically, progressively increasing creep lifetimes would be obtained as the creep stress decreases from the level that yields zero creep lifetime to the level that yields a 100-h lifetime. It is possible that such atypical behavior of the Sylramic-iBN fiber tows is caused by the variability of the fiber tow within the batch. Additionally, because it was expected that no measurable creep would be observed at such low temperatures, there exists a possibility that what was being recorded was due to progressive fiber failure of the fiber tow.

Examination of the fiber microstructure under an SEM did not reveal any significant changes to the appearance or microstructure of the fiber surface due to exposure to elevated temperature under load. The surface characteristics of all fibers tested in this work were similar to those of the untested fiber. Test temperature (400°C vs. 500°C) had no effect. Likewise test environment (dry air vs. steam saturated with silicic acid) had little influence. Neither did test duration (failure upon loading vs. 100 h of creep) affect the appearance or microstructure of the fiber surface. All fibers examined in this work had rough surface as described in literature [48]. The rough

surface of the Sylramic-iBN fibers is attributed to the manufacturing process and is likely responsible for dramatic scatter in test results.

Sylramic-iBN fiber tow exhibits significant batch-to-batch variability as well considerable variability within a single batch. Therefore multiple batches of fiber must be included in a study and a large number of fiber tow specimens from each batch must be tested in order to characterize mechanical properties and behavior of the Sylramic-iBN fiber tow.

6.2 Recommendations for Future Research

Based on the results of this work, the following directions for future research may be considered.

- The erratic test data is most likely not due to the test facility and procedure, as any issues were carefully controlled or mitigated. The test procedure was refined such that high confidence was placed in the accuracy and viability of the test facility and procedure. The most likely cause of the inconsistencies is due to variations within the tested material. In order to better understand the creep and tensile behavior of Sylramic-iBN fiber tow material, tests should be conducted on multiple batches and multiple specimens tested from each batch to characterize mechanical properties and behavior of this material. Furthermore, multiple tests must be performed for each test condition to assure statistical confidence.
- The mechanical behavior of Sylramic-iBN fibers should be investigated in steam at temperatures above 500°C in order to elucidate the effects of steam

(beneficial, degrading, or none) on tensile strength and creep resistance. It is also important to identify the temperature at which the effects of steam (if any) become pronounced.

- Auger Electron Spectroscopy (AES) should be used to determine any compositional changes in the surface of the fibers tested under different conditions. The AES analysis may be able to detect higher atomic concentration of oxygen on the fiber surface, indicating the formation of an oxide layer. The AES analysis may also be used to measure the thickness of an oxide scale, which then could be correlated with the applied load and test duration.
- Energy Dispersive X-ray diffraction (EDX) could be conducted to identify the elemental composition of the tested fibers. EDX provides elemental analysis of the tested material by identifying elements that are present, but not their exact ratios. However, the relative size of the EDX peak can be correlated to the amount or concentration of those elements identified. Transmission Electron Microscopy (TEM) analysis could be used to assess the structure of the CVI BN interface coating (crystalline, mostly amorphous or completely amorphous) and to determine whether the fibers contain any carbon or oxygen impurities [49].

Appendix A: Stress-Weight Index Table

Engineering Stress = Force / Cross-sectional Area Total

Force = (mass) x (gravity)
 Newtons = (kg) x (9.81 m/s²)

$$\text{Engineering Stress (Newtons/m}^2\text{)} = \frac{\text{Mass (kg)} \times \text{Gravity (9.81 m/s}^2\text{)}}{\text{Cross-sectional Area Total (m}^2\text{)}}$$

Cross Sectional Area Total = n * Cross-sectional Area of Filaments

Cross-Sectional Area of Filaments = $\pi * r^2$

Sylramic-iBN Fiber Data:

Avg filament diameter (r) = 0.000005 m

filaments per tow (n) = 800

Cross-Sectional Area Total = 6.28319 E -08 m²

Engineering Stress [MPa]	Mass [kg]	Sequence of Weights
762	4.88	A,N,O,P,V
635	4.07	C,D,G,N,O,P,T
572	3.66	C,D,O,P,Q,R
508	3.25	C,G,M,O,R,S,V,W,X
444	2.85	C,G,T,V,W
381	2.44	C,S,V,W
317	2.03	F,G,I,R,S
254	1.63	F,G,M,N,V
190	1.22	F,N,O,T,V
127	0.81	G,N,O,P

* Load Train Weight (LT) = 0.01055 kg

Weight Cross-Reference Chart

	(kg)		(kg)		(kg)		(kg)
A=	4.505	H=	0.455	O=	0.115	V=	0.02
B=	4.51	I=	0.455	P=	0.115	W=	0.02
C=	2.295	J=	0.455	Q=	0.115	X=	0.02
D=	0.91	K=	0.455	R=	0.1	Y=	0.02
E=	0.915	L=	0.455	S=	0.1	Z=	0.01
F=	0.92	M=	0.113	T=	0.05		
G=	0.455	N=	0.115	U=	0.05		

A-F weighed on Acculab SV-30 (+/- .005 kg)

G-Z weighed on Voyager Pro (+/- .001 kg)

Appendix B: Specifications of Furnace and Steam Generator Settings

		Air	Steam
400	Upper Furnace Heating Element (°C)	390	397
	Lower Furnace Heating Element (°C)	383	387
	Preheater (°C)	600	550
	Steam Generator Power (%)	-	65
	Water Pump (mL/min)	-	8
500			
	Upper Furnace Heating Element (°C)	490	497
	Lower Furnace Heating Element (°C)	480	489
	Preheater (°C)	700	675
	Steam Generator Power (%)	-	68
	Water Pump (mL/min)	-	8

Appendix C: Supporting SEM Micrographs

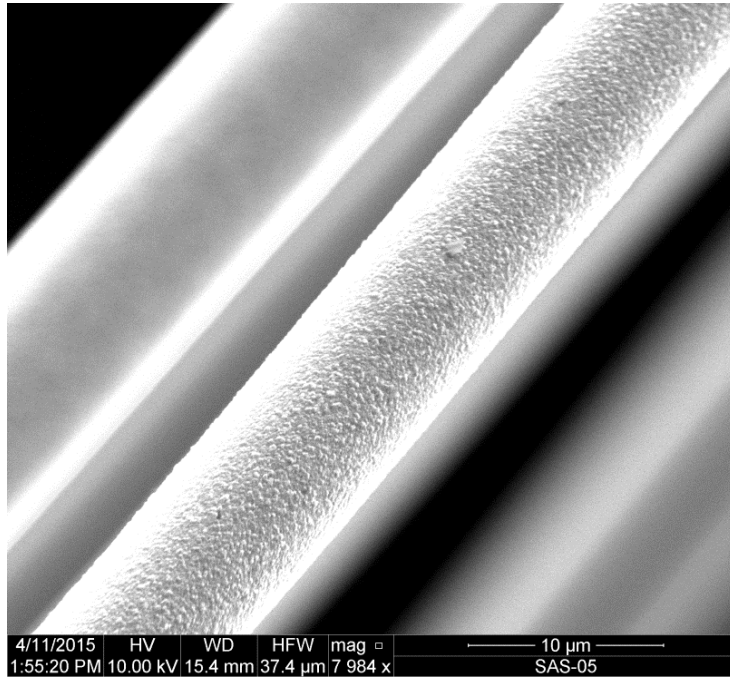


Figure 59: SEM micrograph of a virgin Sylramic-iBN fiber (1)

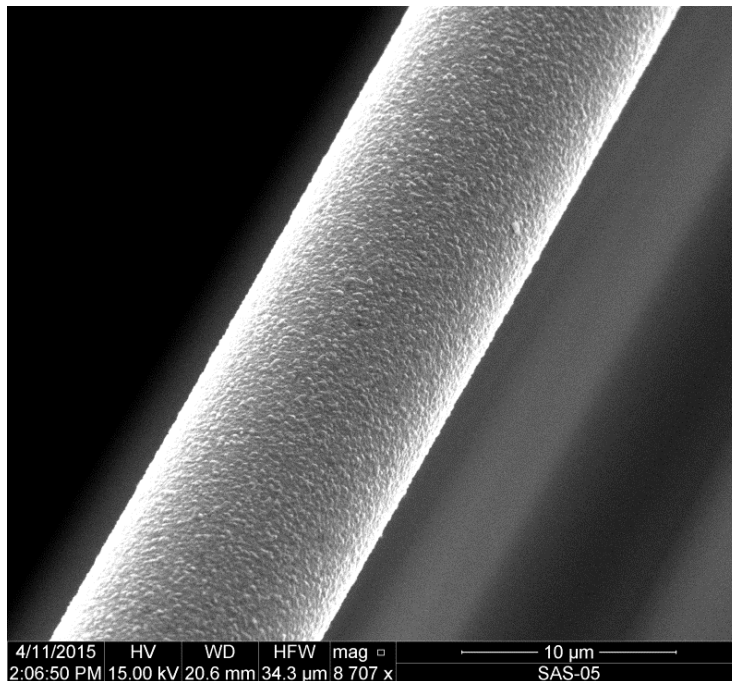


Figure 60: SEM micrograph of a virgin Sylramic-iBN fiber (2)

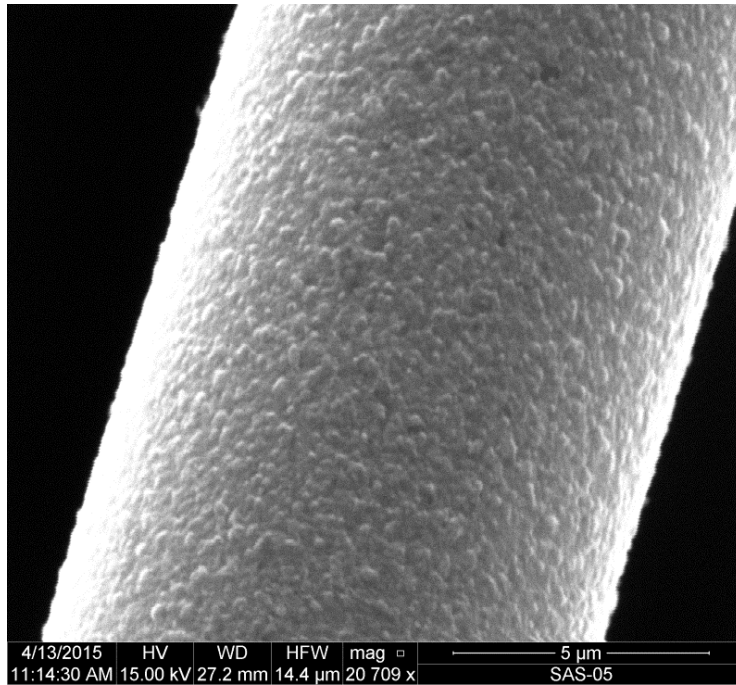


Figure 61: SEM micrograph of a virgin Sylramic-iBN fiber (3)

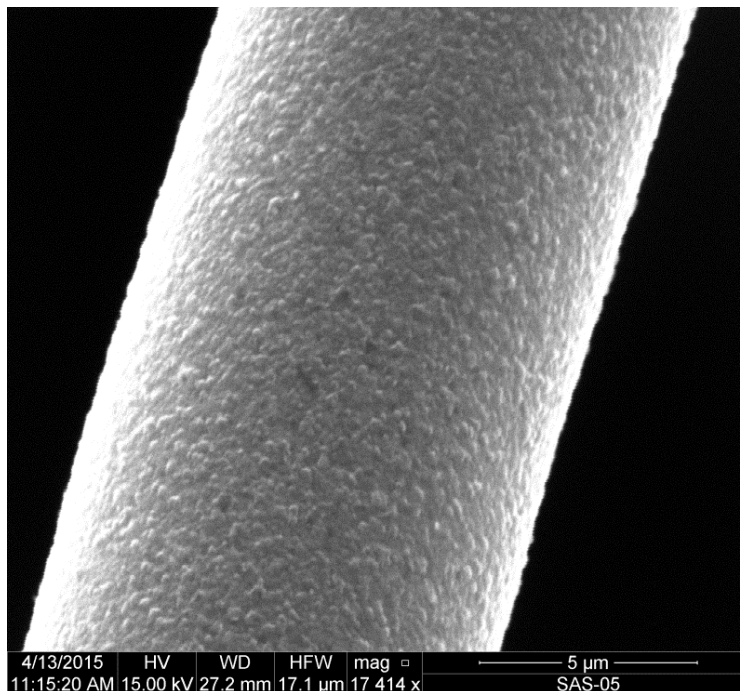


Figure 62: SEM micrograph of a virgin Sylramic-iBN fiber (4)

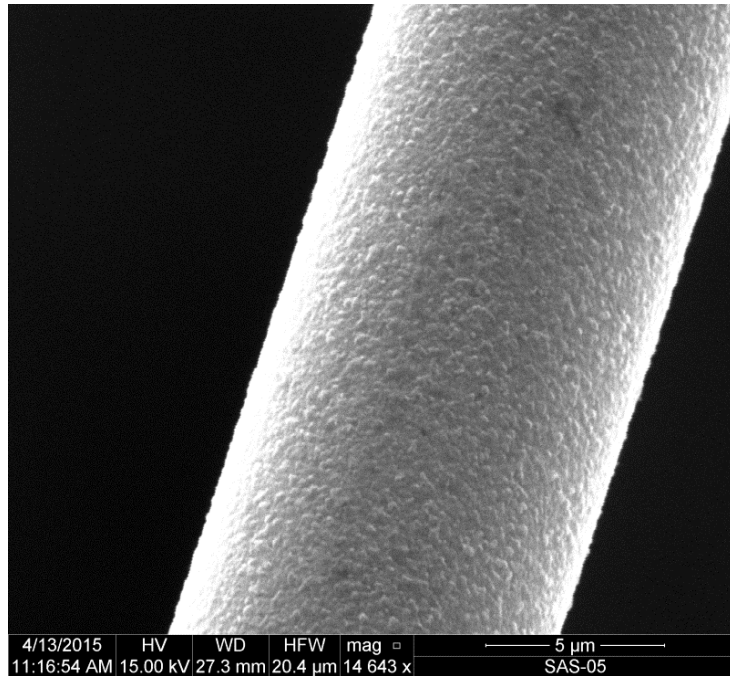


Figure 63: SEM micrograph of a virgin Sylramic-iBN fiber (5)

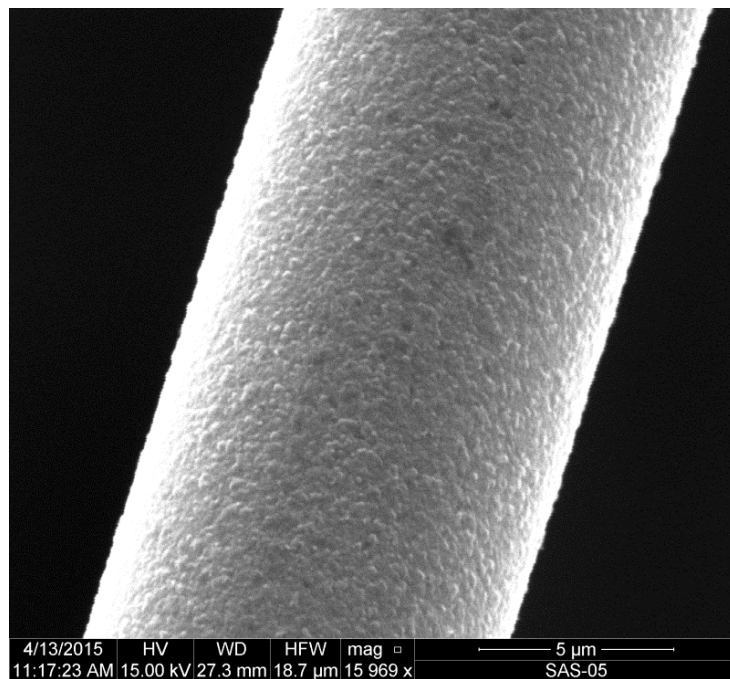


Figure 64: SEM micrograph of a virgin Sylramic-iBN fiber (6)

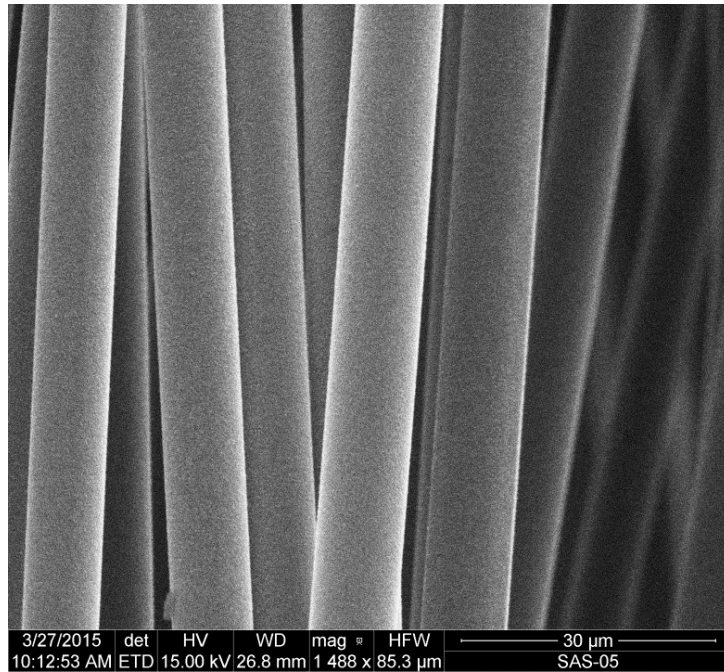


Figure 65: SEM micrograph of a virgin Sylramic-iBN fiber; note the uniformity amongst the fibers (1)

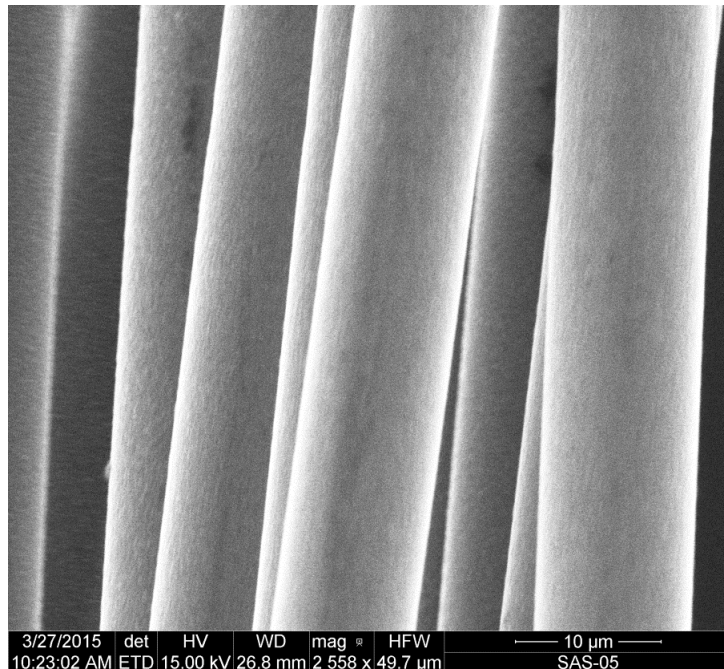


Figure 66: SEM micrograph of a virgin Sylramic-iBN fiber; note the uniformity amongst the fibers (2)

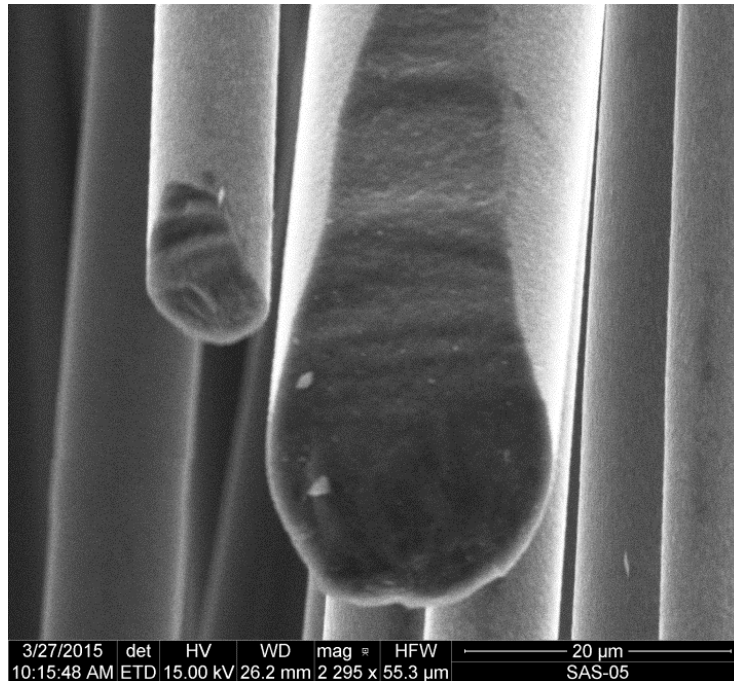


Figure 67: SEM micrograph of a virgin Sylramic-iBN fiber observed at a cut surface (1)

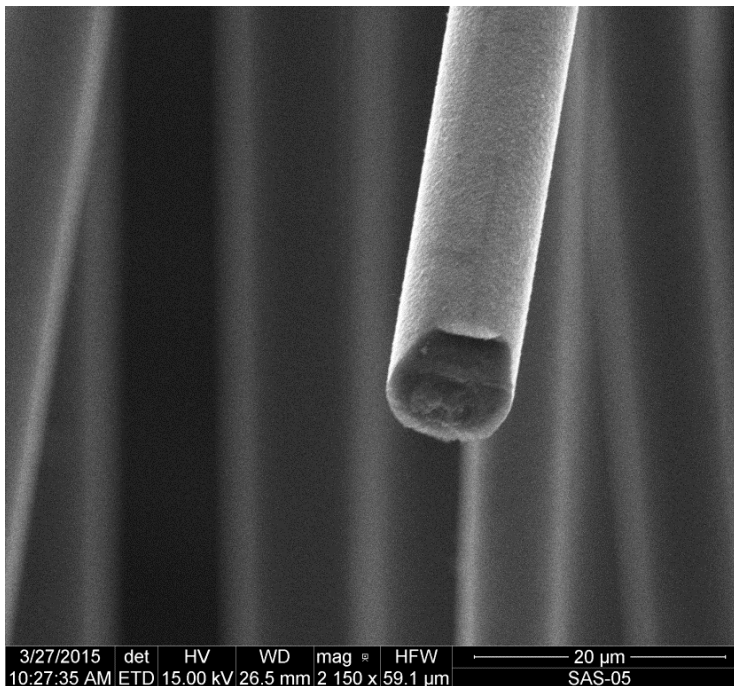


Figure 68: SEM micrograph of a virgin Sylramic-iBN fiber observed at a cut surface (2)

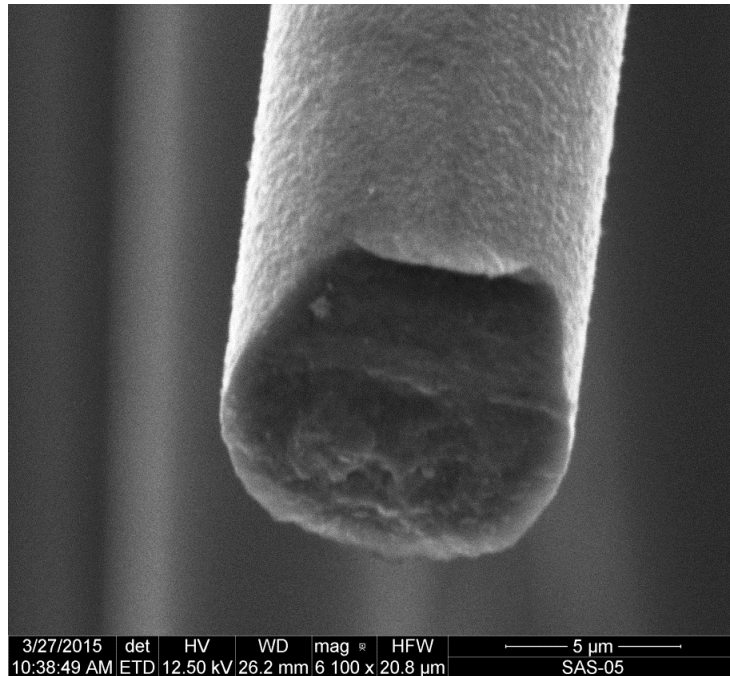


Figure 69: SEM micrograph of a virgin Sylramic-iBN fiber observed at a cut surface (3)

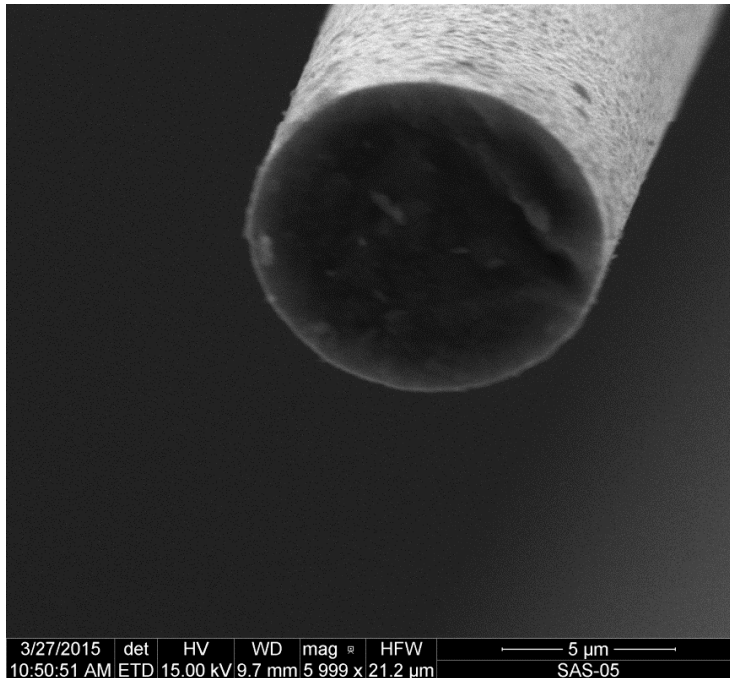


Figure 70: SEM micrograph of the cross section of a virgin Sylramic-iBN fiber

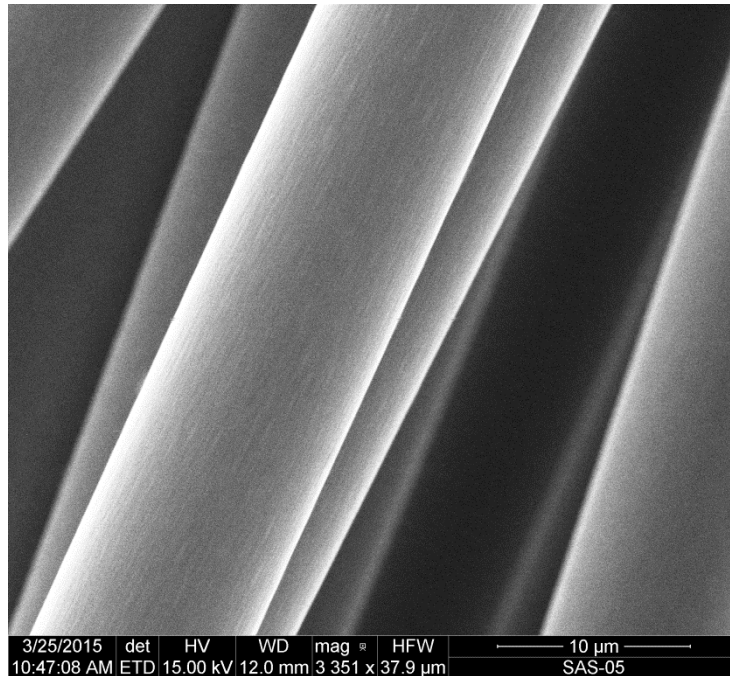


Figure 71: SEM micrograph of the Sylramic-iBN specimen “Air 4” examining general surface characteristics of fibers at mid-fiber length ($\sigma_{cr} = 444$ MPa, $t_f > 100$ h)

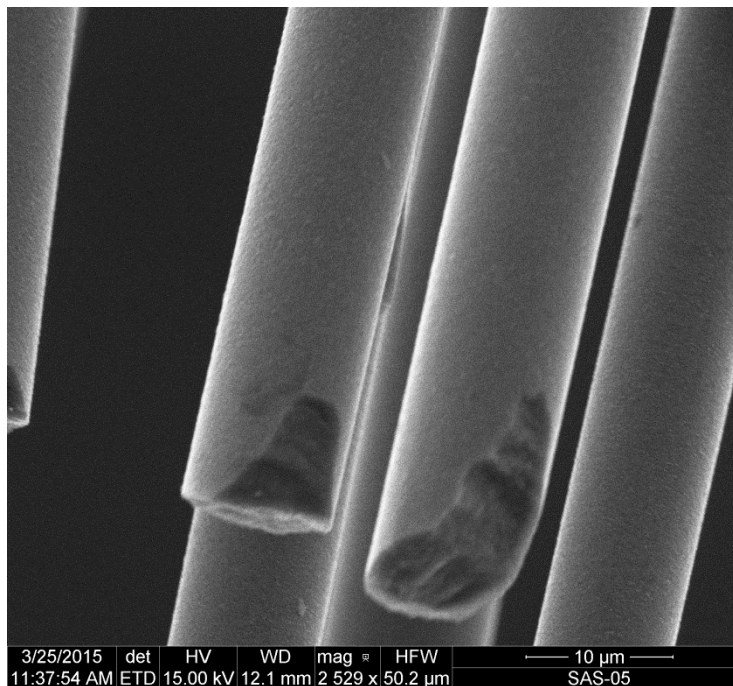


Figure 72: SEM micrograph of the Sylramic-iBN specimen “Air 5” examining general surface characteristics of fibers at mid-fiber length ($\sigma_{cr} = 508$ MPa, $t_f = 0$ s)

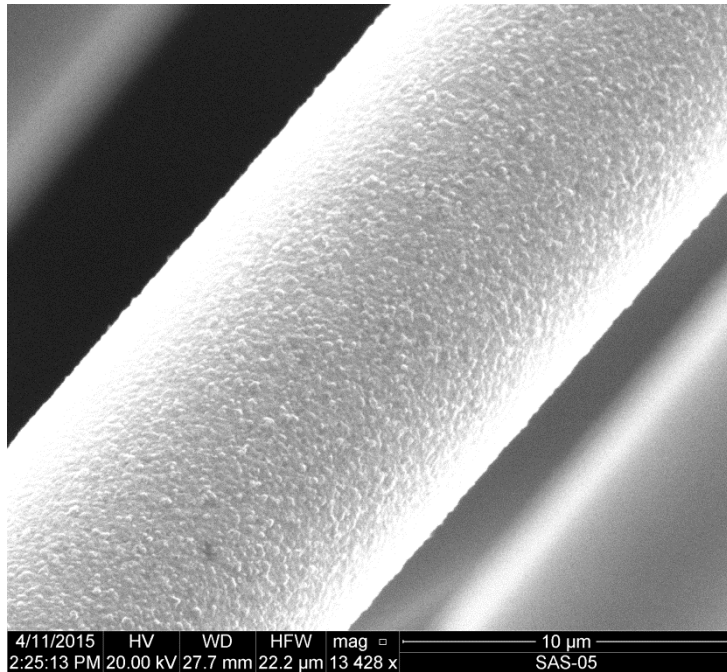


Figure 73: SEM micrograph of the Syramic-iBN specimen “Air 4” examining rough surface of a fiber at mid-fiber length ($\sigma_{cr} = 444$ MPa, $t_f > 100$ h)

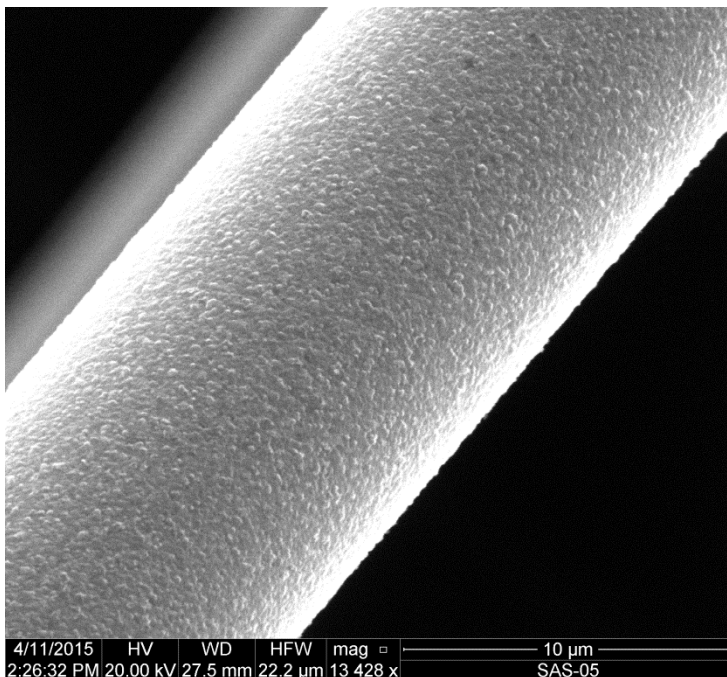


Figure 74: SEM micrograph of the Syramic-iBN specimen “Air 4” examining rough surface of a fiber at mid-fiber length ($\sigma_{cr} = 444$ MPa, $t_f > 100$ h)

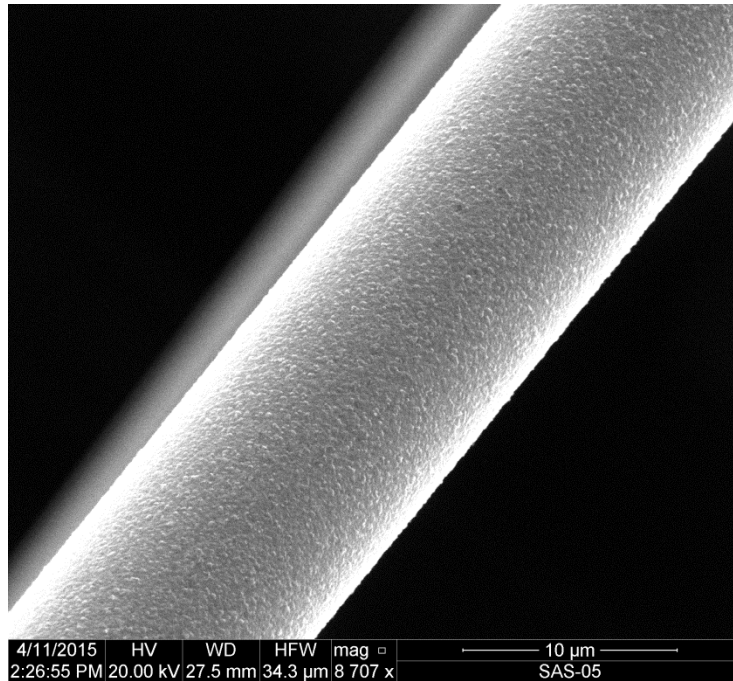


Figure 75: SEM micrograph of the Sylramic-iBN specimen “Air 4” examining rough surface of a fiber at mid-fiber length ($\sigma_{cr} = 444$ MPa, $t_f > 100$ h)

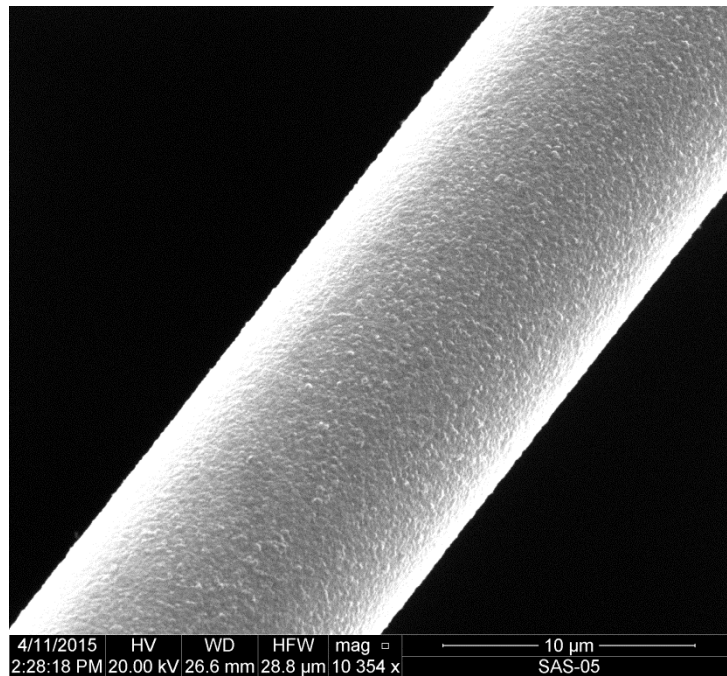


Figure 76: SEM micrograph of the Sylramic-iBN specimen “Air 4” examining rough surface of a fiber at mid-fiber length ($\sigma_{cr} = 444$ MPa, $t_f > 100$ h)

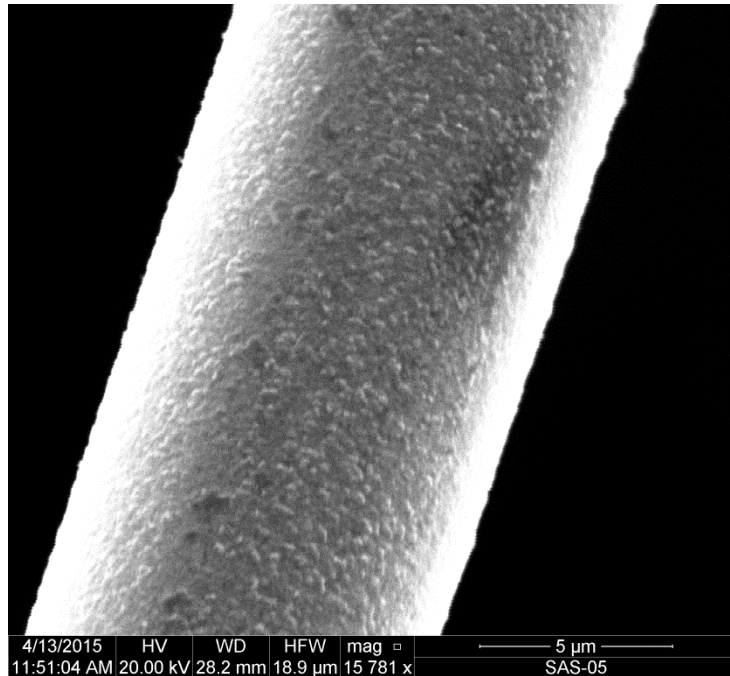


Figure 77: SEM micrograph of the Sylramic-iBN specimen “Air 5” examining rough surface of a fiber at mid-fiber length ($\sigma_{cr} = 508$ MPa, $t_f = 0$ s)

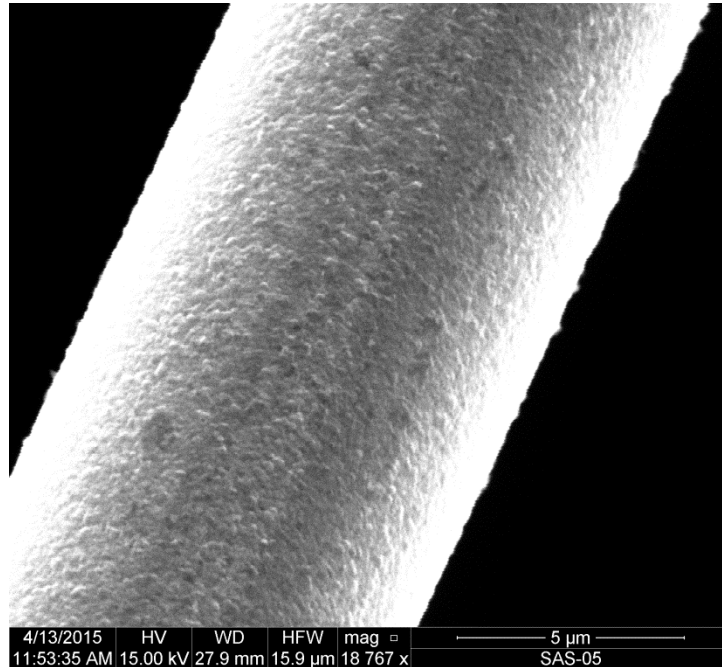


Figure 78: SEM micrograph of the Sylramic-iBN specimen “Air 5” examining rough surface of a fiber at mid-fiber length ($\sigma_{cr} = 508$ MPa, $t_f = 0$ s)

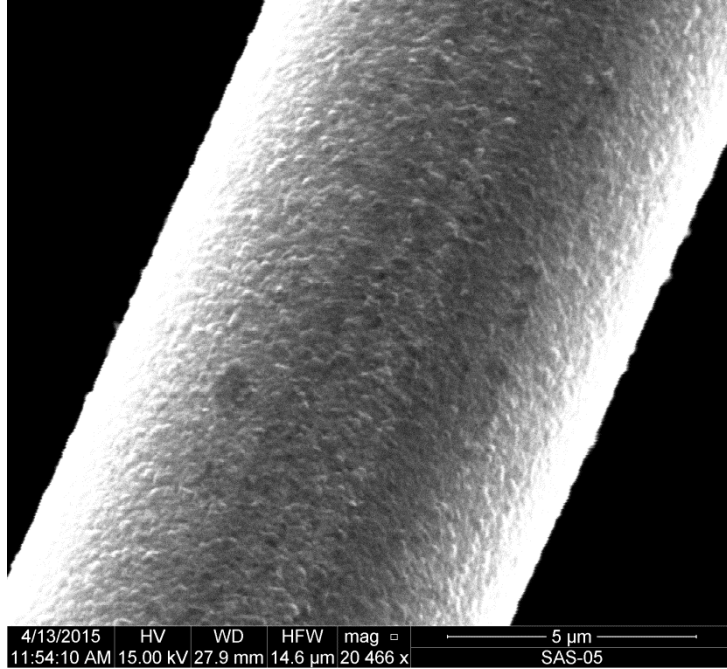


Figure 79: SEM micrograph of the Syramic-iBN specimen “Air 5” examining rough surface of a fiber at mid-fiber length ($\sigma_{cr} = 508$ MPa, $t_f = 0$ s)

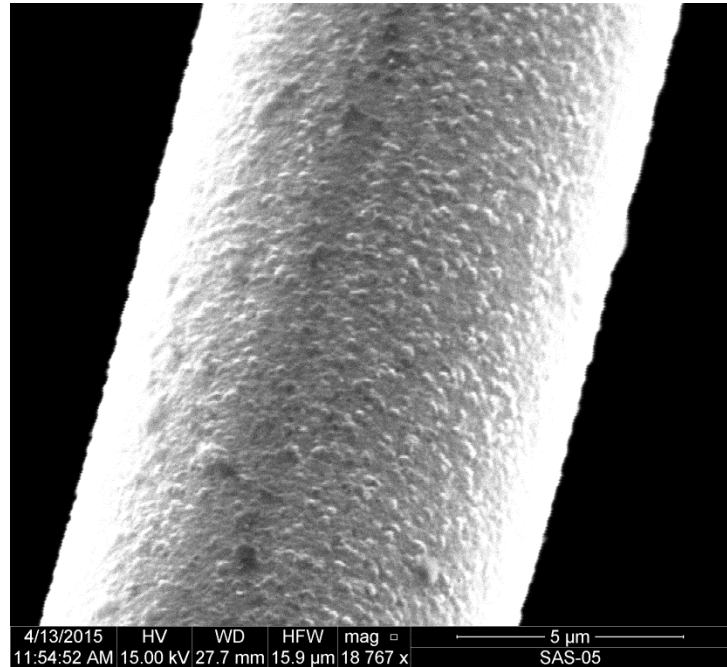


Figure 80: SEM micrograph of the Syramic-iBN specimen “Air 5” examining rough surface of a fiber at mid-fiber length ($\sigma_{cr} = 508$ MPa, $t_f = 0$ s)

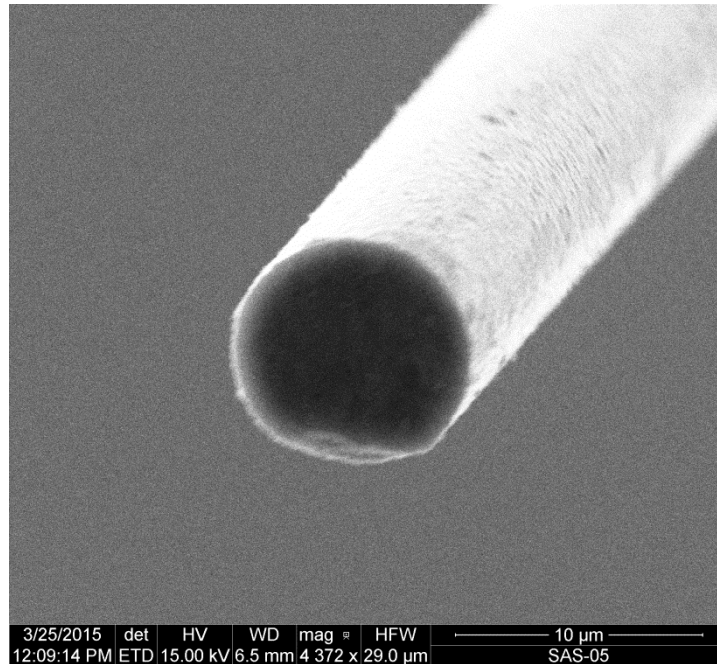


Figure 81: SEM micrograph of the Sylramic-iBN specimen “Air 5” examining cross section of a fiber ($\sigma_{cr} = 508$ MPa, $t_f = 0$ s)

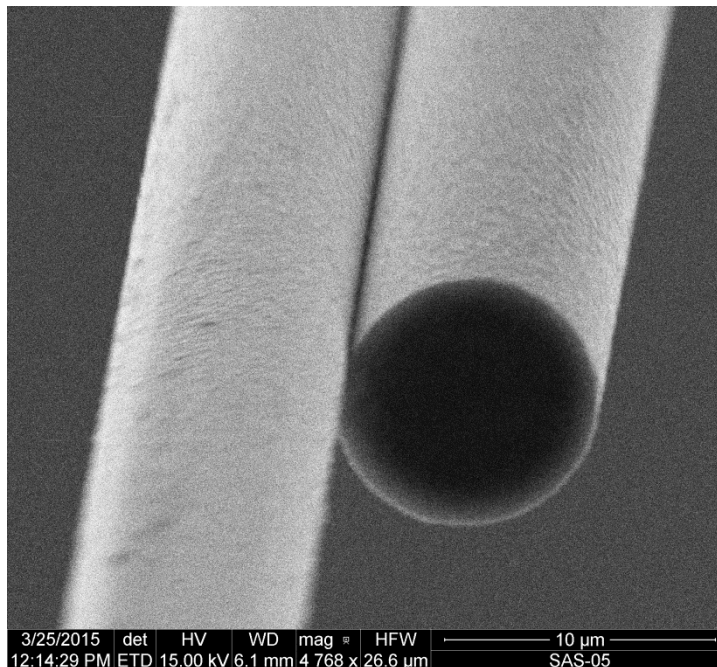


Figure 82: SEM micrograph of the Sylramic-iBN specimen “Air 5” examining cross section of a fiber ($\sigma_{cr} = 508$ MPa, $t_f = 0$ s)

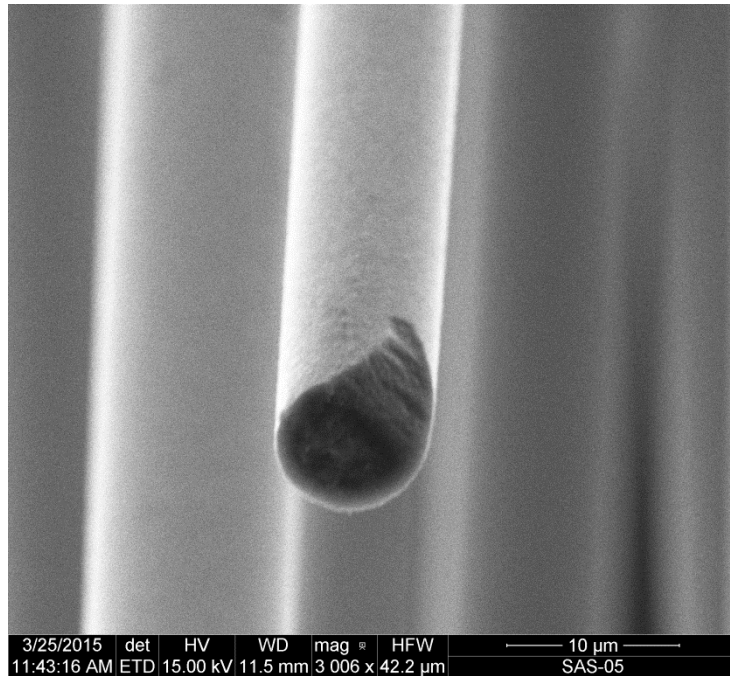


Figure 83: SEM micrograph of the Sylramic-iBN specimen “Air 5” examining fracture surface of a fiber ($\sigma_{cr} = 508$ MPa, $t_f = 0$ s)

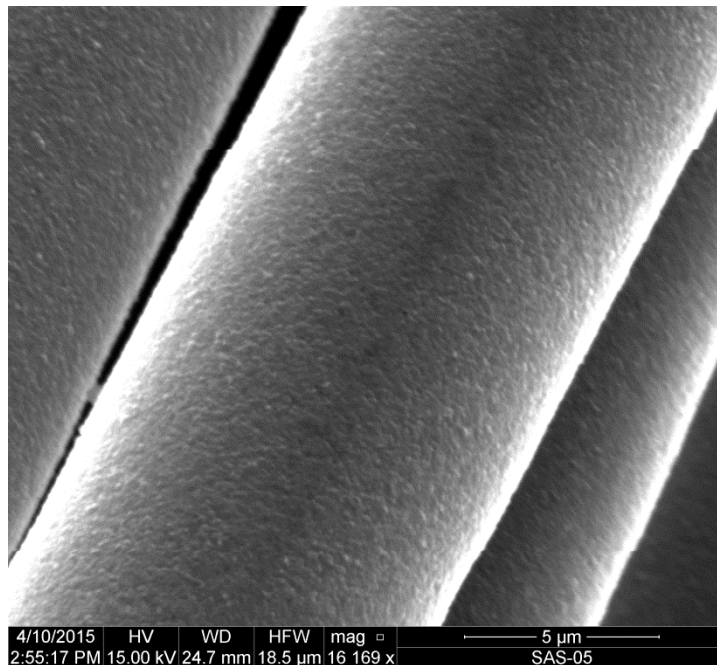


Figure 84: SEM micrograph of the Sylramic-iBN specimen “Air 11” examining rough surface of several fibers at mid-fiber length ($\sigma_{cr} = 508$ MPa, $t_f = 0$ s)

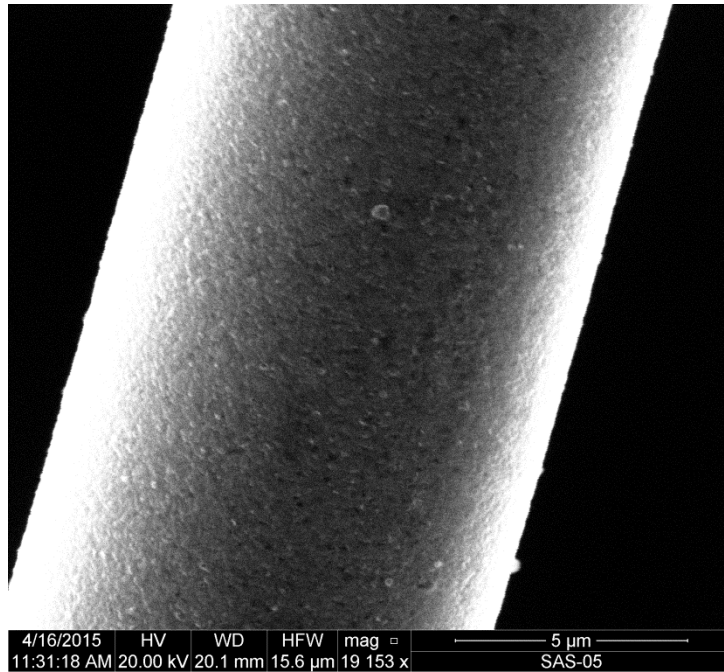


Figure 85: SEM micrograph of the Syramic-iBN specimen “Air 11” examining rough surface of a fiber at mid-fiber length ($\sigma_{cr} = 508$ MPa, $t_f = 0$ s)

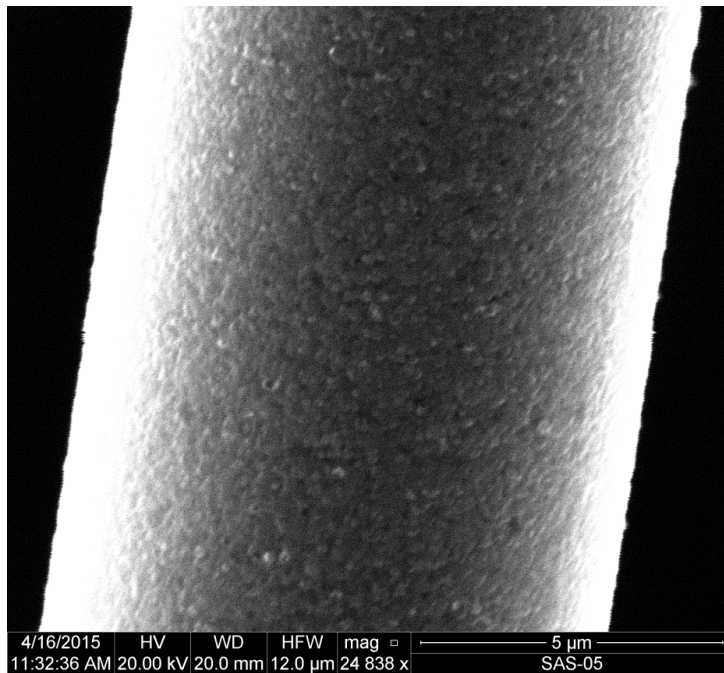


Figure 86: SEM micrograph of the Syramic-iBN specimen “Air 11” examining rough surface of a fiber at mid-fiber length ($\sigma_{cr} = 508$ MPa, $t_f = 0$ s)

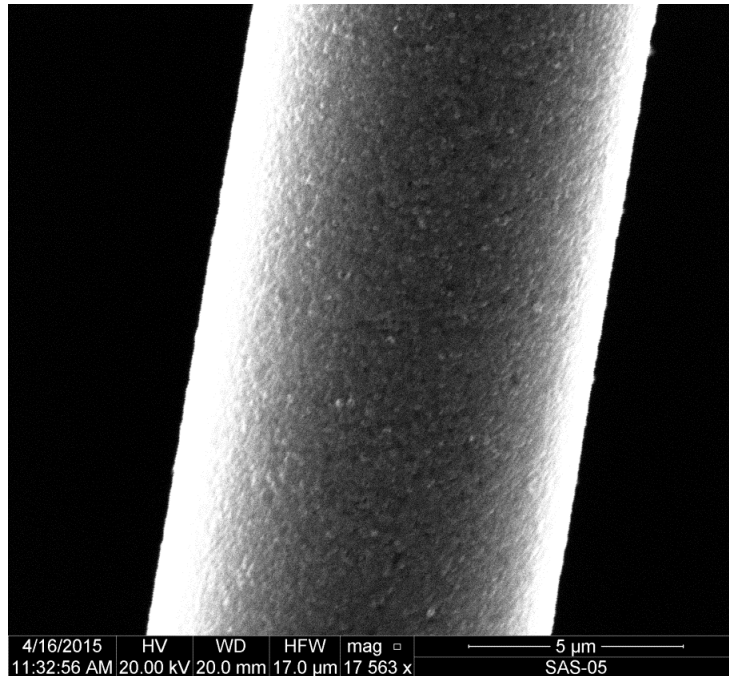


Figure 87: SEM micrograph of the Sylramic-iBN specimen “Air 11” examining rough surface of a fiber at mid-fiber length ($\sigma_{cr} = 508$ MPa, $t_f = 0$ s)

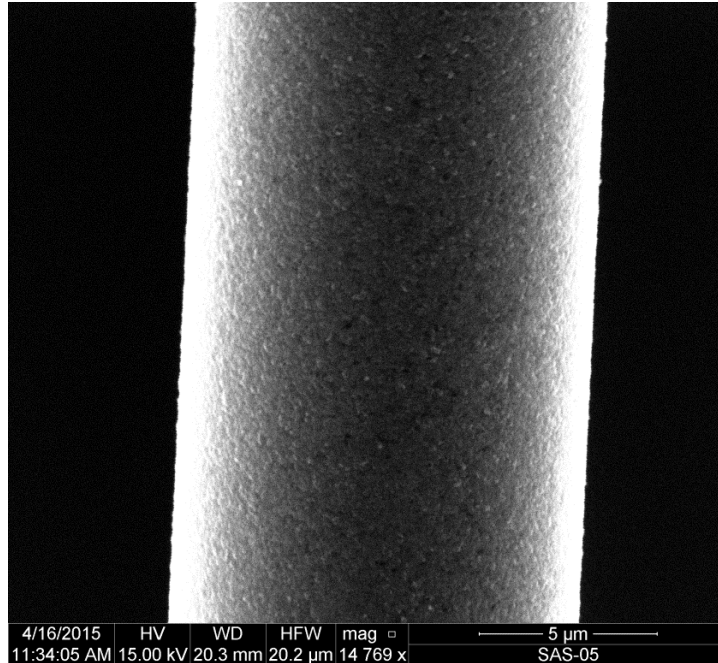


Figure 88: SEM micrograph of the Sylramic-iBN specimen “Air 11” examining rough surface of a fiber at mid-fiber length ($\sigma_{cr} = 508$ MPa, $t_f = 0$ s)

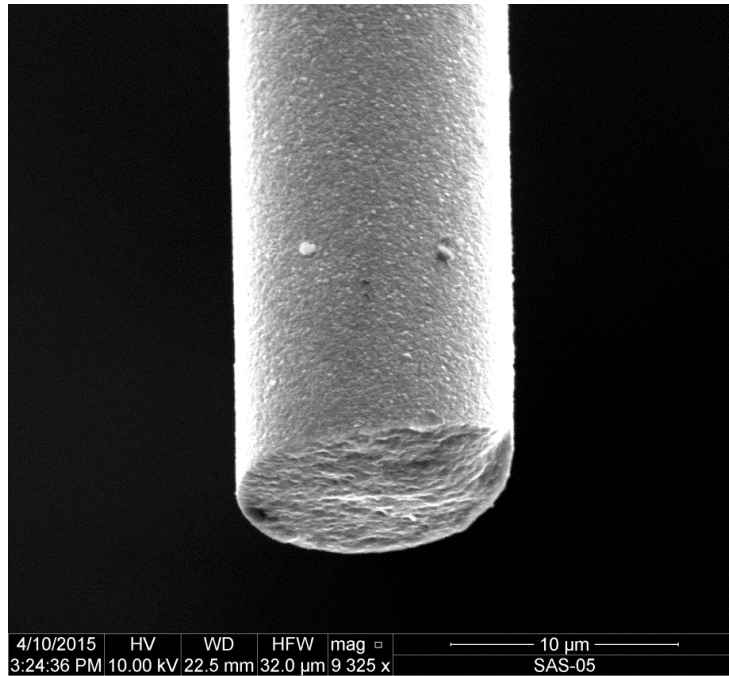


Figure 89: SEM micrograph of the Sylramic-iBN specimen “Air 11” examining fracture surface of a fiber ($\sigma_{cr} = 508$ MPa, $t_f = 0$ s)

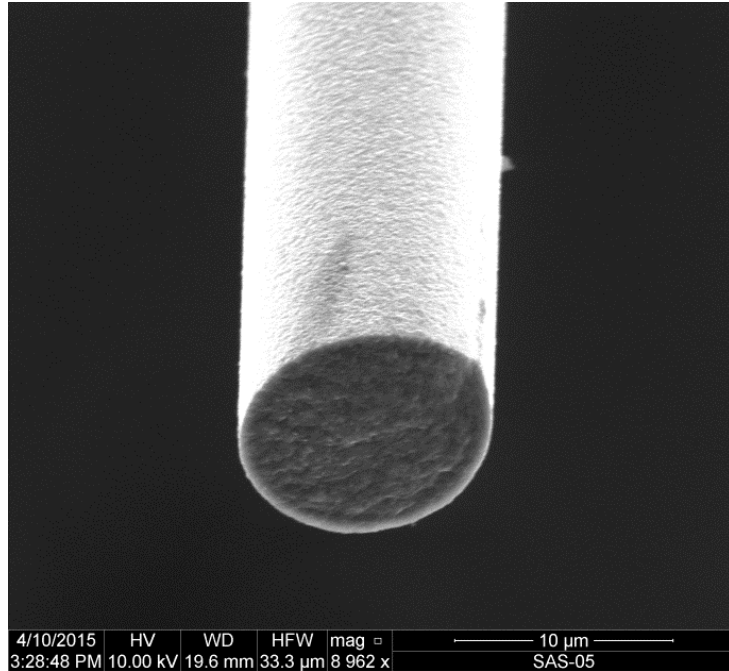


Figure 90: SEM micrograph of the Sylramic-iBN specimen “Air 11” examining fracture surface of a fiber ($\sigma_{cr} = 508$ MPa, $t_f = 0$ s)

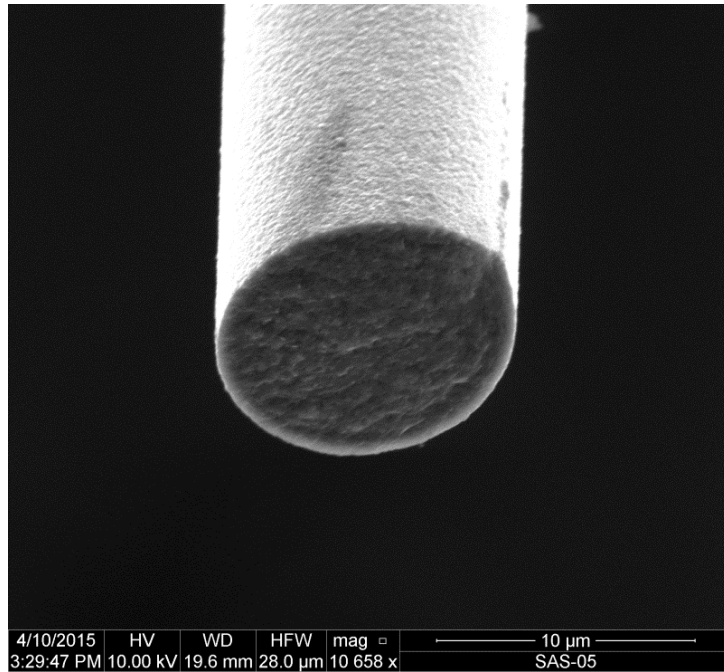


Figure 91: SEM micrograph of the Sylramic-iBN specimen “Air 11” examining fracture surface of a fiber ($\sigma_{cr} = 508$ MPa, $t_f = 0$ s)

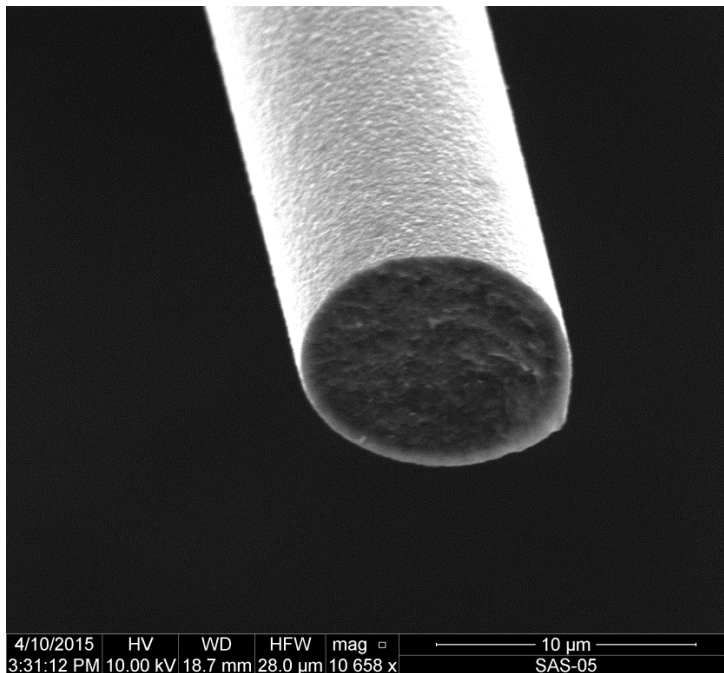


Figure 92: SEM micrograph of the Sylramic-iBN specimen “Air 11” examining fracture surface of a fiber ($\sigma_{cr} = 508$ MPa, $t_f = 0$ s)

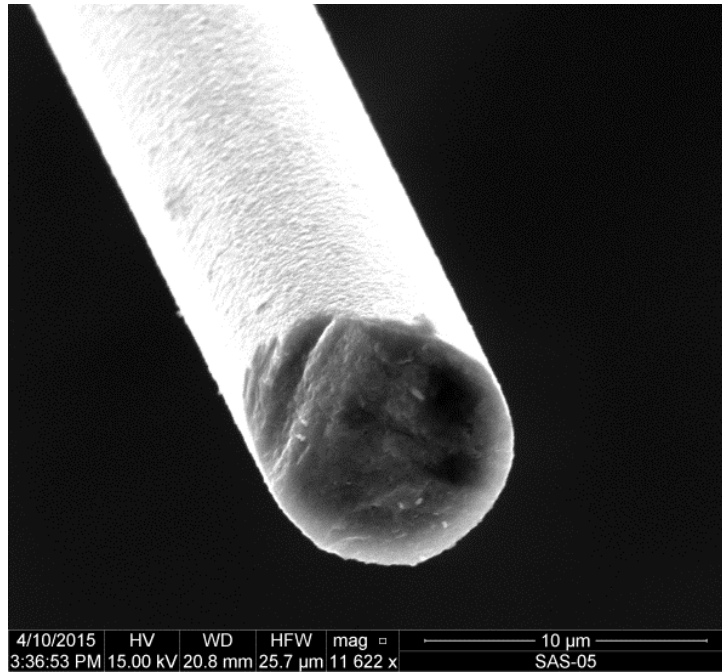


Figure 93: SEM micrograph of the Sylramic-iBN specimen “Air 11” examining fracture surface of a fiber ($\sigma_{cr} = 508$ MPa, $t_f = 0$ s)

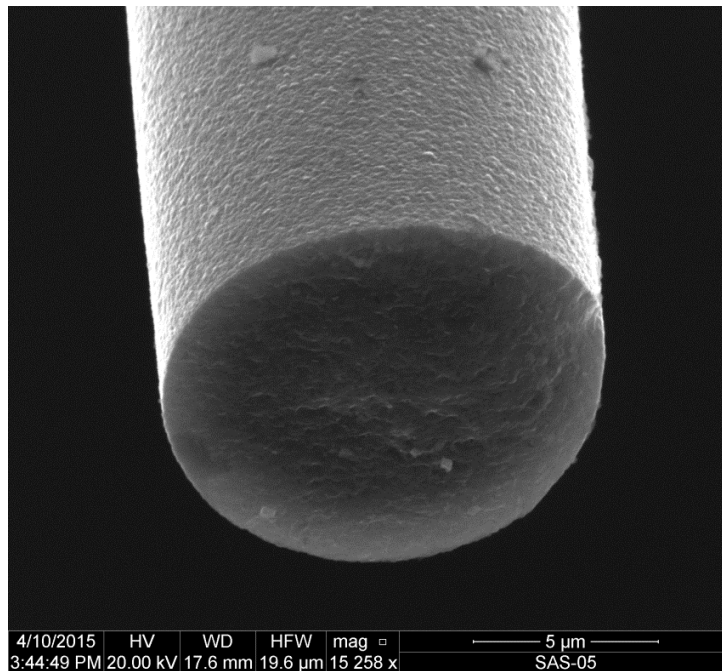


Figure 94: SEM micrograph of the Sylramic-iBN specimen “Air 11” examining fracture surface of a fiber ($\sigma_{cr} = 508$ MPa, $t_f = 0$ s)

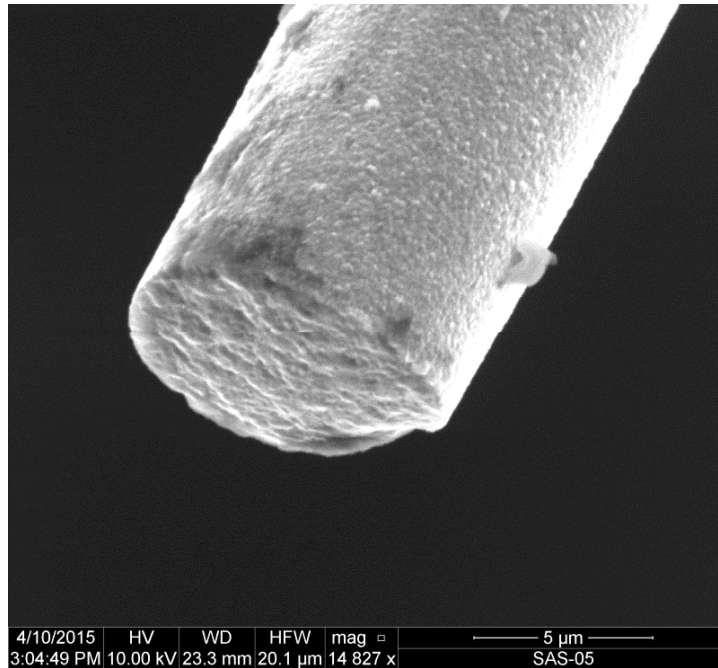


Figure 95: SEM micrograph of the Sylramic-iBN specimen “Air 11” examining a cut surface of a fiber at mid-fiber length ($\sigma_{cr} = 508$ MPa, $t_f = 0$ s)

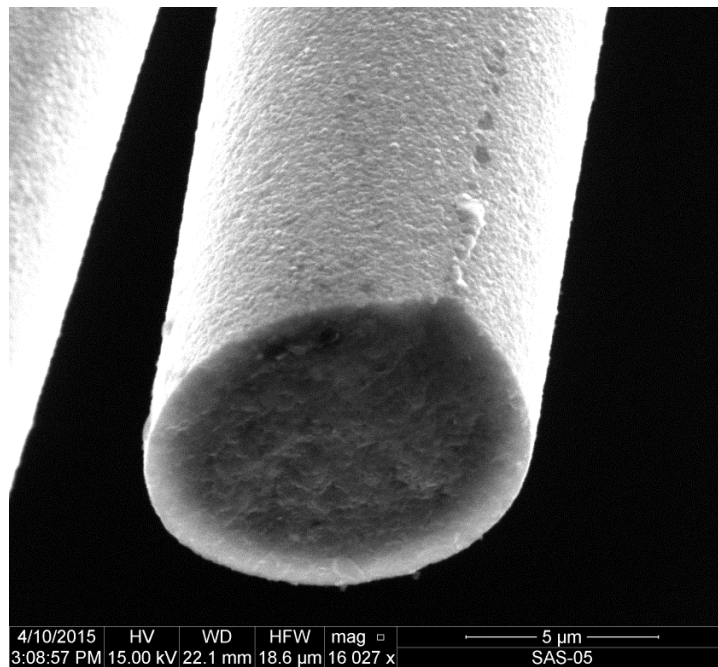


Figure 96: SEM micrograph of the Sylramic-iBN specimen “Air 11” examining a cut surface of a fiber at mid-fiber length ($\sigma_{cr} = 508$ MPa, $t_f = 0$ s)

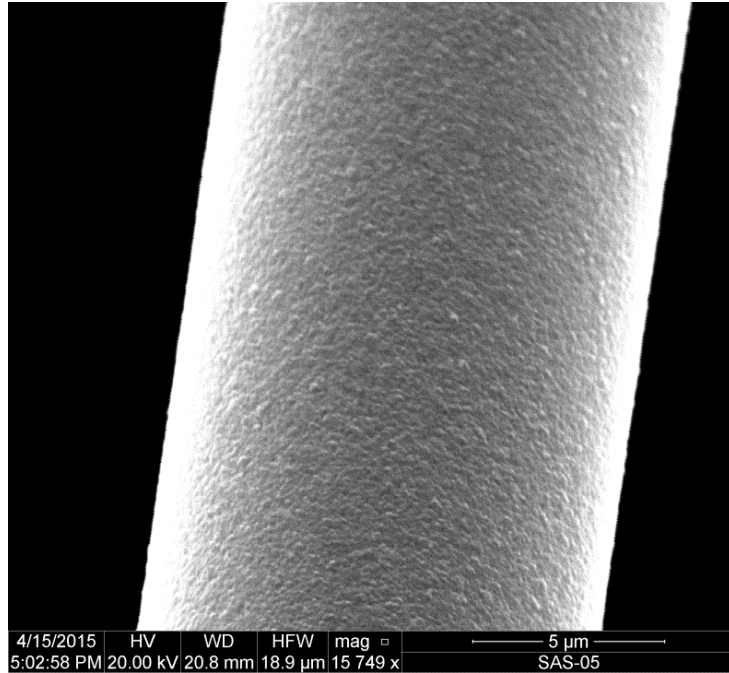


Figure 97: SEM micrograph of the Sylramic-iBN specimen “Air 16” examining general surface characteristics of a fiber ($\sigma_{cr} = 127$ MPa, $t_f \geq 100$ h)

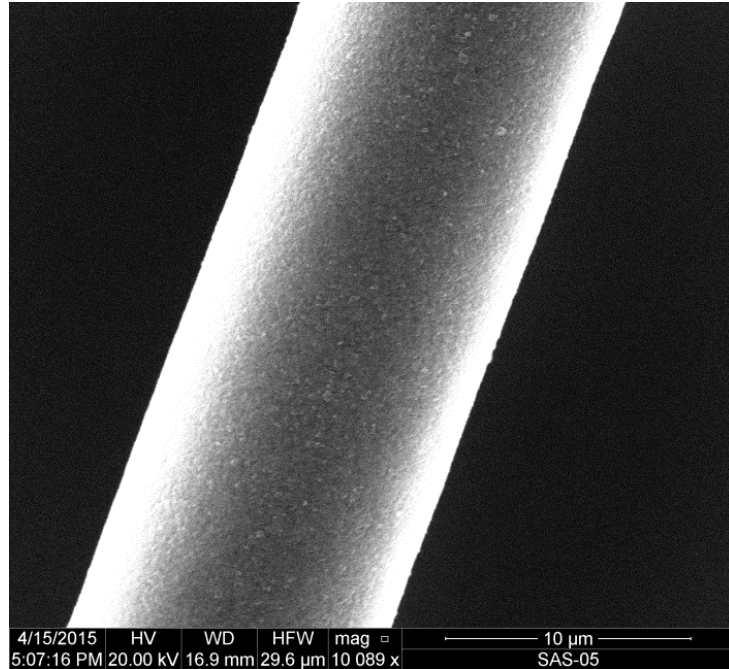


Figure 98: SEM micrograph of the Sylramic-iBN specimen “Air 16” examining general surface characteristics of a fiber ($\sigma_{cr} = 127$ MPa, $t_f \geq 100$ h)

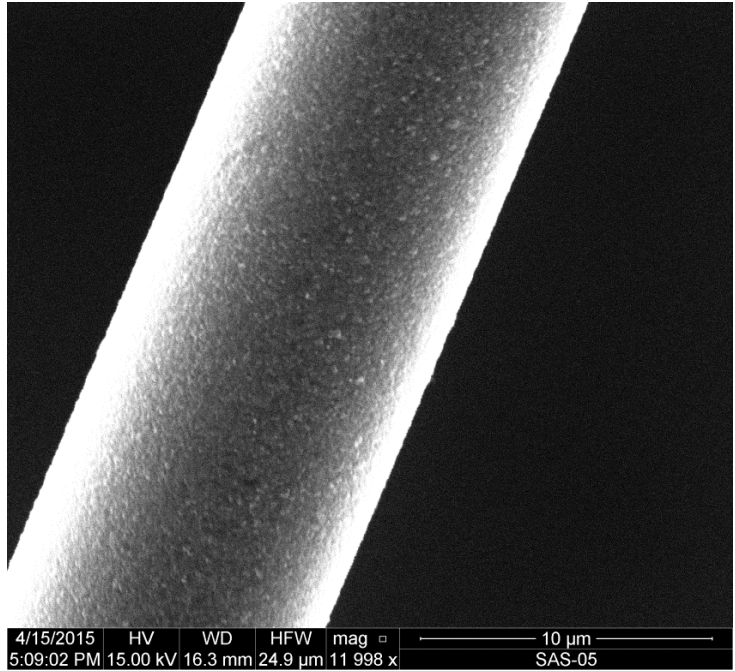


Figure 99: SEM micrograph of the Sylramic-iBN specimen “Air 16” examining general surface characteristics of a fiber ($\sigma_{cr} = 127$ MPa, $t_f \geq 100$ h)

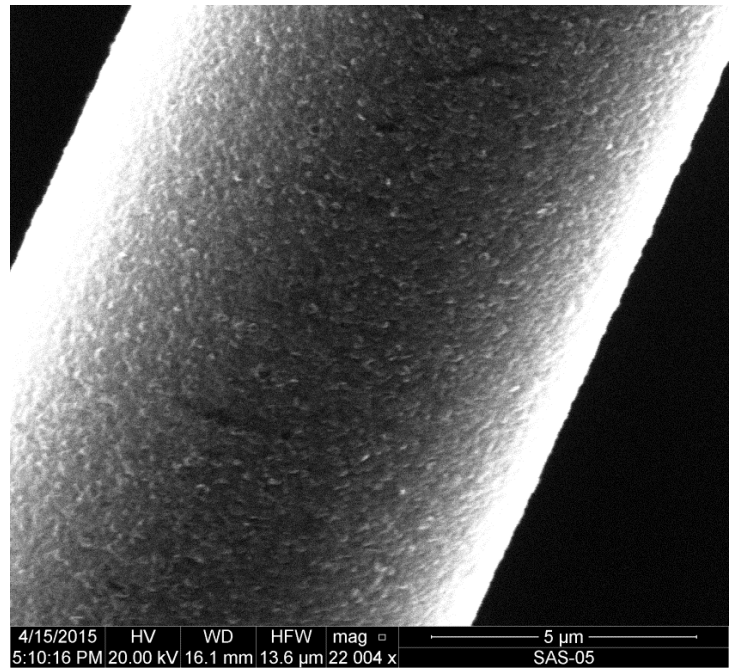


Figure 100: SEM micrograph of the Sylramic-iBN specimen “Air 16” examining rough surface of a fiber ($\sigma_{cr} = 127$ MPa, $t_f \geq 100$ h)

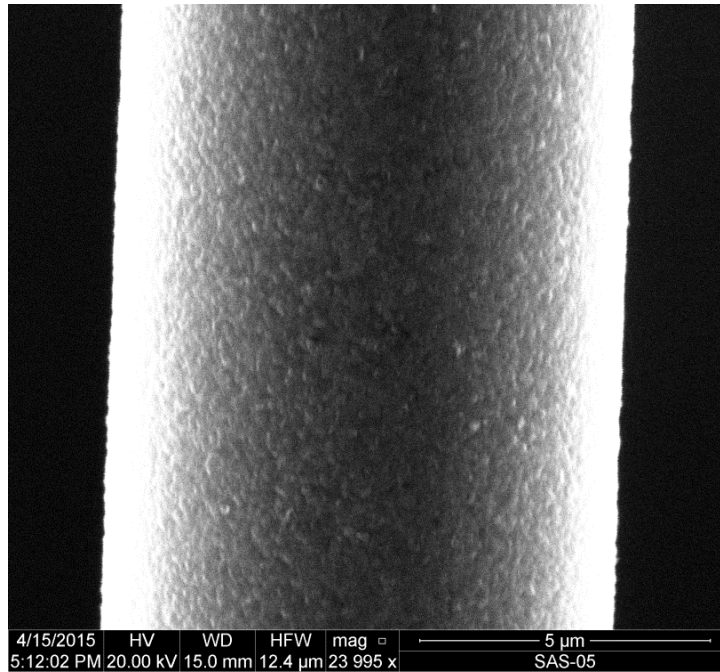


Figure 101: SEM micrograph of the Sylramic-iBN specimen “Air 16” examining rough surface of a fiber ($\sigma_{cr} = 127$ MPa, $t_f \geq 100$ h)

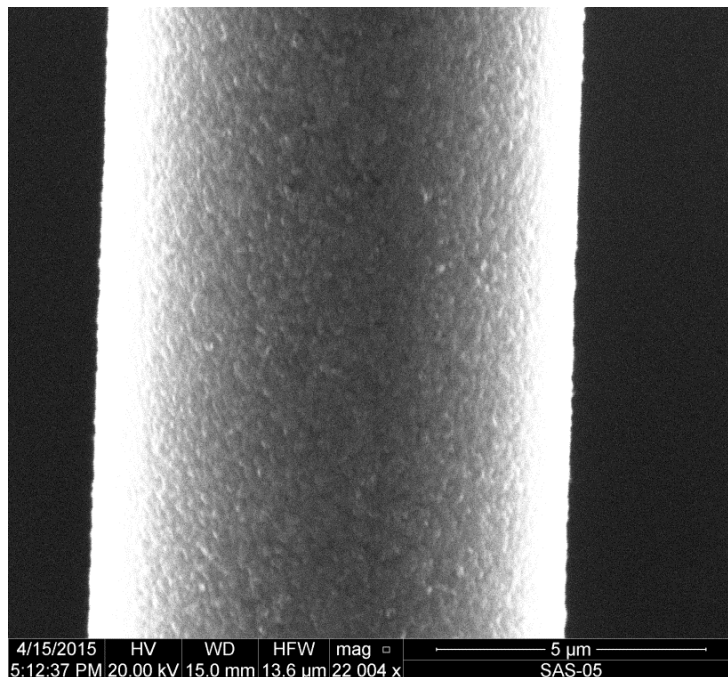


Figure 102: SEM micrograph of the Sylramic-iBN specimen “Air 16” examining rough surface of a fiber ($\sigma_{cr} = 127$ MPa, $t_f \geq 100$ h)

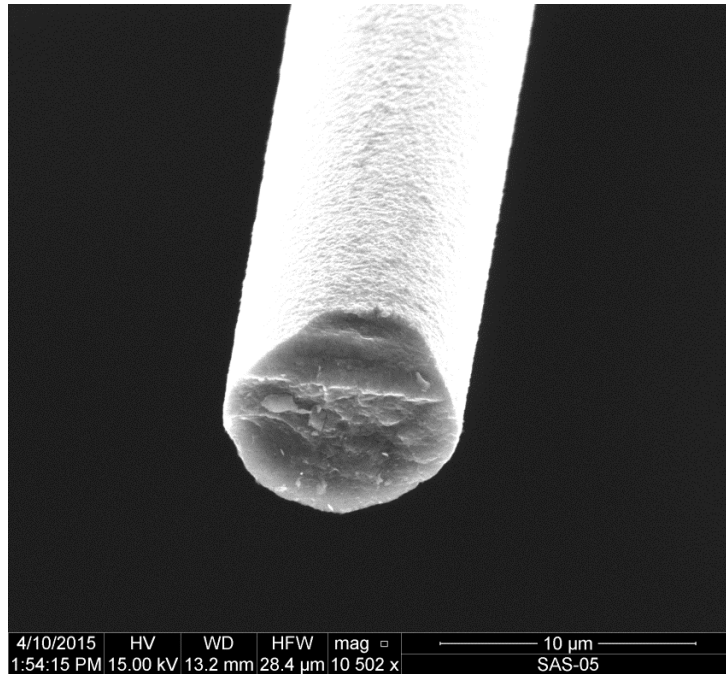


Figure 103: SEM micrograph of the Syramic-iBN specimen “Air 6” examining a cut surface of a fiber at mid-fiber length ($\sigma_{cr} = 508$ MPa, $t_f > 25$ h)

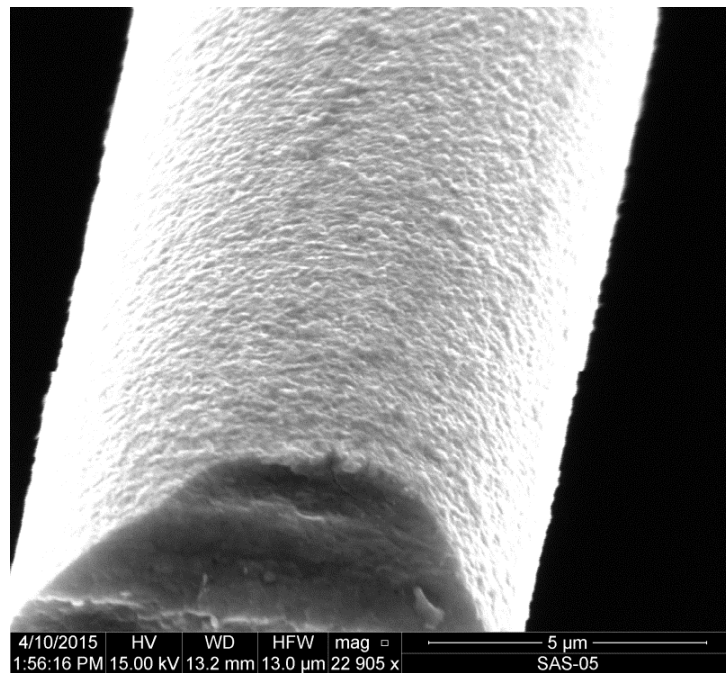


Figure 104: SEM micrograph of the Syramic-iBN specimen “Air 6” examining rough surface of a fiber at mid-fiber length ($\sigma_{cr} = 508$ MPa, $t_f > 25$ h)

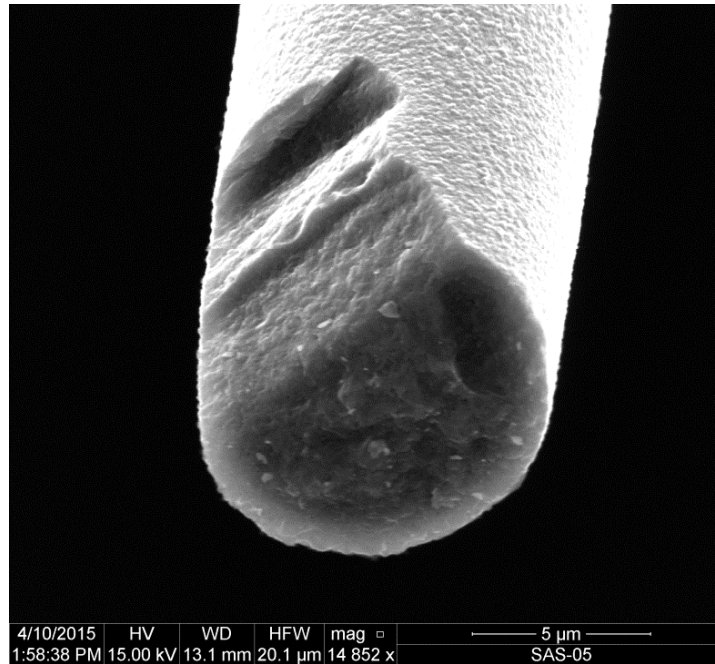


Figure 105: SEM micrograph of the Sylramic-iBN specimen “Air 6” examining a cut surface of a fiber at mid-fiber length ($\sigma_{cr} = 508$ MPa, $t_f > 25$ h)

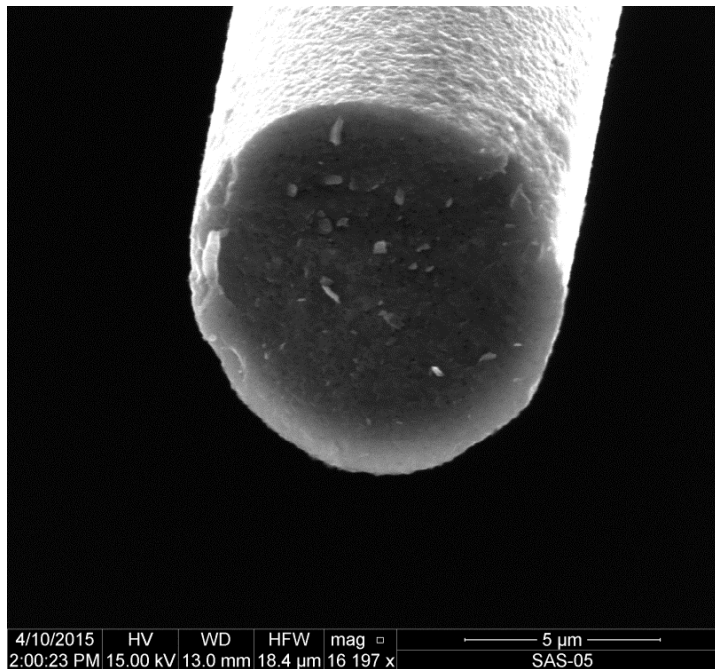


Figure 106: SEM micrograph of the Sylramic-iBN specimen “Air 6” examining a cross section of a cut surface of a fiber ($\sigma_{cr} = 508$ MPa, $t_f > 25$ h)

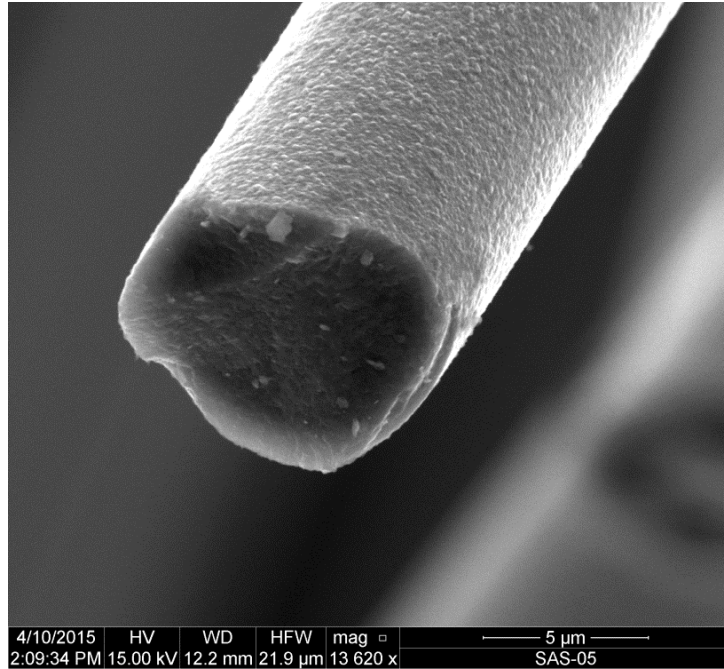


Figure 107: SEM micrograph of the Syramic-iBN specimen “Air 6” examining a cut surface of a fiber at mid-fiber length ($\sigma_{cr} = 508$ MPa, $t_f > 25$ h)

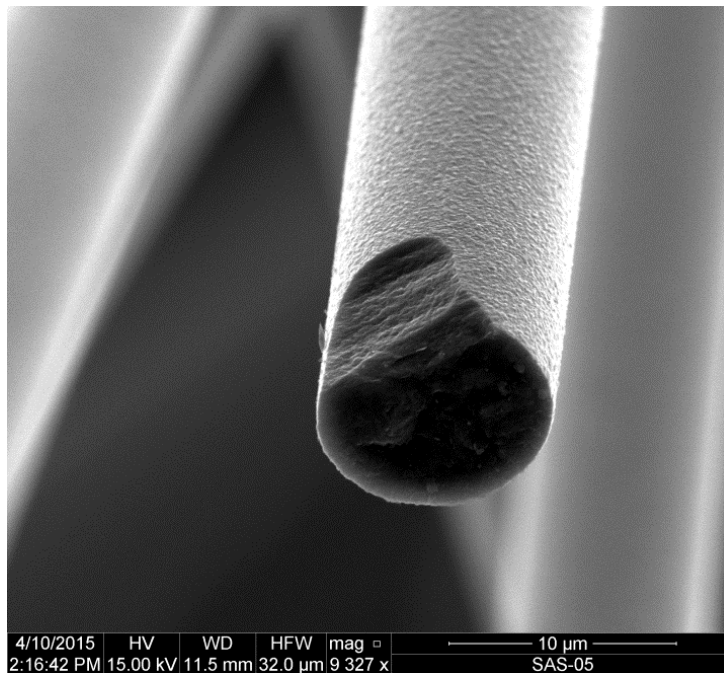


Figure 108: SEM micrograph of the Syramic-iBN specimen “Air 6” examining a cut surface of a fiber at mid-fiber length ($\sigma_{cr} = 508$ MPa, $t_f > 25$ h)

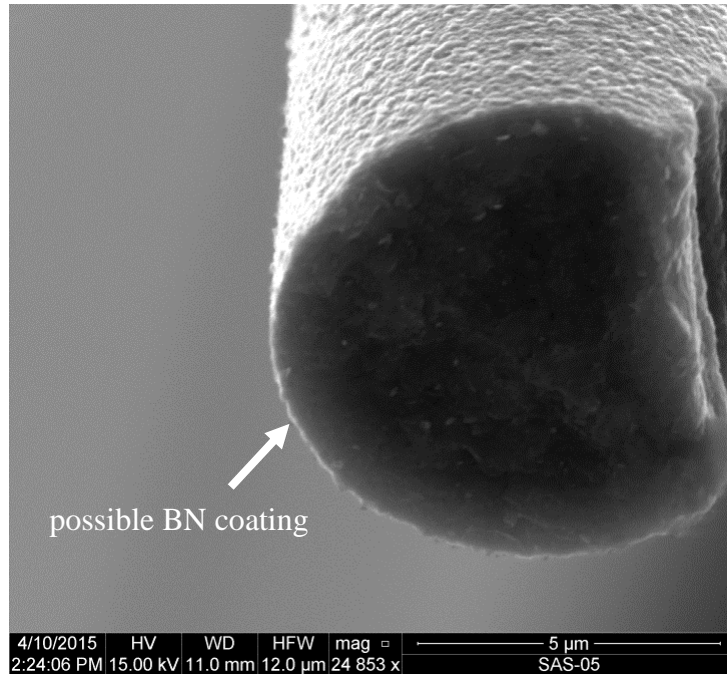


Figure 109: SEM micrograph of the Sylramic-iBN specimen “Air 6” examining a cut surface of a fiber at mid-fiber length; notice the rough surface and BN coating ($\sigma_{cr} = 508$ MPa, $t_f > 25$ h)

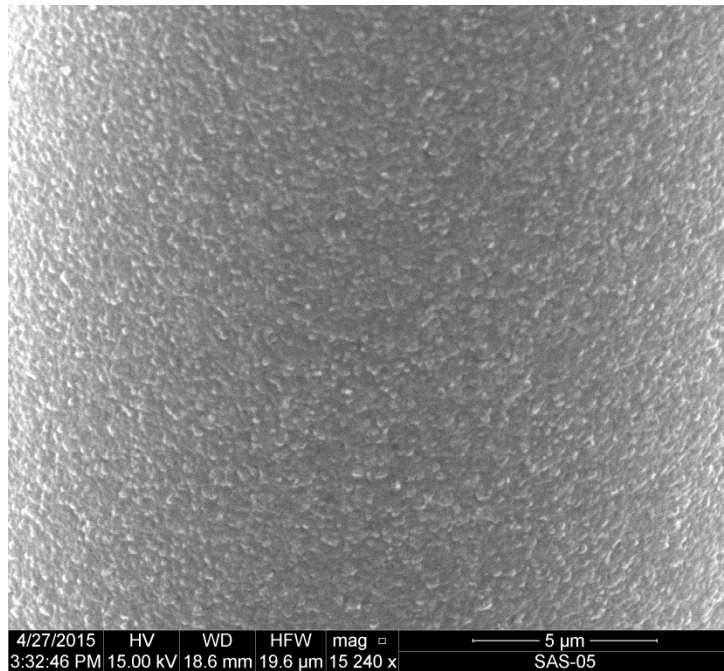


Figure 110: SEM micrograph of the Sylramic-iBN specimen “SS 17” examining rough surface of a fiber at mid-fiber length ($\sigma_{cr} = 444$ MPa, $t_f \geq 100$ h)

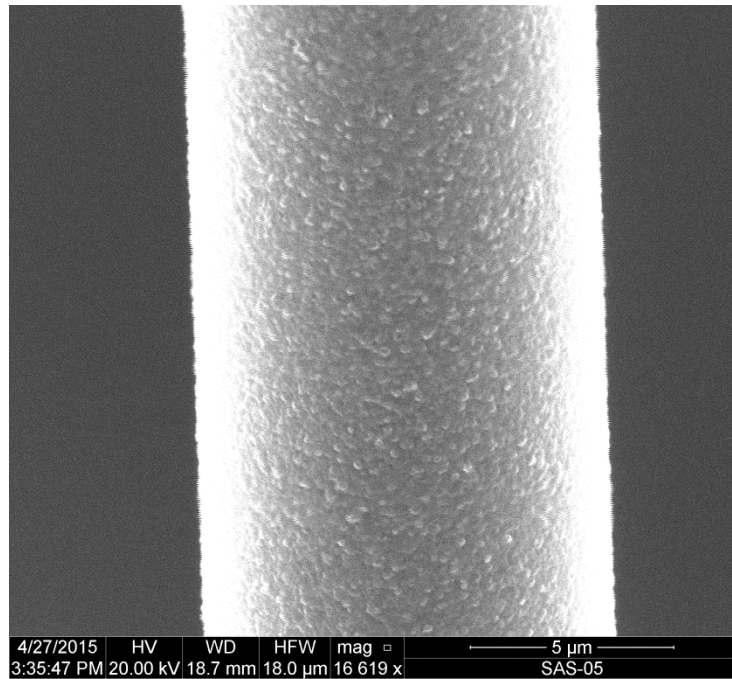


Figure 111: SEM micrograph of the Sylramic-iBN specimen “SS 17” examining rough surface of a fiber at mid-fiber length ($\sigma_{cr} = 444$ MPa, $t_f \geq 100$ h)

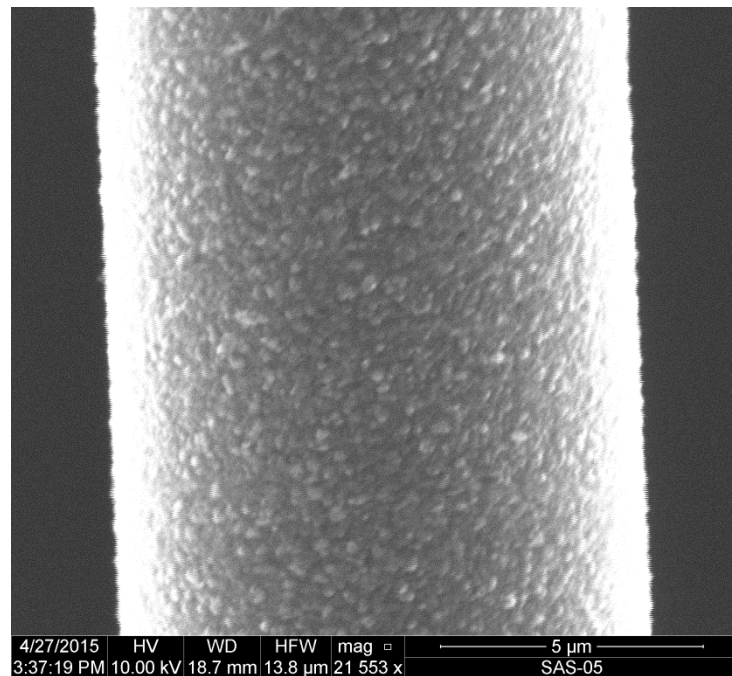


Figure 112: SEM micrograph of the Sylramic-iBN specimen “SS 17” examining rough surface of a fiber at mid-fiber length ($\sigma_{cr} = 444$ MPa, $t_f \geq 100$ h)

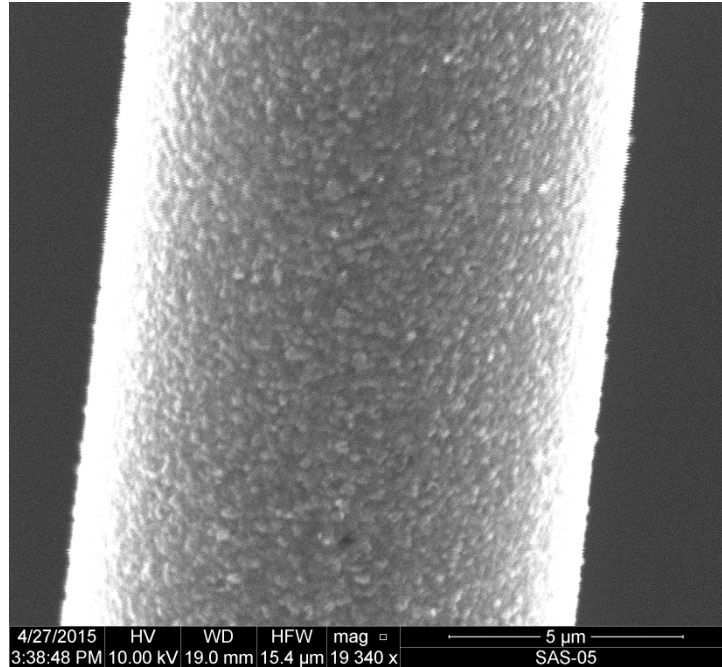


Figure 113: SEM micrograph of the Sylramic-iBN specimen “SS 17” examining rough surface of a fiber at mid-fiber length ($\sigma_{cr} = 444$ MPa, $t_f \geq 100$ h)

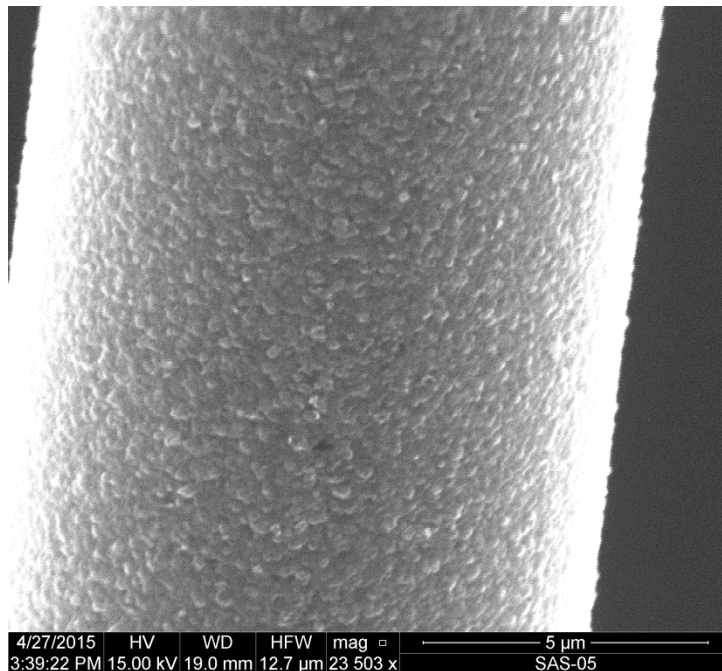


Figure 114: SEM micrograph of the Sylramic-iBN specimen “SS 17” examining rough surface of a fiber at mid-fiber length ($\sigma_{cr} = 444$ MPa, $t_f \geq 100$ h)

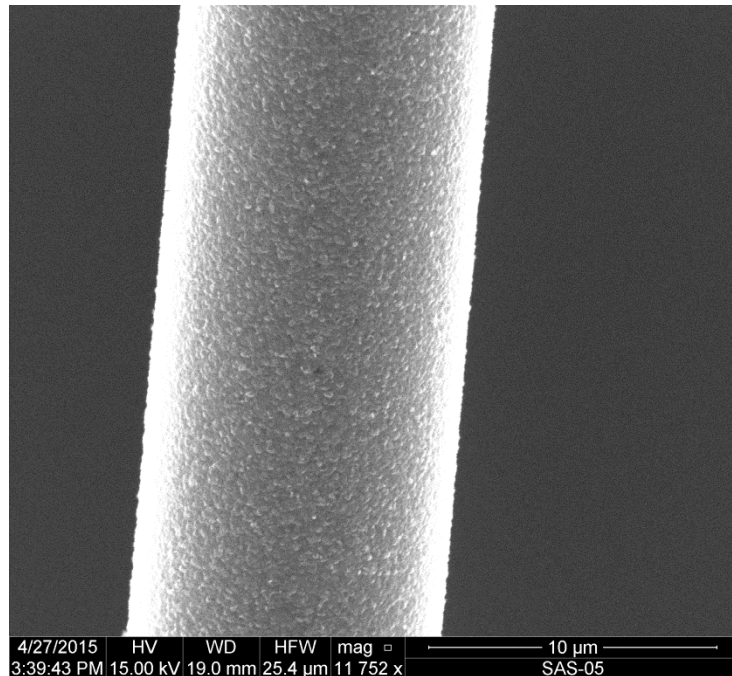


Figure 115: SEM micrograph of the Sylramic-iBN specimen “SS 17” examining general surface characteristics of a fiber at mid-fiber length ($\sigma_{cr} = 444$ MPa, $t_f \geq 100$ h)

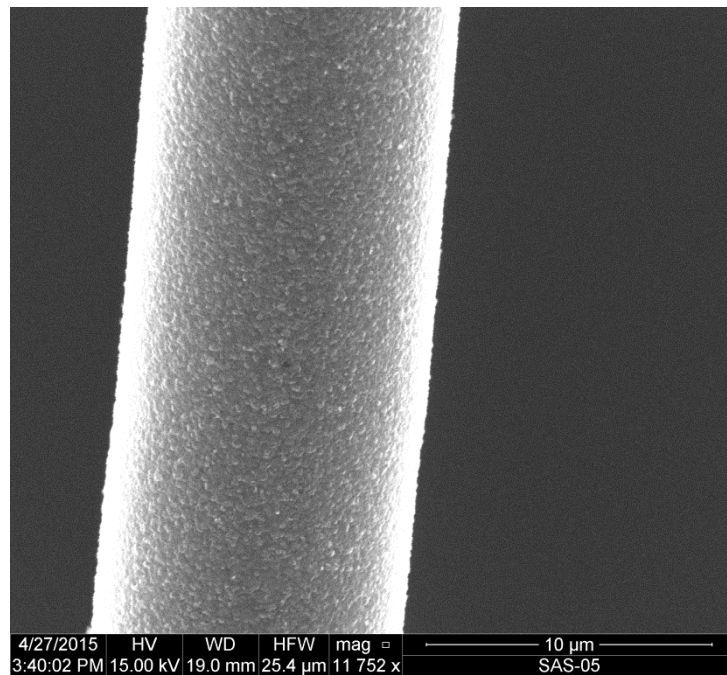


Figure 116: SEM micrograph of the Sylramic-iBN specimen “SS 17 examining general surface characteristics of a fiber at mid-fiber length ($\sigma_{cr} = 444$ MPa, $t_f \geq 100$ h)

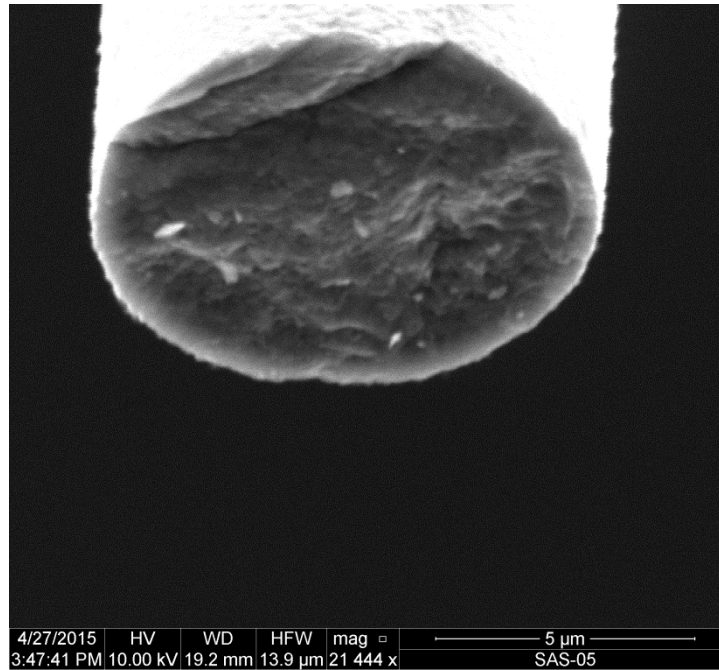


Figure 117: SEM micrograph of the Sylramic-iBN specimen “SS 17” examining a cut surface of a fiber at mid-fiber length ($\sigma_{cr} = 444$ MPa, $t_f \geq 100$ h)

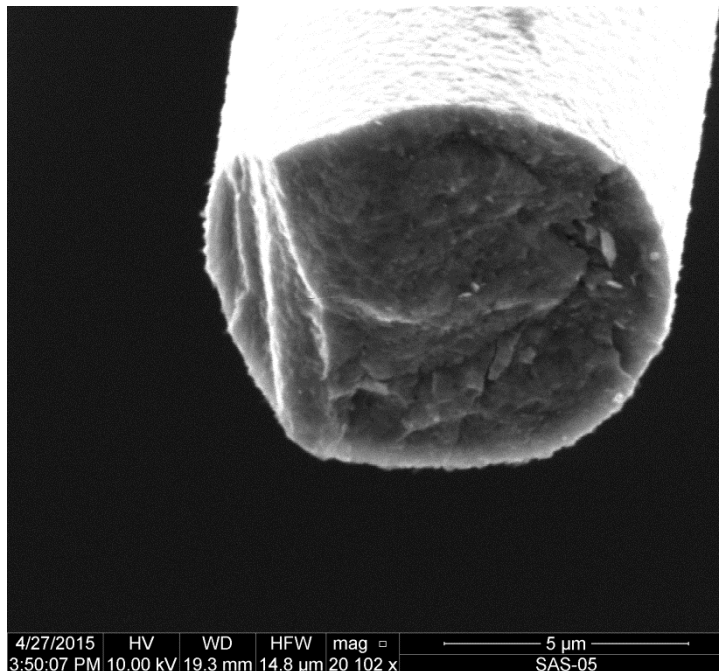


Figure 118: SEM micrograph of the Sylramic-iBN specimen “SS 17” examining a cut surface of a fiber at mid-fiber length; notice the rough surface ($\sigma_{cr} = 444$ MPa, $t_f \geq 100$ h)

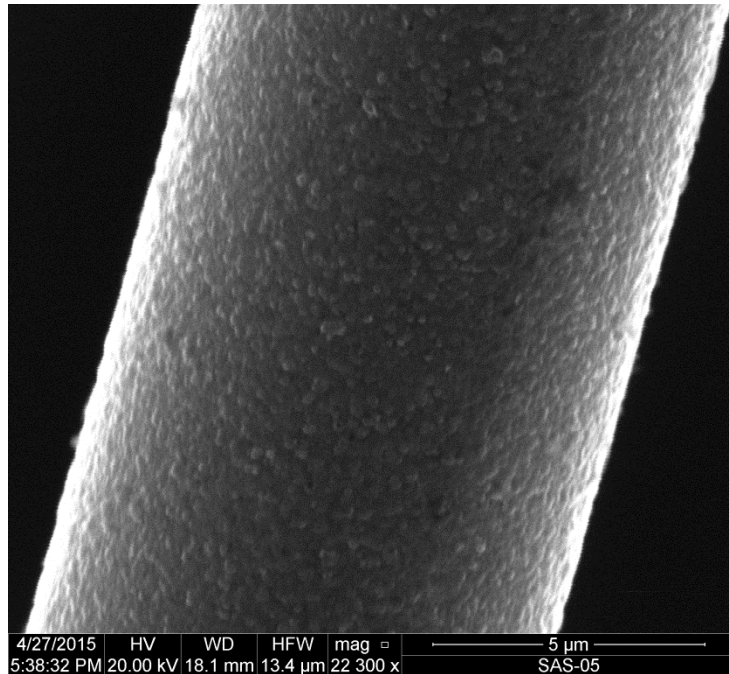


Figure 119: SEM micrograph of the Sylramic-iBN specimen “SS 20” examining rough surface of a fiber toward mid-fiber length ($\sigma_{cr} = 508$ MPa, $t_f = 0$ s)

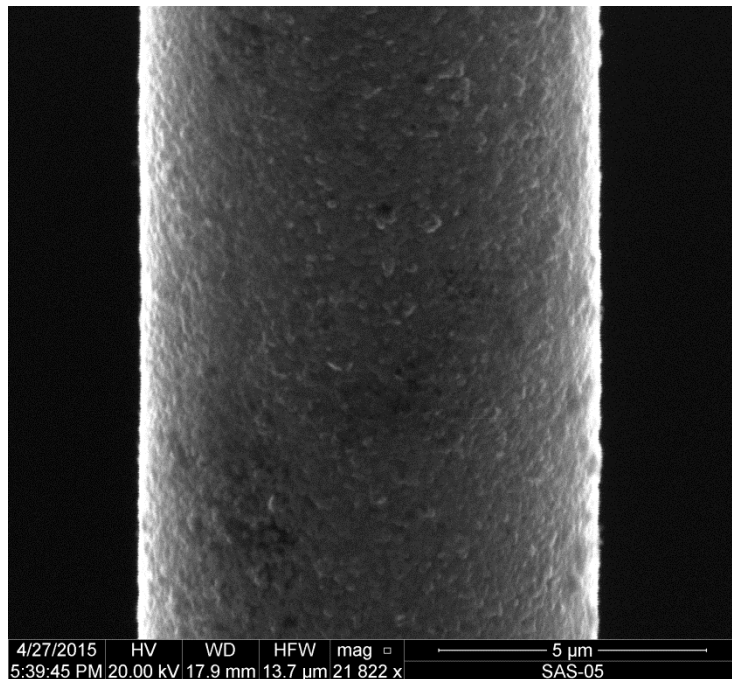


Figure 120: SEM micrograph of the Sylramic-iBN specimen “SS 20” examining rough surface of a fiber toward mid-fiber length ($\sigma_{cr} = 508$ MPa, $t_f = 0$ s)

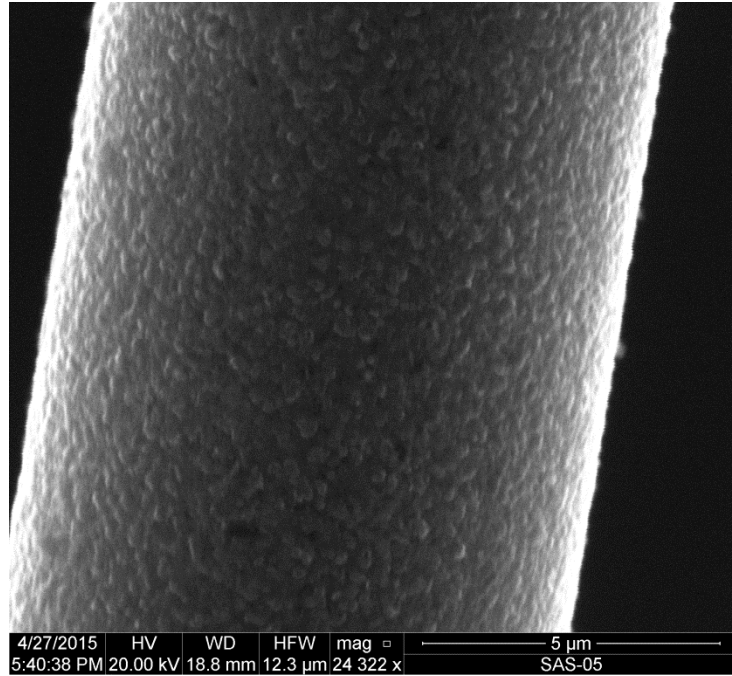


Figure 121: SEM micrograph of the Syramic-iBN specimen “SS 20” examining rough surface of a fiber toward mid-fiber length ($\sigma_{cr} = 508$ MPa, $t_f = 0$ s)

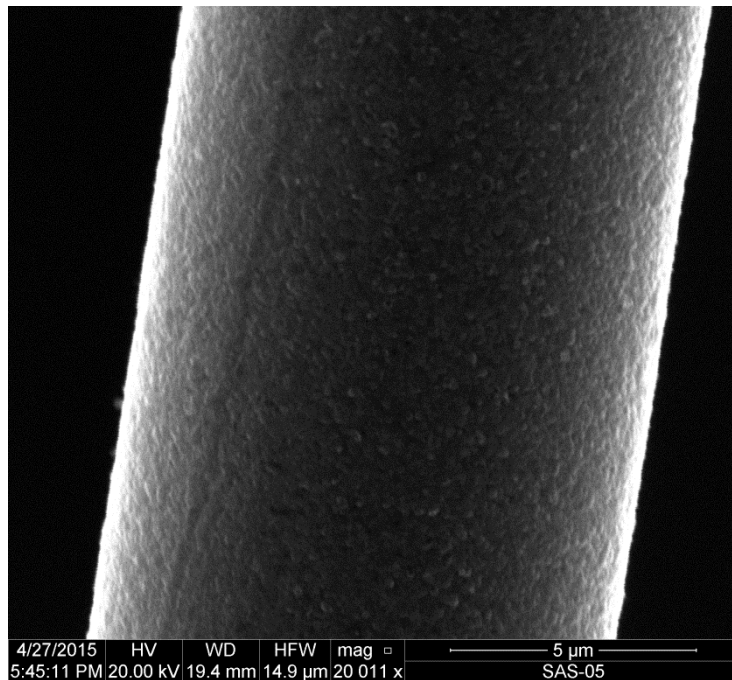


Figure 122: SEM micrograph of the Syramic-iBN specimen “SS 20” examining rough surface of a fiber toward mid-fiber length ($\sigma_{cr} = 508$ MPa, $t_f = 0$ s)

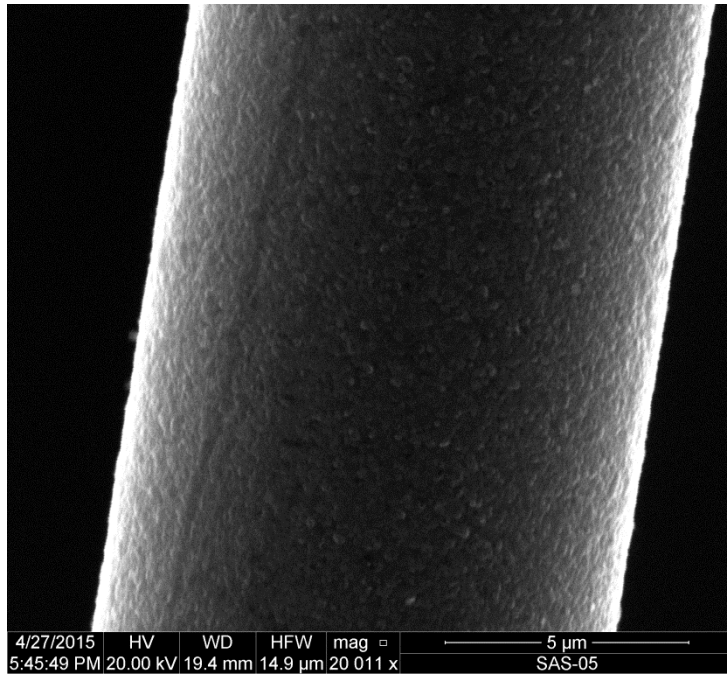


Figure 123: SEM micrograph of the Syramic-iBN specimen “SS 20” examining rough surface of a fiber toward mid-fiber length ($\sigma_{cr} = 508$ MPa, $t_f = 0$ s)

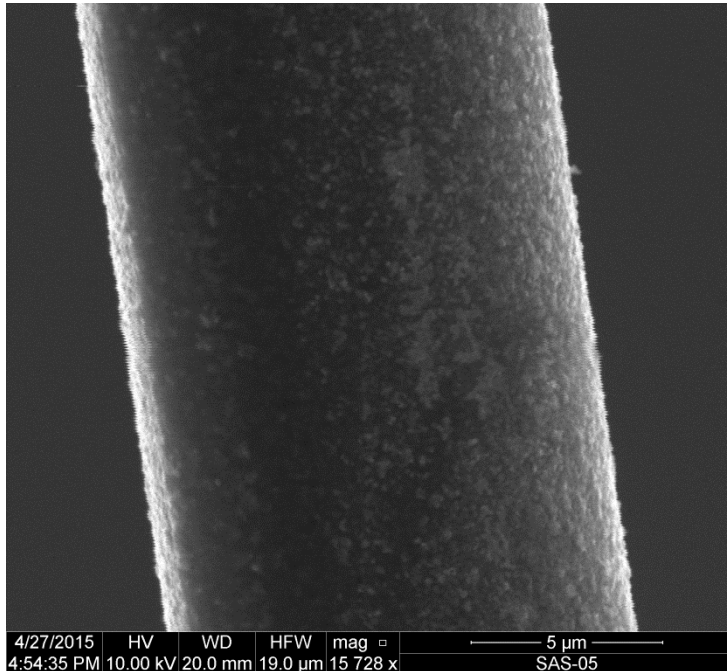


Figure 124: SEM micrograph of the Syramic-iBN specimen “SS 20” examining rough surface of a fiber at mid-fiber length; notice surface pieces have stripped off ($\sigma_{cr} = 508$ MPa, $t_f = 0$ s)

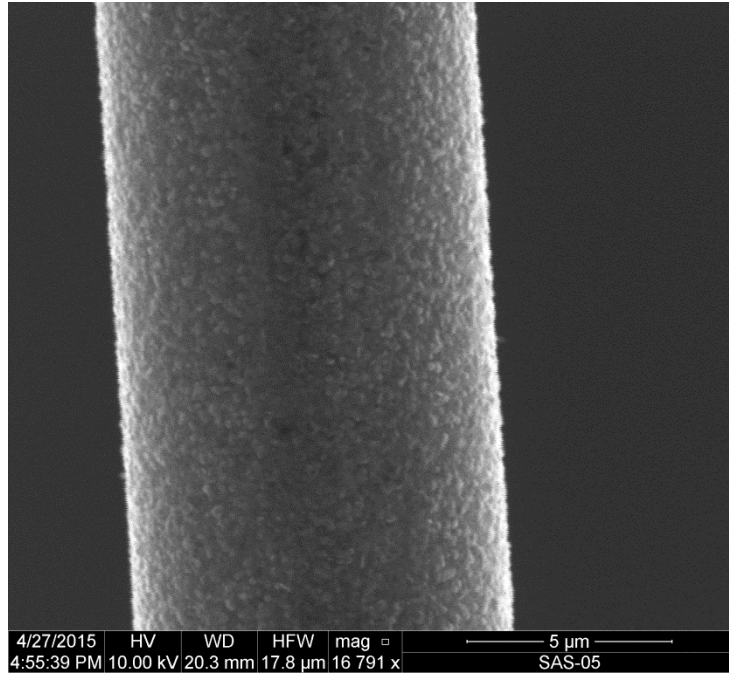


Figure 125: SEM micrograph of the Sylramic-iBN specimen “SS 20” examining rough surface of a fiber toward fracture end ($\sigma_{cr} = 508$ MPa, $t_f = 0$ s)

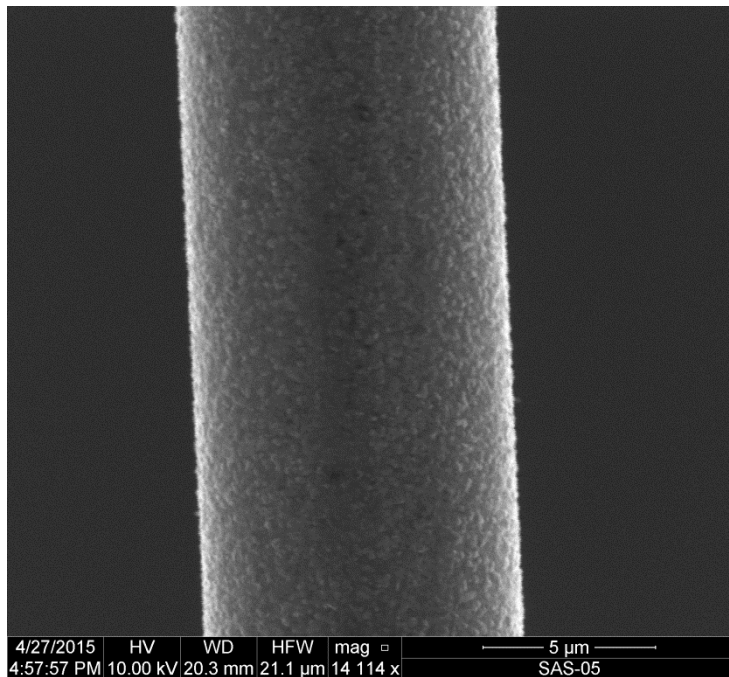


Figure 126: SEM micrograph of the Sylramic-iBN specimen “SS 20” examining rough surface of a fiber toward fracture end ($\sigma_{cr} = 508$ MPa, $t_f = 0$ s)

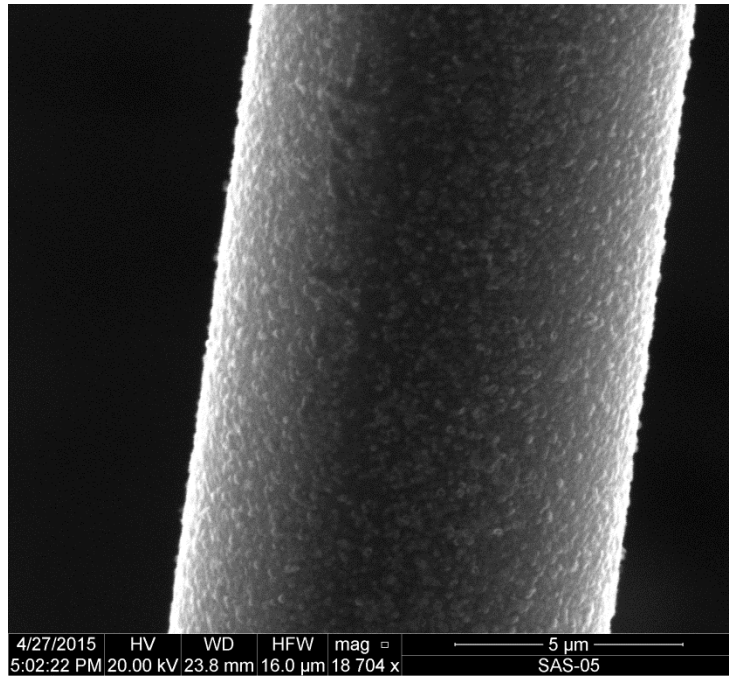


Figure 127: SEM micrograph of the Sylramic-iBN specimen “SS 20” examining rough surface of a fiber toward fracture end ($\sigma_{cr} = 508$ MPa, $t_f = 0$ s)

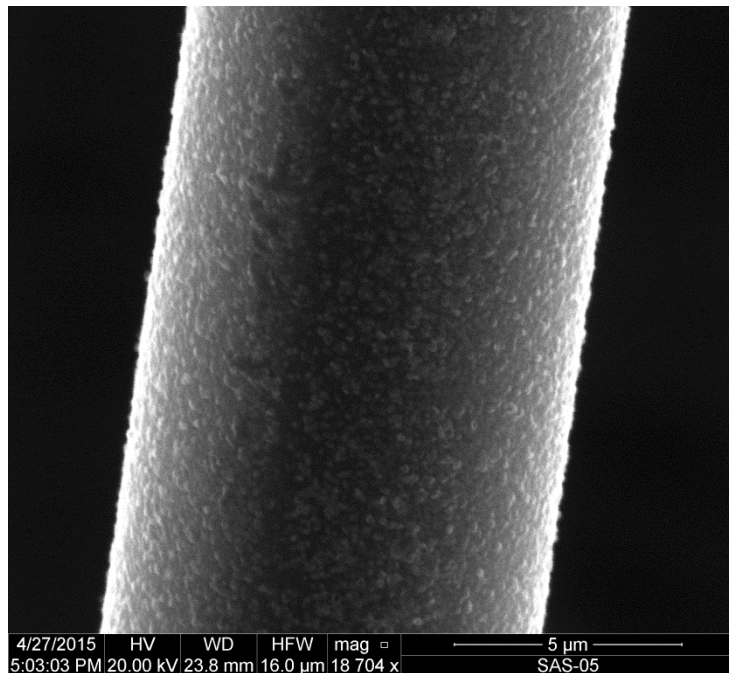


Figure 128: SEM micrograph of the Sylramic-iBN specimen “SS 20” examining rough surface of a fiber toward fracture end ($\sigma_{cr} = 508$ MPa, $t_f = 0$ s)

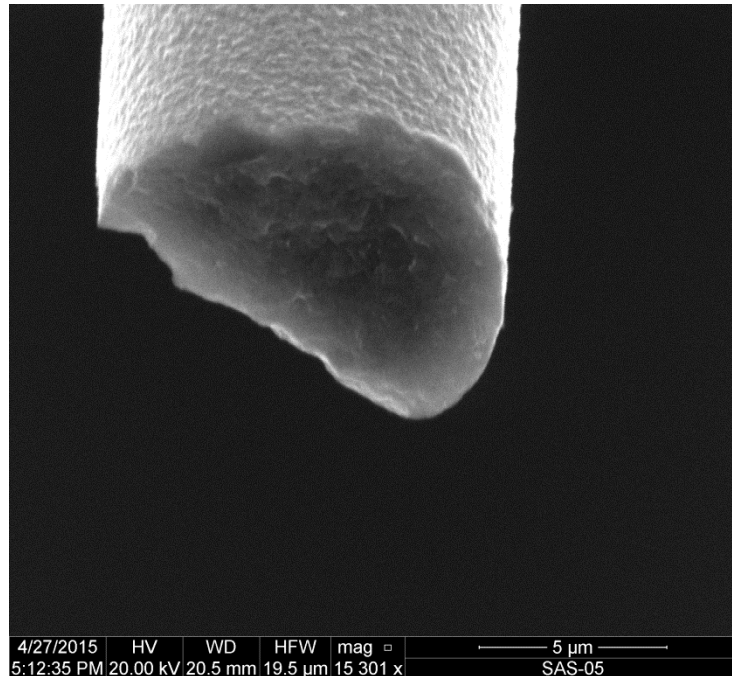


Figure 129: SEM micrograph of the Sylramic-iBN specimen “SS 17” examining fracture end of a fiber; notice the rough surface ($\sigma_{cr} = 444$ MPa, $t_f \geq 100$ h)

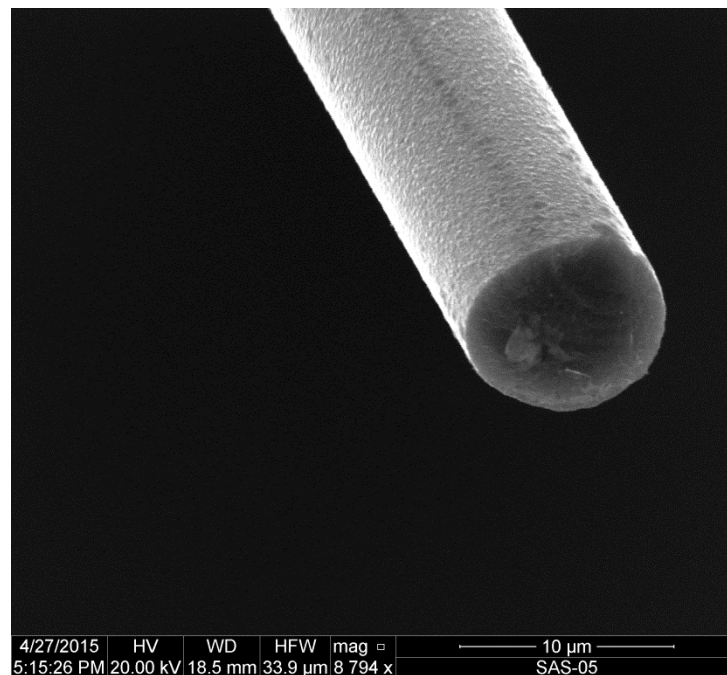


Figure 130: SEM micrograph of the Sylramic-iBN specimen “SS 17” examining fracture end of a fiber ($\sigma_{cr} = 444$ MPa, $t_f \geq 100$ h)

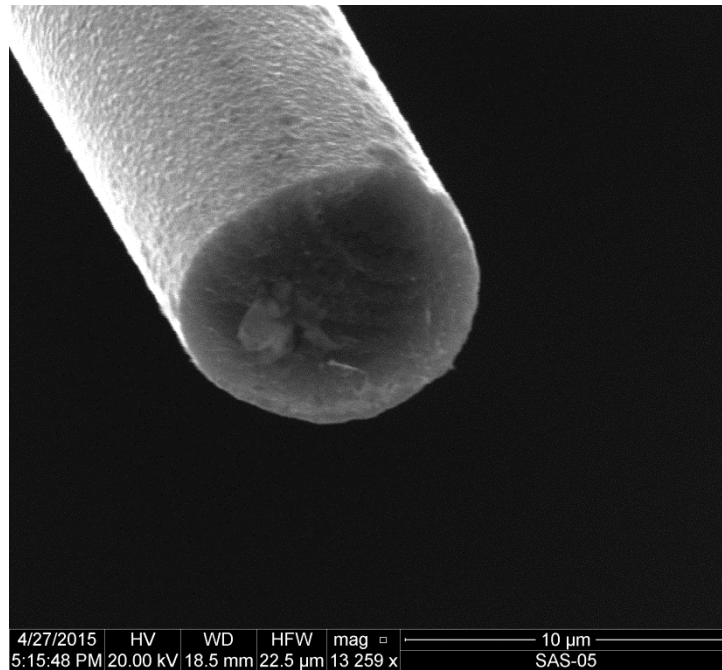


Figure 131: SEM micrograph of the Sylramic-iBN specimen “SS 17” examining fracture end of a fiber; notice the rough surface ($\sigma_{cr} = 444$ MPa, $t_f \geq 100$ h)

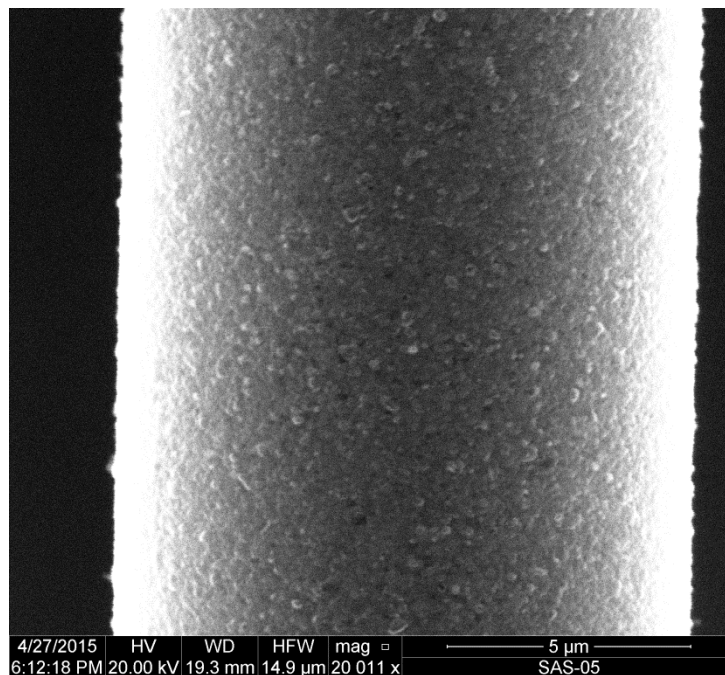


Figure 132: SEM micrograph of the Sylramic-iBN specimen “SS 23” examining rough surface of a fiber toward mid-fiber length ($\sigma_{cr} = 381$ MPa, $t_f = 0$ s)

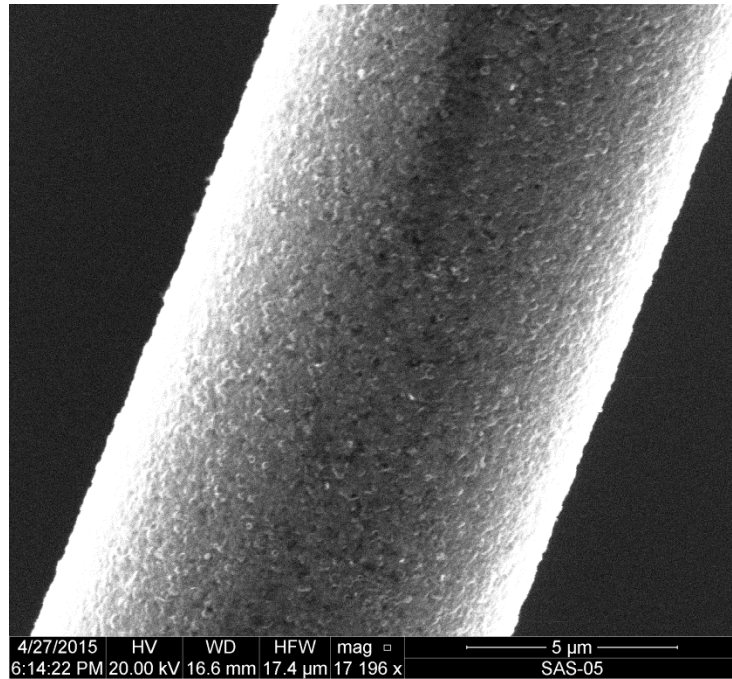


Figure 133: SEM micrograph of the Sylramic-iBN specimen “SS 23” examining rough surface of a fiber toward mid-fiber length ($\sigma_{cr} = 381$ MPa, $t_f = 0$ s)

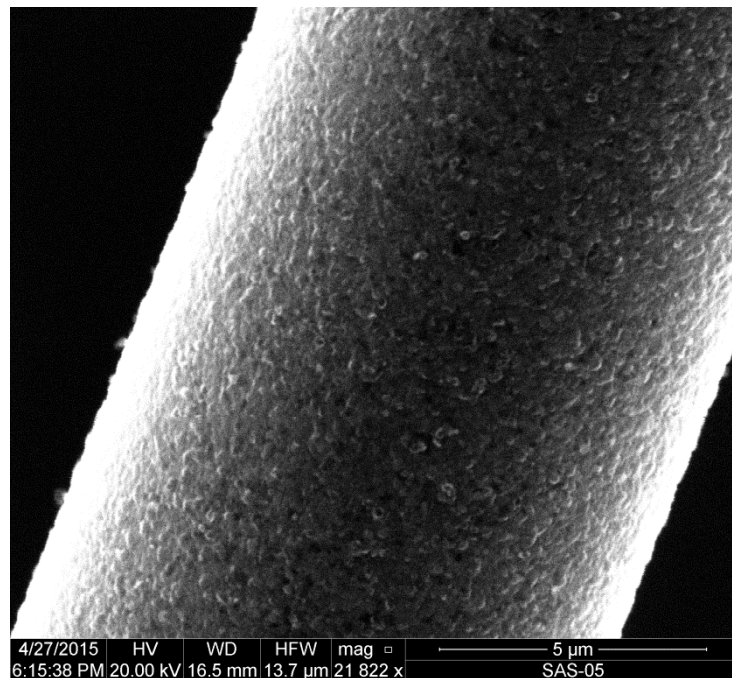


Figure 134: SEM micrograph of the Sylramic-iBN specimen “SS 23” examining rough surface of a fiber toward mid-fiber length ($\sigma_{cr} = 381$ MPa, $t_f = 0$ s)

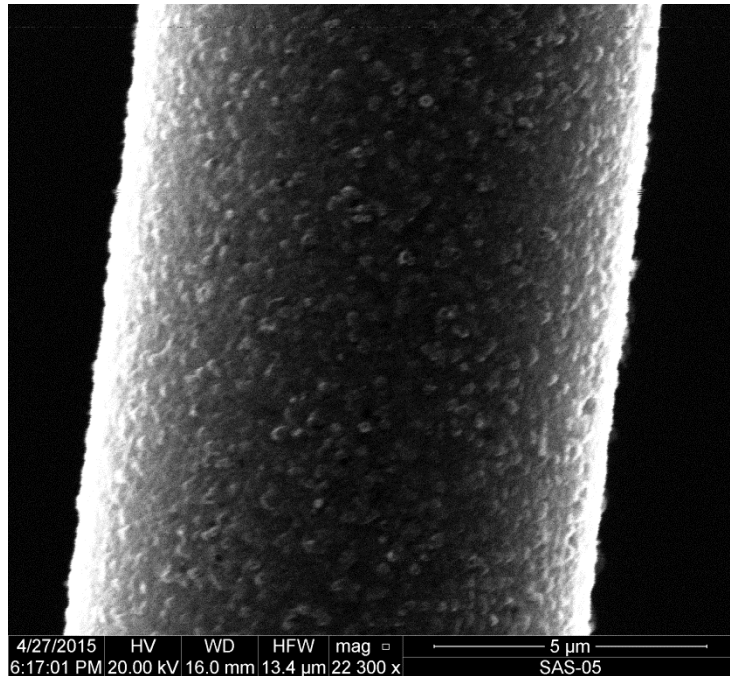


Figure 135: SEM micrograph of the Sylramic-iBN specimen “SS 23” examining rough surface of a fiber toward mid-fiber length ($\sigma_{cr} = 381$ MPa, $t_f = 0$ s)

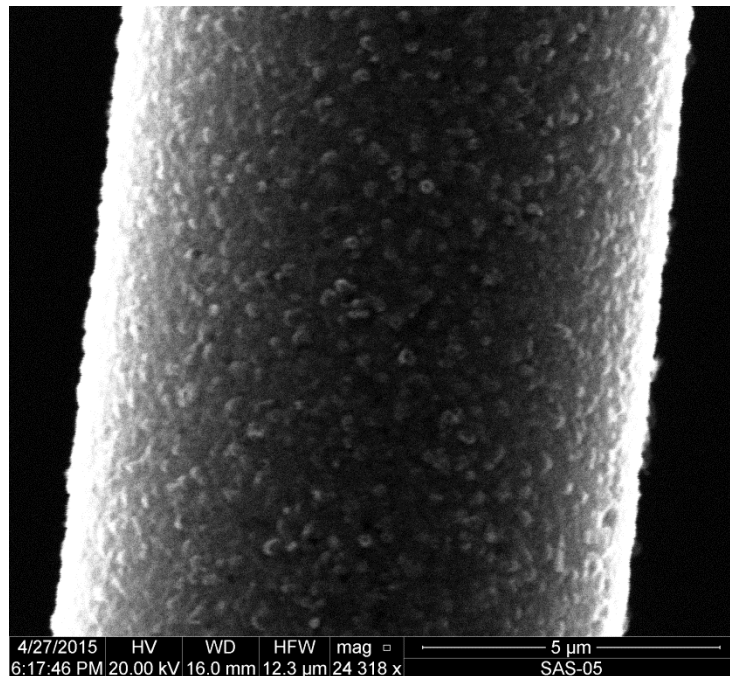


Figure 136: SEM micrograph of the Sylramic-iBN specimen “SS 23” examining rough surface of a fiber toward mid-fiber length ($\sigma_{cr} = 381$ MPa, $t_f = 0$ s)

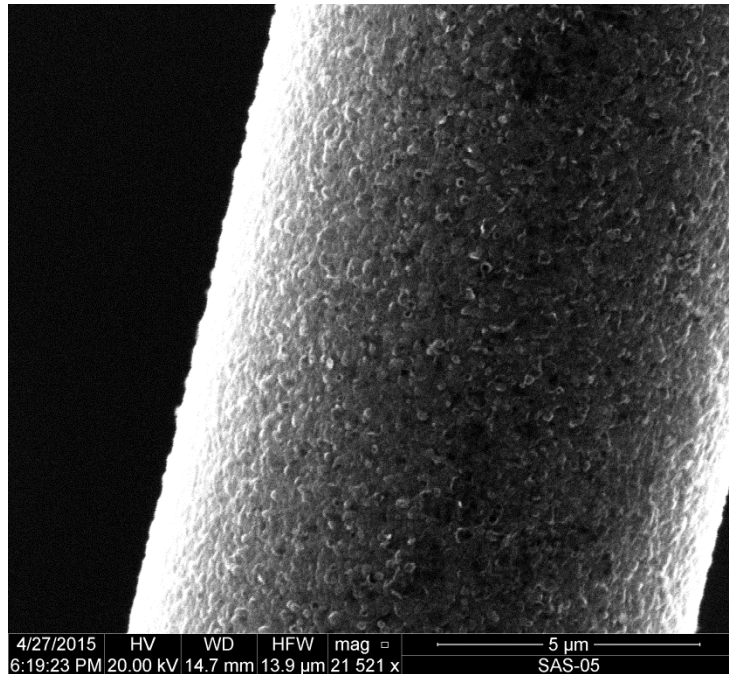


Figure 137: SEM micrograph of the Sylramic-iBN specimen “SS 23” examining rough surface of a fiber toward mid-fiber length ($\sigma_{cr} = 381$ MPa, $t_f = 0$ s)

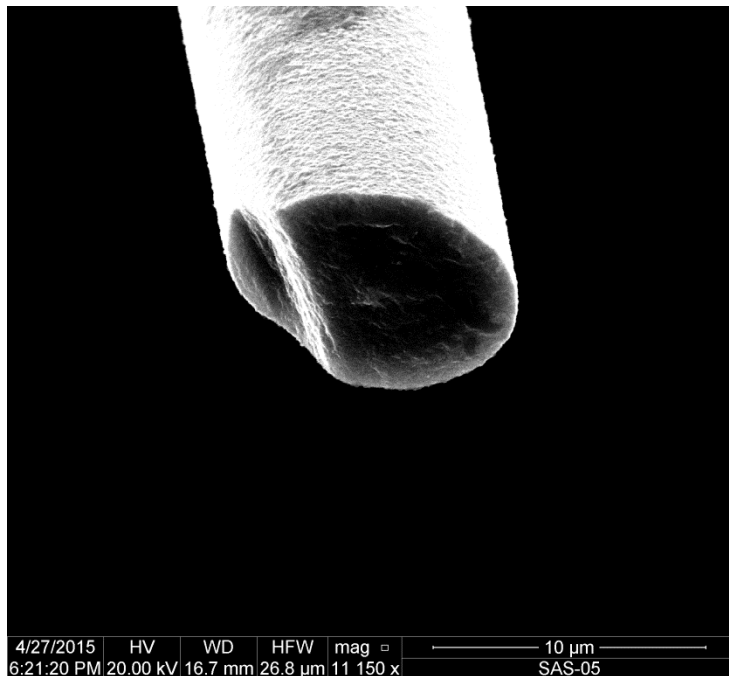


Figure 138: SEM micrograph of the Sylramic-iBN specimen “SS 23” examining cut surface of a fiber at mid-fiber length ($\sigma_{cr} = 381$ MPa, $t_f = 0$ s)

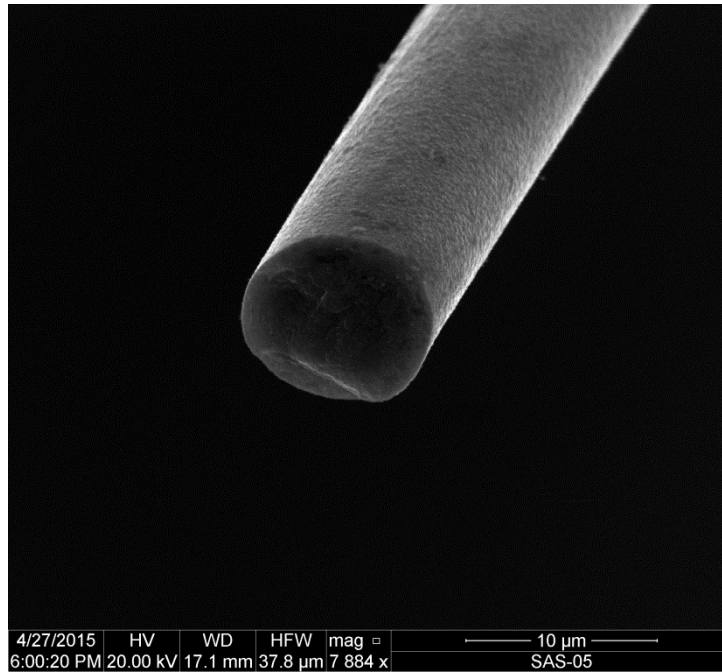


Figure 139: SEM micrograph of the Sylramic-iBN specimen “SS 23” examining fracture surface of a fiber ($\sigma_{cr} = 381$ MPa, $t_f = 0$ s)

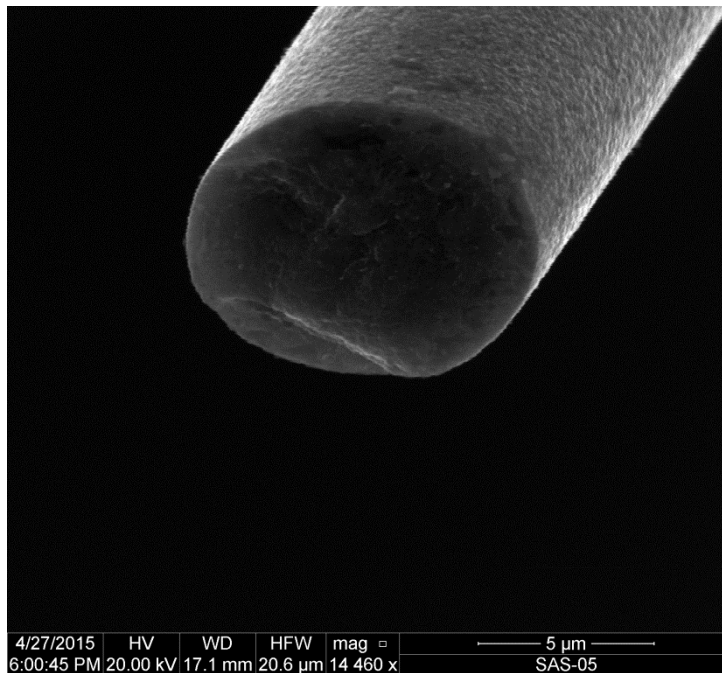


Figure 140: SEM micrograph of the Sylramic-iBN specimen “SS 23” examining fracture surface of a fiber ($\sigma_{cr} = 381$ MPa, $t_f = 0$ s)

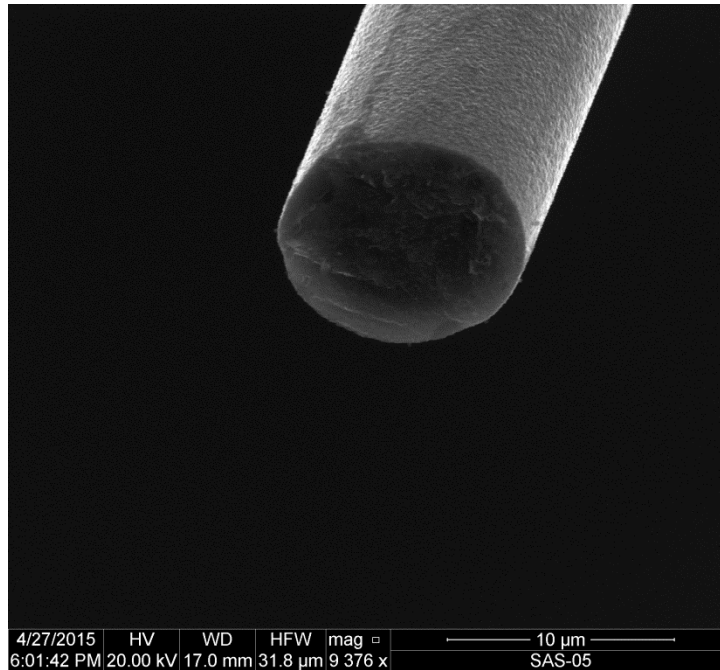


Figure 141: SEM micrograph of the Sylramic-iBN specimen “SS 23” examining fracture surface of a fiber ($\sigma_{cr} = 381$ MPa, $t_f = 0$ s)

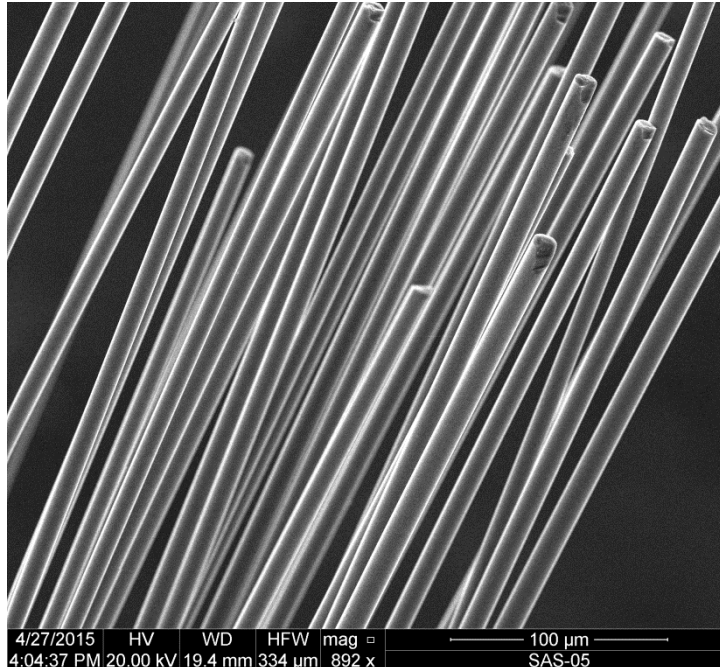


Figure 142: SEM micrograph of the Sylramic-iBN specimen “SS 24” examining general surface characteristics of multiple fibers; notice the uniformity between the fibers ($\sigma_{cr} = 254$ MPa, $t_f > 100$ h)

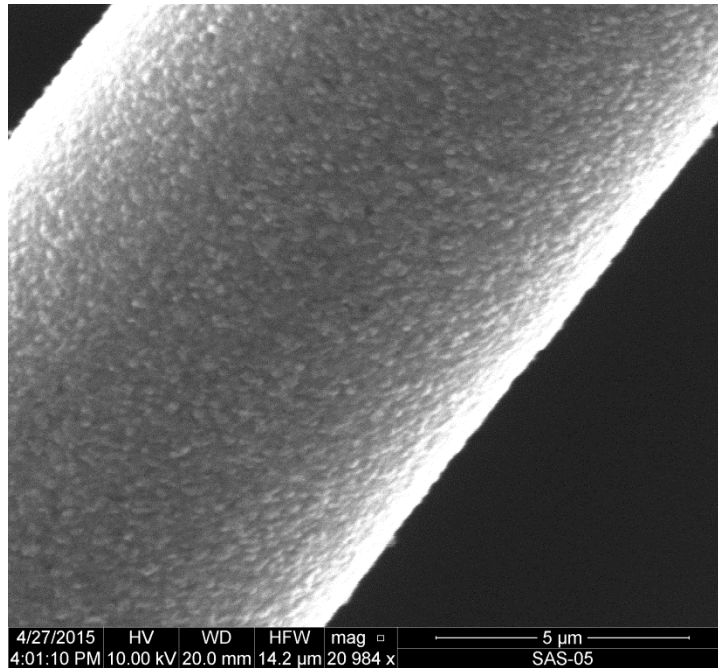


Figure 143: SEM micrograph of the Sylramic-iBN specimen “SS 24” examining rough surface of a fiber toward mid-fiber length ($\sigma_{cr} = 254$ MPa, $t_f > 100$ h)

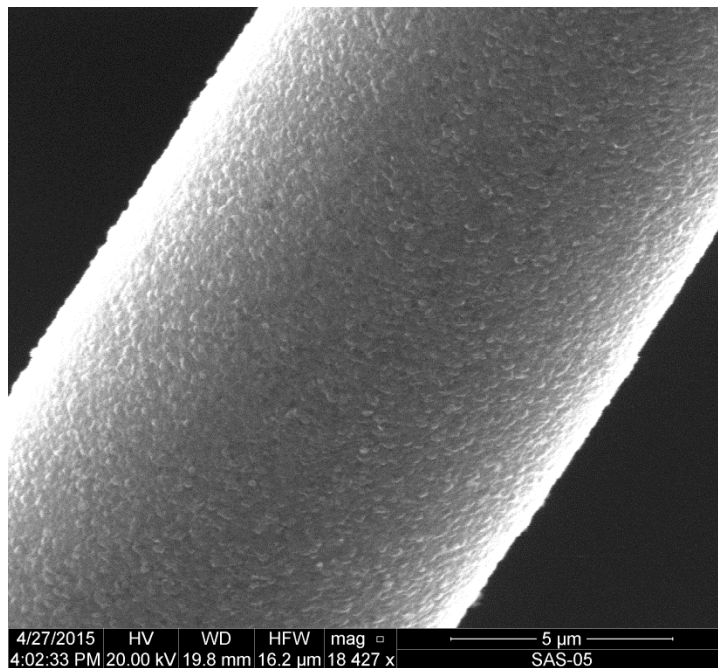


Figure 144: SEM micrograph of the Sylramic-iBN specimen “SS 24” examining rough surface of a fiber toward mid-fiber length ($\sigma_{cr} = 254$ MPa, $t_f > 100$ h)

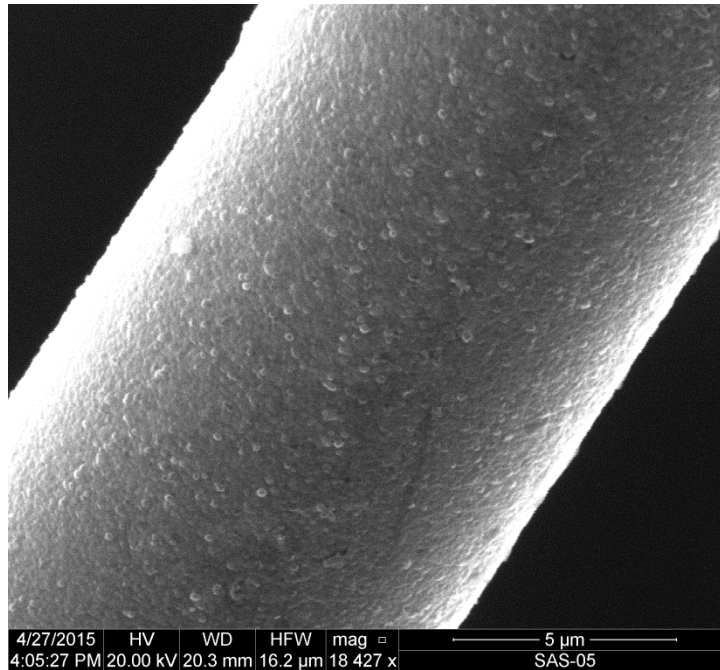


Figure 145: SEM micrograph of the Sylramic-iBN specimen “SS 24” examining rough surface of a fiber toward mid-fiber length ($\sigma_{cr} = 254$ MPa, $t_f > 100$ h)

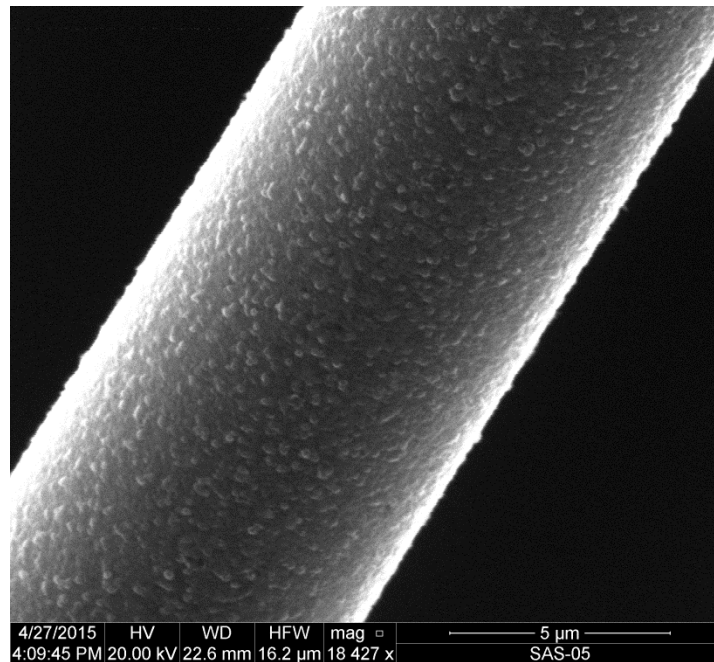


Figure 146: SEM micrograph of the Sylramic-iBN specimen “SS 24” examining rough surface of a fiber toward mid-fiber length ($\sigma_{cr} = 254$ MPa, $t_f > 100$ h)

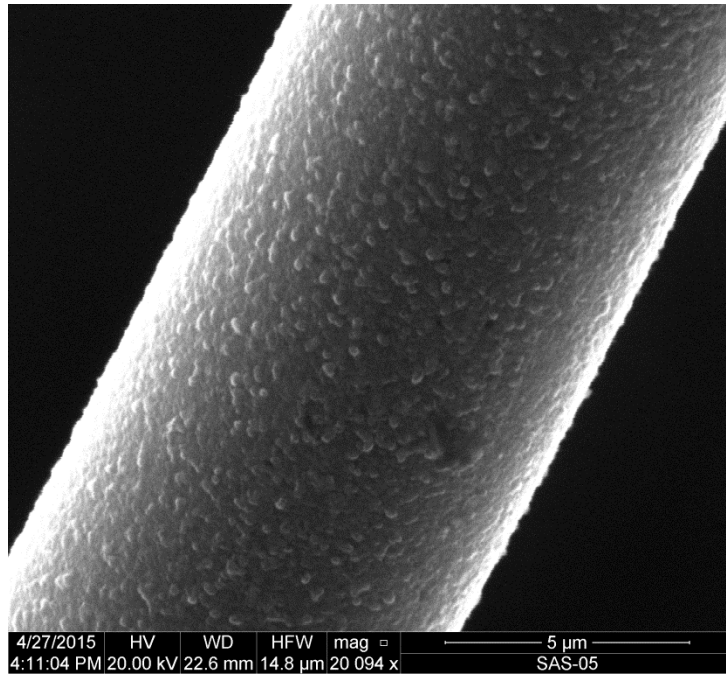


Figure 147: SEM micrograph of the Sylramic-iBN specimen “SS 24” examining rough surface of a fiber toward mid-fiber length ($\sigma_{cr} = 254$ MPa, $t_f > 100$ h)

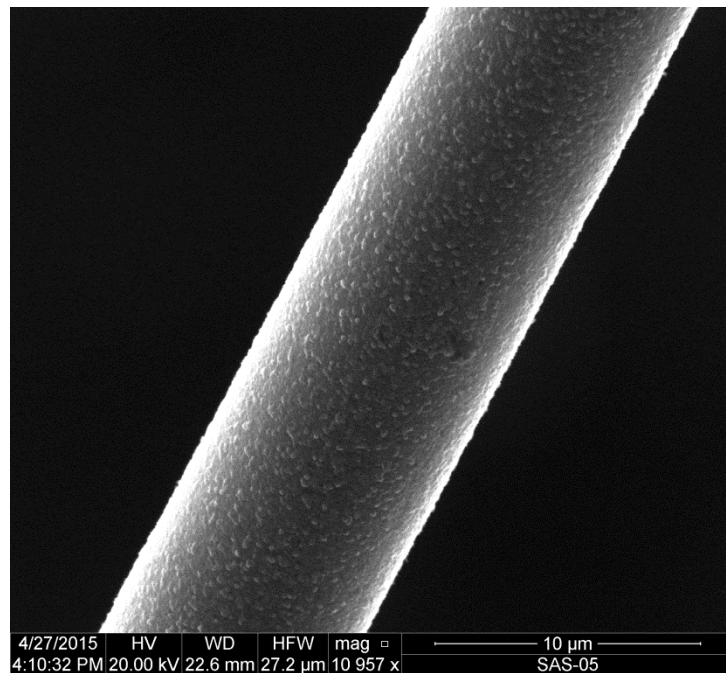


Figure 148: SEM micrograph of the Sylramic-iBN specimen “SS 24” examining rough surface of a fiber toward mid-fiber length ($\sigma_{cr} = 254$ MPa, $t_f > 100$ h)

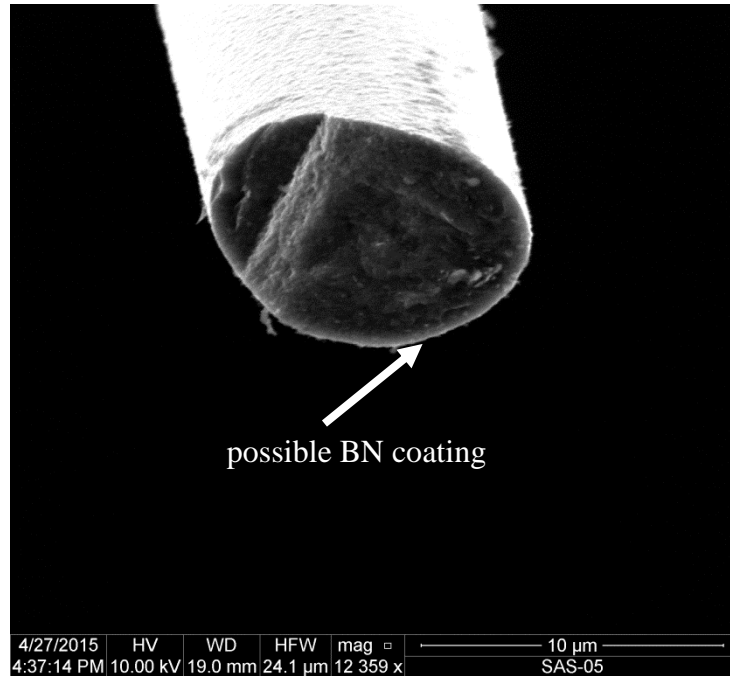


Figure 149: SEM micrograph of the Sylramic-iBN specimen “SS 24” examining cut surface of a fiber at mid-fiber length; notice the BN coating ($\sigma_{cr} = 254$ MPa, $t_f > 100$ h)

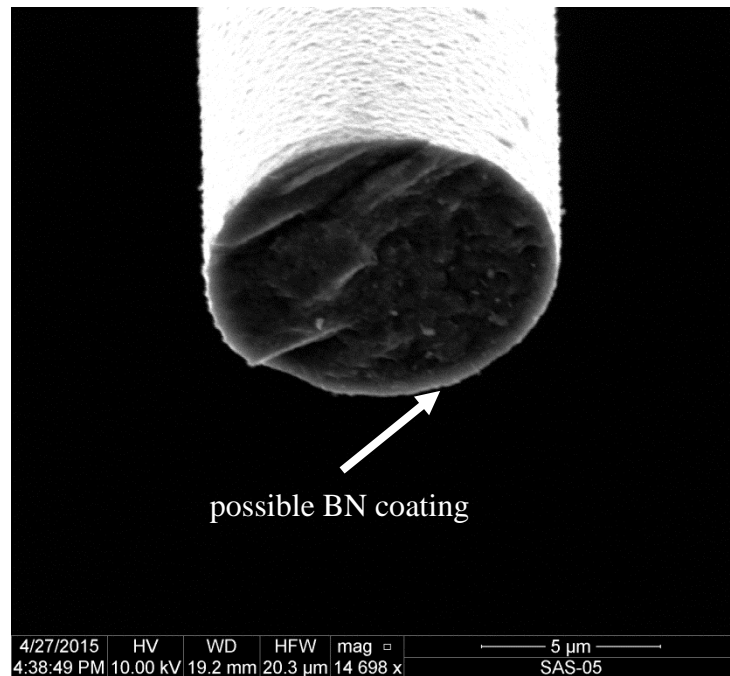


Figure 150: SEM micrograph of the Sylramic-iBN specimen “SS 24” examining cut surface of a fiber at mid-fiber length; notice the BN coating ($\sigma_{cr} = 254$ MPa, $t_f > 100$ h)

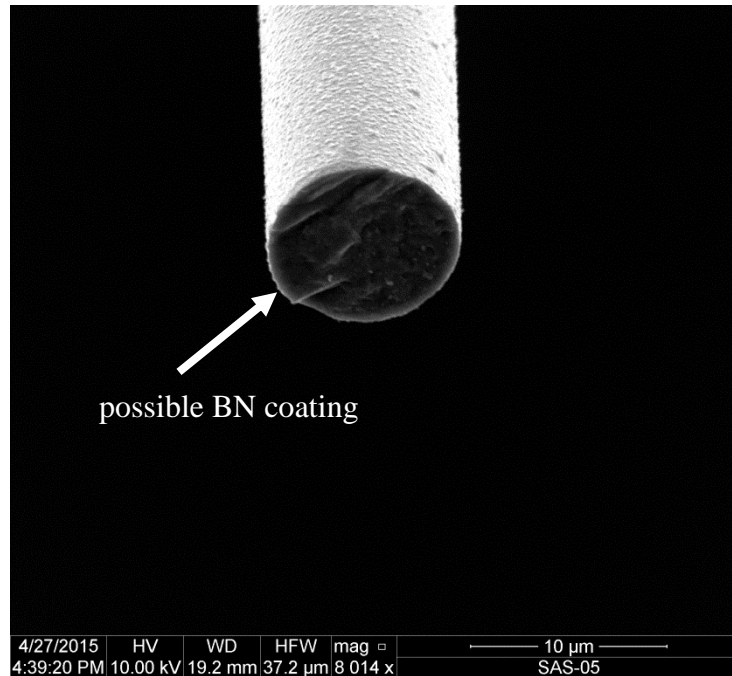


Figure 151: SEM micrograph of the Sylramic-iBN specimen “SS 24” examining cut surface of a fiber at mid-fiber length; notice the BN coating ($\sigma_{cr} = 254$ MPa, $t_f > 100$ h)

Bibliography

- [1] K. K. Chawla, *Ceramic Matrix Composites*, Boston: Kluwer Academic, 2003.
- [2] D. J. Vaughan, "Fiberglass Reinforcement," in *Handbook of Composites, Second Edition*, New York, Chapman and Hall, 1998.
- [3] C. T. Herakovich, *Mechanics of Fibrous Composites*, New York: John Wiley & Sons, 1998.
- [4] H. R. Clauser, "Advanced Composite Materials," *Scientific American*, vol. 229, pp. 36-44, 1973.
- [5] F. Smith, "The Use of Composites in Aerospace: Past, Present and Future Challenges," 2013.
- [6] M. G. Jenkins, S. T. Gonczy, E. Lara-Curzio, J. A. DiCarlo and H. M. Yun, "Fiber Test Development for Ceramic Composite Thermomechanical Properties," in *Mechanical, Thermal and Environmental Testing and Performance of Ceramic Composites and Components: (STP 1392)*, ASTM International, 2000.
- [7] "Lockheed Martin Extends Cytec Contract for F-35 Prepreg," Gardner Business Media, Inc, 2 May 2011. [Online]. Available: <http://www.compositesworld.com/news/lockheed-martin-extends-cytec-contract-for-f-35-prepreg>. [Accessed November 2014].
- [8] K. ., E. D. S. Jost, "Ceramic Matrix Composites," *Composite Materials Handbook*, vol. 5, 2002.
- [9] T. R. Shillig, "Creep of Hi-Nicalon S Fiber Tows at Elevated Temperature in Air and in Steam," *MS Thesis. Air Force Institute of Technology (AU), Wright-Patterson Air Force Base*, March 2013.
- [10] J. A. DiCarlo, H. M. Yun, G. N. Morscher and R. T. Bhatt, "SiC/SiC Composites for 1200°C and Above," in *Handbook of Ceramic Composites*, Springer US, 2005, pp. 77-98.
- [11] S. Schmidt, H. Knabe, H. Immich, R. Mestring and A. Gessler, "Advanced Ceramic Matrix Composite Material for Current and Future Propulsion Technology Application," *Acta Astronautica*, vol. 55, pp. 409-420, 2004.
- [12] H. N. Wadley, "High Temperature Coatings," University of Virginia, 24 April 2013. [Online]. Available: <http://www.virginia.edu/ms/research/wadley/high-temp.html>.

[Accessed February 2015].

- [13] N. P. Bansal, *Handbook of Ceramic Composites*, Boston: Springer US, 2005.
- [14] N. E. Dowling, *Mechanical Behavior of Materials: Engineering Methods of Deformation, Fracture, and Fatigue: 3rd Edition*, Pearson Prentice Hall, 2007.
- [15] C. J. Armani, "Creep Performance of Oxide Ceramic Fiber Materials at Elevated Temperature in Air and in Steam," *PhD Dissertation. Air Force Institute of Technology (AU), Wright-Patterson Air Force Base*, March 2011.
- [16] F. W. Zok and C. G. Levi, "Mechanical Properties of Porous-Matrix Ceramic Composites," *Advanced Engineering Materials*, vol. 3, no. 1, pp. 15-23, 2001.
- [17] M. Ruggles-Wrenn, J. Delapasse, A. Chamberlain, J. Lane and T. Cook, "Fatigue Behavior of a Hi-NicalonTM/SiC-B4C Composite at 1200°C in Air and in Steam," *Materials Science and Engineering: A*, vol. 534, pp. 119-128, 2012.
- [18] F. E. Heredia, J. C. McNulty, F. W. Zok and A. G. Evans, "An Oxidation Embrittlement Probe for Ceramic Matrix Composites," *Journal of American Ceramic Society*, vol. 78, pp. 2097-2100, 1995.
- [19] J. A. DiCarlo and H. M. Yun, "Overview of NASA Studies on High-Temperature Ceramic Fibers," *2000 NASA Seal/Secondary Air System Workshop*, vol. 1, pp. 439-448, 2001.
- [20] J. A. DiCarlo and H. M. Yun, "Thermomechanical Characterization of SiC Fiber Tows and Implications for CMC," NASA, 1999.
- [21] G. N. Morscher and V. V. Pujar, "Design Guidelines for In-Plane Mechanical Properties of SiC Fiber-Reinforced Melt-Infiltrated SiC Composites," *International Journal of Applied Ceramic Technology*, vol. 6, no. 2, pp. 151-163, 2009.
- [22] J. B. Wachtman, *Mechanical Properties of Ceramics*, John Wiley, 1996.
- [23] S. J. Robertson, "Creep of Hi-Nicalon S Ceramic Fiber Tows at Intermediate Temperatures in Air and in Steam," *PhD Dissertation. Air Force Institute of Technology (AU), Wright-Patterson Air Force Base*, (projected for publication in September 2015).
- [24] J. B. Wachtman, W. R. Cannon and M. J. Matthewson, *Mechanical Properties of Ceramics: Second Edition*, John Wiley & Sons, 2009.
- [25] A. Bunsell and A. Piant, "A Review of the Development of Three Generations of Small Diameter Silicon Carbide Fibers," *Journal of Material Science*, vol. 41, pp.

823-839, 2006.

- [26] R. Naslain, "Design, Preparation and Properties of Non-Oxide CMCs for Applications in Engines and Nuclear Reactors: An Overview," *Composites Science and Technology*, vol. 64, no. 1, pp. 155-170, 2004.
- [27] H. Ichikawa, K. Okamura and T. Seguchi, "High Temperature Ceramic Matrix Composites II," *American Ceramic Society*, vol. 58, pp. 65-74, 1995.
- [28] M. H. Berger, "Advances in Ceramic Matrix Composites IX," *American Ceramic Society*, vol. 153, p. 3, 2003.
- [29] T. Ishikawa, "Advances in Inorganic Fibers," *Polymeric and Inorganic Fibers*, vol. 178, 2005.
- [30] J. A. DiCarlo and H. M. Yun, "New High-Performance SiC Fiber Developed for Ceramic Composites," in *Research & Technology*, DIANE Publishing, 2002, pp. 8-9.
- [31] J. A. DiCarlo and H. M. Yun, "Comparison of the Tensile, Creep, and Rupture Strength Properties of Stoichiometric SiC Fibers," *23rd Annual Conference on Composites, Advanced Ceramics, Materials, and Structures : A*, vol. 20, no. 3, p. Chapter 31, article (1999); book (2008).
- [32] B. R. Steffens, "Creep of Hi-Nicalon S Ceramic Fiber Tows at Elevated Temperature in Air and in Steam," *MS Thesis. Air Force Institute of Technology (AU), Wright-Patterson Air Force Base*, March 2012.
- [33] R. Naslain, R. Pailler and J. Lamon, "Single and Multilayered Interphases in SiC/SiC Composites Exposed to Severe Environmental Conditions: An Overview," *International Journal of Applied Ceramic Technology*, vol. 7, no. 3, pp. 263-275, 2010.
- [34] R. Naslain, "The Design of the Fibre-Matrix Interfacial Zone in Ceramic Matrix Composites," *Composites Part A*, vol. 29A, pp. 1145-1155, 1998.
- [35] R. Naslain, R. Pailler, X. Bourrat, S. Bertrand, F. Heurtevent, P. Dupel and F. Lamouroux, "Synthesis of Highly Tailored Ceramic Matrix Composites by Pressure-Pulsed CVI," *Solid State Ionics*, vol. 541, pp. 141-142, 2001.
- [36] P. Forio, F. Lavaire and J. Lamon, "Delayed Failure at Intermediate Temperatures (600-700°C) in Air in Silicon Carbide Multifilament Tows," *Journal of the American Ceramic Society*, vol. 87, no. 5, p. 888, 2004.

- [37] W. Gauthier and J. Lamon, "Delayed Failure of Hi-Nicalon and Hi-Nicalon S Multifilament Tows and Single Filaments at Intermediate Temperatures (500-800°C)," *Journal of American Ceramic Society*, vol. 92, no. 3, pp. 702-709, 2009.
- [38] W. Gauthier, F. Pailler, J. Lamon and R. Pailler, "Oxidation of Silicon Carbide Fibers During Static Fatigue in Air at Intermediate Temperatures," *Journal of American Ceramic Society*, vol. 92, no. 9, pp. 2067-2073, 2009.
- [39] P. Ladeveze and M. Genet, "A New Approach to the Subcritical Cracking of Ceramic Fibers," *Composites Science and Technology*, vol. 70, pp. 1575-1583, 2010.
- [40] J. A. DiCarlo, "Modeling Creep of SiC Fibers and Its Effects on High-Temperature SiC/SiC CMC," NASA Glenn Research Center, Cleveland, OH, 2014.
- [41] V. Carland and J. Lamon, "Failure of Fiber Bundles," *Composites Science and Technology*, vol. 64, no. 5, pp. 701-710, 2004.
- [42] K. G. Dassios, M. Steen and C. Filiou, "Mechanical Properties of Alumina Nextel 720 Fibers at Room and Elevated Temperatures: Tensile Bundle Testing," *Materials Science and Engineering*, vol. 349, no. 1-2, pp. 63-72, 2003.
- [43] R. M. Morrell, "A Tenile Creep-Testing Apparatus for Ceramic Materials Using Simple Knife-Edge Universal Joints," *Journal of Physics E: Scientific Instruments*, vol. 5, no. 5, pp. 465-467, 1972.
- [44] F. A. Kandil and B. F. Dyson, "Tensile Creep of Ceramics: The Development of a Testing Facility," *International Journal of High Technology Ceramics*, vol. 4, no. 2-4, pp. 243-262, 1988.
- [45] J. A. DiCarlo, "Property Goals and Test Methods for High Temperature Ceramic Fiber Reinforcement," *Ceramics International*, vol. 23, no. 4, pp. 283-289, 1997.
- [46] S. J. Robertson, K. B. Sprinkle and M. B. Ruggles-Wrenn, "An Apparatus for Testing SiC Fiber Tows at Elevated Temperatures in Silicic Acid-Saturated Steam," *Air Force Institute of Technology (AU), Wright-Patterson Air Force Base*, (submitted for publication 2015).
- [47] R. S. Hay, *Personal Communication: discussion regarding inconsistent results with tensile testing of Sylramic-iBN fiber tows*, April 9, 2015.
- [48] K. Ozawa, Y. Katoh, E. Lara-Curzio, L. Snead and T. Nozawa, "Comparative Study of Tensile Properties of Uni-Directional Single-Tow SiC-Matrix Composites Reinforced with Various Near-Stoichiometric SiC Fibers," in *Mechanical Properties and Performance of Engineering Ceramics and Composites V: Ceramic Engineering and Science Proceedings*, vol. 31, Hoboken, NJ, John Wiley & Sons, 2010, pp. 207-

220.

- [49] R. T. Bhatt, Y. L. Chen and G. N. Morscher, "Microstructure and Tensile Properties of BN/SiC Coated Hi-Nicalon, and Sylramic SiC Fiber Preforms," *Journal of Material Science*, vol. 37, no. 18, pp. 3991-3998, 2002.

REPORT DOCUMENTATION PAGE			Form Approved OMB No. 0704-0188		
<p>The public reporting burden for this collection of information is estimated to average 1 hour per response, including the time for reviewing instructions, searching existing data sources, gathering and maintaining the data needed, and completing and reviewing the collection of information. Send comments regarding this burden estimate or any other aspect of this collection of information, including suggestions for reducing this burden to Department of Defense, Washington Headquarters Services, Directorate for Information Operations and Reports (0704-0188), 1215 Jefferson Davis Highway, Suite 1204, Arlington, VA 22202-4302. Respondents should be aware that notwithstanding any other provision of law, no person shall be subject to any penalty for failing to comply with a collection of information if it does not display a currently valid OMB control number.</p> <p>PLEASE DO NOT RETURN YOUR FORM TO THE ABOVE ADDRESS.</p>					
1. REPORT DATE (DD-MM-YYYY) 26-05-2015		2. REPORT TYPE Master's Thesis		3. DATES COVERED (From - To) August 2013 – June 2015	
4. TITLE AND SUBTITLE Creep of Sylramic-iBN Fiber Tows at Elevated Temperature in Air and in Silicic Acid-Saturated Steam			5a. CONTRACT NUMBER		
			5b. GRANT NUMBER		
			5c. PROGRAM ELEMENT NUMBER		
6. AUTHOR(S) Sprinkle Kevin B, Capt, USAF			5d. PROJECT NUMBER		
			5e. TASK NUMBER		
			5f. WORK UNIT NUMBER		
7. PERFORMING ORGANIZATION NAME(S) AND ADDRESS(ES) Air Force Institute of Technology Graduate School of Engineering and Management (AFIT/EN) 2950 Hobson Way WPAFB OH 45433-7765			8. PERFORMING ORGANIZATION REPORT NUMBER AFIT-ENY-15-J-46		
9. SPONSORING / MONITORING AGENCY NAME(S) AND ADDRESS(ES) Air Force Research Laboratory Dustin Shaw 2977 Hobson Way, Building 652 Wright-Patterson AFB, OH 45433 dustin.shaw.1@us.af.mil			10. SPONSOR/MONITOR'S ACRONYM(S) AFRL/RXSSR		
			11. SPONSOR/MONITOR'S REPORT NUMBER(S)		
12. DISTRIBUTION / AVAILABILITY STATEMENT Distribution Statement A. Approved for Public Release: Distribution Unlimited					
13. SUPPLEMENTARY NOTES This work is declared a work of the U.S. Government and is not subject to copyright protection in the United States.					
14. ABSTRACT Stressed oxidation experiments on Sylramic-iBN fiber tows were performed to evaluate the novel fiber's mechanical performance, creep behavior, and creep mechanisms. This research effort investigated creep response of Sylramic-iBN fiber tows at elevated temperatures in both air and in silicic acid-saturated steam environments. Creep experiments were conducted at creep stresses ranging from 127 to 762 MPa at 400°C and 500°C in order to examine the mechanical behavior of the Sylramic-iBN fiber tows at temperatures below and above the melting point of boria (450°C). Sylramic-iBN fibers are known to have excellent creep resistance, better than most other non-oxide fibers and significantly better than oxide fibers. These fibers have a near-stoichiometric SiC composition, so they are a strong candidate for use in advanced aerospace CMCs. This research effort is a pilot program on the study of the effects of steam on Sylramic-iBN fibers. Previous attempts to study creep of SiC fiber tows in steam at elevated temperatures at the Air Force Institute of Technology's (AFIT) Mechanics of Advanced Aerospace Materials Research Laboratory have yielded inconclusive results. Prior work at AFIT showed that the steam extracted silicon from the fiber tow and became saturated with silicic acid (Si[OH]4). As the steam traveled along the SiC fiber, it also chemically altered the fiber surface producing inconsistent chemical compositions along the length of the fiber tow specimen. Along the fiber portion exposed to the unsaturated steam, the fiber experienced a chemical change leading to material loss, while the fiber portion exposed to the saturated steam experienced a silica scale growth along the fiber surface. A new test facility had to be designed to accurately evaluate the effects of steam on SiC fibers. The facility design incorporated an apparatus for saturating steam with silicic acid prior to entering the test chamber. The facility was validated by performing creep tests of SiC fiber tows in saturated steam at elevated temperature.					
15. SUBJECT TERMS Ceramic Matrix Composites, Composite Materials, Ceramic Fibers, Fiber Tows, Ceramic Materials, Fiber Reinforced Composites, Creep, Sylramic Fiber, Sylramic-iBN Fiber, Steam, Air, Saturated Steam, Silicic Acid, Elevated Temperature					
16. SECURITY CLASSIFICATION OF:			17. LIMITATION OF ABSTRACT	18. NUMBER OF PAGES	19a. NAME OF RESPONSIBLE PERSON
a. REPORT U	b. ABSTRACT U	c. THIS PAGE U	UU	178	Dr. Marina B. Ruggles-Wrenn, AFIT/ENY
19b. TELEPHONE NUMBER (Include Area Code) 9372553636x4641 marina.ruggles-wrenn@afit.edu					

Standard Form 298 (Rev. 8-98)
Prescribed by ANSI Std. Z39.18